Impact of turbine- and farm-scale flow effects on wind farm performance

Andrew Kirby

Trinity College

University of Oxford

A thesis submitted for the degree of

Doctor of Philosophy

Trinity 2024

A person is a person through other persons
Ubuntu saying

You gotta protect that ambition from taking over
Jon Batiste

If we take time to look around,
we see ourselves surrounded by lovely moments
Haemin Sunim

The world is made up of many worlds
Wim Wenders and Takuma Takasaki

Acknowledgements

I would firstly like to thank my supervisor Dr. Takafumi Nishino. His continuous support throughout my D.Phil contributed greatly to making my D.Phil an enjoyable experience. It was a true pleasure to work together with his empathetic supervising style and commitment to student wellbeing. In addition, I benefited greatly from his deep technical knowledge on the subject of fluid mechanics. Thank you.

I would also like to thank my secondary supervisor Dr Tom Dunstan. His technical guidance was very helpful to the work presented in this thesis. I am grateful for his work facilitating my placement in the Informatics Lab at the UK Met Office and for making me feel so welcome there.

I believe working with others is one of the best ways to learn new things. Therefore I am grateful to the external collaborators whom I worked with during my D.Phil: Dr François-Xavier Briol (University College London), Professor Johan Meyers (KU Leuven) and Luca Lanzilao (KU Leuven). It was great working with you and I learnt a lot in the process.

I also acknowledge the NERC-Oxford Doctoral Training Partnership in Environmental Research (NE/S007474/1) for funding and training. I would like to thank everyone involved in this program as this research would not have happened without it.

I would like to thank everyone in the 'Tidal and Wind' research group at the University of Oxford. It's been great to work with you all. Equally, I would like to thank everyone in the 'Informatics Lab' at the UK Met Office for welcoming me for 6 months.

I don't believe any piece work is the result of just one person. I believe everyone is supported by a large number of people doing their jobs. I would like to thank all administrative and support staff at the University of Oxford, the Department of Engineering Science, Trinity College Oxford and the UK Met Office. I also thank all my teachers I've had over the years, I owe you a great deal.

Thanks also to all my friends I've met during the process, including in Room 11 and 'The Penthouse'. I'm also grateful to my friends Dimitrios and Gioannis, and for their insightful conversations. I'm grateful to the community provided by the Met Office Cricket Club, Exmouth Cricket Club and Oxenford Cricket Club.

I would like to thank my family for everything they have done over the years. A big thank you to Lena and Neil for hosting me for 6 months in Exmouth. Your warmth and generosity will stay with me for a long time. Lastly, thank you Maddie, you're awesome.

Abstract

When wind turbines are placed together in a farm, they produce less power than in isolation. Behind every turbine is a low speed wake which can reduce the power output of downstream turbines. These turbine-wake interactions depend highly on the wind direction and turbine layout. The interaction between the atmosphere and the farm as a whole also causes power losses. Understanding and predicting these power losses is vital for the offshore wind energy sector.

To better understand farm performance, we propose new measures of 'turbine-scale loss' and 'farm-scale loss'. The 'turbine-scale loss' quantifies the power loss due to internal flow interactions only (i.e. turbine-wake interactions). The 'farm-scale loss' gives the loss due to the farm-atmosphere interaction. We conduct a combined theoretical and computational study to show that, for large offshore wind farms, the power losses on the farm-scale is typically more than twice as large as on the turbine-scale. This is contrary to the current consensus that turbine-wake interactions are the most important effects for wind farms.

Traditionally, power losses in farms are classified into 'wake losses' and 'farm blockage losses'. However, we show that neither loss is well correlated to the overall wind farm efficiency. In contrast, the new 'farm-scale loss' is shown to be strongly correlated with the overall farm efficiency. These new metrics give a novel and clear understanding of the aerodynamics influencing wind farm efficiency.

We also develop new low-cost models to predict the turbine- and farm-scale losses in wind farms. To predict turbine-scale losses, we develop statistical emulators to predict the turbine-wake interactions as a function of the turbine layout. The statistical emulators are trained using a multi-fidelity Gaussian Process on high-fidelity large-eddy simulations and low-fidelity wake model predictions. The trained emulators predict the farm

‘internal’ turbine thrust coefficient with a mean absolute error of less than 1% compared to the high-fidelity simulations.

To predict farm-scale losses, we derive a simple analytical model to predict the farm-atmosphere interactions. The model is derived using a quasi-one-dimensional control volume analysis. An initial comparison with high-fidelity wind farm simulations shows a satisfactory agreement in the prediction of farm-scale losses. These two new models could be used to predict the performance of large wind farms at a very low computational cost, and to optimise the design of future farms.

Nomenclature

Greek symbols

α	Turbine-scale wind speed reduction factor
β	Farm wind-speed reduction factor
β_{local}	Spanwise- and vertically-averaged wind speed reduction factor
η_f	Farm efficiency
η_w	Wake efficiency
η_{FS}	Farm-scale efficiency
η_{nl}	'Non-local' farm efficiency
η_{TS}	Turbine-scale efficiency
γ	Bottom friction exponent
λ	Array density
Π	Total loss factor
Π_F	Farm-scale loss factor
Π_T	Turbine-scale loss factor
τ_t	Shear stress at the top of the farm control volume
τ_w	Bottom shear stress
θ	Wind direction relative to reference x direction
ζ	Wind extractability factor

Roman symbols

A	Rotor swept area

C Streamwise component of the Coriolis force averaged over the control volume

C_p Turbine power coefficient

C_p^* 'Local' or 'internal' turbine power coefficient

C_T' Turbine resistance coefficient

C_T^* 'Local' or 'internal' turbine thrust coefficient

C_{f0} Natural friction coefficient of the surface

$C_{p,Betz}$ Power coefficient of an isolated ideal turbine

D Turbine diameter

h Atmospheric boundary layer height

H_F Height of nominal farm-layer

H_{hub} Turbine hub-height

L Wind farm length

M Momentum availability factor

M_F Total net momentum flux into the farm control volume

n Total number of turbines in the farm

P_1 Front-row-averaged turbine power

P_∞ Power of an isolated turbine

P_i Power of turbine i in the farm

P_{farm} Farm-averaged turbine power

S_F Wind farm area

S_x Turbine spacing in the x direction

S_y Turbine spacing in the x direction

T_i Thrust of turbine i in the farm

U Velocity in the hub-height wind direction

V_{CV} Volume of the control volume

W	Wind farm width
X	Net streamwise momentum injection through the top and side boundaries of the farm control volume
x_F	Hub-height wind direction

Contents

List of Figures

Chapter 1

Introduction

1.1 Context

Atmospheric carbon dioxide levels are at the highest levels for 800,000 years (figure 1.1). The increased levels of carbon dioxide amplify the greenhouse effect and cause global warming. In 2022, the planet was 1.15 ^{o}C warmer than the pre-industrial average (1850-1990) and the last 8 years were the warmest on record [134].

Many changes in the climate system become larger with increasing global warming. These include increases in the frequency and intensity of hot extremes, marine heatwaves, heavy precipitation; an increase in the proportion of intense tropical cyclones; and reductions in Arctic sea ice, snow cover and permafrost [49].

To limit the impacts of global warming, there exists global agreements and frameworks to guide progress. As an example, the 'Paris Agreement' is a legally binding international treaty on climate change adopted in 2015 [1]. It sets out to hold 'the increase in the global average temperature to well below 2 ^{o}C above pre-industrial levels' and 'pursue efforts to limit the temperature increase to 1.5 ^{o}C above pre-industrial levels'. To meet these targets a rapid transition from fossil fuels to renewable energy sources is needed [48].

In 2022, wind energy met 17% of the electricity demand in the EU and UK [36]. The roll-out of wind energy is increasing rapidly. The total installed capacity of wind energy in Europe has roughly doubled in the past 10 years (figure 1.2). Across Europe, offshore wind made up 13% of new wind energy capacity. In the UK this figure is 70% [36].

The average size of offshore wind farms is increasing and set to increase further in the future [129]. In the UK, the average size of operating offshore wind farms is 0.3 GW. However, the average size of farms currently under construction is 1.1 GW [35]. As wind farms become larger, the aerodynamics of energy extraction changes [95].

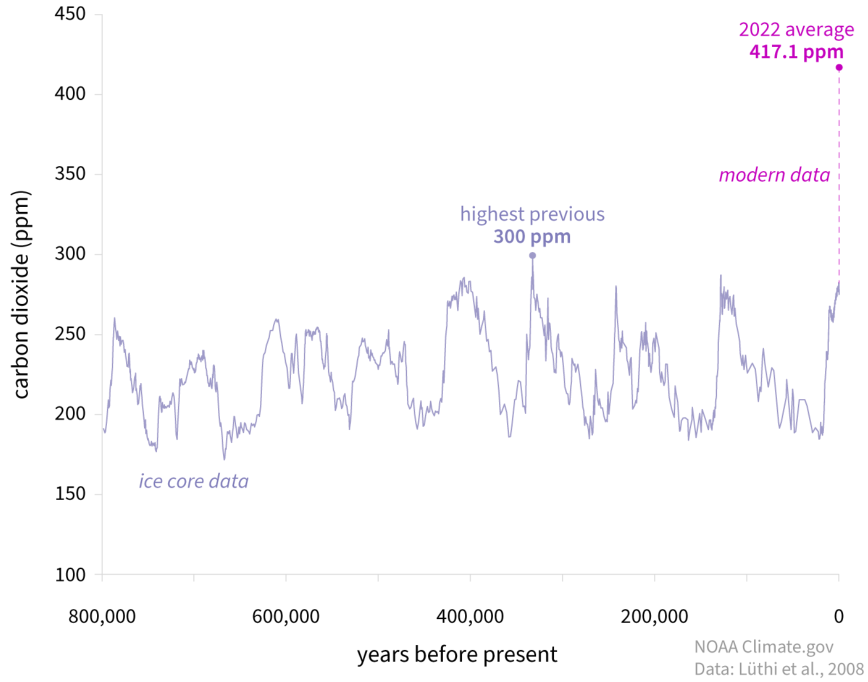

Figure 1.1: Atmospheric carbon dioxide (CO_2) in parts per million (ppm) for the past 800,000 years based on ice-core data [28].

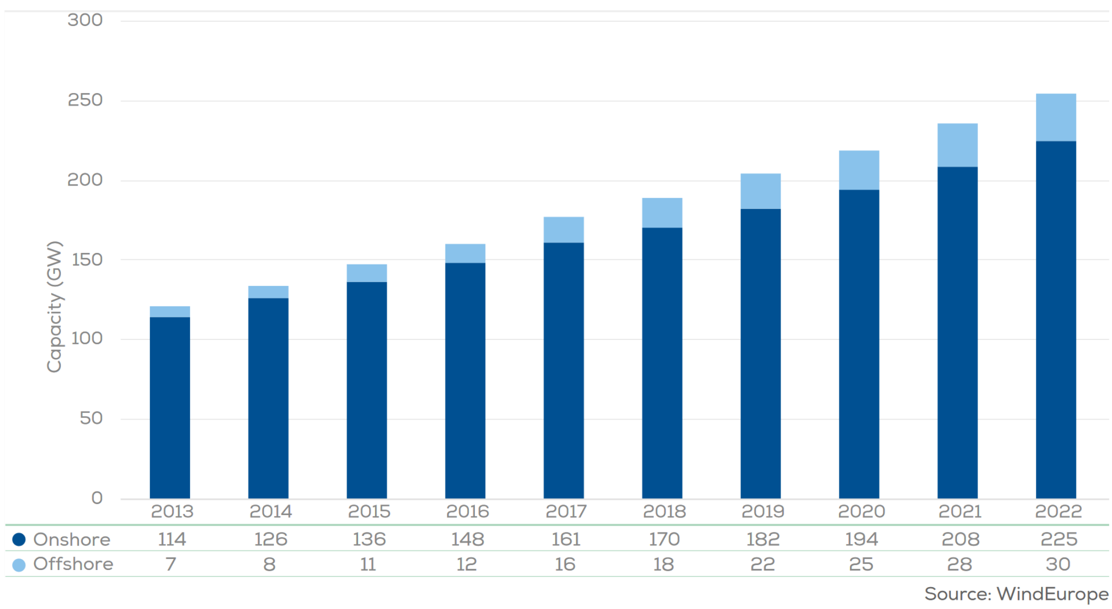

Figure 1.2: Installed wind power capacity in Europe, 2013-2022 [36].

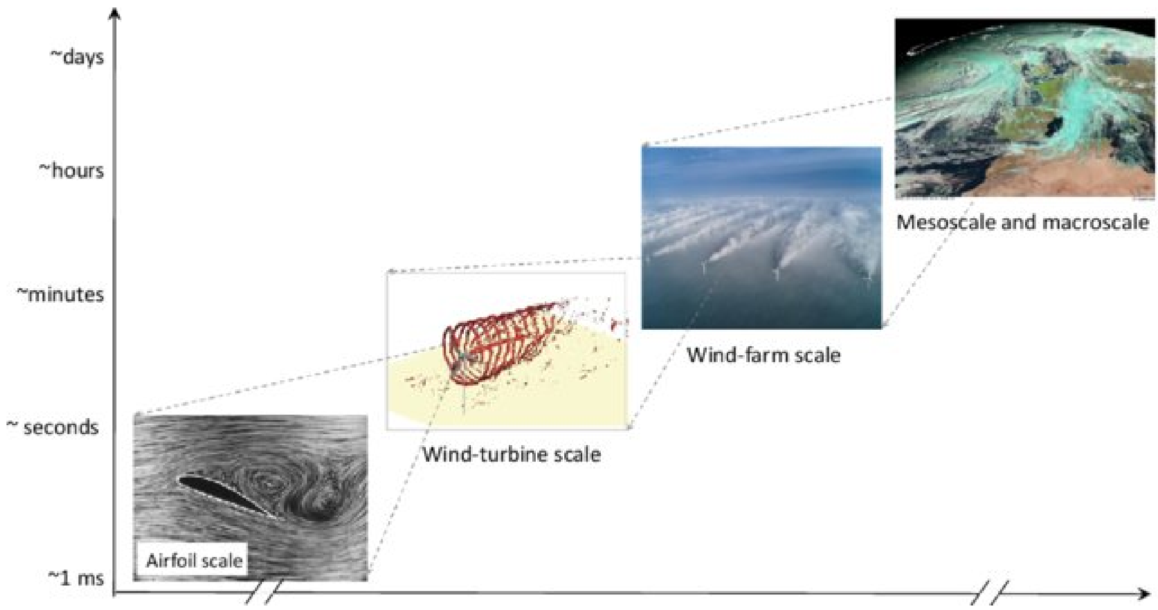

Figure 1.3: Range of flow scales relevant to wind energy. Reproduced from [95].

Existing wind farm models can, in some cases, give 'dramatic' errors in farm performance [85]. This motivates the development of new tools to predict farm performance and for wind farm design.

When wind turbines are placed together in a farm, they produce less power than in isolation. Behind every turbine, there is a turbulent wake which has a reduced wind speed. When turbine wakes interact with other turbines within a farm, this can cause substantial power losses. Power losses also occur because of the interaction of the farm with the atmospheric boundary layer (ABL). Predicting the power output of wind farms remains an unsolved challenge [95]. This is due to the large range of relevant flow scales which impact wind farm performance (figure 1.3). The work presented in this thesis aims to improve the understanding of wind farm aerodynamics and predictions of farm performance.

1.2 Wind farm aerodynamics

1.2.1 Atmospheric stability

Wind farms operate in the ABL. Within the ABL the wind speed and direction changes with height. The temperature also changes with height. The changes in temperature cause buoyancy forces. When describing buoyancy it is convenient to introduce potential temperature θ defined as

$$\theta = T \left(\frac{p}{p_{ref}} \right)^{-\frac{R_d}{C_p}} \tag{1.1}$$

where p is the atmospheric pressure, p_{ref} the reference pressure, R_d is the gas constant for dry air and C_p is the specific heat capacity for air at constant pressure. The potential temperature is the temperature of an air parcel which is brought adiabatically to a reference pressure p_{ref} [45].

Buoyancy has a significant impact on ABL dynamics. Buoyancy can produce or suppress vertical motions, which can alter the turbulence characteristics. A stable ABL is characterised by a potential temperature which increases with height. An unstable ABL has decreasing potential temperature with height and a neutral ABL has a constant vertical profile. Due to the suppression of vertical motions, stable ABLs have a lower levels of turbulence [141, 3, 6]. As such stable ABLs are thinner than unstable ABLs [141, 3, 6].

Atmospheric stability changes both in space and time. Over land there is a strong diurnal cycle [124]. Typically, unstable conditions occur during the day and stable conditions during the night. Over the ocean the temperature remains nearly constant throughout the day so there is no clear diurnal cycle. Conventionally neutral boundary layers (CNBLs) commonly occur in offshore locations [50, 64, 66, 65]. CNBLs consist of a neutrally stratified boundary layer topped by a stable capping inversion and free atmosphere above. As such, it is common to investigate wind farm performance in CNBLs [135, 7, 62].

1.2.2 Turbine-scale flows

The turbulent wake behind a single turbine has been studied extensively [95]. These studies have included field measurements [11], laboratory experiments [14] and numerical simulations [137, 138, 3]. Due to turbulent entrainment, the wake grows in lateral and vertical directions (see figure 1.4). The streamwise velocity increases until it recovers completely. The wake recovers faster when the inflow is more turbulent [138].

Turbine-wake interactions cause substantial power losses in wind farms. Wake losses are normally measured by reporting the normalised turbine power, i.e. turbine power normalised by the power of a front row turbine. Measurements from the Nysted and Horns Rev wind farms show the wake losses can be as high as 40% [12, 10] (figure 1.5). Large-Eddy Simulations (LES) of extended wind farms showed wake losses of up to 50% [114].

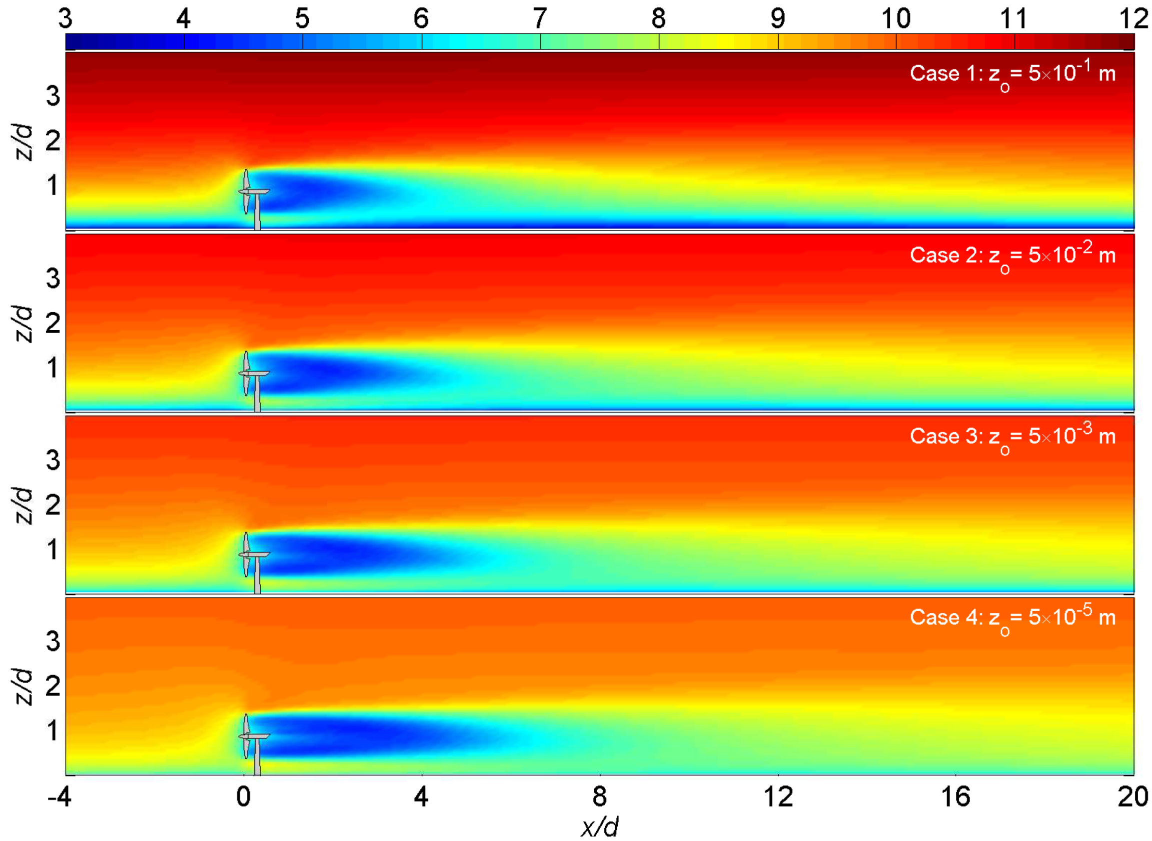

Figure 1.4: Contours of streamwise velocity in the middle vertical plane for turbines over different surface roughness lengths. Reproduced from [138].

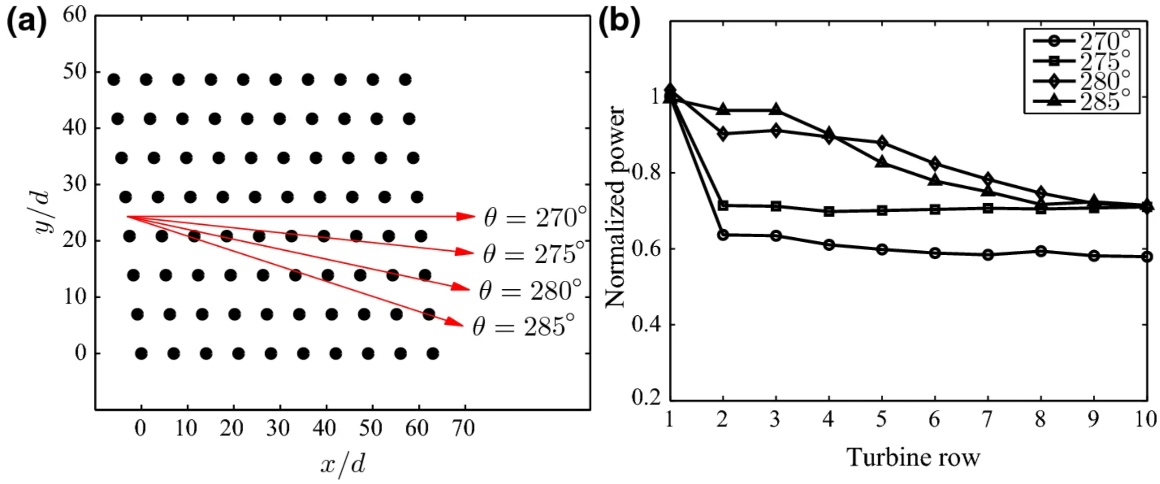

Figure 1.5: Horns Rev wind farm power [12] for different wind direction: a) schematic of wind direction and b) normalised power of turbine rows. Reproduced from [95].

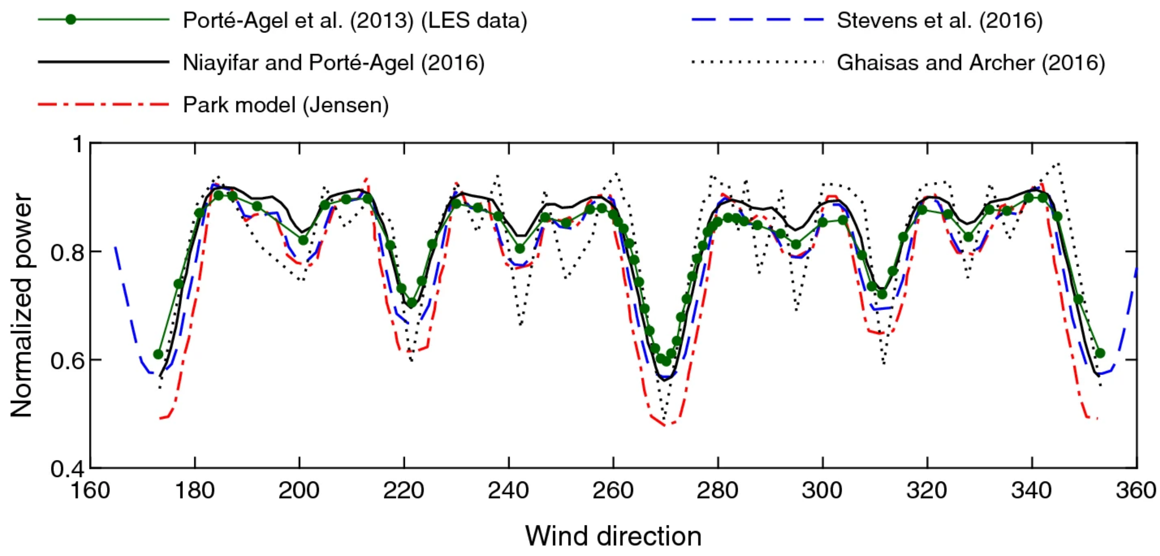

Figure 1.6: Variation of Horns Rev wind farm normalised power with wind direction. Reproduced from [95].

Wake losses depend on turbine layout and wind direction. There are two basic wind turbine layouts commonly considered: aligned (where the turbines are in perfectly aligned rows) and staggered layouts (where rows are offset in a checkerboard arrangement). A staggered layout has a larger power production because the streamwise distance between turbines is larger [139, 135, 136]. LES of the Horns Rev wind farm showed that the normalised power was sensitive to wind direction [97] (figure 1.6). A 10^o change in wind direction was found to change farm power by up to 43% [97]. This is because the wind direction changes the effective turbine layout of the wind farm [97]. A partially staggered layout refers to a farm where each row is slightly offset in the lateral direction. Partially staggered layouts produce more power than perfectly staggered layouts [112]. The power output of large farms with staggered layouts is a function of turbine density only [114]. For aligned layouts, the power production tends to be a stronger function of streamwise distance between turbines [114, 118].

Atmospheric turbulence has a significant impact on wake recovery. LES, wind tunnel and field studies have shown that a turbine wake recovers faster in ABLs with higher turbulence intensity [13, 138] (see figure 1.4). Atmospheric stability can change wake recovery by changing the turbulence intensity. Wakes recover faster in unstable conditions than in stable conditions [3, 6, 33].

Atmospheric stability influences wake losses in wind farms. LES of a semi-finite farm showed a strong diurnal variation of wake losses [5]. During the day with

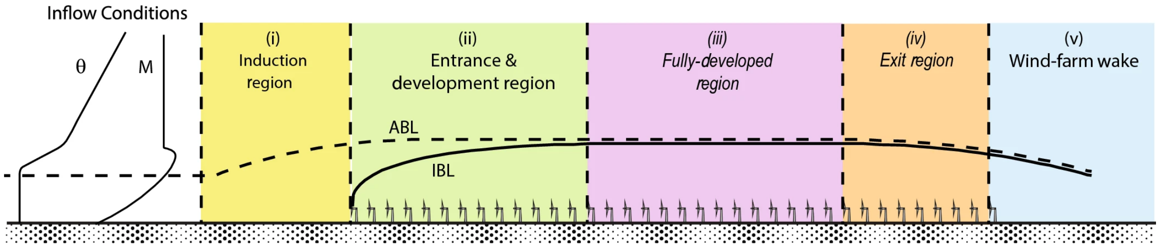

Figure 1.7: Schematic showing the flow regions in a large wind farm under conventionally neutral conditions. Figure modified from [95].

unstable atmospheric stability the farm had wake losses of 28%. However, during the night with stable conditions the wake losses were 57%. LES of a wind farm cluster showed wake losses of 34% in stable conditions and 12-14% in unstable conditions [72]. However, increasing atmospheric stability does not always result in increased wake losses [47]. Due to reduced lateral expansion of wakes in stable conditions, some layouts experienced reduced wake losses.

Turbine interactions can also increase turbine efficiency due to the 'local blockage' effect [81, 125]. When turbines are placed together with close lateral spacing, the performance can exceed that of an isolated turbine [19]. The local blockage effect was also found to increase with turbine tip speed ratio [101].

1.2.3 Farm-scale flows

Large wind farms can interact with the ABL causing farm-scale flows [95]. This results in several flow regions shown in figure 1.7. Upstream of the wind farm there is a deceleration region known as the induction region of 'farm blockage'. This is an accumulated induction by the farm as a whole in addition to the individual turbine induction. Downstream of the farm leading edge, there exists an entrance and development region. This region is highly heterogeneous and dominated by individual turbine wakes. In the fully developed region the spanwise- row-averaged flow is uniform in the streamwise direction. Some farms have an exit region where the flow can accelerate causing an increase in turbine power. Note that the fully developed and exit regions are not always seen in farms depending on the atmospheric conditions. Finally, there is the farm wake with a reduced wind speed which can persist over long distances.

Large wind farms can cause a velocity reduction in front of a wind farm (see figure 1.8). This is known as the 'wind farm blockage' or 'global blockage' effect. Historically, it has been assumed that the first row of turbines in a farm had been operating

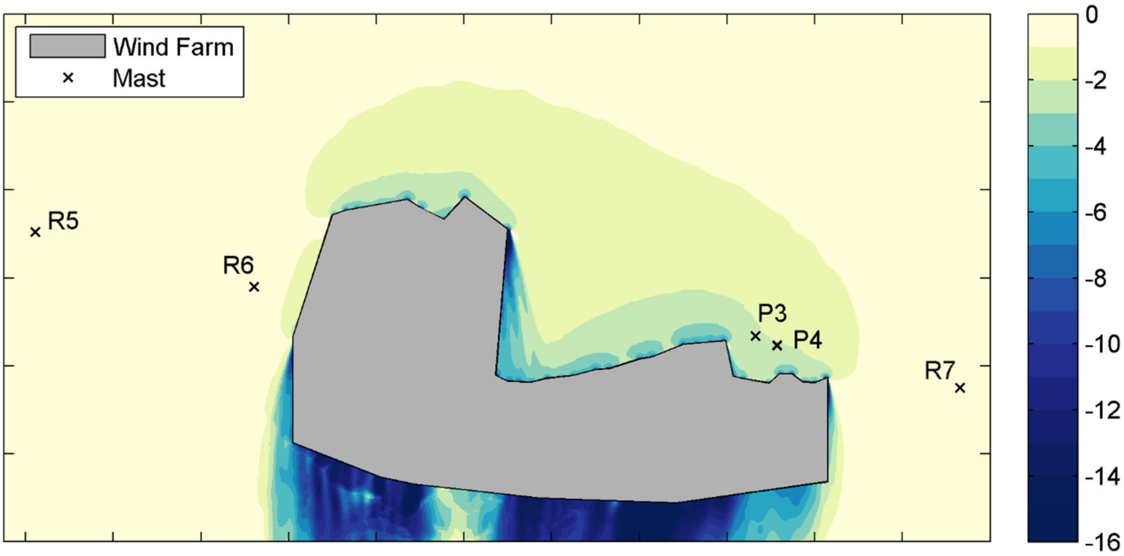

Figure 1.8: Impact of a wind farm on turbine hub height speed predicted using Reynolds-Averaged Navier-Stokes (RANS) simulations. Reproduced from [20].

in undisturbed conditions. However, met-mast measurements before and after the construction of a farm showed a velocity reduction of 3.4% two turbine diameters upstream and 1.9% ten diameters upstream [20]. Similar velocity reductions were later observed using scanning lidar [102].

Velocity reductions can be observed tens of kilometres in front of a farm. LES of semi-finite wind farms showed that farm blockage around 5 kilometres in front of a farm [135, 8]. Here a semi-finite farm refers to a hypothetical wind farm which is infinite in the spanwise direction and finite in the streamwise direction. More recently, LES of wind farms in larger numerical domains show that wind farm blockage can reduce the velocity more than 10 kilometres upstream [57, 59].

Farm blockage causes an overestimation of farm performance. Blockage effects cause front row turbines to produce less energy than in isolation. This causes a systematic overprediction bias if global blockage is neglected [20, 55]. In 2019, Ørsted announced its wind farms were producing less power than expected [151]. This was attributed to underestimating the farm blockage and wake effects.

Atmospheric stability has a significant impact on farm blockage. SCADA [26] and lidar measurements [102] show the farm blockage effect is greater for stable boundary layers and lower inversion layer heights. Wind farm LES also shows greater farm blockage for stable boundary layers and lower inversion layer heights [8, 121, 72, 57, 59]. Farm blockage may be related to the atmospheric Froude number at the farm leading edge [135, 120].

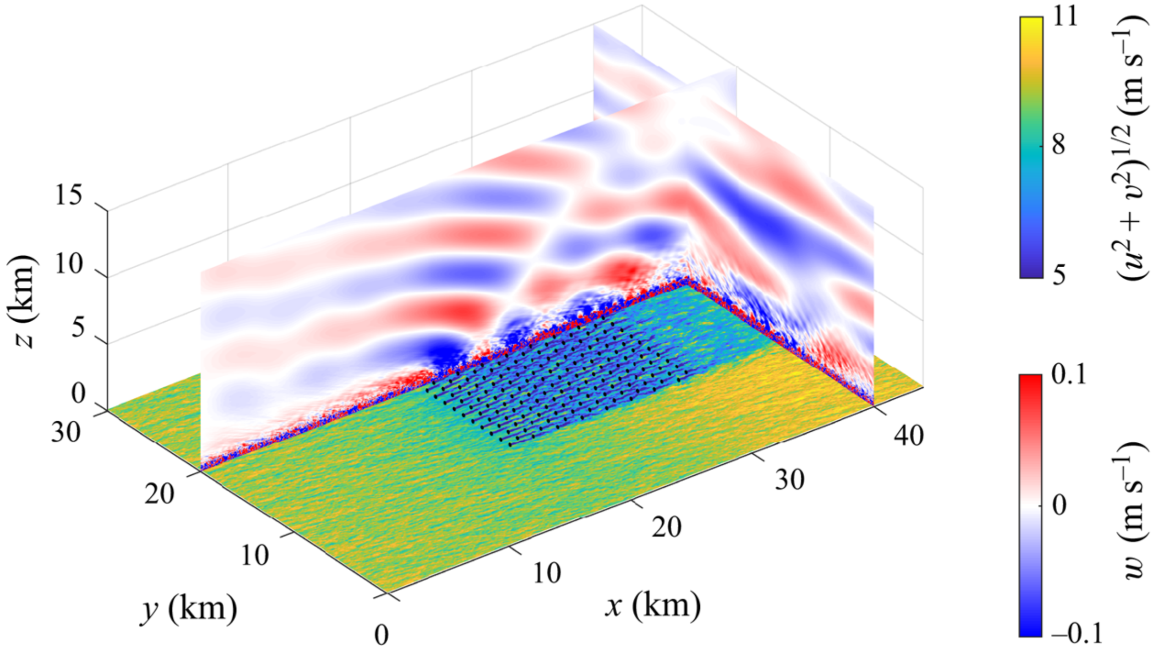

Figure 1.9: Instantaneous flow field for a wind farm operating in a CNBL. Figure modified from [59].

Wind farms operating in stably stratified atmospheres can excite gravity waves (see figure 1.9). The gravity waves are created by the upward displacement of flow by the wind farm. For thin CNBLs, the waves can induce additional pressure gradients across the farm [7]. This pressure gradient causes a flow deceleration at the front of the farm and an increased driving force through the farm. The pressure gradients from gravity waves can be an order of magnitude larger than the case without gravity waves. [59].

Farm size, turbine thrust and spacing also influence farm blockage. LES has shown that dense arrays of turbines cause a larger wind farm blockage effect [123]. Farm blockage was observed to increase with increasing turbine thrust coefficient using LES [122]. Both of these trends have been recorded in Reynolds-Averaged Navier-Stokes (RANS) simulations [41]. Wind tunnel experiments have also shown that wind farms with more turbine rows experience greater farm blockage [104].

Simulations of large farms show significant power losses due to farm blockage. Power losses due to farm blockage are commonly calculated using a 'non-local' efficiency η_{nl} [8]

$$\eta_{nl} = \frac{P_1}{P_\infty} \tag{1.2}$$

where P_1 is the power of front row turbines and P_∞ is the power of an isolated turbine. Recent simulations have shown that power losses due to farm blockage can be very significant for large wind farms. Wind farm LES has shown that η_{nl} can be as low as 68% [71], 50% [8] or 28% [59]. There remains significant uncertainty about wind farm blockage. A major project is underway to provide more detailed measurements of farm blockage [25].

In the fully developed region of wind farm the power output is balanced by the turbulent transport of kinetic energy. This flow region has been extensively studied using LES with periodic boundary conditions in horizontal directions [23, 67, 2, 68, 143, 145]. However, this region is not always observed even in farms close to 20 km long in the streamwise direction [135].

1.3 Wind farm models

1.3.1 High-fidelity wind farm simulations

Computational Fluid Dynamics (CFD) techniques have been used extensively to investigate wind farm aerodynamics [95]. These simulations give predictions under controlled conditions whilst relying on physical and numerical approximations [117]. RANS simulations have been used in many studies [100]. Standard RANS $k-\varepsilon$ models overpredict wake recovery [22, 128] and therefore overpredict the power output of waked turbines. Recently, improvements have been made to this model by including a new term in the turbulent kinetic energy equation [147].

To overcome the limitations of RANS, LES is often used to research wind turbine and wind farm flows [95]. Unlike RANS where all scales of turbulence are modelled, in LES the larger scales of turbulence are resolved [94]. As such, LES can give accurate predictions of turbulent mixing within turbine wakes [112]. However LES is more computationally expensive than RANS. LES requires a parameterisation for the sub-grid scales of turbulence. The most basic sub-grid turbulence model is the Smagorinsky model [108]. More complex 'dynamic' [94] and 'scale-dependent Lagrangian dynamic' [112, 96] sub-grid models have also been developed.

Wind turbines are modelled using LES by applying the turbine thrust onto the numerical grid. The simplest turbine model is the actuator disc model (ADM) without rotation [23]. The turbine thrust can either be applied with a uniform flow resistance or uniform thrust across the disc area. The uniform thrust gives similar far-wake predictions compared to more complex force projections [99]. The turbine force can be calculated using either the area of overlap between the disc and numerical grid or by using a convolution filter [75]. A large convolution filter size can cause the overprediction of disc velocity and therefore turbine thrust and power [105]. A post-processing correction factor can be applied to the simulated turbine thrust and power [105, 82]. This correction factor can also be applied 'online' during LES [119]. Adding a rotation component to the actuator disc model gives better near-wake velocity predictions [137]. More detailed actuator line methods (ALM) [74] and actuator surface [107] give better predictions of the wake velocity deficits. However, these methods are more computationally expensive than the actuator disc method.

The simple actuator disc without rotation model can give acceptable predictions of the far-wake velocity [144]. The actuator line model gives better predictions of the near-wake [113]. For a comparison between ADM, ALM and wind tunnel results see figure 1.10. Actuator disc and actuator line methods gave similar predictions of the far-wake velocity deficit [73, 96]. The far-wake velocity predictions of the LES models [113] match well with wind tunnel experiments [27].

LES has been shown to give accurate power predictions of entire wind farms. LES matched well with the measured normalised power from the Lillgrund wind farm [79]. LES results also matched well with measurements from the Horns Rev wind farm [140] (see figure 1.11). The actuator disc with rotation model was more accurate than the standard actuator disc model. It was also found that LES was much more accurate than commercial software 'WAsP' and 'WindSim' which both underestimated farm power [140] (see figure 1.11). However, significant statistical errors exist in turbine power output between LES and measurements for stratified atmospheric conditions [110]. LES farm power was also found to be sensitive to domain width for thin ABLs [59]. This highlights the remaining uncertainty in accurately reproducing farm-scale flow effects using LES.

For larger scale flow effects, wind farms can be modelled using numerical weather prediction (NWP) models. In NWP models the horizontal grid resolution is typically large enough to contain several turbines in one grid cell (see figure 1.12a). The vertical resolution is fine enough to cover the rotor area with multiple grid points (figure 1.12b). To model wind farms, NWP models include wind farm parameterisations (WFPs) [37].

In NWP models, wind farms can be modelled implicit as a region of enhanced roughness [37]. The farm roughness length varies according to turbine density and hub height. The roughness length is often calculated using the 'top-down' wind farm models described in section 1.3.2. For example, the Frandsen top-down model [43]

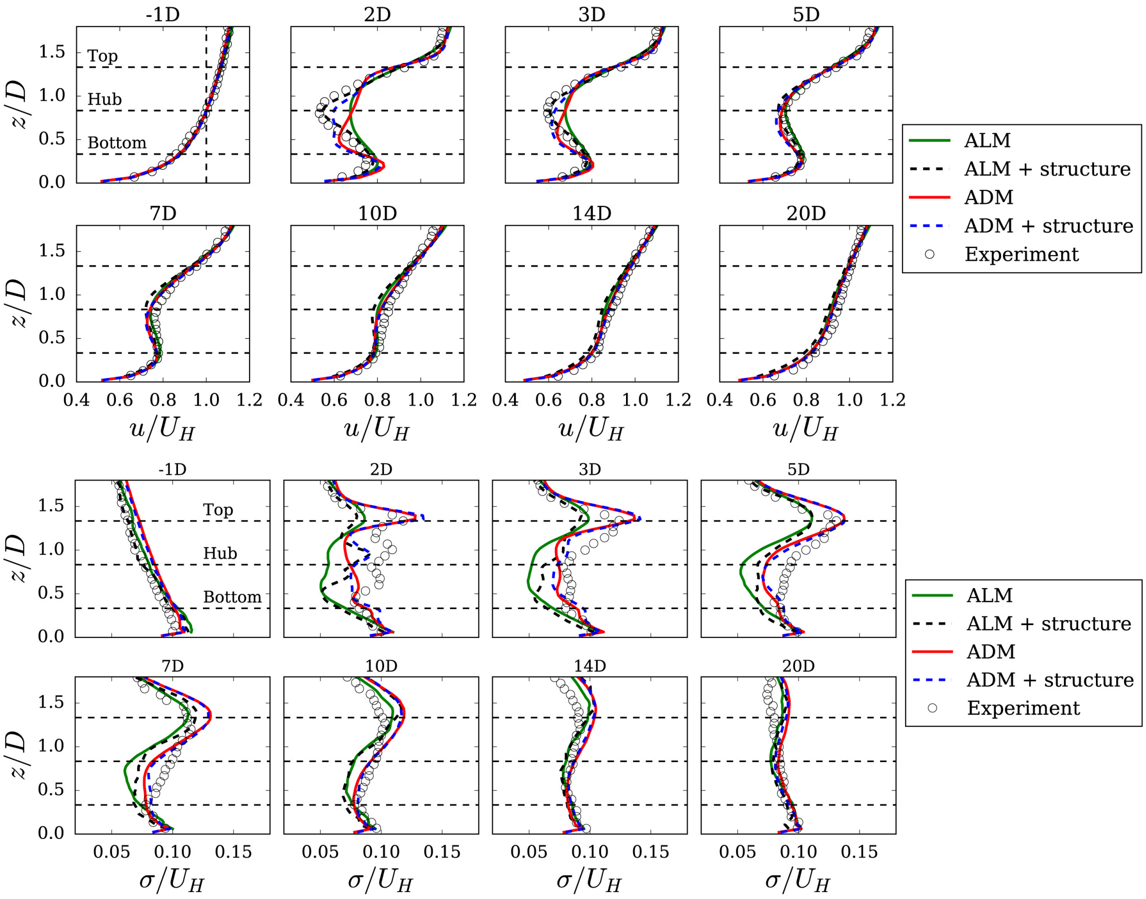

Figure 1.10: Comparison of wind tunnel experiments [27] with LES [116]. The top panels show the streamwise velocity at different distances downstream of a turbine and the bottom panels the turbulence intensity. Reproduced from [116].

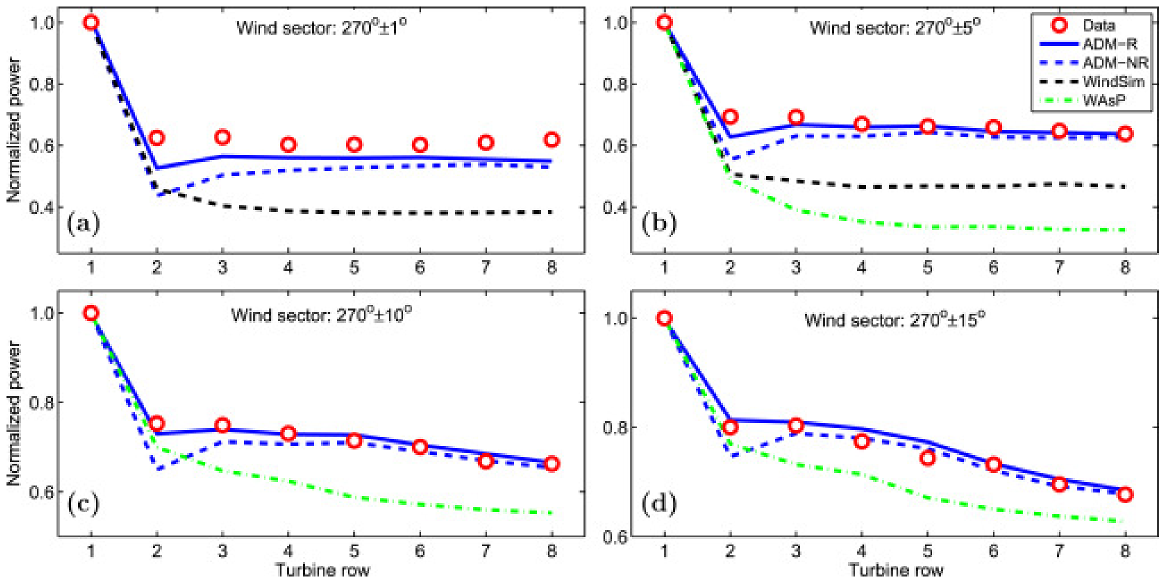

Figure 1.11: Comparison of observed and simulated power data for the Horns Rev for four different wind sectors. Reproduced from [140].

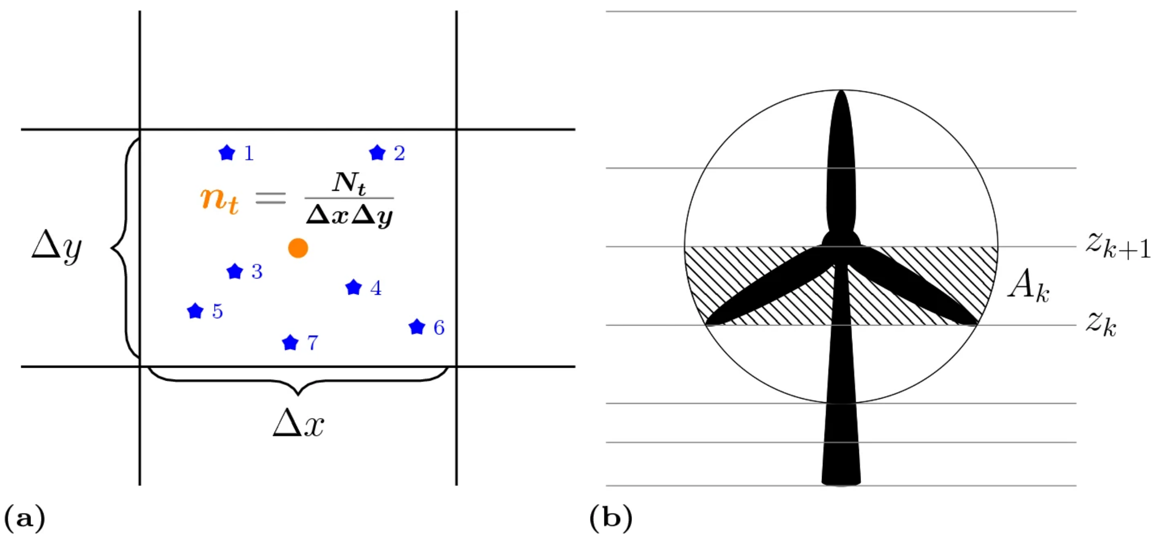

Figure 1.12: Schematic showing a) NWP horizontal grid resolution Δx and Δy and wind turbines shown by blue stars and b) vertical NWP grid. Reproduced from [37].

was used to calculate the farm roughness length in an NWP model [44]. Other studies [39] have used a roughness length obtained from LES [24] to model wind farms.

Explicit WFPs consist of an elevated momentum sink and often a source of turbulent kinetic energy (TKE). The most commonly used WFPs were developed by Fitch et al. [40] and Volker et al. [130]. The model of Volker et. al. does not include a TKE source. In this approach, the momentum sink increases shear which implicitly produces TKE. However, this results in increased TKE downstream of a farm. The model of Fitch et al. includes an explicit TKE source at the farm site. The TKE source term is calculated as the difference between the kinetic energy extracted from the flow and power produced by the turbines, similarly to the concept of 'blade-induced turbulence' for RANS actuator disc models [84]. Another WFP was later developed which analytically derived the TKE source term by considering the TKE transport equation [4].

The enhanced roughness model is not as accurate as explicit WFP. The implicit model was found to exaggerate the wind speed reduction during the day and underestimates it at night [39]. Similar results were observed in a global study [38]. WFPs have been validated using in-situ measurements, remote sensing technologies and high-fidelity LES [37].

1.3.2 Low-fidelity wind farm models

High-fidelity wind farm simulations are too computationally expensive to be used for wind farm design. As such cheaper low-fidelity farm models are required. Traditional wind farm models predict the low-speed wake behind a single turbine. One of the first analytical wake models (known as the 'Jensen' model) assumes a top-hat wake deficit [52] (see figure 1.13a). This initial wake model does not conserve momentum [13]. Later, a new model top-hat wake deficit model was proposed which conserved both mass and momentum [43]. Wake velocity deficits from LES and wind tunnel experiments were found to collapse onto a single self-similar Gaussian curve [13]. As such, a new self-similar Gaussian wake deficit was proposed (see figure 1.13b) which gave more accurate predictions of wake interactions [13].

Individual wake models have been extended to capture more detailed flow physics. The original Jensen top-hat wake model [52] was altered to include turbine-induced turbulence [87]. To better model the near-wake velocity deficit, a super Gaussian model was proposed [106, 21]. Similarly, a double Gaussian model has also been developed [54, 103] to model the near-wake velocity. The Gaussian model has been

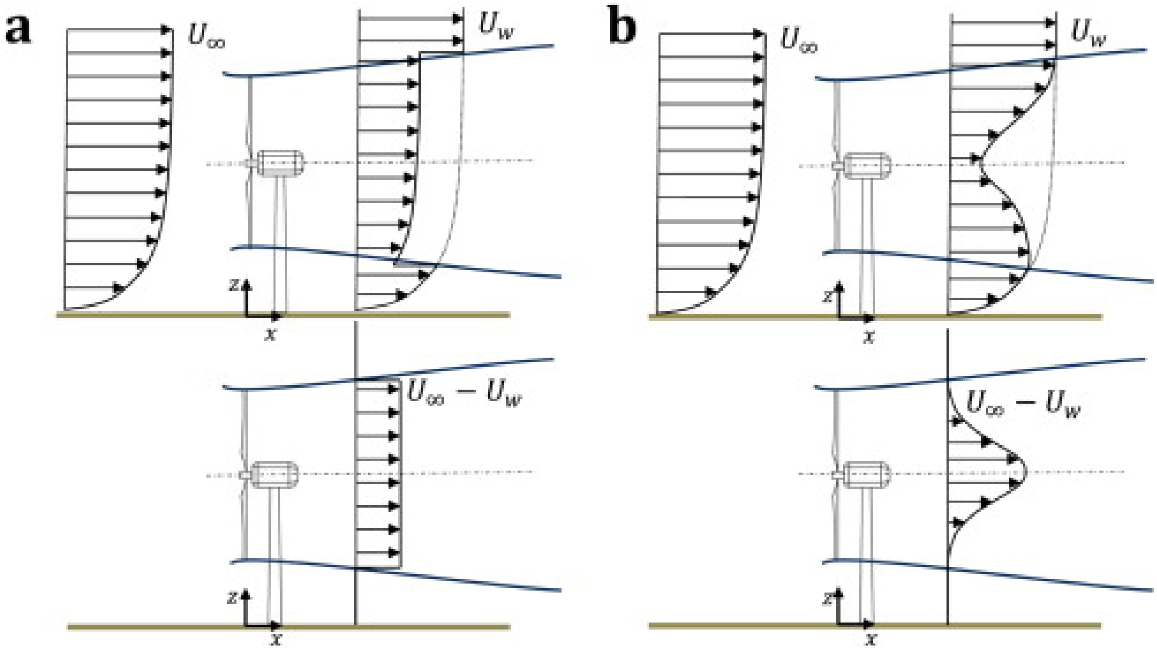

Figure 1.13: Schematic showing wake velocity (top) and wake velocity deficit (bottom) for a) top-hat wake deficit and b) Gaussian wake deficit. Reproduced from [13].

extended to model the wakes of yawed turbines [15] and the effect of pressure gradients [29]. Depending on atmospheric stability conditions, wake growth can be non-axisymmetric and the original Gaussian wake model was modified to include this effect [3].

To model an entire wind farm, individual wakes are superposed (see figure 1.14). There are two main ways of superposing wakes: summing velocity deficits [63, 78] and summing the squared velocity deficits [53, 131]. These methods are solely ad-hoc empirical methods. More recently, a physics-based method was developed using mean advection velocity for each wake [150]. Wakes can also be superposed by solving the governing equations directly [16]. A new technique has been proposed to superpose wake deficits in the presence of heterogeneous velocity fields [58].

Wake models struggle to make accurate predictions for large wind farms. These models do not consider the interaction between the farm and the ABL [117]. This effect is likely to be more important for larger farms. Field measurements from large wind farms showed that the Jensen model [52] sometimes overpredicted and others underpredicted wake losses [85]. Wind farm LES also show that wake models can over- or underpredict farm performance [115]. A large-scale model benchmarking showed that the Jensen model systematically underestimated wake losses [86]. Wake models are more sensitive to wind direction than LES [97] and wind farm measurements [93].

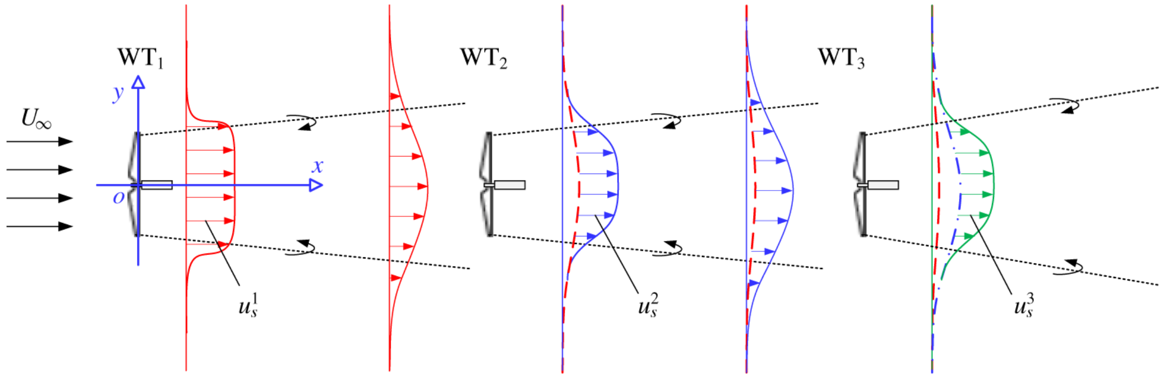

Figure 1.14: Sketch of wind turbine wake superposition where u_s^i refers to the wake deficit caused by the ith wind turbine. Reproduced from [150].

The power output of the 'London Array' wind farm was less sensitive to wind direction than both a basic and extended wake model [92]. A common issue of wake models is that they overestimate the efficiency of some wind farms whilst underestimating others [86].

An alternative approach is to use 'top-down' models which consider the fully developed region of a very large farm. These models assume the farm is infinite in streamwise and spanwise directions. Commonly the wind farm is modelled as an enhanced surface roughness [95]. The original top-down model assumed a logarithmic velocity profile above and below the turbine hub height, a continuous velocity profile at the hub height and that dispersive stress are negligible [42, 43] (see figure 1.15). LES of infinite wind farms showed a third logarithmic layer across the turbine and a new top-down model was proposed accordingly [23]. Using top-down models it was found that the optimal turbine spacing for infinite farms is much larger than current wind farm design [76]. Using a similar approach, the optimal spacing for finite farms was found to be similar to current wind farms [111].

Traditional 'top-down' models only predict the impact of turbine density and thrust coefficient. One limitation of top-down models is that they cannot account for the turbine layout or wind direction. The layout was later accounted for by considering the farm area to be the area affected by the turbine wakes [143]. These models are derived for a purely neutral ABL. However, these conditions rarely occur in reality. The Frandsen model [42] was later adapted to capture the effect of free atmosphere stratification [2].

The 'coupled wake boundary layer method' [113, 115] models both individual wakes and the atmospheric response. This is achieved by a two-way coupling of the Jensen wake model [52] with the top-down model in [23]. The wake model portion

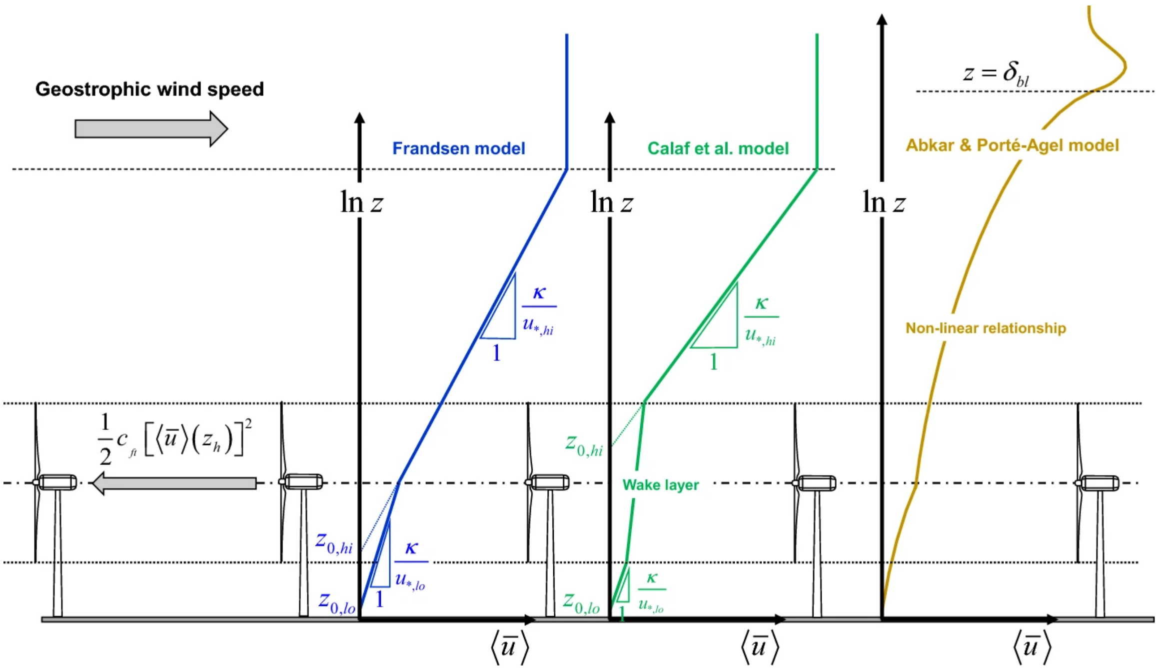

Figure 1.15: Schematic showing different top-down models to predict the effective surface roughness of a wind farm. Reproduced from [95].

captures the impact of turbine layout whereas the top-down portion predicts the interaction between the farm and the atmosphere. This coupling gives improved predictions of farm performance compared to its individual components [115].

Another class of models use the classical entrainment theory [77, 34] to model the farm-atmosphere interaction. The exchange of energy between a layer containing the wind turbines and the atmosphere above is parameterised using entrainment theory [69]. This was later extended to finite-length wind farms [17].

Linearised flow models can predict the farm-atmosphere interaction and farm blockage. The atmospheric response to farm drag can be predicted by dividing the atmosphere into two layers [109]. The two layers represent the ABL and the free atmosphere above. A three-layer model (TLM) was later developed [9] by introducing a third wind-farm layer. The TLM has been extended to account for vertically varying conditions in the free atmosphere [30]. Recently, the TLM method has been altered to match velocities within the farm [31] and to satisfy the 'separation of scales' assumption [120]. This modelling approach was also coupled with an optimisation framework to maximise farm power [56].

The 'two-scale momentum theory' [80, 82] splits the multi-scale flow problem of wind farm aerodynamics into 'internal' (turbine-scale) and 'external' (farm-scale) problems. By considering the conservation of momentum, a generic coupling can be

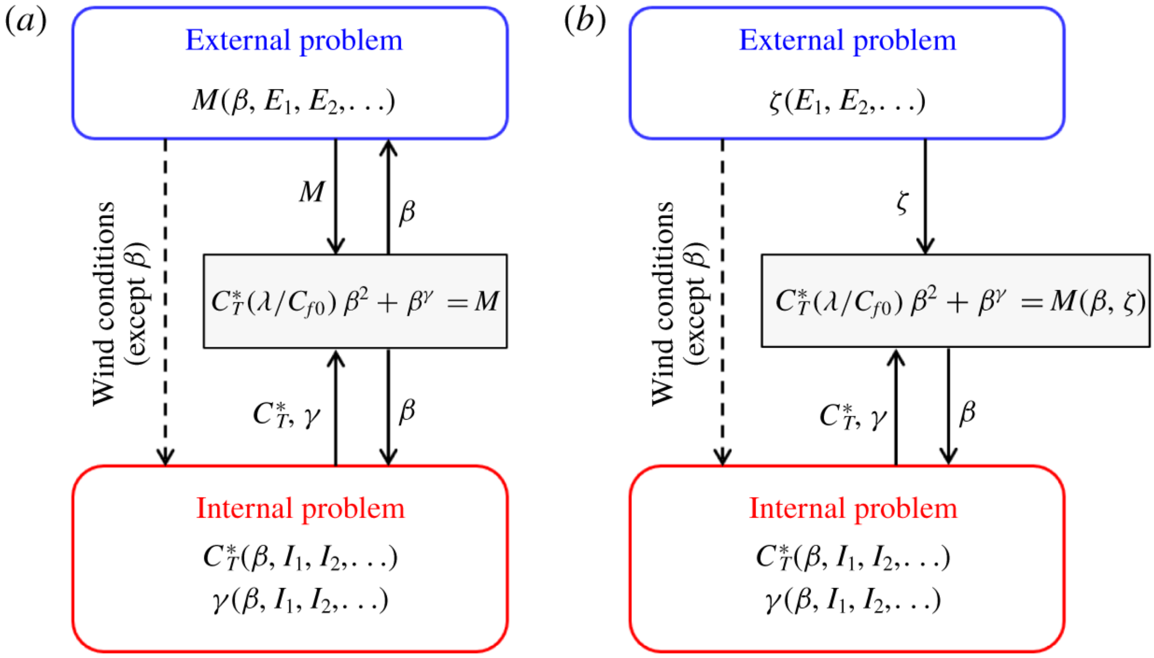

Figure 1.16: Two-scale coupling of 'internal' and 'external' problems a) general case b) simplified case where 'internal' and 'external' problems are coupled only in a 'one-way' manner. Reproduced from [82].

derived between turbine and farm-scale flows [82] (see figure 1.16). A simple analytical equation for the power output of very large wind farms can then be derived. This expression was validated against LES [32, 132]. Using this model, it was shown that the optimal turbine resistance varied with the array density [146]. This model was also later extended to consider the impact of support structure drag [70].

The two-scale momentum theory was also extended to finite-sized wind farms [83, 82]. A key parameter in this model is the 'wind extractability' ζ. This parameter describes how the farm-averaged wind speed at a site changes as the number of turbines installed is increased. Using NWP simulations, ζ was found to vary with atmospheric conditions [91]. This approach was coupled with a wake model to predict the annual energy prediction (AEP) for an offshore wind farm site in the North Sea [60, 89].

More recently, data-driven machine learning approaches have been used to model wind farms [148]. The advantage of this approach is that data from high-fidelity simulations can be used to make predictions with low computational cost. The data used for these models come from measurements [98, 88, 51, 142], LES [149] and RANS [133, 126, 127].

Commonly, machine learning approaches are used to predict the velocity deficit behind a single turbine. A limitation of this approach is that the models are not generalisable to different turbine layouts unless they rely on ad-hoc wake superposition techniques. Another approach is to model turbine-wake interactions using geometric parameters to describe the turbine layout [46, 142]. Alternatively graph neural networks (GNN) can be used to include the turbine layout as an input [90, 18]. The GNN approach was found to outperform the original Jensen wake model when predicting the performance of existing farms [61].

1.4 Aims and objectives

This thesis aims to improve the understanding and modelling of wind farm efficiency. To do this it is important to investigate the influence of different fluid mechanical processes on farm performance. The two-scale momentum theory offers a new way of investigating the physics of wind power generation. This theory can be used to decompose power losses into flow effects on the turbine- and farm-scale, providing new insight into wind farm aerodynamics. Currently, within the two-scale framework, there is a need to develop low-cost models to predict turbine-wake interactions and the wind extractability factor ζ.

The research objectives of this DPhil are:

1. Clarify the impact of turbine-scale and farm-scale flows on the performance of large wind farms
2. Develop a new data-driven model to predict turbine-wake interactions
3. Develop new model to predict impact of farm-scale flows on wind farm performance

1.4.1 Thesis structure

Chapter 1 describes the current understanding of wind farm aerodynamics. Wind farm models of varying fidelity are summarised. The motivation and research objectives are also outlined.

Chapter 2 contains a journal article published in the '*Journal of Fluid Mechanics*'. We present a large suite of LES of infinitely large wind farms. New concepts of 'turbine-scale power losses' and 'farm-scale power losses' are introduced. We show that, for large offshore wind farms, the power losses due to the farm-atmosphere interaction are at least twice as large as due to turbine-wake interactions.

In **Chapter 3** we present a journal article published in '*Wind Energy*'. Machine learning techniques are used to predict the 'internal' turbine thrust coefficient as function of turbine layout. We use multi-fidelity Gaussian Process regression to combine data from high-fidelity LES and low-fidelity wake model simulations.

The farm-atmosphere interaction can have a large impact on the performance of large wind farms. In **Chapter 4** we propose a new analytical model to predict the impact of farm-atmosphere interactions for large but finite-sized wind farms. This work was published as a journal article in the '*Journal of Fluid Mechanics*'.

In **Chapter 5** we apply the concepts of turbine- and farm-scale efficiencies (first described in Chapter 2) to a suite of 38 wind farm large-eddy simulations. We also assess the accuracy of the analytical model described in Chapter 4 to predict the farm-atmosphere interaction. This work has been submitted as a journal article to *'Wind Energy Science'* and published in *'Wind Energy Science Discussion'*.

Chapter 6 gives concluding remarks to the thesis. We summarise the main findings presented in the thesis and comment on the future outlook for this research.

Chapter 2

Two-scale interaction of wake and blockage effects in large wind farms

This chapter presents a journal article titled *'Two-scale interaction of wake and blockage effects in large wind farms'* published in the *'Journal of Fluid Mechanics'* (`https://doi.org/10.1017/jfm.2022.979`). The article spans the pages 22-51 in the thesis. Note that there are some minor differences in the text from the published version.

When turbines are placed together in a farm, they produce less power than in isolation. There are low-speed wakes behind every turbine which reduce the performance of downstream turbines. The farm can also act as an additional resistance to the atmosphere, reducing the velocity within the farm. Traditionally, the wakes have been considered the most important effect in wind farms.

Our results suggest the farm-atmosphere interaction is the more important effect. We introduce two new concepts for understanding farm efficiencies. Firstly, 'farm-scale' losses due to the atmospheric response to the whole farm. Secondly, the 'turbine-scale' losses due to the internal flow interactions within the farm (i.e. turbine-wake interactions). This chapter shows that, as wind farms become larger, the farm-scale losses could be more than twice as high as turbine-scale losses. As wind farms become larger, turbine-scale power losses may decrease.

This suggests there could be limited potential of layout optimization for large offshore wind farms. Instead, the focus should be on optimising the farm-atmosphere interaction.

Two-scale interaction of wake and blockage effects in large wind farms

Andrew Kirby[1] †, Takafumi Nishino[1], and Thomas D. Dunstan[2]

[1]Department of Engineering Science, University of Oxford, Parks Road, Oxford OX1 3PJ, UK

[2]Met Office, FitzRoy Road, Exeter EX1 3PB, UK

(Received xx; revised xx; accepted xx)

Turbine wake and farm blockage effects may significantly impact the power produced by large wind farms. In this study, we perform Large-Eddy Simulations (LES) of 50 infinitely large offshore wind farms with different turbine layouts and wind directions. The LES results are combined with the two-scale momentum theory (Nishino & Dunstan 2020, J. Fluid Mech. 894, A2) to investigate the aerodynamic performance of large but finite-sized farms as well. The power of infinitely large farms is found to be a strong function of the array density, whereas the power of large finite-sized farms depends on both the array density and turbine layout. An analytical model derived from the two-scale momentum theory predicts the impact of array density very well for all 50 farms investigated and can therefore be used as an upper limit to farm performance. We also propose a new method to quantify turbine-scale losses (due to turbine-wake interactions) and farm-scale losses (due to the reduction of farm-average wind speed). They both depend on the strength of atmospheric response to the farm, and our results suggest that, for large offshore wind farms, the farm-scale losses are typically more than twice as large as the turbine-scale losses. This is found to be due to a two-scale interaction between turbine wake and farm induction effects, explaining why the impact of turbine layout on farm power varies with the strength of atmospheric response.

Key words: Authors should not enter keywords on the manuscript, as these must be chosen by the author during the online submission process and will then be added during the typesetting process (see Keyword PDF for the full list). Other classifications will be added at the same time.

1. Introduction

The global wind energy production is set to rise in the next few decades. To achieve this, wind farm clusters are expected to be built which are an order of magnitude larger than existing ones (Maas & Raasch 2022). To optimise their design, it is important to accurately predict the total farm power as well as aerodynamic loads on each turbine. However, it is very difficult to model the aerodynamics of wind farms because of the multi-scale nature of the

† Email address for correspondence: andrew.kirby@trinity.ox.ac.uk

wind farm flows (Porté-Agel *et al.* 2020). In 2019 Ørsted, one of the largest offshore wind farm developers, announced that its wind farms were producing less power than expected (Ørsted 2019). The underprediction of farm power was attributed to two effects: wake and farm blockage effects.

Behind every turbine there is a turbulent wake which has a reduced wind speed. When turbine wakes interact with other turbines within a farm this can cause substantial power losses. This is known as the 'wake effect' and has been measured to reduce the power of turbines in an existing wind farm by up to 40% in the worst case (Barthelmie *et al.* 2010). This effect has been extensively investigated in the literature using Large-Eddy Simulations (LES) (Porté-Agel *et al.* 2013; Wu & Porté-Agel 2015; Stevens *et al.* 2016*a*). The 'farm blockage' is a recently observed effect in large wind farms (Bleeg *et al.* 2018). The flow resistance caused by a wind farm reduces the wind speed upstream as well inside the farm. Hence, the total power produced by the wind farm is reduced compared to the ideal situation where the upstream wind speed is not affected by the farm (Nishino & Dunstan 2020).

Wind farm aerodynamics have been traditionally modelled using 'wake' models, which predict the velocity behind a turbine (e.g., Jensen 1983; Bastankhah & Porté-Agel 2014). To account for interactions between multiple turbines, the wake velocity deficits are superposed (e.g., Katic *et al.* 1986; Zong & Porté-Agel 2020). However, these models do not account for the response of the atmospheric boundary layer (ABL) to the farm. As such they tend to perform poorly for large wind farms (Stevens *et al.* 2016*a*). A different approach to modelling wind farms is to use 'top-down' models (e.g., Frandsen 1992; Frandsen *et al.* 2006; Calaf *et al.* 2010). They model the response of an idealised ABL (which follows a logarithmic law) to an infinitely large wind farm but cannot take into account the details of turbine-wake interactions explicitly. Hence, these wind farm models cannot correctly capture the two-way interactions of turbine-scale and farm-scale flow effects which determine the performance of large wind farms.

To capture this two-way interaction, it has been proposed to couple wake and top-down models; for example, by adjusting parameters in both models to match the hub-height-averaged velocities (Stevens *et al.* 2016*b*; Starke *et al.* 2021). Examples of two-way coupling can also be found in existing engineering software, e.g., the 'Deep Array Wake Model' (Brower & Robinson 2012). However, these models involve the coupling of low-order flow models and are therefore limited by the assumptions made by the constituent models, e.g., wake superposition or a log-law wind profile. To account for the effects of more realistic flow physics, it would be beneficial to use an approach based on more fundamental laws of fluid mechanics.

The optimal design of a large wind farm under realistic atmospheric conditions remains a challenge as it requires consideration of the complex atmospheric response to the farm. It is often too expensive to run a large number of simulations which resolve both individual turbines and the atmospheric response to the farm. In addition, to find an optimal design for the long-term performance of a wind farm, such as the annual energy production (AEP), the range of timescales we would need to consider is too wide. As such, Nishino & Dunstan (2020) proposed the 'two-scale momentum theory' to split the multi-scale flow problem into 'internal' turbine/array-scale and 'external' farm/atmospheric-scale problems. West & Lele (2020) performed LES of infinitely-large wind farms and the results showed a good agreement with the two-scale momentum theory. However, their LES study was limited to 'fully aligned' turbine layouts, and their discussion was also limited to the special case where the momentum supplied by the atmosphere to the wind farm site was fixed. In reality, the strength of atmospheric response to the wind farm resistance depends on mesoscale weather patterns (Patel *et al.* 2021) as well as atmospheric stability and gravity waves (Allaerts & Meyers 2017, 2018, 2019).

The aim of the present study is to better understand the fluid mechanics processes which determine the power production of large wind farms, using a combined theoretical and computational approach. First, we will perform a large suite of LES of infinitely large wind farms with different turbine layouts and wind directions. We then combine the results of LES with the two-scale momentum theory to investigate and explain expected performance of large finite-sized wind farms with a realistic range of atmospheric response strengths. Using this approach allows the combined effects of turbine-scale and farm-scale flow characteristics on wind farm power to be determined.

In section 2 we summarise the definitions of key wind farm parameters in the two-scale momentum theory (Nishino & Dunstan 2020). Section 3 details the methodology of the LES and wind turbine implementation. In section 4 we present the results including validation of the LES code. These results are discussed in section 5 and concluding remarks are given in section 6.

2. Theory

2.1. *Two-scale momentum theory*

Figure 1 shows a pair of control volumes for a given farm site. We first consider the momentum balance of the control volume without the turbines (figure 1a). For this scenario the following equation can be derived for a 'short-time-averaged' flow:

$$\frac{\partial[\rho U_0]}{\partial t} = X_0 - C_0 - \left[\frac{\partial p_0}{\partial x_{F0}}\right] - \frac{\langle\tau_{w0}\rangle S_F}{V_{CV}} \tag{2.1}$$

where U is the velocity in the hub-height wind direction (i.e. streamwise direction) x_F, X represents the net streamwise momentum injection through the top and side boundaries of the control volume (due to advection and Reynolds stress), C is the streamwise component of the Coriolis force averaged over the control volume, $\partial p/\partial x_F$ is the pressure gradient in the direction x_F, τ_w is the bottom shear stress, S_F is the wind farm area and V_{CV} is the volume of the control volume. The subscript 0 refers to values without the turbines present, $[\square]$ refers to control-volume-averaged values and $\langle\square\rangle$ refers to farm-area-averaged values.

By considering the control volume with the turbines present (figure 1b) the following equation can be derived:

$$\frac{\partial[\rho U]}{\partial t} = X - C - \left[\frac{\partial p}{\partial x_F}\right] - \frac{\langle\tau_w\rangle S_F + \sum_{i=1}^{n} T_i}{V_{CV}} \tag{2.2}$$

where T_i is the thrust of turbine i in the farm and n is the total number of turbines in the farm. Equations 2.1 and 2.2 can be combined to obtain the non-dimensional farm momentum (NDFM) equation (Nishino & Dunstan 2020):

$$C_T^* \frac{\lambda}{C_{f0}} \beta^2 + \beta^\gamma = M \tag{2.3}$$

where β is the farm wind-speed reduction factor defined as $\beta \equiv U_F/U_{F0}$ (with U_F defined as the average wind speed in the nominal farm-layer of height H_F, and U_{F0} is the farm-layer-averaged speed without the presence of the turbines); λ is the array density defined as $\lambda \equiv nA/S_F$ (where A is the rotor swept area); C_T^* is the (farm-averaged) 'local' or 'internal' turbine thrust coefficient defined as $C_T^* \equiv \sum_{i=1}^{n} T_i/\frac{1}{2}\rho U_F^2 nA$; C_{f0} is the natural friction coefficient of the surface defined as $C_{f0} \equiv \langle\tau_{w0}\rangle/\frac{1}{2}\rho U_{F0}^2$; γ is the bottom friction exponent defined as $\gamma \equiv \log_\beta(\langle\tau_w\rangle/\langle\tau_{w0}\rangle)$; and M is the momentum availability factor given by:

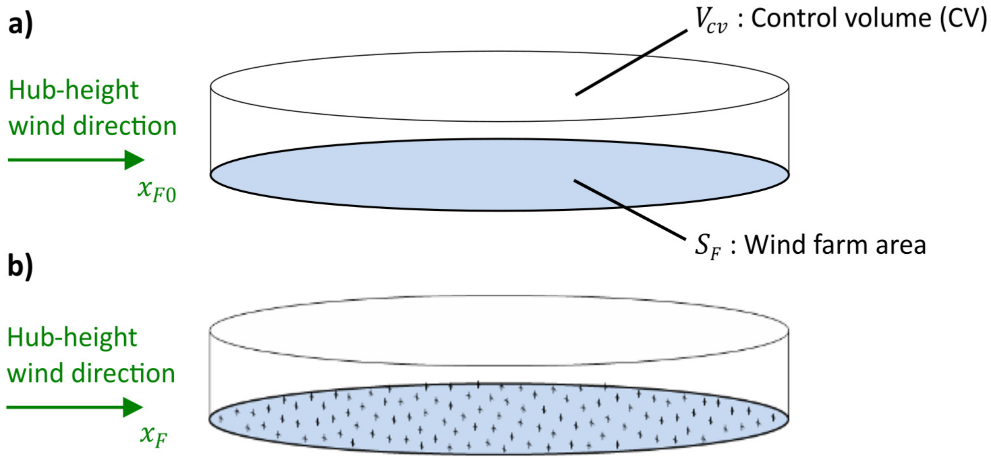

Figure 1: Control volume for an entire wind farm site: a) without turbines and b) with turbines.

$$M = \frac{X - C - \left[\frac{\partial p}{\partial x_F}\right] - \frac{\partial[\rho U]}{\partial t}}{X_0 - C_0 - \left[\frac{\partial p_0}{\partial x_{F0}}\right] - \frac{\partial[\rho U_0]}{\partial t}}. \tag{2.4}$$

Note that the first term in the left-hand-side of equation 2.3 can be extended to include the impact of support structure drag (see Ma *et al.* 2019) but their impact is usually small and is therefore neglected in this study for simplicity.

The height of the farm-layer, H_F, is used to define the reference velocities U_F and U_{F0}. H_F is typically between $2H_{hub}$ and $3H_{hub}$ (where H_{hub} is the turbine hub-height); the NDFM equation (2.3) is valid as long as the same H_F value is used for both 'internal' and 'external' problems. In this study we use a fixed definition of $H_F = 2.5H_{hub}$. This is discussed further in appendix A.

The equation 2.3 helps the analysis of large wind farm aerodynamics. This is because C_T^* and γ on the left hand side are expected to depend primarily on the turbine/array-scale flow physics or 'internal' conditions, for example the turbine layout, operating conditions and local wind conditions, whereas M on the right hand side is expected to depend largely on 'external' conditions. Following Nishino & Dunstan (2020), in this study we assume that the 'internal' problem (to be modelled using LES in section 3 to calculate C_T^* and γ) can be modelled without explicitly considering the effects of 'external' conditions such as wind farm size and location, and the response strength of the atmosphere.

The 'external' problem is to determine the parameter M, which represents how much the amount of momentum available to the farm site differs from its 'natural' value. This problem is largely independent of the small-scale flow features and can be modelled using a numerical weather prediction (NWP) model with a wind farm parameterisation, i.e., without resolving individual turbines. Patel *et al.* (2021) used such an NWP model to demonstrate that, for most cases, M varied almost linearly with β (for a realistic range of β between 1 and 0.8). Therefore, M can be approximated by

$$M = 1 + \zeta(1 - \beta) \tag{2.5}$$

where ζ is called the 'momentum response' factor or 'wind extractability' factor. Patel *et al.* (2021) found ζ to vary between 5 and 25 for a typical offshore wind farm site. Note that $\zeta = 0$ corresponds to the case where momentum available to the farm site is assumed to be fixed, i.e., $M = 1$. An infinitely-large value of ζ corresponds to the case where there is no wind speed reduction in the farm-layer, i.e., $\beta = 1$. Preliminary results of an extended study from Patel *et al.* (2021) show that ζ changes according to atmospheric conditions and decreases exponentially with increasing farm size (see appendix B). Although the details of how ζ changes with weather conditions are still unclear and need to be clarified in future studies, in the present study we take $0 < \zeta < 25$ as a typical range of the wind extractability for large offshore wind farms.

Using β obtained from equation (2.3) for a set of C_T^*, γ and ζ, the following equation can be used to calculate the power coefficient of the turbines within the farm,

$$C_p = \beta^3 C_p^* \tag{2.6}$$

where C_p is the (farm-averaged) turbine power coefficient defined as $C_p \equiv \sum_{i=1}^{n} P_i / \frac{1}{2}\rho U_{F0}^3 nA$ (P_i is power of turbine i in the farm) and C_p^* is the (farm-averaged) 'local' or 'internal' turbine power coefficient defined as $C_p^* \equiv \sum_{i=1}^{n} P_i / \frac{1}{2}\rho U_F^3 nA$.

2.2. *Analytical model of ideal wind farm performance*

In this study we consider arrays of actuator discs (or aerodynamically ideal turbines operating below the rated wind speed). For an actuator disc $C_p^* = \alpha C_T^*$ where α is the turbine-scale wind speed reduction factor defined as $\alpha \equiv U_T/U_F$ (U_T is the streamwise velocity averaged over the rotor swept area). We can estimate α using the expression $\alpha = \sqrt{C_T^*/C_T'}$ where $C_T' \equiv T/\frac{1}{2}\rho U_T^2 A$ is a turbine resistance coefficient describing the turbine operating conditions (noting that this is strictly valid only for infinitely large regular arrays of turbines where the farm-averaged turbine thrust is identical to the thrust of each individual turbine). The theoretical C_p of an actuator disc is therefore given by

$$C_p = \beta^3 \alpha C_T^* = \beta^3 {C_T^*}^{\frac{3}{2}} {C_T'}^{-\frac{1}{2}}. \tag{2.7}$$

where C_T^* may be predicted using a simple analytical model (Nishino 2016) given by

$$C_T^* = 4\alpha(1-\alpha) = \frac{16C_T'}{(4+C_T')^2} \tag{2.8}$$

using the expression $C_T' = C_T^*/\alpha^2$ to express C_T^* as a function of C_T'. The model predicts C_T^* as a function of turbine-scale wind-speed reduction by using an analogy to the classical actuator disc theory. This simple analytical model will be compared with LES results later in section 4. Using the analytical model of C_T^* (equation 2.8), and the linear approximation of M (equation 2.5), equations 2.3 and 2.7 can be solved to give a theoretical prediction of C_p, which we will call $C_{p,Nishino}$. Note that West & Lele (2020) also introduced this but only for the special case with $\zeta = 0$. As shown by Nishino & Dunstan (2020), $C_{p,Nishino}$ is sensitive to ζ but much less sensitive to γ. If we assume that $\gamma = 2.0$, then we can obtain an analytical expression for $C_{p,Nishino}$, i.e.,

$$C_{p,Nishino} = \frac{64C_T'}{(4+C_T')^3}\left[\frac{-\zeta + \sqrt{\zeta^2 + 4\left(\frac{16C_T'}{(4+C_T')^2}\frac{\lambda}{C_{f0}} + 1\right)(1+\zeta)}}{2\left(\frac{16C_T'}{(4+C_T')^2}\frac{\lambda}{C_{f0}} + 1\right)}\right]^3. \tag{2.9}$$

It is worth noting that the power coefficient of an isolated turbine, $C_{p,Betz}$, is given by

$$C_{p,Betz} = \frac{64C_T'}{(4+C_T')^3}, \tag{2.10}$$

which takes the well-known maximum value of $16/27$ at $C_T' = 2$. This equation can be obtained by substituting 2.8 into 2.7 with $\beta = 1$ (i.e., assuming flow mechanisms as described by the classical actuator disc theory and no farm-scale wind speed reduction). Note that this is the same as solving equation 2.9 for two special cases: (1) with $\lambda/C_{f0} = 0$; and (2) with an infinitely large value of ζ.

3. LES modelling

3.1. *Governing equations of the flow*

We performed LES of flow over periodic turbine arrays using the MetOffice/NERC Cloud (MONC) Model (Brown *et al.* 2018). The flow is driven by an imposed pressure gradient and is neutrally stratified. The flow is governed by the incompressible Navier-Stokes equations, i.e.,

$$\frac{\partial u_i}{\partial x_i} = 0 \tag{3.1}$$

$$\frac{\partial u_i}{\partial t} + u_j \frac{\partial u_i}{\partial x_j} = -\frac{\partial}{\partial x_i}\left(\frac{p'}{\rho}\right) + \frac{1}{\rho}\frac{\partial \tau_{ij}}{\partial x_j} + f_i - \frac{1}{\rho}\frac{\partial p_\infty}{\partial x_i} \tag{3.2}$$

where u_i is the resolved velocity in the i direction, p' is the pressure perturbation from the reference state, ρ is the reference density, τ_{ij} is the subgrid stress term, f_i is the force added to model the wind turbines and $\partial p_\infty/\partial x_i$ is the imposed pressure gradient.

The subgrid stress model is a standard Smagorinsky model (Smagorinsky 1963) given by $\tau_{ij} = \rho \nu S_{ij}$ where ν is the subgrid-scale eddy viscosity and S_{ij} is the rate of strain tensor. The eddy viscosity is given by a mixing length model $\nu = l^2 S$ where l is the mixing length scale and S is the modulus of the rate of strain tensor $S = \|S_{ij}\|/\sqrt{2}$. Near the bottom boundary, the mixing length scale l is damped using the function $1/l^2 = 1/(l_0)^2 + 1/[\kappa(z+z_0)]^2$ described in Brown *et al.* (1994) where l_0 is the basic mixing length scale. l_0 is given by $l_0 = c_s\Delta$ with a coefficient of $c_s = 0.23$ and a grid spacing given by $\Delta = \max(\Delta x, \Delta y)$ (Brown *et al.* 1994).

All velocity components are set to zero at the bottom boundary. The shear stress at the surface is parameterised by specifying ν following the classical Monin-Obukhov similarity theory. The horizontal boundary conditions are periodic for all prognostic quantities. The top boundary has a zero vertical velocity boundary condition and a damping layer for the top 200 metres of the domain (which was not necessary in the present study for neutrally stratified flows but still included for future studies to explore the effect of atmospheric stability).

3.2. *Actuator disc implementation*

We model individual turbines as actuator discs following the methodology used by the KULeuven code described in Calaf *et al.* (2010). The approach uses a Gaussian convolution filter to apply the turbine force from the rotor plane onto the LES grid. This allows the position and orientation of turbines to be changed easily. The thrust force exerted by a single turbine is given by

$$F = -\frac{1}{2}\rho C_T' \widehat{U_T}^2 \frac{\pi}{4} D^2 \tag{3.3}$$

where $\widehat{U_T}$ is the time-filtered disc-averaged velocity and D is the turbine diameter. This turbine thrust force is spatially distributed using a normalised indicator function $\mathcal{R}(\boldsymbol{x})$, defined as

$$\mathcal{R}(\boldsymbol{x}) = \frac{4}{\pi D^2} \iint G(\boldsymbol{x} - \boldsymbol{x}')\, d^2\boldsymbol{x}' \tag{3.4}$$

where $G(\boldsymbol{x})$ is a filtering kernel. This integral is calculated over the surface of the disc. We divide the disc area into 10 segments in the radial and angular directions, respectively. This was sufficient for $\mathcal{R}(\boldsymbol{x})$ to be independent of the number of segments. MONC uses a staggered grid where the u and v velocities are evaluated at different points. As such, two different indicator functions, $\mathcal{R}_x(\boldsymbol{x})$ and $\mathcal{R}_y(\boldsymbol{x})$, are calculated for the x and y directions. We use the same filtering kernel as described in Shapiro *et al.* (2019),

$$G(\boldsymbol{x}) = \left(\frac{6}{\pi\delta^2}\right)^{\frac{3}{2}} \exp\left(-\frac{6\|\boldsymbol{x}\|}{\delta^2}\right) \tag{3.5}$$

where δ is the filter width, which following the approach of Shapiro *et al.* (2019) is given by $\delta = 1.5\sqrt{\Delta x^2 + \Delta y^2 + \Delta z^2}$.

The force per unit density at a given grid point $\boldsymbol{x}$ in the direction i is given by

$$f_i = \frac{1}{2} C_T' \widehat{U_T}^2 \frac{\pi}{4} D^2 \mathcal{R}_i(\boldsymbol{x}). \tag{3.6}$$

The disc-averaged turbine velocity U_T is calculated using the indicator function $\mathcal{R}(\boldsymbol{x})$ as a weighting function,

$$U_T = \iiint u(\boldsymbol{x})\mathcal{R}_x(\boldsymbol{x}) \cos\theta\, d^3\boldsymbol{x} + \iiint v(\boldsymbol{x})\mathcal{R}_y(\boldsymbol{x}) \sin\theta\, d^3\boldsymbol{x} \tag{3.7}$$

where θ is the wind direction relative to the x direction. We use a constant value for θ which is the direction of the pressure gradient forcing. Note that u refers to the velocity in the x direction whereas U describes velocities in the wind direction.

The spatially-averaged velocity U_T is then temporally averaged using a one-sided exponential time filter with a time window of 10 minutes to calculate $\widehat{U_T}$. To calculate C_T^* from the LES we use the following relationship,

$$C_T^* = \frac{C_T'}{nU_F^2} \sum_{i=1}^{n} \left(\widehat{U_T}^2\right)_i \tag{3.8}$$

noting that turbine velocity U_T is time filtered before being squared and then averaged over all n discs. U_F is calculated by integrating the streamwise velocity ($u\cos\theta + v\sin\theta$) between the surface and $2.5H_{hub}$ across the entire domain. Unlike $\widehat{U_T}$, no time filter is used to calculate U_F. C_T^* varies with time during the LES so is time-averaged over a long period to give a single value of $\overline{C_T^*}$.

To calculate the (farm-averaged) turbine power coefficient from the LES we use the expression,

$$C_p = \frac{C_T'}{nU_{F0}^3} \sum_{i=1}^{n} \left(\widehat{U_T}^3\right)_i \tag{3.9}$$

where U_{F0} is the farm-layer-averaged velocity in an LES without turbines. C_p varies with time so $\overline{C_p}$ is calculated by time averaging over a long period.

4. Results

4.1. *LES code validation*

We firstly validate our LES framework with the new actuator disc implementation by comparing with the benchmark cases reported in Calaf *et al.* (2010). We then investigate the sensitivity of our results to horizontal resolution, domain size and pressure solver.

For the validation cases summarised in table 1 we use a surface roughness length of $z_0 = 0.1$m and a pressure gradient of $(1/\rho)\ dp_\infty/dx = 1\times10^{-3}$m/s^2. The turbines all have a hub height of 100m and a diameter of 100m. We use a turbine resistance of $C_T' = 1.33$ and the same turbine spacing as for Case A1 in Calaf *et al.* (2010) ($S_x = 7.85D$ and $S_y = 5.23D$). The surface roughness length, pressure gradient, turbine design and resistance are chosen to match the values used by Calaf *et al.* (2010). Validation cases V-1, V-2 and V-3 use a FFT pressure solver whereas V-4 uses an iterative pressure solver. Cases V-1, V-3, V-4 have a domain size $L_x \times L_y \times L_z$ of $3.14\times3.14\times1$ km (with 24 turbines) and case V-2 has a domain size of $6.28 \times 6.28 \times 1$ km (with 96 turbines). All validation cases were run for 100,000 seconds and flow data averaged between t = 30,000 and 100,000 seconds. The convergence of two flow statistics for case V-1 are shown in figure 2. Figure 3 shows the instantaneous streamwise velocity plotted on a cross-streamwise plane $2.5D$ behind a row of turbines in the validation case with a double horizontal resolution.

Figure 4a shows the time and horizontally averaged streamwise velocity for the four validation cases. The velocity profiles agree well with the results in Calaf *et al.* (2010). Figure 4b shows the profiles of total shear stress and the results reported in Calaf *et al.* (2010). The shear stress profiles match well except for the region near the bottom surface. Note that the shear stress in our LES does not approach zero at the bottom surface as it includes both modelled and resolved components; the latter of which approaches zero as in the results of Calaf *et al.* (2010). The velocity profiles are insensitive to the horizontal domain size and the pressure solver.

In wind farm LES using the actuator disc method, the disc-averaged velocity is usually overpredicted (Shapiro *et al.* 2019). This is because at coarse resolutions, the vorticity shed from the disc edge is not fully captured. This can be seen in our results by considering cases V-1 and V-3 in figure 4a. In the coarse grid case V-1, the disc-averaged velocity is overpredicted so the turbine thrust applied is greater. This results in a slightly lower $\langle\overline{u}\rangle$ throughout the entire domain. This effect is also seen in the higher uncorrected $\overline{C_T^*}$ value in case V-1 compared to V-3 (table 1), which is due to the overprediction of the disc-averaged velocity.

To correct the overprediction of disc velocity in coarse LES the following correction factor was proposed in Shapiro *et al.* (2019),

$$N = \left(1 + \frac{C_T'}{2}\frac{1}{\sqrt{3\pi}}\frac{\delta}{D}\right)^{-1}. \tag{4.1}$$

We apply this correction factor to the disc-averaged velocity by multiplying our uncorrected $\overline{C_T^*}$ values by N^2. Unlike the correction performed by Nishino & Dunstan (2020), we explicitly use the filter width δ for the correction here (equation 4.1). The correction is applied after the simulation and not during. After correction, the horizontal resolution used in cases V-1 and V-3 only had a small impact on $\overline{C_T^*}$, suggesting that this correction factor can be successfully

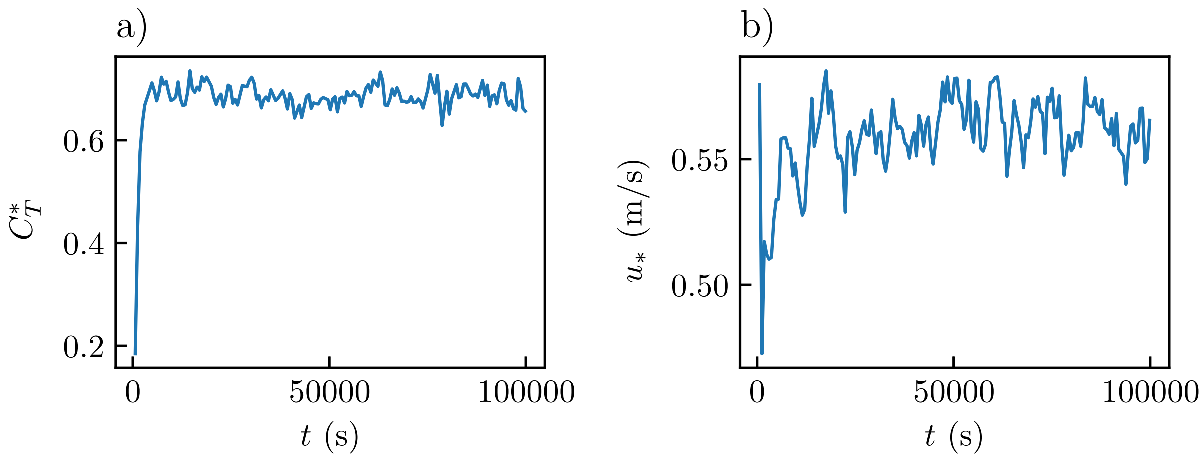

Figure 2: Time series of 10-minute-time-averaged a) internal turbine thrust coefficient C_T^* and b) friction velocity u_* for validation case V-1. Note that the time-averaging here is different from the time-filtering used to calculated $\widehat{U_T}$.

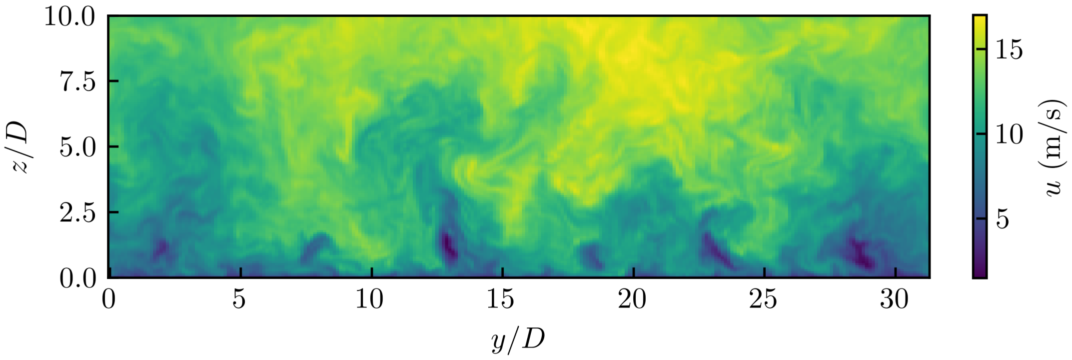

Figure 3: Instantaneous streamwise velocity behind a row of turbines in validation case V-3.

Case	$\Delta x/D$	$\Delta y/D$	$\Delta z/D$	$L_x \times L_y \times L_z$ (km)	Pressure solver	Uncorrected $\overline{C_T^*}$	$\overline{C_T^*}$
V-1	0.245	0.245	0.0787	$3.14 \times 3.14 \times 1$	FFT	0.8517	0.6845
V-2	0.245	0.245	0.0787	$6.28 \times 6.28 \times 1$	FFT	0.8587	0.6902
V-3	0.1225	0.1225	0.0787	$3.14 \times 3.14 \times 1$	FFT	0.7844	0.6957
V-4	0.245	0.245	0.0787	$3.14 \times 3.14 \times 1$	Iterative	0.8603	0.6914

Table 1: Summary of validation cases.

applied to a periodic array of actuator discs. For the value of C_T' used here the analytical model of C_T^* in (2.8) gives a value of 0.75. All the validation cases in table 1 have a lower $\overline{C_T^*}$ than this because of wake interactions between turbines.

We also consider the effect of resolution on the wake velocity deficit. Figure 5 shows the average wake profiles for each of our validation cases in table 1. The wake velocity profiles are normalised by the farm-averaged velocity $\overline{U_F}$ for each validation case. This shows the far wake velocity deficit does not vary with the domain size, horizontal resolution and pressure solver. Comparing the wake profiles for V-1 and V-3 at $2D$ downstream (figure 5a) shows a small difference in the velocity deficit at the centre. This is because V-3 uses a different filter size for the projection of the turbine area (see section 3.2). When comparing the wake

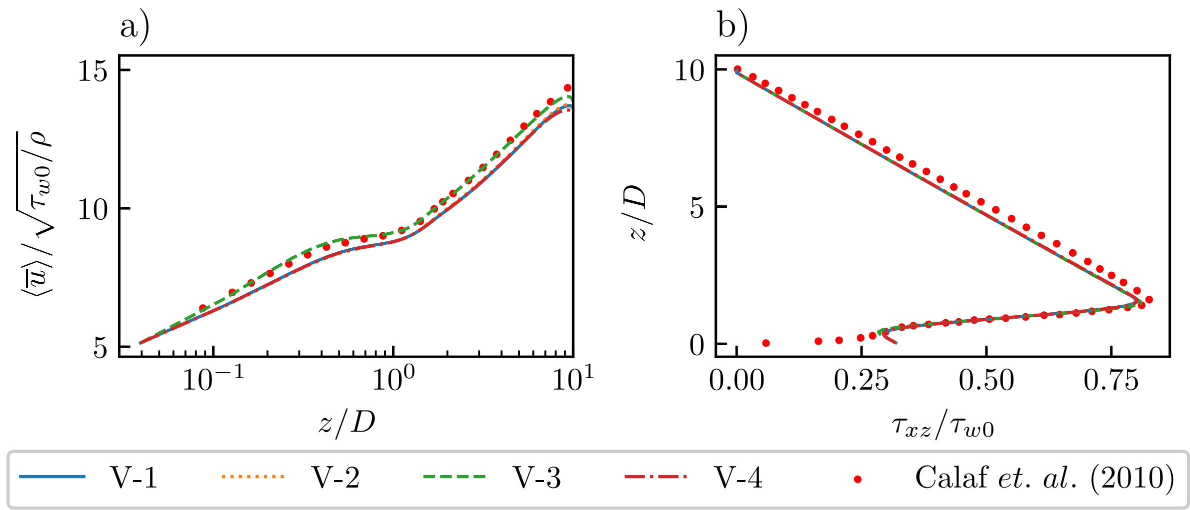

Figure 4: a) Mean velocity profiles and b) mean shear stress profiles for all validation cases, compared with Case A1 in Calaf *et al.* (2010).

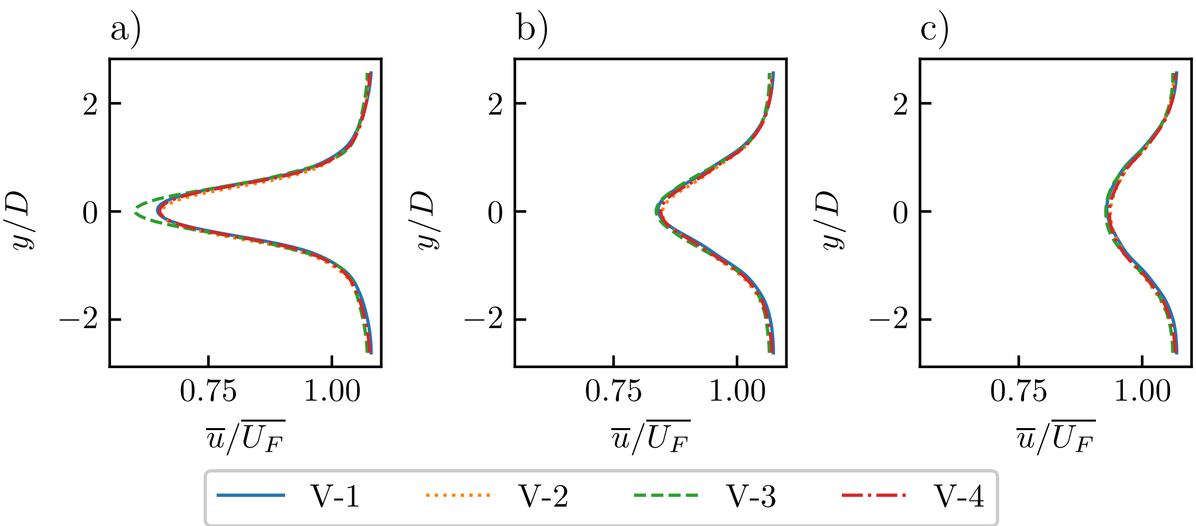

Figure 5: Normalised wake velocity deficit for each validation case a) 2D b) 4D and b) 6D downstream.

profiles $4D$ and $6D$ downstream this difference is negligible. This shows that the far wake velocity profile is insensitive to the filter size used for the turbine area projection.

To validate the capability of the code to simulate different wind directions, we also performed a simulation with a wind direction of 45°. The turbine layout in this simulation corresponds to Case K in Calaf *et al.* (2010) and is shown in figure 6b. We used a resolution of $\Delta x/D \times \Delta y/D \times \Delta z/D$ of $0.227 \times 0.227 \times 0.0787$ and a domain size of $L_x \times L_y \times L_z$ of $3.61 \times 3.61 \times 1$ km (with 32 turbines). The horizontally averaged streamwise velocity is shown in figure 6a. There is an excellent agreement with the results of Calaf *et al.* (2010) for the same turbine layout, demonstrating that our new actuator disc implementation for various wind directions (see section 3.2) is valid.

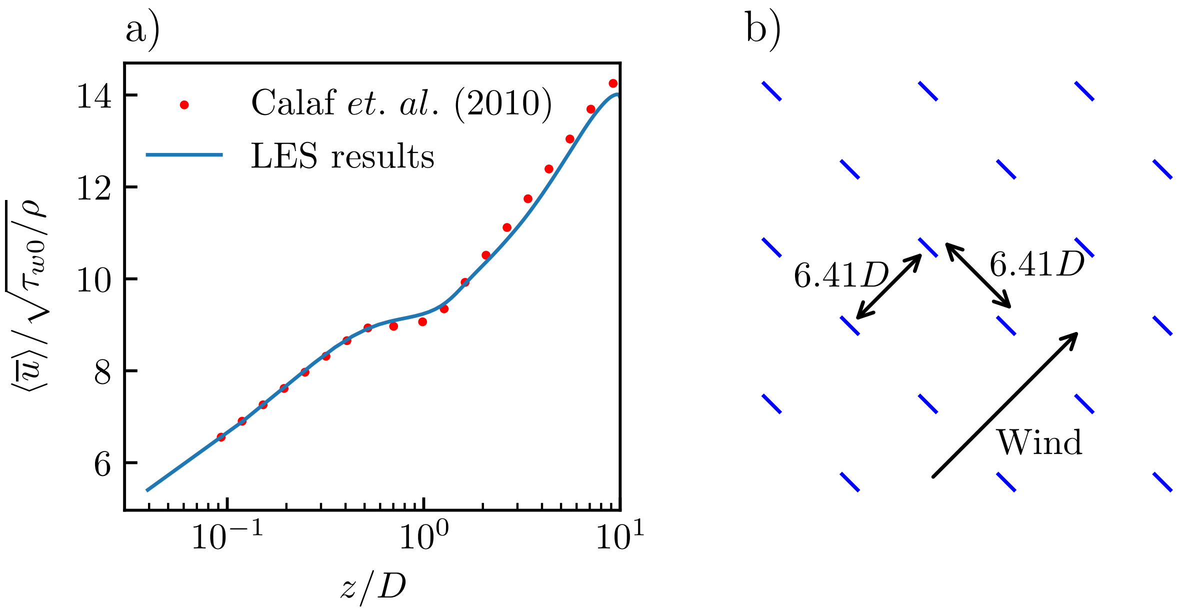

Figure 6: Validation case with 45^o wind direction: a) mean profile of the horizontally average streamwise velocity and b) turbine layout.

4.2. *LES results*

The LES cases for this study have the same setup as the validation case V-4 (see section 4.1) except for the domain size, the surface roughness length and the streamwise pressure gradient. To model offshore wind farms, we use a surface roughness length of 1×10^{-4}m and a pressure gradient of $(1/\rho)\ dp_\infty/dx_F = 8.38 \times 10^{-5}$m/s^2 in the wind direction x_F, which results in $U_{F0} = 10.103$m/s and $C_{f0} = 1.607 \times 10^{-3}$ for a fixed nominal farm-layer height of $H_F = 250$m (both obtained from LES with no turbines). All cases were run for 100,000 seconds and flow data averaged between $t = 60{,}000$ and 100,000 seconds. Note that we adopted a different spin-up and averaging period (compared to section 4.1) because of the different pressure gradient forcing.

We performed a suite of 50 simulations with different turbine layouts which are described by the parameters S_x, the turbine spacing in the x direction, S_y, the turbine spacing in the y direction and θ, the wind direction relative to the x direction (see figure 7a). The turbine operating conditions are the same for all simulations and is given by $C_T' = 1.33$. We consider a realistic range of turbine layouts and wind directions: $S_x \in [5D, 10D]$, $S_y \in [5D, 10D]$ and $\theta \in [0^o, 45^o]$. We only consider regular arrays and so by symmetry we only need to consider wind directions up to 45^o. We adopt the minimum possible horizontal domain size (L_x and L_y) within the range between 3.14km and 6.28km (depending on S_x and S_y) as the validation results presented in section 4.1 suggest that the results would be insensitive to the domain size within this range.

We use a space filling maximin design (Johnson *et al.* 1990; Santner *et al.* 2018) to select different turbine layouts in the parameter space (S_x, S_y, θ). The maximin algorithm iteratively selects a point which maximises the minimum distance to other points and to the boundaries of the parameter space. Figure 7b shows the 50 different turbine layouts selected in the parameter space.

Figure 8 shows the time-averaged flow fields from 4 of 50 cases. Figure 8a is for a case where the wind direction is almost perfectly aligned with a relatively small streamwise spacing between turbines of $5.76D$. This case gives a low $\overline{C_T^*}$ value of 0.585 due to strong wake effects. High speed regions between rows of turbines are formed because of the large cross-

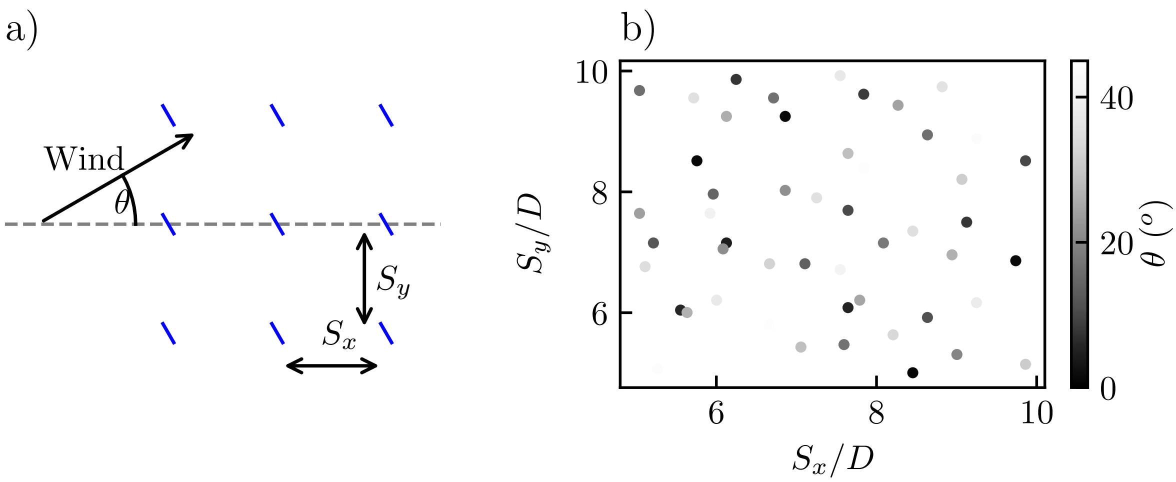

Figure 7: Design of numerical experiments: a) input parameters, and b) maximin design of 50 wind farm layouts.

streamwise turbine spacings and aligned wind direction. Figure 8b is for a case with a high turbine density and the wind direction almost aligned along the diagonal. This arrangement is similar to a staggered layout. The streamwise spacings between turbines is larger than for figure 8a so the $\overline{C_T^*}$ has a higher value of 0.669 because of the increased wake recovery between turbines.

The flow field for a case with an intermediate wind angle is shown in figure 8c. The turbine wakes are mostly misaligned with downstream turbines which minimises wake effects and gives a high $\overline{C_T^*}$ value of 0.752. This result agrees qualitatively with Stevens *et al.* (2014) in which it was found that the maximum farm power was produced by an intermediate wind direction. The results also give further evidence that the analytical model of C_T^* proposed by Nishino (2016) can be used to give a useful reference wind farm performance as it gives $C_T^* = 0.75$ in this case. Figure 8d shows the streamwise velocity for a partially waked turbine layout. The partial wake effects cause the $\overline{C_T^*}$ to be reduced slightly to 0.713.

Figure 8 also shows the effect of the turbine layout on the farm-averaged wind speed U_F. The farm shown in figure 8a has a low array density and so has a high farm-averaged wind speed of $\beta = 0.347$ (shown by the brighter colour). Figure 8b shows a farm with a high array density which resulted in a low farm-averaged speed of $\beta = 0.248$. Figures 8c and 8d have similar intermediate array densities and so had intermediate farm-averaged wind speeds of $\beta = 0.289$ and $\beta = 0.284$.

Figure 9 shows that $\overline{C_T^*}$ was not a strong function of S_x or S_y. $\overline{C_T^*}$ was found to be a much stronger function of θ (see figure 10). The lowest $\overline{C_T^*}$ values were for small values of θ because of the high degree of turbine-wake interactions. When θ was very small $\overline{C_T^*}$ was also sensitive to the value of S_x (see figure 10a). As θ increases $\overline{C_T^*}$ increases rapidly until the maximum value around 15^o. As θ increases further $\overline{C_T^*}$ slowly decreases. This is because turbines start to become aligned along the diagonal (similar to the layout shown in figure 8b). When θ is greater than 15^o, the minimum $\overline{C_T^*}$ value tends to be observed when $S_x \tan(\theta)/S_y$ is close to 1 (figure 10b). This corresponds to layouts where turbines are aligned along the diagonal (similar to the layout shown in figure 8b).

Figure 11 shows that the range of $\overline{\gamma}$ from the wind farm LES is small (varying between 1.7 and 1.8). Nishino (2016) suggested that γ would be slightly less than 2 because the presence of turbines would increase the turbulence intensity in the ABL. These results, along with the

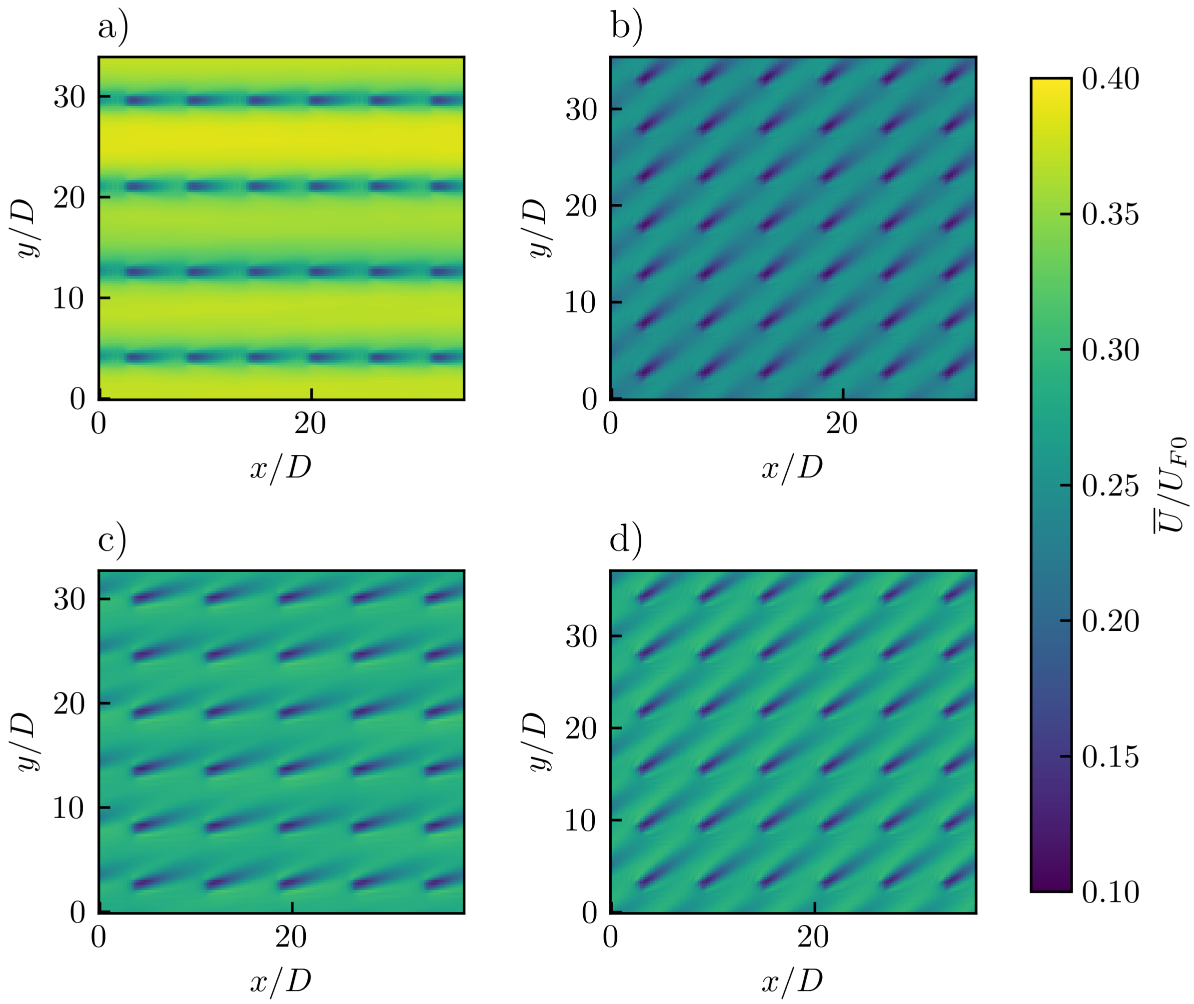

Figure 8: Time-averaged streamwise velocity at the turbine hub height for a) $S_x = 5.76D, S_y = 8.51D, \theta = 1.32^o$ b) $S_x = 5.27D, S_y = 5.07D, \theta = 43.8^o$ c) $S_x = 7.59D, S_y = 5.47D, \theta = 16.7^o$ d) $S_x = 6.00D, S_y = 6.21D, \theta = 37.6^o$.

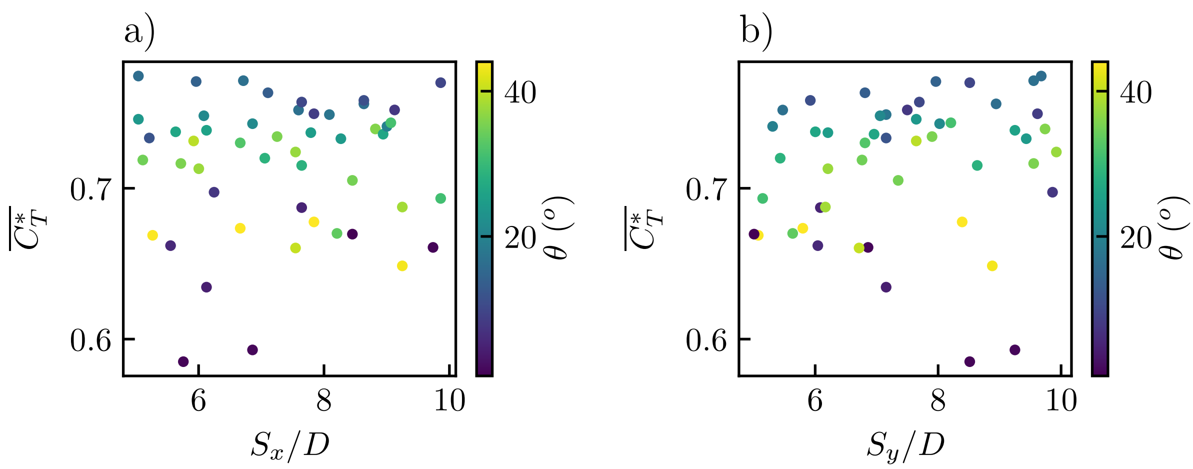

Figure 9: $\overline{C_T^*}$ against a) turbine spacing in the x direction S_x/D and b) turbine spacing in the y direction S_y/D with the colour given by the wind direction θ.

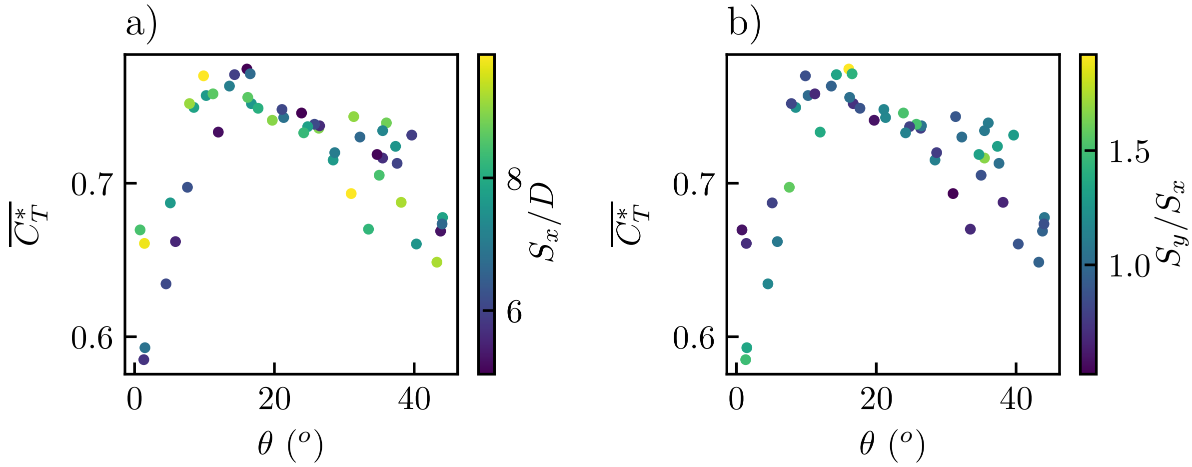

Figure 10: $\overline{C_T^*}$ against wind direction with the colour given by a) turbine spacing in the x direction S_x/D and b) $S_x \tan(\theta)/S_y$.

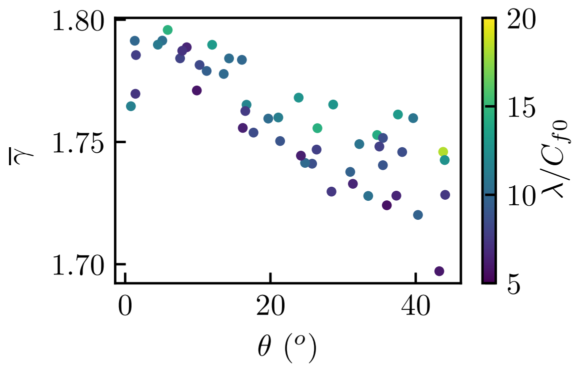

Figure 11: $\overline{\gamma}$ against the wind direction θ with the colour given by the effective array density λ/C_{f0}.

findings of Dunstan *et al.* (2018), provide evidence for this. Figure 11 shows that there is a slight variation of $\overline{\gamma}$ with wind direction and effective array density.

4.3. *Prediction of wind farm performance*

Now we compare the (farm-averaged) turbine power coefficient $\overline{C_p}$ from the wind farm LES with the analytical model derived from the two-scale momentum theory, $C_{p,Nishino}$ (equation 2.9).

To make a fair comparison of C_p between the theory and the LES, we need to consider the fact that the coarse LES resolution caused the turbine thrust to be overpredicted. For $\overline{C_T^*}$ this was corrected for in post-processing using the correction factor N (equation 4.1). However, for $\overline{C_p}$ there are two simultaneous factors that need to be corrected. The first is that the disc velocity (relative to the farm-layer velocity) has been overpredicted, which increases the turbine power. The second is that the farm-layer velocity has been underpredicted (as shown earlier in figure 4a), which reduces the turbine power. The first effect can be corrected by using the correction factor N (i.e., multiplying the raw $\overline{C_p}$ from the LES by N^3) but the second effect cannot be corrected in this manner.

To adjust for the second effect we estimate the farm wind-speed reduction that would be obtained if a sufficiently fine resolution was used for the LES, $\beta_{fine,LES}$. This should be higher than the value obtained from the coarse resolution LES, $\beta_{coarse,LES}$. To calculate $\beta_{fine,LES}$ we assume

$$\frac{\beta_{fine,LES}}{\beta_{coarse,LES}} = \frac{\beta_{fine,theory}}{\beta_{coarse,theory}} \tag{4.2}$$

where $\beta_{fine,theory}$ and $\beta_{coarse,theory}$ are the predictions from the two-scale momentum theory. $\beta_{fine,theory}$ is calculated by solving equation 2.3 (with $M = 1$) using $\overline{C_T^*}$ from the LES and the corresponding array density λ/C_{f0}. To calculate $\beta_{coarse,theory}$ we do the same but with the uncorrected turbine thrust (i.e., $\overline{C_T^*}/N^2$). Since equation 2.3 is derived from the law of momentum conservation, the only assumption we are making in equation 4.2 is that the flow is independent of Reynolds number (which is a reasonable assumption as the change in Reynolds number between the fine and the coarse resolution cases is only of the order of 10%). We can therefore estimate the turbine power from a fine resolution LES, using the expression

$$\begin{aligned}\frac{\overline{C_P}_{fine,LES}}{\overline{C_P}_{coarse,LES}} = \left(\frac{U_{T\,fine,LES}}{U_{T\,coarse,LES}}\right)^3 &= \left(\frac{U_{T\,fine,LES}/U_{F\,fine,LES}}{U_{T\,coarse,LES}/U_{F\,coarse,LES}}\right)^3\left(\frac{U_{F\,fine,LES}}{U_{F\,coarse,LES}}\right)^3 \\ &= N^3\left(\frac{\beta_{fine,LES}}{\beta_{coarse,LES}}\right)^3\end{aligned} \tag{4.3}$$

where $\overline{C_P}_{coarse,LES}$ is from the coarse resolution wind farm LES (equation 3.9).

The green symbols marked by ζ=0 in figure 12 show the corrected $\overline{C_p}$ for each of the 50 wind farm LES runs. These are plotted against the effective array density λ/C_{f0}. The blue line shows the C_p prediction using the theoretical model (equation 2.9). The theory matches remarkably well with the LES results, despite that the theory does not account for the turbine layout parameters, namely S_x, S_y and θ. The reason for this excellent agreement for $\zeta = 0$ will be discussed later in section 5.

Next, we use the results from LES of infinitely large wind farms to estimate the average power coefficients for large but finite-sized wind farms, following the concept of the two-scale momentum theory. We combine the infinite wind farm LES results with the simple linear model of the momentum availability factor M (equation 2.5). This does not capture the finite-size effects observed near the edge of the farm but reveals general trends of turbine layout effects with different atmospheric responses. We assume that the farms are still sufficiently large that the flow over the farm is mostly fully developed (or more specifically, the dependency of C_T^* on S_x, S_y and θ is still approximately the same as that in the corresponding infinitely-large farm). ‘Sufficiently large’ depends on atmospheric conditions (Wu & Porté-Agel 2017) but it is likely to be on the order of 10km.

Firstly, we consider the balance of the pressure gradient forcing (PGF) with surface stress and turbine thrust in our LES,

$$\rho(S_F C_f^* + nAC_T^*)U_F^2/2 = S_F L_z \Delta p/\Delta x \tag{4.4}$$

where C_f^* is the ‘local’ or ‘internal’ friction coefficient $C_f^* \equiv \langle\tau_w\rangle/\frac{1}{2}\rho U_F^2$ and $\Delta p/\Delta x$ is the PGF applied to the LES of an infinitely large wind farm.

If we assume C_f^* and C_T^* are independent of the PGF (as the Reynolds number of the flow

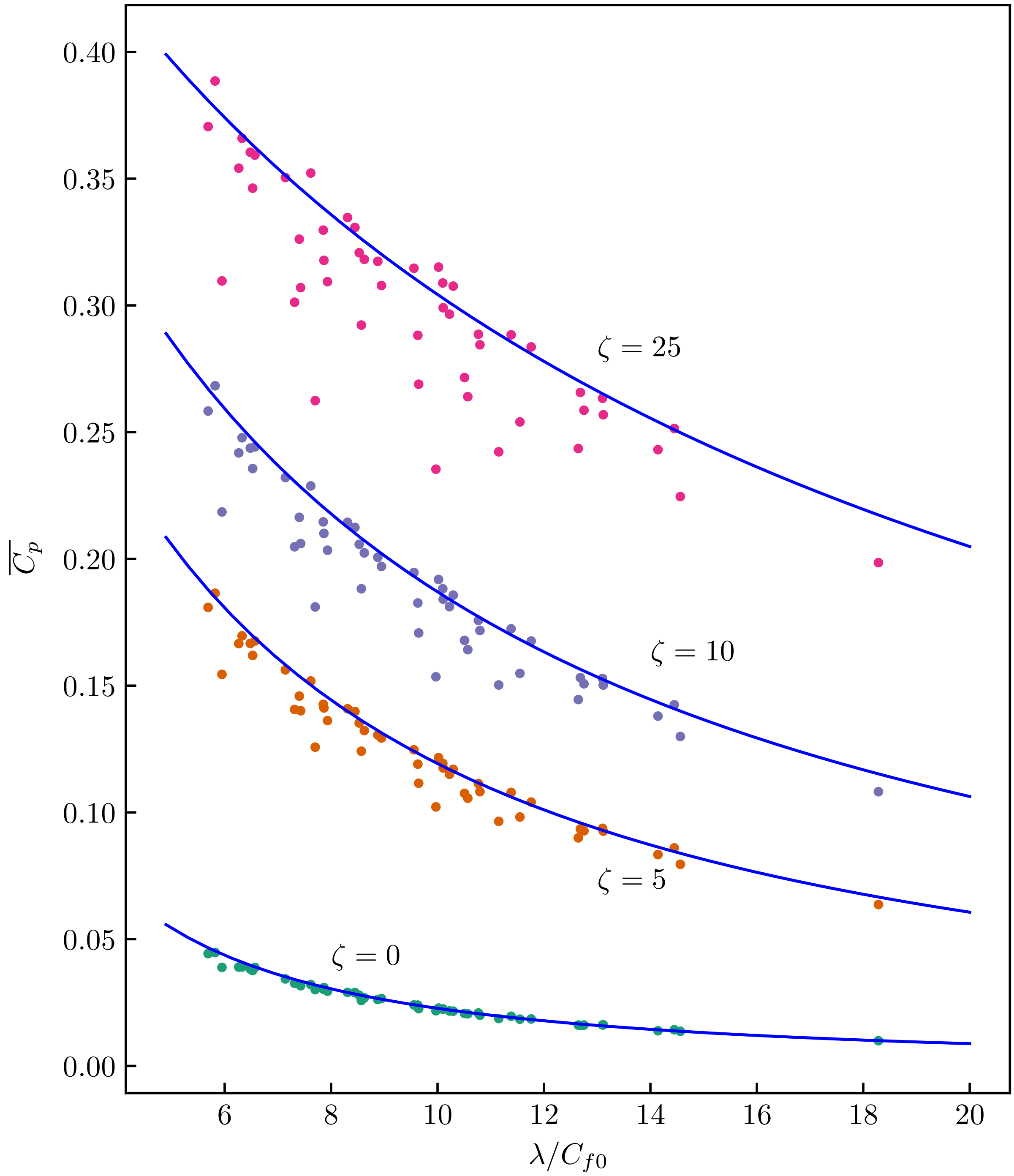

Figure 12: Average turbine power coefficient $\overline{C_p}$ from the 50 wind farm LES adjusted for different wind extractability factors (ζ). The C_p predicted by the two-scale momentum theory (equation 2.9 with $C_T' = 1.33$) is shown by the blue lines for comparison.

is very high), then equation 4.4 shows that U_F^2 should be proportional to $\Delta p/\Delta x$; hence

$$\frac{U_{F,finite}^2}{U_F^2} = \frac{\Delta p_{finite}}{\Delta x} / \frac{\Delta p}{\Delta x} \tag{4.5}$$

where U_F is the farm-layer-averaged wind speed in the LES and $\Delta p/\Delta x$ is the corresponding PGF, $U_{F,finite}$ is the new farm-layer-averaged wind speed that would result from an unknown PGF for a finite-sized wind farm, $\Delta p_{finite}/\Delta x$.

As the flow is quasi-steady and horizontally periodic with no Coriolis force in this study (meaning that we ignore the contributions of all terms except the PGF in equation 2.4), the right hand side of equation 4.5 is equivalent to the momentum availability factor M in equation 2.4. This will not be true for real wind farms under real atmospheric conditions. However, this is valid for our simplified analysis where the flow across the farm is mostly fully developed and is driven purely by a PGF. As noted earlier, it was found in Patel *et al.* (2021) that M can be well approximated by $M = 1 + \zeta(1 - \beta)$ and ζ was typically between 5 and 25 for an offshore wind farm site. Substituting this expression for M into equation 4.5 gives

$$\frac{U_{F,finite}^2}{U_F^2} = 1 + \zeta\left(1 - \frac{U_{F,finite}}{U_{F0}}\right). \tag{4.6}$$

Since U_F and U_{F0} are both known from LES results, $U_{F,finite}$ can be calculated analytically for a given ζ. Finally we assume (again based on the Reynolds number independency) that the disc-averaged velocity U_T scales with U_F and as such

$$C_{p,finite} = C_p\left(\frac{U_{F,finite}}{U_F}\right)^3. \tag{4.7}$$

where $C_{p,finite}$ is the average turbine power coefficient of the large finite-sized wind farm.

Figure 12 also shows the average power coefficients $\overline{C_p}$ estimated for three different ζ values. This shows that the atmospheric response can significantly impact the farm power. $\overline{C_p}$ for $\zeta = 25$ are roughly an order of magnitude higher than $\overline{C_p}$ for the same layout with $\zeta = 0$. Note that these results are with a constant turbine operating condition of $C_T' = 1.33$ which may not be optimal for a given ζ. Figure 4 in Nishino & Dunstan (2020) shows how the theoretically optimal turbine power coefficient, $C_{p,max}$ varies with the strength of atmospheric response.

Of particular interest in figure 12 is that, for a given λ/C_{f0}, the variation of $\overline{C_p}$ (due to different turbine layouts) increases with ζ. To better understand this trend, the $\overline{C_p}$ values for the 50 turbine layouts are presented together with their $\overline{C_T^*}$ values in figure 13 for 6 different ζ values separately. Figure 13a shows the results for infinitely large farms with ζ=0. This shows that the average turbine power coefficient is a strong function of the effective array density and insensitive to $\overline{C_T^*}$ meaning that turbine-wake interactions have little effect on the farm power. However, for finite-sized farms (figures 13b-f) the layouts with high wake interactions and a low $\overline{C_T^*}$ value tend to produce less power. These are shown by the darker plots which fall well below the theoretical prediction (blue line). Interestingly, some of the layouts seem to produce slightly higher power than predicted by the two-scale momentum theory. These layouts have a $\overline{C_T^*}$ slightly higher than 0.75 (the value for an isolated turbine) and this seems to be due to locally accelerated flow caused by the local blockage effect (Nishino & Draper 2015; Ouro & Nishino 2021). These results suggest that both the array density and turbine-wake interactions are important for the performance for large finite-sized wind farms.

Figure 13 also suggests that finite-sized wind farms are less sensitive to the effective array density than infinitely-large farms. Figure 13a shows a roughly inverse relationship between $\overline{C_p}$ and λ/C_{f0} whereas figures 13b-f show a more linear decrease of $\overline{C_p}$. Overall, the analytical model (equation 2.9) predicts the variation of $\overline{C_p}$ with the effective array density well for all of the atmospheric responses. The theoretical model does not predict the effect of turbine-wake interactions because the model of C_T^* (equation 2.8) is a function of turbine

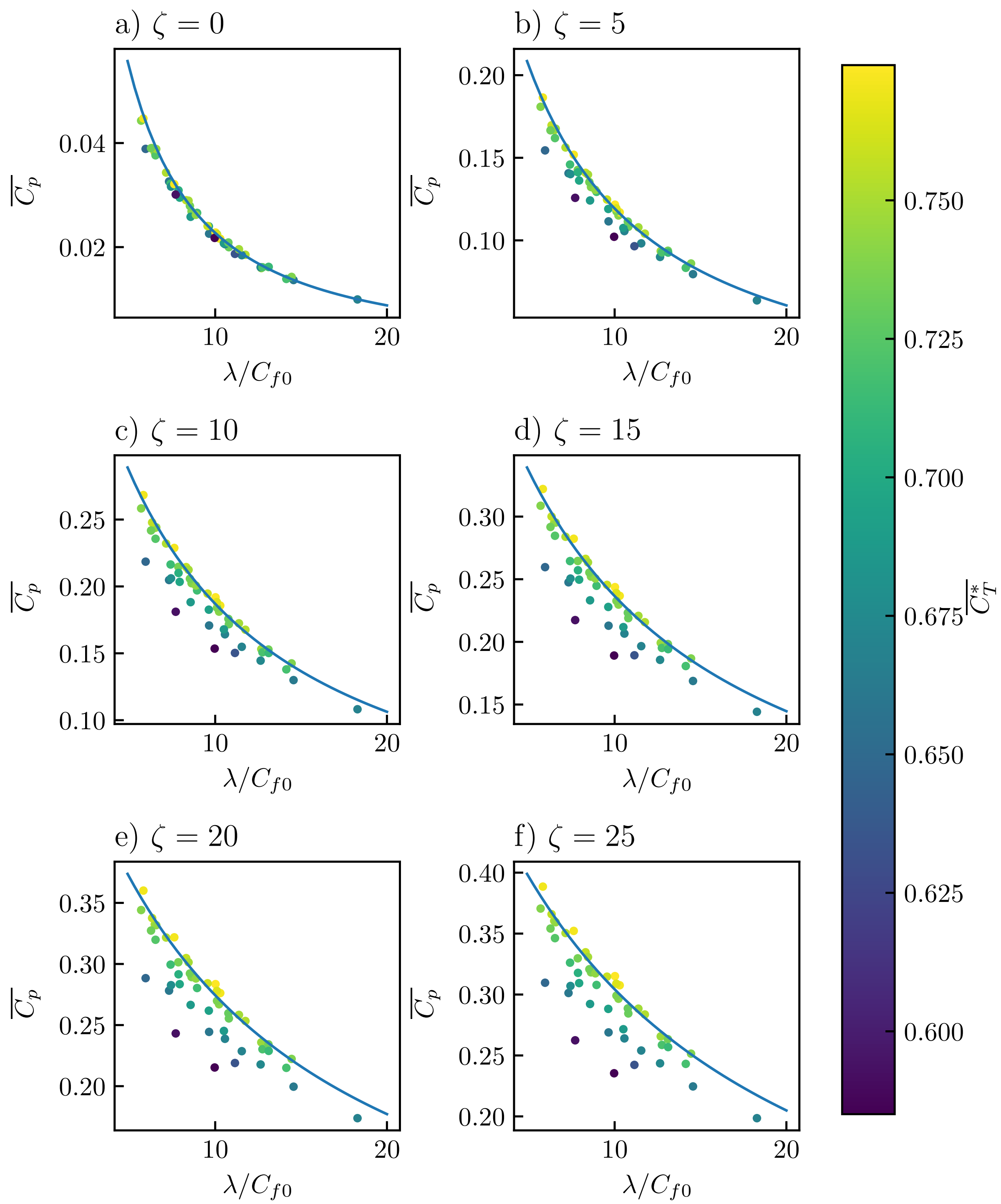

Figure 13: Turbine power coefficient $\overline{C_p}$ for a) infinite wind farms ($\zeta = 0$) and b) to f) finite wind farms with the colour giving the $\overline{C_T^*}$ recorded for each layout. The C_p predicted by the two-scale momentum theory is shown by the blue line.

operating conditions only. These results support the argument that the two-scale momentum theory can be used to provide a 'near ideal' reference value for wind farm performance.

5. Discussion

The analytical model of C_T^* (equation 2.8) has been shown in this study to provide a 'near-ideal' reference value for wind farm performance. The model is based on the classical actuator disc theory with an upstream velocity of U_F. Equation 2.8 would provide accurate predictions of C_T^* if the following two conditions are met: (1) the wind speed upstream of each turbine in the farm is U_F; and (2) the mechanism of the flow around each turbine is the same as that around an isolated actuator disc. In reality, the wind speed upstream of each turbine is often lower than U_F due to wake effects, reducing C_T^* (and thus C_p). Conversely, local blockage effects (Nishino & Draper 2015) may increase C_T^* because (1) it creates locally accelerated flows which may allow the upstream velocity of most turbines to be higher than U_F (see e.g., Ouro & Nishino 2021); and (2) it changes the mechanism of the flow around each turbine, allowing for a higher U_T (for a given C_T') than that predicted by the classical actuator disc theory. However, such a positive effect of local blockage can be exploited only when the layout is carefully optimised for a specific wind direction. As such, equation 2.8 can be used to predict the approximate 'near-ideal' farm performance, or the performance of an ideal wind farm without the negative effect of turbine-wake interactions.

Note that the analytical model of C_T^* (equation 2.8) should not be interpreted as a strict upper limit to wind farm performance. Rather it gives the performance of an actuator disc experiencing an upstream velocity equal to the farm-averaged velocity U_F. As such it is instead a novel reference turbine performance which allows the separation of power losses due to farm-scale wind speed reduction rather than local turbine-scale wind speed variations.

The results from this study also show that the $\overline{C_p}$ of infinitely large wind farms depends mainly on the effective array density (see figure 13a), i.e., the farm power is insensitive to the turbine-scale flow interactions. A closer look at the results suggest that the limited impact of turbine-scale interactions is due to the fact that the turbine drag is typically much greater than the surface drag. The ratio of total turbine drag to surface drag is given by:

$$\frac{\sum_{i=1}^{n} T_i}{\langle \tau_w \rangle S_F} = \frac{\frac{1}{2}\rho C_T^* n A U_F^2}{\frac{1}{2}\rho C_f^* S_F U_F^2} = \frac{\lambda C_T^*}{C_f^*}. \tag{5.1}$$

We measured the time-averaged value of $\lambda C_T^*/C_f^*$ for all 50 turbine layouts simulated. The mean value was 5.22, the minimum value was 2.93 and the maximum was 8.59. Therefore, the turbine drag was typically 5 times greater than the surface drag. Consider an offshore farm where $\lambda C_T^*/C_f^* = 5$, $\lambda/C_{f0} = 10$ (both typical values) and $\zeta = 0$. This means the turbine drag is 5 times greater than the surface drag and the momentum supplied by the atmosphere does not change in response to the farm. The composition of the total drag (normalised by $\langle \tau_{w0} \rangle S_F$) for this scenario is shown by the bar 1 in figure 14a. This state 1 is an equilibrium state, i.e., the normalised drag is balanced by M as in equation 2.3. If there is a sudden small change in wind direction which increases the degree of wake interactions then this will decrease C_T^* (or the ratio of T to U_F^2) for the farm. In this example, the turbine drag is now only 4 times greater than the surface drag (bar 2 in figure 14a). This corresponds to C_T^* decreasing from 0.75 to 0.6 (which is close to the largest difference observed in the 50 wind farm LES). This state 2 is a non-equilibrium state, i.e., the normalised drag is not balanced by M (due to the sudden small change of wind direction). However, if the momentum supplied by the atmosphere is unchanged the wind speed in the farm U_F will eventually increase to compensate for the reduced turbine drag. The surface and turbine drag both scale with U_F^2 so they are both expected to increase at the same rate. Bar 3 in figure 14a shows the new equilibrium state with a new composition of turbine and surface drag after the increase in U_F. Comparing states 1 and 3, the total turbine drag has been reduced only slightly because of the constant amount of momentum supplied by the atmosphere to the farm site. Therefore, for aerodynamically ideal turbines (or turbines operating below the rated wind speed), the

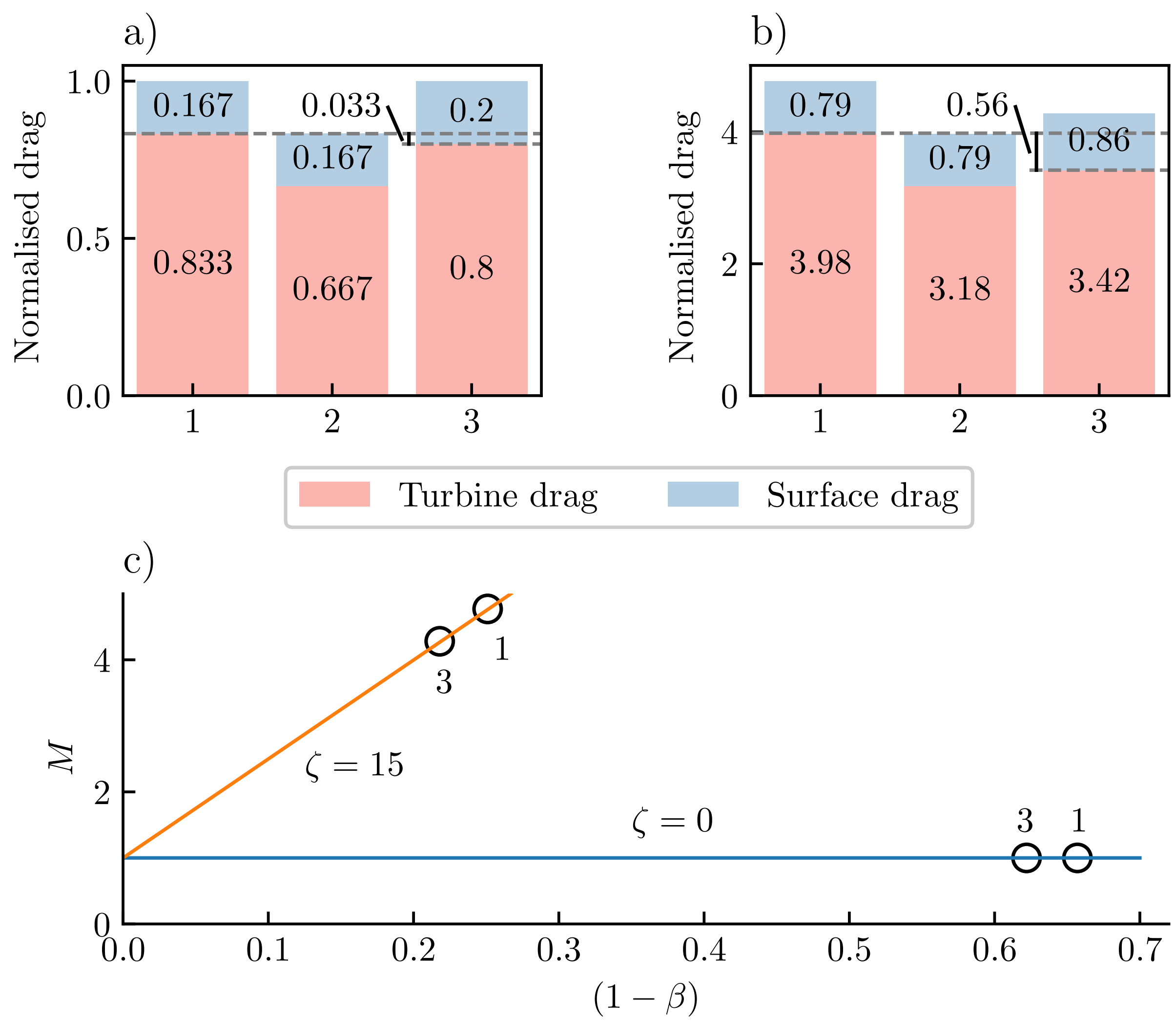

Figure 14: Examples of offshore wind farm drag composition at 3 different states: 1) equilibrium state before wind direction change, 2) non-equilibrium state immediately after a small change of wind direction, and 3) new equilibrium state after atmospheric response, for a) $\zeta = 0$ and b) $\zeta = 15$. c) schematic of the three states on the M vs $(1-\beta)$ plot.

average turbine power coefficient C_p is also insensitive to turbine-scale flow interactions when the momentum supplied by the atmosphere is constant ($\zeta = 0$).

Figure 14b explains why turbine-scale flow interactions become more important as ζ increases. Now the momentum supplied by the atmosphere changes with the farm wind-speed reduction factor β according to $M = 1 + \zeta(1-\beta)$. The ratios between turbine and surface drag for states 1 and 2 are exactly the same as for the $\zeta = 0$ case in figure 14a. However, now when the wind speed increases in response to the reduced turbine drag the momentum supplied by the atmosphere to the farm site changes. As the wind speed U_F increases, β increases so the momentum supplied by the atmosphere decreases (see figure 14c). Therefore the sum of the turbine and surface drag for state 3 decreases compared to state 1. This explains why there is a much greater reduction in turbine drag (and thus power) for the non-zero ζ case than for ζ=0. As ζ increases there will be a larger decrease in the total drag in response to an increased wind speed. Therefore the power losses due to turbine-scale flow interactions also increase as ζ increases.

To better understand the factors which determine the power output of wind farms we propose three power loss factors. Firstly, the turbine-scale loss factor Π_T which is defined by

$$\Pi_T \equiv 1 - \frac{C_p}{C_{p,Nishino}} \tag{5.2}$$

where $C_{p,Nishino}$ is given by equation 2.9. Π_T represents the power losses due to turbine-scale (or internal) flow interactions only, separate from the losses due to the farm-scale atmospheric response. For real turbines, Π_T would also include turbine design losses (i.e., power losses due to a non-ideal rotor design for a given C_T'). Figure 15a shows that the losses caused by turbine interactions are small for infinitely large farms, typically less than 5%. For some turbine layouts Π_T is negative, meaning that C_p exceeds $C_{p,Nishino}$. These layouts have $\overline{C_T^*}$ values greater than 0.75 which is the value given by equation 2.8. As discussed earlier, this is likely to be due to local blockage effects increasing the turbine incident velocity above the farm-layer velocity U_F. Figures 15b-f show that the turbine-scale losses are greater in finite-sized farms with the same turbine layout. Under different atmospheric conditions, the same turbine layout can give different turbine-scale losses. Across a realistic range of wind extractability factors, the turbine-scale losses from the same layout can vary significantly. As an example, the losses from one layout varies from 13% to 22% as ζ changes from 5 to 25. Figure 15 suggests the maximum losses due to turbine-scale flow interactions is likely to be about 20% for large offshore wind farms.

The farm-scale loss factor, Π_F, represents the power loss due to the atmospheric response to the whole farm, and is defined by

$$\Pi_F \equiv 1 - \frac{C_{p,Nishino}}{C_{p,Betz}} \tag{5.3}$$

where $C_{p,Betz}$ is given by equation 2.10. Note that in this study $C_T' = 1.33$ and hence $C_{p,Betz} = 0.563$ ($C_T' = 2$ would give the optimal performance for an isolated turbine of $C_{p,Betz} = 16/27$). Π_F represents the power loss accompanied by the reduction of the farm-average wind speed. Figure 16 shows that the farm-scale losses are typically more than twice the turbine-scale losses (i.e., Π_T/Π_F is generally less than 0.5). This suggests that for large offshore wind farms the atmospheric response to the array density is more important than the turbine-scale interactions (i.e., wake effects). Similarly the total power loss factor, Π, can also be defined as

$$\Pi \equiv 1 - \frac{C_p}{C_{p,Betz}} = 1 - (1 - \Pi_T)(1 - \Pi_F). \tag{5.4}$$

The fact that farm-scale losses may be larger than turbine-scale losses for large offshore farms does not mean that turbine wakes are not important. Porté-Agel *et al.* (2013) showed that wake effects can reduce farm power by up to 30%. Rather this study suggests that as wind farms become larger farm-scale flow effects will have an increasing impact on the farm performance. This is a slightly different framework for viewing farm performance. Here we suggest splitting the mutli-scale flow effects into a farm-scale wind speed reduction due to the farm-atmosphere interaction. This is in addition to turbine-scale flow heterogeneity due to turbine wakes.

It is important to note that different turbine layouts will have different stresses throughout the farm. This study considered only regular turbine arrays with a set turbine spacing and wind direction. It is possible that there may be some difference for irregular turbine layouts. This may have implications on the values of turbine-scale and farm-scale losses for realistic wind farms with irregular layouts. This should be investigated further in future research.

Another important note is that the turbine-scale loss factor discussed above is smaller than

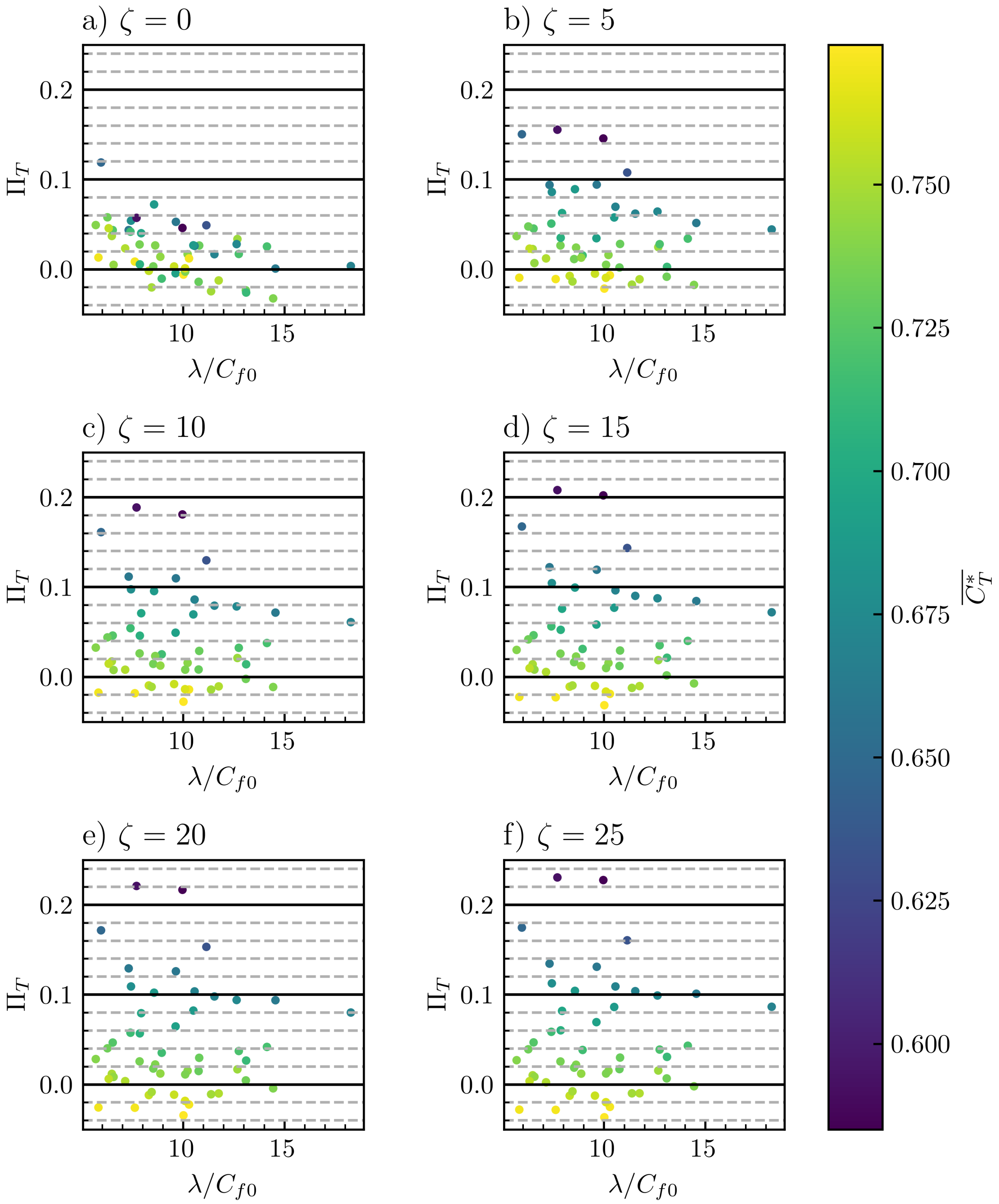

Figure 15: Turbine-scale loss factor Π_T for a) infinite wind farms ($\zeta = 0$) and b) to f) finite wind farms with the colour giving the $\overline{C_T^*}$ recorded for each layout.

what is typically referred to as 'wake losses' (see figure 17). 'Wake losses' are traditionally evaluated by comparing the farm power with the power produced by the first row of turbines ($C_{p,1}$ in figure 17). However, this includes not only the losses due to wake interactions between turbines but also the atmospheric response to the array density. In contrast, Π_T represents the power losses solely due to the interactions between turbines. For the same reason, the farm-scale loss factor, Π_F, is larger than what is often referred to as 'farm blockage losses'. These two different classifications of power losses (one using $C_{p,Nishino}$

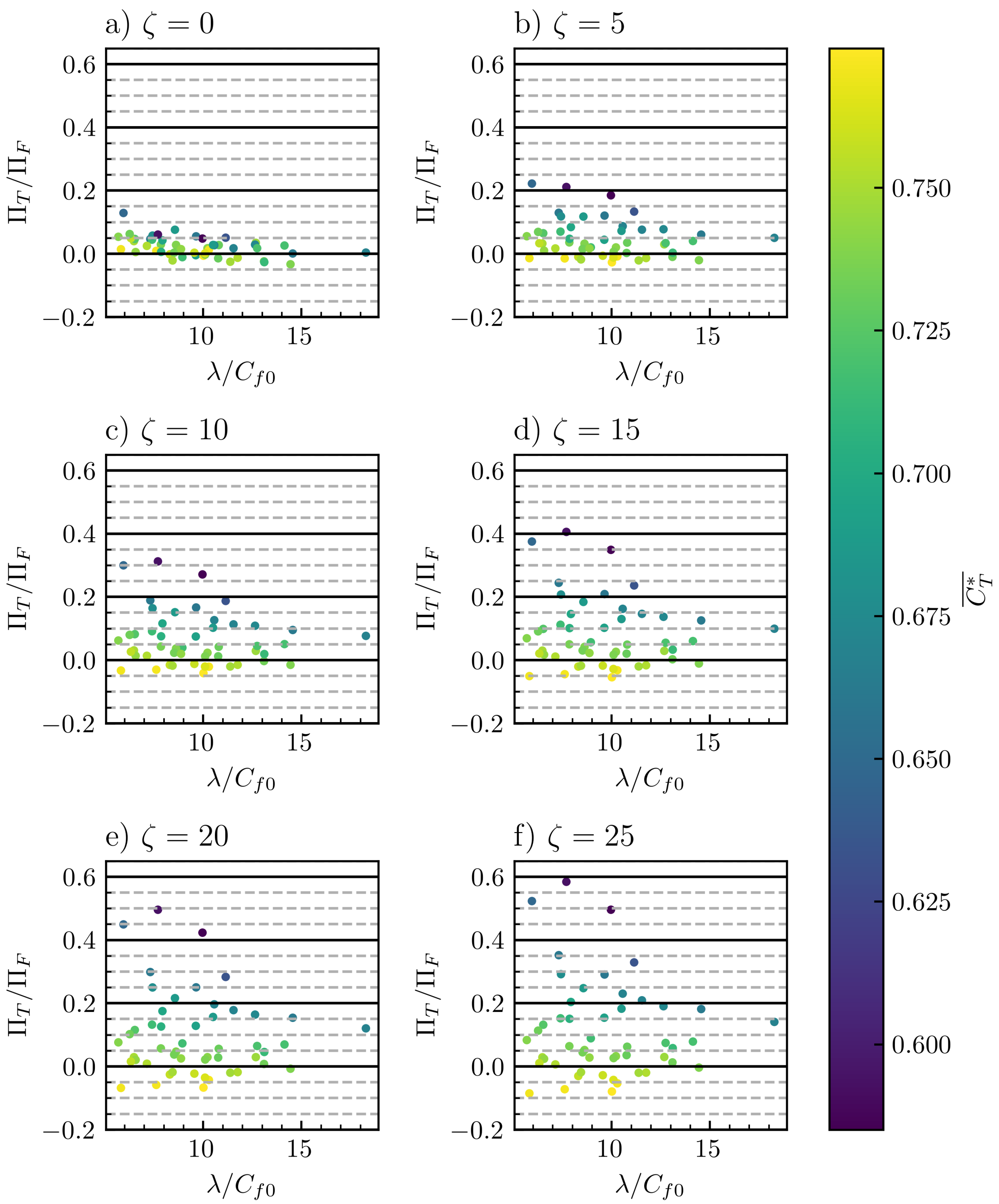

Figure 16: Ratio of turbine-scale to farm-scale loss factors Π_T/Π_F for a) infinite wind farms ($\zeta = 0$) and b) to f) finite wind farms with the colour giving the $\overline{C_T^*}$ recorded for each layout.

and the other using $C_{p,1}$ as a point of reference) are both useful in different ways. The latter classification is straightforward when the value of $C_{p,1}$ is known; however, sometimes $C_{p,1}$ cannot be defined unambiguously (e.g., when there is no regular 'front row' which is perpendicular to the wind direction). The merit of using $C_{p,Nishino}$ is that this can be predicted analytically using equation 2.9.

It should be noted that figure 17 is for actuator discs (i.e., ideal turbines). Real turbines will experience additional power losses due to practical (non-ideal) turbine design.

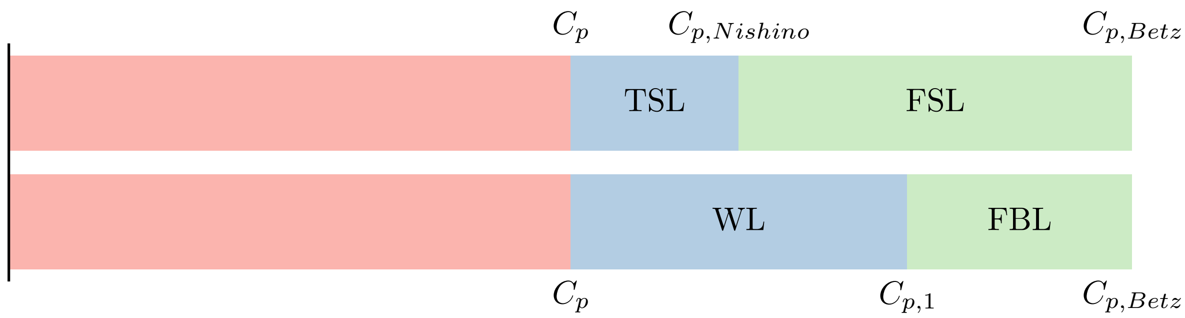

Figure 17: Comparison of turbine-scale loss (TSL) and farm-scale loss (FSL) with what is known as wake loss (WL) and farm blockage loss (FBL). $C_{p,1}$ is the power coefficient recorded by the first row of turbines in a farm.

As demonstrated earlier in figures 13, 15 and 16, the strength of atmospheric response alters wind farm performance. The importance of array density and turbine layout vary with the large-scale atmospheric conditions. The results shown in appendix B suggests that the value of ζ tends to decrease as the wind farm size increases (at least within the range between 10km to 30km; note that the values of ζ reported in Patel *et al.* (2021) were for a fixed wind farm size of 20km). These results seem to suggest that larger wind farms will be less sensitive to turbine-scale wake effects and more sensitive to farm-scale losses. This could have significant implications for the design of future wind farms.

It is also worth noting that similar trends of large wind farm aerodynamics have already been reported in the literature, e.g., in the wind farm LES performed by Wu & Porté-Agel (2017) in which they also used a relatively low surface roughness length of 0.05m. They performed LES of finite and infinite wind farms under a weak and strong free-atmosphere stratification, using a rotational actuator disc model (representing Vestas V-80 2MW turbine) with an aligned and a staggered turbine layout with the same array density. The varying free-atmosphere stratifications changes the strength of atmospheric response, which affects the wind farm blockage. Figure 11 in Wu & Porté-Agel (2017) shows the power production of different turbine rows for the different wind farms. For both atmospheric conditions, the layout of the infinite wind farm did not change the farm power. This agrees with our finding that the power output of infinite wind farms are insensitive to turbine interactions. The stronger free-atmosphere stratification induced a larger pressure gradient across the farm which implies a larger ζ value. The power output of the finite farm under the strong free-atmosphere stratification was more sensitive to the turbine layout. Under a weak stratification the layout had a smaller impact on farm power. This is further confirmation that the large-scale atmospheric response changes the importance of turbine-scale interactions. Other LES studies have also generally found that the power output of finite wind farms (e.g., Porté-Agel *et al.* 2013; Stevens *et al.* 2014; Archer *et al.* 2013) is more sensitive to turbine layout than infinite farms (e.g., Yang *et al.* 2012; Yang & Sotiropoulos 2014; Abkar & Porté-Agel 2013). However, these previous studies used surface roughness lengths typical of rough onshore locations rather than offshore, meaning that the ratio of total turbine drag to surface drag (equation 5.1) was smaller than the present study.

The impact of turbine layout on wind farm performance is typically investigated by reporting the normalised turbine power, where the turbine power is normalised by either the power of a turbine in the first row or that of a standalone turbine. The normalised power is often used as a measure of turbine-wake interactions within the wind farm. However, this could be misleading for a large wind farm where the power is also reduced due to the ABL response to the farm resistance. The turbine-scale loss factor, Π_T, gives the power losses due to wake interactions separated from farm-scale effects. Our results suggest that the power losses in large farms with the same layout can change with the strength of large-scale atmospheric response. Hence, the relative performance of different turbine layouts can also vary with the strength of atmospheric response. Layouts which produce more power with a specific large-scale atmospheric response may not perform as well under different responses.

A limitation of this study is that the wind farm LES consider only neutrally stratified atmospheric boundary layers. One uncertainty is how different stratifications would affect wake recovery within large wind farms, which could affect the $\overline{C_T^*}$ value for a given turbine layout. However, since the two-scale momentum theory has been derived from the principle of momentum conservation which is valid for all atmospheric conditions, we expect that the trends found in this study (on how the importance of turbine-scale interactions changes with the strength of the atmospheric response) would be observed generally. The study also used a fixed turbine operating condition given by $C_T' = 1.33$. This is typical for the current wind turbines operating below their rated wind speed (at which the farm blockage effects are most significant). Therefore the results of this study give the trends for large farms if the operating conditions are similar to those currently used. As discussed earlier, the trends found in this study have also been observed in LES of finite wind farms with different atmospheric conditions and a different turbine model, supporting the generality of our findings.

6. Conclusions

In this study we performed a combined theoretical and computational analysis of large wind farms, using the two-scale momentum theory (Nishino & Dunstan 2020) and new LES of infinitely large wind farms with different turbine layouts and wind directions. To consider a range of wind directions, we used a new implementation of the actuator disc model which is not aligned with the structured grid. Firstly, we validated the LES against the results published by Calaf *et al.* (2010) and found an excellent agreement. We also confirmed that, when the correction factor proposed by Shapiro *et al.* (2019) is applied, the average internal turbine thrust coefficient $\overline{C_T^*}$ (representing the turbine thrust relative to the square of the average wind speed across the wind farm layer) is insensitive to the grid resolution. We then performed 50 wind farm LES with different turbine spacings and wind directions. $\overline{C_T^*}$ was found to be a strong function of wind direction with a weaker dependence on turbine spacings.

This study adopted an approach to adjust the average power coefficient $\overline{C_p}$ of an infinitely large wind farm to estimate the power of large but finite-sized farms with the same layout, following the concept of the two-scale momentum theory. A full validation of this approach is currently infeasible as it would require a large set of finite-size wind farm LES, which will be the subject of future studies. However, we have provided detailed theoretical arguments on why we can estimate the power of large finite-size farms from the results of infinitely large farm LES. For infinitely large farms, $\overline{C_p}$ was found to be a strong function of the array density and agree remarkably well with the analytical model (equation 2.9). The power produced by large finite-sized farms was found to depend on both the array density and turbine layout (including the effect of wind direction), although the analytical model still provides an approximate upper limit of the power (for a given array density). These results confirm that, to model large but finite-sized wind farms it is important to consider both the effect of array density and the turbine layout.

The impact of array density and turbine layout on farm power varies with the strength of atmospheric response or the ‘wind extractability’. The analytical model seems to predict very well the impact of array density for a given farm-scale atmospheric response. As such, we propose a new classification of power losses in large wind farms by introducing new metrics, namely a turbine-scale loss factor Π_T, a farm-scale loss factor Π_F and a total loss factor Π. The turbine-scale loss factor describes the power losses due to turbine-scale wake interactions only (which is smaller than what is commonly called 'wake losses'). Importantly, the turbine-scale loss factor varies with the strength of large-scale atmospheric response. As an example, Π_T varied from 0.13 to 0.22 for a given layout across a realistic range of the extractability factor (from $\zeta = 5$ to 25 in this study). Although further studies are required to better quantify the extractability factor, the results obtained to date suggest that as wind farms get larger the proportion of power losses due to turbine-wake interactions will decrease. This is because (1) having a better turbine layout (with less wake interactions and higher C_T^*) does not substantially increase the momentum available to the farm site when ζ is small (figure 14) and (2) ζ seems to decrease as the wind farm size increases. The farm-scale loss factor describes the power loss due to the atmospheric response to the array density (which is larger than what is often called 'farm blockage losses'). Π_F was typically more than twice as large as Π_T for the 50 offshore wind farms considered in this study with a realistic range of atmospheric responses. This suggests that farm-scale flow effects have a greater impact than turbine-scale flow effects on the performance of large offshore wind farms.

Acknowledgements. The first author (AK) acknowledges the NERC-Oxford Doctoral Training Partnership in Environmental Research (NE/S007474/1) for funding and training. We acknowledge use of the Monsoon2 system, a collaborative facility supplied under the Joint Weather and Climate Research Programme, a strategic partnership between the Met Office and the Natural Environment Research Council. We also thank Dr François-Xavier Briol for helpful discussions and assistance with the design of numerical experiments (figure 7b) and Joseph Ashton for assistance with the analysis of NWP data shown in appendix B.

Funding. This work was supported by the Natural Environmental Research Council (NERC) award NE/S007474/1.

Declaration of Interests. The authors report no conflict of interest.

Data availability statement. The data that support the findings of this study are openly available at https://github.com/AndrewKirby2/wind-farm-modelling. This includes the wind farm LES results and the code used to calculate the data for figures 13, 15 and 16.

Author ORCID. A. Kirby, https://orcid.org/0000-0001-8389-1619; T. Nishino, https://orcid.org/0000-0001-6306-7702.

Author contributions. T.N. derived the theory, A.K. and T.D.D. performed the simulations, A.K. and T.N. analysed the data. A.K. wrote the paper with corrections from T.N. and T.D.D.

Appendix A. Sensitivity of results to nominal farm-layer height H_F

The height of the farm-layer, H_F, can be defined in several ways. This study uses the definition $H_F = 2.5H_{hub}$ where H_{hub} is the turbine hub height. Differences in the value of H_F will change the values of U_F, U_{F0}, $\overline{C_T^*}$ and C_{f0} of the LES results presented in section 4. However, as noted by Nishino & Dunstan (2020), the conservation of momentum arguments used to derive equation 2.3 and to eventually predict C_p from equation 2.6, are valid irrespective of the H_F value, provided that the same H_F value is used in both 'internal' and 'external' sub-problems. The question here is how much the results of 'internal' sub-problem (i.e., LES results in this study) and 'external' sub-problem (i.e., the value of ζ obtained from NWP simulations) change with the choice of H_F. Although the 'external' sub-problem is outside the scope of this paper, Patel *et al.* (2021) reported that the sensitivity of their NWP results to the choice of H_F was minor. In the following, we present how the sensitivity of the LES results to the choice of H_F eventually affects the value of C_p obtained (assuming that ζ is not affected by H_F).

To investigate the sensitivity of the results to H_F, we repeat the analysis with $\zeta = 25$ using

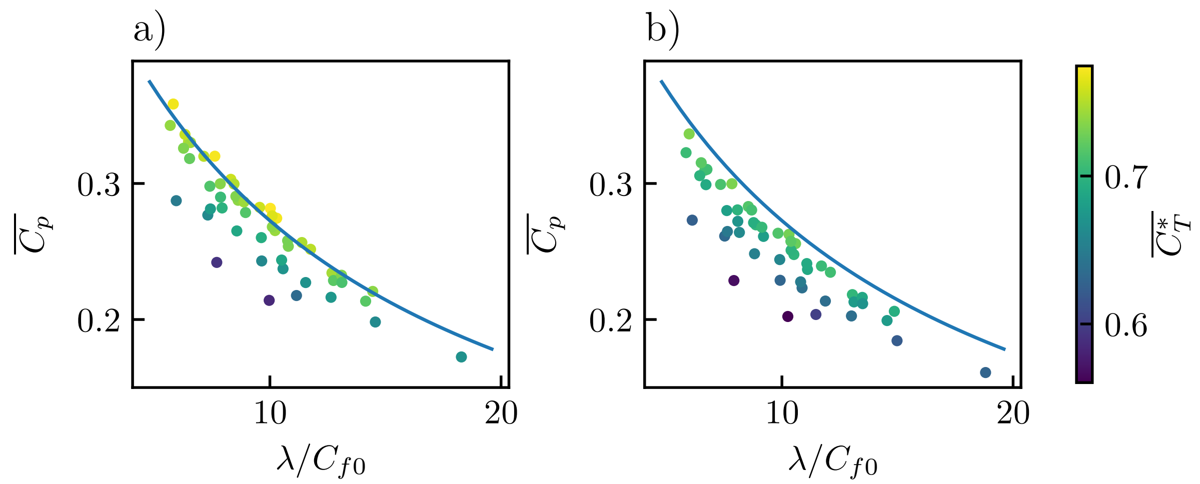

Figure 18: LES and theoretical results for $\overline{C_p}$ with $\zeta = 25$ for a) H_F=250m and b) H_F=300m.

$H_F = 3H_{hub}$. Figure 18 compares the $\overline{C_p}$ values obtained for $H_F = 2.5H_{hub}$ and $3H_{hub}$. Changing the value of H_F has no effect on the theoretical predictions of C_p for a given ζ. Increasing H_F decreases the LES-based results of $\overline{C_p}$ for each farm because the reference velocity U_{F0} slightly increases. The increase in U_{F0} is the same for all wind farm cases. Therefore, increasing H_F to $3H_{hub}$ reduces the $\overline{C_p}$ of all wind farm cases by the same factor of 1.043 in this study. The absolute values of $\overline{C_p}$ are affected by the value of H_F but the trends reported in this study remain unchanged. The $\overline{C_T^*}$ values obtained from the LES are also reduced when the farm-layer height is increased. This is because the reference velocity U_F slightly increases. Nevertheless, the two-scale momentum theory still captures the trend well and can provide an upper bound estimate to wind farm performance.

Nishino & Dunstan (2020) proposed a definition for H_F based on the undisturbed velocity profile $\overline{U_0(z)}$. H_F is defined as the farm-layer height with which the farm-layer average of the undisturbed velocity is equal to that of the rotor average, i.e.,

$$\frac{\int_0^{H_F} \overline{U_0} dz}{H_F} = \frac{\int \overline{U_0} dA}{A}. \tag{A 1}$$

Using this definition, the exact value of H_F will vary with turbine design and (undisturbed) ABL profile. Figure 19 shows the value of H_F according to A 1 for a wide range of velocity profiles and turbine designs. We assume that the velocity profile is given by the logarithmic law for a wide range of surface roughness lengths that includes onshore and offshore locations. For the turbine design, we assume that the distance between the surface and bottom of the rotor is fixed at 50m. The range of D/H_{hub} used corresponds to turbine diameters from 100m up to 300m. Across a wide range of turbine design and velocity profiles the value of H_F obtained from equation A 1 only varies between $2.5H_{hub}$ and $3H_{hub}$.

The average turbine power coefficient $\overline{C_p}$ is changed only slightly when H_F is increased from $2.5H_{hub}$ to $3H_{hub}$. The trends reported in this study are unaffected by a change in H_F. H_F is relatively insensitive to velocity profiles and turbine design and is expected to be in the range $2.5H_{hub}$ to $3H_{hub}$. Therefore, the results of the present study are insensitive to the exact value of H_F.

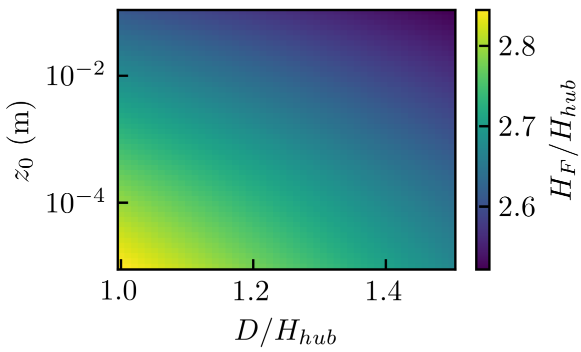

Figure 19: Variation of normalised wind farm-layer height H_F/H_{hub} with surface roughness length z_0 and turbine design parameter D/H_{hub} for a log law wind profile.

Appendix B. Effect of wind farm size on the wind extractability factor ζ

To explore the effect of wind farm size on the wind extractability factor ζ, we performed additional twin NWP simulations using the same methodology as Patel *et al.* (2021). Within the simulations, the diameter of a hypothetical circular wind farm (located off the east coast of Scotland) was varied from 10km to 30km. Example results for a 24-hour period with a relatively constant wind speed across the farm site (corresponding to Case B of figure 9 of Patel *et al.* (2021)) are shown in figure 20. It can be seen that the value of ζ tends to decrease with increasing the wind farm size for all the time. Further simulations are required in future studies to derive a correction function for the effect of wind farm size on ζ, but our preliminary results suggest that an exponential relationship may exist between the wind farm size and ζ. Such an exponential correction would satisfy the expected asymptotic behaviour of ζ (i.e., ζ approaches to $+\infty$ and 0 as the farm size approaches to 0 and $+\infty$, respectively). Figure 20 also shows that ζ varies significantly with time due to changing atmospheric conditions. These preliminary results show that ζ depends both on wind farm size and atmospheric conditions.

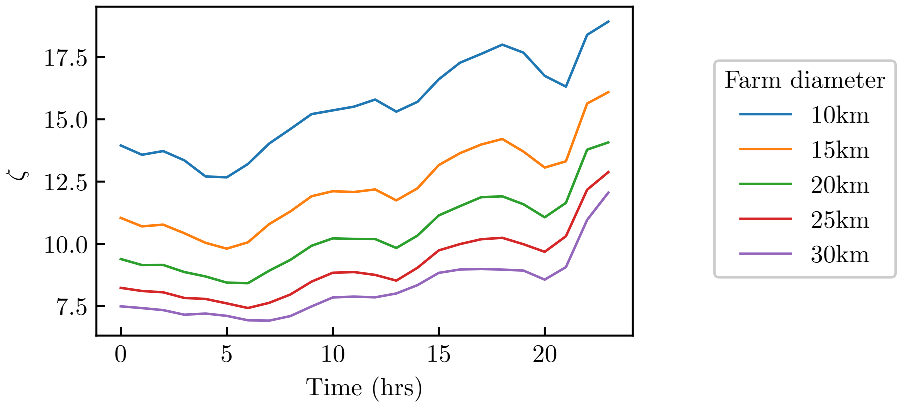

Figure 20: Variation of ζ throughout a 24 hour period (corresponding to Case B in figure 9 of Patel *et al.* (2021)) for different wind farm diameters.

REFERENCES

Abkar, M. & Porté-Agel, F. 2013 The effect of free-atmosphere stratification on boundary-layer flow and power output from very large wind farms. *Energies* **6**, 2338–2361.

Allaerts, D. & Meyers, J. 2017 Boundary-layer development and gravity waves in conventionally neutral wind farms. *Journal of Fluid Mechanics* **814**, 95–130.

Allaerts, D. & Meyers, J. 2018 Gravity waves and wind-farm efficiency in neutral and stable conditions. *Boundary-Layer Meteorology* **166**, 269–299.

Allaerts, D. & Meyers, J. 2019 Sensitivity and feedback of wind-farm-induced gravity waves. *Journal of Fluid Mechanics* **862**, 990–1028.

Archer, C. L., Mirzaeisefat, S. & Lee, S. 2013 Quantifying the sensitivity of wind farm performance to array layout options using large-eddy simulation. *Geophysical Research Letters* **40**, 4963–4970.

Barthelmie, R. J., Pryor, S. C., Frandsen, S. T., Hansen, K. S., Schepers, J. G., Rados, K., Schlez, W., Neubert, A., Jensen, L. E. & Neckelmann, S. 2010 Quantifying the impact of wind turbine wakes on power output at offshore wind farms. *Journal of Atmospheric and Oceanic Technology* **27**, 1302–1317.

Bastankhah, M. & Porté-Agel, F. 2014 A new analytical model for wind-turbine wakes. *Renewable Energy* **70**, 116–123.

Bleeg, J., Purcell, M., Ruisi, R. & Traiger, E. 2018 Wind farm blockage and the consequences of neglecting its impact on energy production. *Energies* **11**, 1609.

Brower, N & Robinson, N 2012 The openwind deep-array wake model: development and validation. *AWS Truepower* .

Brown, A. R., Derbyshire, S. H. & Mason, P. J. 1994 Large-eddy simulation of stable atmospheric boundary layers with a revised stochastic subgrid model. *Quarterly Journal of the Royal Meteorological Society* **120**, 1485–1512.

Brown, N., Weiland, M., Hill, A. & Shipway, B. 2018 In situ data analytics for highly scalable cloud modelling on cray machines. *Concurrency and Computation: Practice and Experience* **30**, 4331.

Calaf, M., Meneveau, C. & Meyers, J. 2010 Large eddy simulation study of fully developed wind-turbine array boundary layers. *Physics of Fluids* **22**, 1–16.

Dunstan, T. D., Murai, T. & Nishino, T. 2018 Validation of a theoretical model for large turbine array performance under realistic atmospheric conditions. *AMS 23rd Symposium on Boundary Layers and Turbulence* .

Frandsen, S. 1992 On the wind speed reduction in the center of large clusters of wind turbines. *Journal of Wind Engineering and Industrial Aerodynamics* **39**, 251–265.

Frandsen, S., Barthelmie, R., Pryor, S., Rathmann, O., Larsen, S., Højstrup, J. & Thøgersen, M. 2006 Analytical modelling of wind speed deficit in large offshore wind farms. *Wind Energy* **9**, 39–53.

Jensen, N. O. 1983 A note on wind generator interaction. *Risø-M-2411 Risø National Laboratory Roskilde* .

Johnson, M. E., Moore, L. M. & Ylvisaker, D. 1990 Minimax and maximin distance designs. *Journal of Statistical Planning and Inference* **26**, 131–148.

Katic, I., Hojstrup, J. & Jensen, N. O. 1986 A simple model for cluster efficiency. *Proceedings of the European wind energy association conference and exhibition, Rome, Italy* pp. 407–409.

Ma, L., Nishino, T. & Antoniadis, A. F. 2019 Prediction of the impact of support structures on the aerodynamic performance of large wind farms. *Journal of Renewable and Sustainable Energy* **11**, 063306.

Maas, O. & Raasch, S. 2022 Wake properties and power output of very large wind farms for different meteorological conditions and turbine spacings: A large-eddy simulation case study for the german bight. *Wind Energy Science* **7**.

Nishino, T. 2016 Two-scale momentum theory for very large wind farms. *Journal of Physics: Conference Series* **753**, 032054.

Nishino, T. & Draper, S. 2015 Local blockage effect for wind turbines. *Journal of Physics: Conference Series* **625**, 012010.

Nishino, T. & Dunstan, T. D. 2020 Two-scale momentum theory for time-dependent modelling of large wind farms. *Journal of Fluid Mechanics* **894**, A2.

Ouro, P. & Nishino, T. 2021 Performance and wake characteristics of tidal turbines in an infinitely large array. *Journal of Fluid Mechanics* **925**.

Patel, K., Dunstan, T. D. & Nishino, T. 2021 Time-dependent upper limits to the performance of large wind farms due to mesoscale atmospheric response. *Energies* **14**, 6437.

Porté-Agel, F., Bastankhah, M. & Shamsoddin, S. 2020 Wind-turbine and wind-farm flows: A review. *Boundary-Layer Meteorology* **174**, 1–59.

Porté-Agel, F., Wu, Y. T. & Chen, C. H. 2013 A numerical study of the effects of wind direction on turbine wakes and power losses in a large wind farm. *Energies* **6**, 5297–5313.

Santner, T. J., Williams, B. J. & Notz, W. 2018 *The design and analysis of computer experiments*, 2nd edn. New York, NY : Springer.

Shapiro, C. R., Gayme, D. F. & Meneveau, C. 2019 Filtered actuator disks: Theory and application to wind turbine models in large eddy simulation. *Wind Energy* **22**, 1414–1420.

Smagorinsky, J. 1963 General circulation experiments with the primitive equations. *Monthly Weather Review* **91**, 99–164.

Starke, G. M., Meneveau, C., King, J. R. & Gayme, D. F. 2021 The area localized coupled model for analytical mean flow prediction in arbitrary wind farm geometries. *Journal of Renewable and Sustainable Energy* **13**.

Stevens, R. J. A. M., Gayme, D. F. & Meneveau, C. 2014 Large eddy simulation studies of the effects of alignment and wind farm length. *Journal of Renewable and Sustainable Energy* **6**, 023105.

Stevens, R. J. A. M., Gayme, D. F. & Meneveau, C. 2016*a* Effects of turbine spacing on the power output of extended wind-farms. *Wind Energy* **19**, 359–370.

Stevens, R. J. A. M., Gayme, D. F. & Meneveau, C. 2016*b* Generalized coupled wake boundary layer model: applications and comparisons with field and les data for two wind farms. *Wind Energy* **19**, 2023–2040.

West, J. R. & Lele, S. K. 2020 Wind turbine performance in very large wind farms: Betz analysis revisited. *Energies* **13**, 1–25.

Wu, K. L. & Porté-Agel, F. 2017 Flow adjustment inside and around large finite-size wind farms. *Energies* **10**, 2164.

Wu, Y. T. & Porté-Agel, F. 2015 Modeling turbine wakes and power losses within a wind farm using les: An application to the horns rev offshore wind farm. *Renewable Energy* **75**, 945–955.

Yang, X., Kang, S. & Sotiropoulos, F. 2012 Computational study and modeling of turbine spacing effects infinite aligned wind farms. *Physics of Fluids* **24**, 11510.

Yang, X. & Sotiropoulos, F. 2014 Les investigation of infinite staggered wind-turbine arrays. *Journal of Physics: Conference Series* **555**, 012109.

Zong, H. & Porté-Agel, F. 2020 A momentum-conserving wake superposition method for wind farm power prediction. *Journal of Fluid Mechanics* **889**, A8.

Ørsted 2019 Ørsted presents update on its long-term financial targets [accessed 27/04/2022]. https://orsted.com/en/company-announcement-list/2019/10/1937002.

2.1 Statement of authorship

Statement of Authorship for joint/multi-authored papers for PGR thesis

To appear at the end of each thesis chapter submitted as an article/paper

The statement shall describe the candidate's and co-authors' independent research contributions in the thesis publications. For each publication there should exist a complete statement that is to be filled out and signed by the candidate and supervisor **(only required where there isn't already a statement of contribution within the paper itself).**

Title of Paper	Two-scale interaction of wake and blockage effects in large wind farms
Publication Status	Published
Publication Details	Kirby A, Nishino T, Dunstan TD. Two-scale interaction of wake and blockage effects in large wind farms. *Journal of Fluid Mechanics*. 2022;953:A39. doi:10.1017/jfm.2022.979

Student Confirmation

Student Name:	Andrew Kirby		
Contribution to the Paper	Performed large-eddy simulations, analysed data from simulations and drafted manuscript.		
Signature Andrew Kirby		Date	05/02/2024

Supervisor Confirmation

By signing the Statement of Authorship, you are certifying that the candidate made a substantial contribution to the publication, and that the description described above is accurate.

Supervisor name and title: Dr Takafumi Nishino		
Supervisor comments I believe that Andrew made a substantial contribution (more than 70%) to this publication, and the description described above is accurate.		
Signature Nishino	Date	25/07/2024

This completed form should be included in the thesis, at the end of the relevant chapter.

Chapter 3

Data-driven modelling of turbine wake interactions and flow resistance in large wind farms

This chapter presents a journal article titled *'Data-driven modelling of turbine wake interactions and flow resistance in large wind farms'* published in the journal *'Wind Energy'* (`https://doi.org/10.1002/we.2851`). The article spans the pages 55-75 in the thesis. Note that there are some minor differences in the text from the published version.

Turbine-wake interactions can significantly reduce the efficiency of wind farms. Wind farm developers model turbine-wake interactions using engineering 'wake' models. To predict the performance of a farm, the individual wakes are combined using empirical ad-hoc superposition techniques. For large farms, this approach can give large errors. To reduce the uncertainty about the performance of new farms, new approaches to predict turbine-wake interactions are required.

In this chapter we present a novel data-driven approach to predicting turbine-wake interactions. To do this we developed emulators of the 'internal' turbine thrust coefficient C_T^* as a function of turbine layout. The models were trained using a multi-fidelity Gaussian Process (GP) approach. This allowed the models to be trained on both low-fidelity wake model simulations and high-fidelity wind farm LES. The multi-fidelity GP models predicted C_T^* with a mean absolute error of less than 1%.

The multi-fidelity GP model of C_T^* can be combined with the two-scale momentum theory to give fast and accurate predictions of wind farm performance. This data-driven approach can predict the impact of turbine layout on farm performance whilst being applicable to different mesoscale atmospheric conditions. This could provide an alternative method to modelling turbine-wake interactions in large wind farms.

Received: Added at production | Revised: Added at production | Accepted: Added at production

DOI: xxx/xxxx

RESEARCH ARTICLE

Data-driven modelling of turbine wake interactions and flow resistance in large wind farms

Andrew Kirby*[1] | François-Xavier Briol[2] | Thomas D. Dunstan[3] | Takafumi Nishino[1]

[1]Department of Engineering Science, University of Oxford, Oxford, UK
[2]Department of Statistical Science, University College London, London, UK
[3]Informatics Lab, UK MetOffice, Exeter, UK

Correspondence
*Andrew Kirby, Department of Engineering Science, University of Oxford, Oxford, OX1 3PJ, UK. Email: andrew.kirby@trinity.ox.ac.uk

Abstract

Turbine wake and local blockage effects are known to alter wind farm power production in two different ways: (1) by changing the wind speed locally in front of each turbine; and (2) by changing the overall flow resistance in the farm and thus the so-called farm blockage effect. To better predict these effects with low computational costs, we develop data-driven emulators of the 'local' or 'internal' turbine thrust coefficient C_T^* as a function of turbine layout. We train the model using a multi-fidelity Gaussian Process (GP) regression with a combination of low (engineering wake model) and high-fidelity (Large-Eddy Simulations) simulations of farms with different layouts and wind directions. A large set of low-fidelity data speeds up the learning process and the high-fidelity data ensures a high accuracy. The trained multi-fidelity GP model is shown to give more accurate predictions of C_T^* compared to a standard (single-fidelity) GP regression applied only to a limited set of high-fidelity data. We also use the multi-fidelity GP model of C_T^* with the two-scale momentum theory (Nishino & Dunstan 2020, J. Fluid Mech. 894, A2) to demonstrate that the model can be used to give fast and accurate predictions of large wind farm performance under various mesoscale atmospheric conditions. This new approach could be beneficial for improving annual energy production (AEP) calculations and farm optimisation in the future.

KEYWORDS:
Class file; LaTeX 2_ε; Wiley NJD

1 | INTRODUCTION

The installed capacity of wind energy is projected to increase rapidly in the next decades. A major challenge in the optimisation of wind farm design is the accurate prediction of wind farm performance[1]. Existing wind farm models struggle to make accurate predictions of wind farm power production. This is partly because the 'global blockage effect' reduces the velocity upstream of large farms and hence the energy yield[2]. It remains unclear how global blockage should be modelled and this is the subject of a large-scale field campaign[3].

Wind farms are typically modelled using engineering 'wake' models. These models predict the velocity deficit in the wakes behind turbines[4 5]. To account for interactions between multiple turbines, the wake velocity deficits are superposed[6,7]. Simple wake models can give predictions of wind farm performance with very low computational cost (10^{-3} CPU hours per simulation[1]). However, wake models do not account for the response of the atmospheric boundary layer (ABL) to the wind farm which is likely to be important for large wind farms [8]. It has been found that wake models compare poorly to Large-Eddy Simulations (LES) of large wind farms [9].

Wind farms are also modelled in numerical weather prediction (NWP) models using farm parameterisation schemes. In these parameterisations, farms are often modelled as a momentum sink and a source of turbulent kinetic energy [10]. Turbine-wake interactions cannot be adequately predicted using these schemes. A new scheme was proposed [11] which uses a correction factor to model turbine interactions. More recently, data-driven approaches have been proposed [12] to model these effects in wind farm parameterisations.

Data-driven modelling of wind farm flows is a promising new approach [13]. Data from high-fidelity simulations with complex flow physics can be used to make predictions with low computational cost. Recent studies have applied machine learning techniques to data from a single turbine or from an existing wind farm. The data for these studies are from measurements [14,15,16,17], LES [18] or Reynolds-Averaged Navier-Stokes (RANS) simulations [19,20,21]. A limitation of these approaches is that they are not generalisable to different turbine layouts unless they rely on wake superposition techniques to model farm flows. Another approach is modelling the effect of turbine layout using geometric parameters [17] or using the layout as a graph input to a neural network [22,23]. However, these alternative approaches may struggle to fully capture the complex two-way interaction with the ABL as it seems impractical to prepare a data set that covers the entire range of scales involved in wind farm flows [1].

The problem of modelling wind farm flows can be split into 'internal' turbine-scale and 'external' farm-scale problems [24]. The 'internal' problem is to determine a 'local' or 'internal' turbine thrust coefficient, C_T^*, which represents the flow resistance inside a wind farm, i.e., how the turbine thrust changes with wind speed within the farm. Nishino [25] proposed an analytical model for an upper limit of C_T^* by using an analogy to the classic Betz analysis. This analytical model is a function of turbine-scale induction factor but is independent of turbine layout and wind direction. Previous studies [24 25 8] showed that C_T^* is usually lower than the limit predicted by Nishino's model and can vary significantly with turbine layout due to wake and turbine blockage effects.

The aim of this study is to develop statistical emulators of C_T^* as a function of turbine layout and wind direction. The novelty of this approach is that we are modelling the effect of turbine-wake interactions on C_T^* rather than turbine power. Both turbine-scale flows (e.g., wake effects) and farm-scale flows (e.g. farm blockage and mesoscale atmospheric response) affect turbine power within a farm. Therefore to create an emulator of turbine power, either (1) a very large set of expensive data such as finite-size wind farm LES is needed which covers a range of large-scale atmospheric conditions or (2) the model would not be generalisable to different mesoscale atmospheric responses. An emulator of C_T^* is however applicable to different atmospheric responses modelled separately, following the concept of the two-scale momentum theory [24 8].

In section 2 we give the definitions of key wind farm parameters in the two-scale momentum theory [24]. Section 3 summarises the methodology of the LES and wake model simulations, followed by the machine learning approaches to develop the emulators in section 4. In section 5 we present the results from the trained emulators. These results are discussed in section 6 and concluding remarks are given in section 7.

2 | TWO-SCALE MOMENTUM THEORY

By considering the conservation of momentum for a control volume with and without a large wind farm over the land or sea surface, the following non-dimensional farm momentum (NDFM) equation can be derived [24],

$$C_T^* \frac{\lambda}{C_{f0}} \beta^2 + \beta^\gamma = M \tag{1}$$

where β is the farm wind-speed reduction factor defined as $\beta \equiv U_F/U_{F0}$ (with U_F defined as the average wind speed in the nominal wind farm-layer of height H_F, and U_{F0} is the farm-layer-averaged speed without the wind farm present); λ is the array density defined as $\lambda \equiv nA/S_F$ (where n is the number of turbines in the farm, A is the rotor swept area and S_F is the farm footprint area);

C_T^* is the internal turbine thrust coefficient defined as $C_T^* \equiv \sum_{i=1}^{n} T_i / \frac{1}{2}\rho U_F^2 nA$ (where T_i is thrust of turbine i in the farm and ρ is the air density); C_{f0} is the natural friction coefficient of the surface defined as $C_{f0} \equiv \langle \tau_{w0} \rangle / \frac{1}{2}\rho U_{F0}^2$ (where τ_{w0} is the bottom shear stress without the farm present); γ is the bottom friction exponent defined as $\gamma \equiv \log_\beta(\langle \tau_w \rangle / \tau_{w0})$ (where $\langle \tau_w \rangle$ is the bottom shear stress averaged across the farm); M is the momentum availability factor defined as,

$$M = \frac{\text{Momentum supplied by the atmosphere to the farm site } \textbf{with} \text{ turbines}}{\text{Momentum supplied by the atmosphere to the farm site } \textbf{without} \text{ turbines}}. \tag{2}$$

noting that this includes pressure gradient forcing, Coriolis force, net injection of streamwise momentum through top and side boundaries and time-dependent changes in streamwise velocity[24]. The height of the farm-layer, H_F, is used to define the reference velocities U_F and U_{F0}. Equation 1 is valid so long as the same of H_F is used for both the internal and external problem. H_F is typically between $2H_{hub}$ and $3H_{hub}$[8] (where H_{hub} is the turbine hub-height) and in this study we use a fixed definition of $H_F = 2.5H_{hub}$.

Patel[26] used an NWP model to demonstrate that, for most cases, M varied almost linearly with β (for a realistic range of β between 0.8 and 1). Therefore, M can be approximated by

$$M = 1 + \zeta(1 - \beta) \tag{3}$$

where ζ is the 'momentum response' factor or 'wind extractability' factor. Patel[26] found ζ to be time-dependent and vary between 5 and 25 for a typical offshore site (note that $\zeta = 0$ corresponds to the case where momentum available to the farm site is assumed to be fixed, i.e., $M = 1$).

Nishino[25] proposed an analytical model for C_T^* given by,

$$C_T^* = 4\alpha(1-\alpha) = \frac{16C_T'}{(4 + C_T')^2} \tag{4}$$

where α is the turbine-scale wind speed reduction factor defined as $\alpha \equiv U_T / U_F$ (U_T is the streamwise velocity averaged over the rotor swept area) and $C_T' \equiv T / \frac{1}{2}\rho U_T^2 A$ is a turbine resistance coefficient describing the turbine operating conditions.

For a given farm configuration at a farm site (i.e., for given set of C_T^*, λ, C_{f0}, γ and ζ) the farm wind-speed reduction factor β can be calculated using equation 1. The (farm-averaged) power coefficient C_p is defined as $C_p \equiv \sum_{i=1}^{n} P_i / \frac{1}{2}\rho U_{F0}^3 nA$ (P_i is power of turbine i in the farm). Using the calculated value of β, C_p can be calculated by using the expression,

$$C_p = \beta^3 C_p^* \tag{5}$$

where C_p^* is the (farm-averaged) 'local' or 'internal' turbine power coefficient defined as $C_p^* \equiv \sum_{i=1}^{n} P_i / \frac{1}{2}\rho U_F^3 nA$.

3 | WIND FARM SIMULATIONS

In this study we model wind farms as arrays of actuator discs (or aerodynamically ideal turbines operating below the rated wind speed). This is because, in real wind farms, the effects of turbine wake interactions on the farm performance are most significant when they operate below the rated wind speed. The 'internal' thrust coefficient C_T^* is an important wind farm parameter which includes the effect of turbine interactions (including both wake and local blockage effects). In this study we will be modelling the effect of turbine layout on C_T^* for aligned turbine layouts with various wind directions and a fixed turbine resistance of $C_T' = 1.33$. We chose $C_T' = 1.33$ because it leads to a turbine induction factor of 1/4 which is close to a typical value for modern large wind turbines. As such we will be considering

$$C_T^* = f(S_x, S_y, \theta) \tag{6}$$

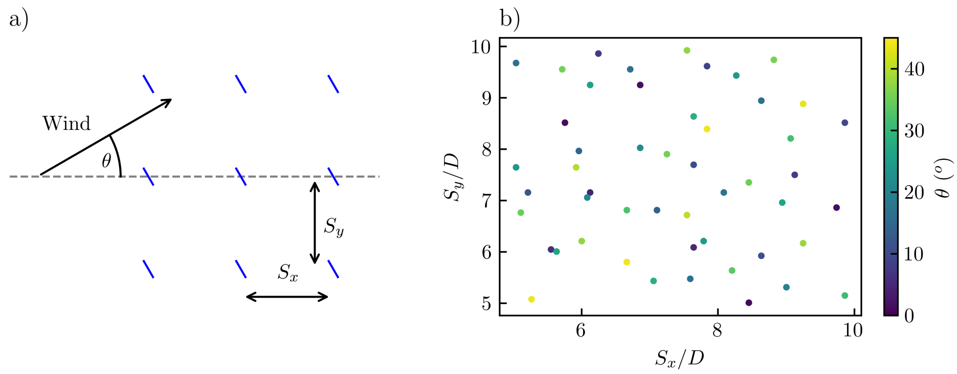

Figure 1 Design of numerical experiments: a) input parameters, b) maximin design of LES.

where S_x is the turbine spacing in the x direction, S_y is the turbine spacing in the y direction and θ is the wind direction relative to the x direction (see figure 1a). However the true function C_T^* cannot be easily evaluated so we will instead investigate C_T^* using computer codes. One computer code we will use is LES (see section 3.1) to estimate C_T^*

$$C^*_{T,LES} = f_{LES}(S_x, S_y, \theta). \tag{7}$$

We assume that the function f_{LES} is close to the true function f because of the accuracy of LES to model wind farm flows. We will also use a wake model (see section 3.2) to provide cheap approximations of C_T^* according to

$$C^*_{T,wake} = f_{wake}(S_x, S_y, \theta). \tag{8}$$

Engineering problems are often investigated using complex computer models. Evaluating the output of such computer models for a given input can be very computationally expensive. Therefore a common objective is to create a cheap statistical model of the expensive computer model; this is commonly known as emulation of computer models [27 28]. In this study we aim to develop a statistical emulator which can cheaply emulate f_{LES}.

The emulators will only be valid for aligned layouts of wind turbines and for a given turbine resistance (here we use $C_T' = 1.33$). We consider the input parameters for a realistic range of turbine spacings [1]: $S_x \in [5D, 10D]$, $S_y \in [5D, 10D]$ and $\theta \in [0^o, 45^o]$ where D is the diameter of the turbine rotor swept area. In this study D is set as 100m and the turbine hub height is also 100m. We only need to consider wind directions of $\theta \in [0^o, 45^o]$ because of symmetry in the aligned turbine layouts. If θ is negative than the turbine layout given by (S_x, S_y, θ) is exactly the same as $(S_x, S_y, -\theta)$. When $\theta > 45^o$, then (S_x, S_y, θ) and $(S_y, S_x, 90^o - \theta)$ give identical layouts.

In this study we build several emulators to predict f_{LES}. The models are trained using data from low-fidelity (wake model) and high fidelity (LES) wind farm simulations. One evaluation of $C^*_{T,wake}$ takes approximately 130 seconds on a single CPU and $C^*_{T,LES}$ requires around 400 CPU hours on a supercomputer. We use a space filling maximin design [29 30] to select training points in the parameter space. The maximin algorithm selects points which maximises the minimum distance to other points and to the boundaries. This provides a good coverage of the domain which ensures that the emulators can give good predictions across the whole of the domain [31]. Figure 1b shows the LES training points in the parameter space.

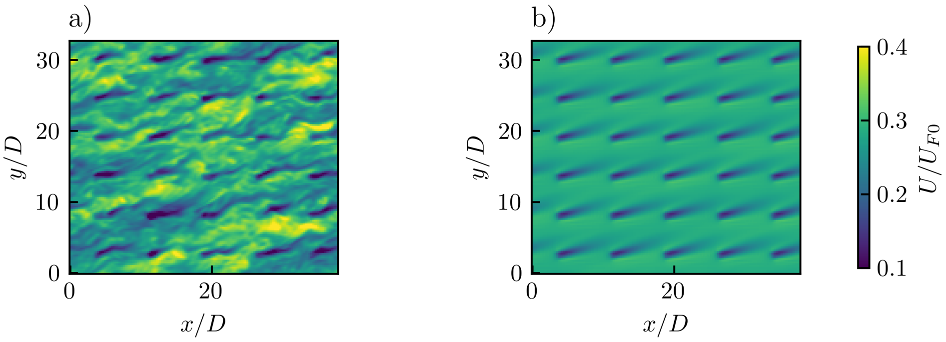

Figure 2 LES a) instantaneous and b) time-averaged flow fields over a periodic turbine array ($S_x/D = 7.59$, $S_y/D = 5.47$ and $\theta = 37.6^o$).

3.1 | Large-Eddy Simulations

This study uses the data from 50 high-fidelity (LES) simulations of wind farms published in a previous study[8]. Here we give a brief summary of the LES methodology. The LES models a neutrally stratified atmospheric boundary layer over a periodic array of actuator discs, which face the wind direction θ and exert uniform thrust. The resolution is 24.5m in the horizontal directions (4 points across the rotor diameter) and 7.87m in the vertical. This is a coarse horizontal resolution; however using a correction factor for the turbine thrust[32] makes the $C^*_{T,LES}$ values insensitive to horizontal resolution[8]. For all simulations the vertical domain size was fixed at 1km and the horizontal extent varied with turbine layout but was at least 3.14km. The horizontal boundary conditions were periodic (essentially an infinitely-large wind farm). The bottom boundary used a no-slip condition with the value of eddy viscosity specified following the Monin-Obukhov similarity theory for a surface roughness length of $z_0 = 1 \times 10^{-4}$m. The top boundary had a slip condition with zero vertical velocity. The flow was driven by a pressure gradient forcing which was constant and in the direction θ throughout the domain. Figure 2 shows the instantaneous and time-averaged hub height velocities from one wind farm LES. See the original paper[8] for further details of the LES.

3.2 | Wake model simulations

Wake models are a cheap low-fidelity approach to modelling wind farm aerodynamics compared to expensive high-fidelity LES simulations[1]. We use the wake model proposed by Niayafar and Porté-Agel[33] to evaluate $C^*_{T,wake}$ as a cheap approximation of C^*_T. We use the Python package PyWake[34] to implement the wake model. The turbine thrust coefficient C_T is needed as an input for the wake model. We use the value of C^*_T predicted by equation 4 as the value of C_T. For the turbine operating conditions used in this study ($C'_T = 1.33$) the wake model has C_T equal to 0.75 for all turbines. To model actuator discs, we consider a hypothetical turbine which has a constant C_T for all wind speeds. We calculate $C^*_{T,wake}$ for a single turbine at the back of a large farm (marked X in figure 3). The farm simulated using the wake model is 10km long in the streamwise direction and 4km long in the cross-streamwise direction. The farm size was chosen so that C^*_T no longer varied with increasing farm size. The wake growth parameter is calculated using $k^* = 0.38I + 0.004$ where I is the local streamwise turbulence velocity. The local streamwise turbulence intensity is estimated using the model proposed by Crespo and Hernández[35]. The background turbulence intensity (TI) is set as a typical value of 10%.

The velocity incident to the turbine is calculated by averaging the velocity across the disc area. We use a 4×3 cartesian grid with Gaussian quadrature coordinates and weights on the disc to average the velocity. The disc-averaged velocity, U_T is then calculated by multiplying the averaged incident velocity by $(1 - a)$ where a is the turbine induction factor set by the value of C'_T (using the expression $a = C'_T/(4 + C'_T)$). To calculate the farm-average velocity, U_F, we average the velocity across a volume around the

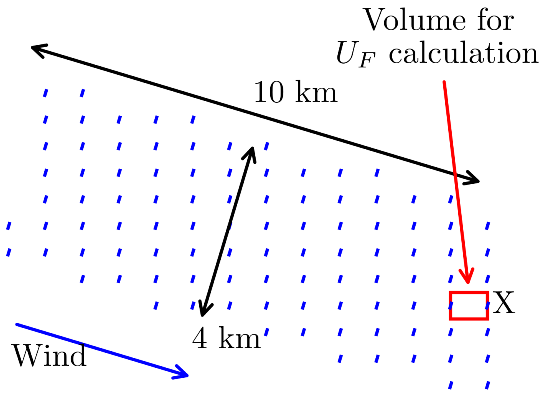

Figure 3 Example of wind farm layout for wake model simulations.

single turbine. The volume has dimensions of S_y in the y direction, S_x in the x direction and 250m in the z direction (the height of the nominal farm layer used in the previous LES study[8]). To calculate the average velocity, we discretise the volume into 200 points in the horizontal directions and 20 points in the vertical. This was sufficient for the calculation of $C^*_{T,wake}$ to not vary with further discretisation. Figure 3 shows an example of the farm layout for the wake model simulations.

4 | MACHINE LEARNING METHODOLOGY

4.1 | Gaussian Process regression

We will use Gaussian process (GP) regression[36] to build statistical emulators of f_{LES}. A Gaussian process is a stochastic process $g \sim \mathcal{GP}(m, k)$ described by a mean function $m(v) = \mathbb{E}[g(v)]$ and a covariance function $k(v, v') = \mathbb{E}[(g(v) - m(v))(g(v') - m(v')]$. In our case $v = (S_x, S_y, \theta)$. We will use such a stochastic process as a model of f_{LES}, the true mapping from v to $C^*_{T,LES}$. Each realisation from this process will therefore be a function which could plausibly represent this mapping. The mean function represents the expected output value at an input $v = (S_x, S_y, \theta)$. The covariance function gives the covariance between output values at v and v'. Examples of covariance functions include squared exponential, rational quadratic and periodic functions[36]. Different covariance functions will give differently shaped GPs. For example the squared exponential covariance function will give very smooth GPs whereas the periodic function will give GPs with a periodic structure. Other types of structure, for example symmetry, can also be encoded in the covariance function. Therefore the expected shape (for example smoothness) of the expected relationship and any properties (for example discontinuities or symmetries) need to be considered when choosing a covariance function for GP regression.

Let $V = (v_1, ..., v_n)^T$ be a collection of design points then $m_V = (m(v_1), ..., m(v_n))^T$ is the mean vector and $k_{VV} = (k(v_i, v_j))$ is the covariance matrix. We will start by positing a GP model with mean m and covariance k (called the 'prior GP'), then condition this GP on LES observations; the outcome is a new GP (called the 'posterior GP'). This gives the posterior distribution $g|V, C^*_{T,LES} \sim \mathcal{GP}(\overline{m}_{\sigma^2}, \overline{k}_{\sigma^2})$. $\overline{m}_{\sigma^2}$ is the posterior mean function given by $\overline{m}_{\sigma^2}(v) = m(v) + k_{vV}(k_{VV} + \sigma^2 I_{n\times n})^{-1}(C^*_{T,LES} - m_V)$ where $k_{vV} = (k(v, v_1), ..., k(v, v_n))$ and $I_{n\times n}$ is the identity matrix of size n. The posterior mean function $\overline{m}_{\sigma^2}$ is used to make predictions at $v = (S_x, S_y, \theta)$. The posterior covariance function $\overline{k}_{\sigma^2}$ quantifies the uncertainty in our prediction at $v = (S_x, S_y, \theta)$. The posterior covariance function is given by $\overline{k}_{\sigma^2}(v, v') = k(v, v') - k_{vV}(k_{VV} + \sigma^2 I_{n\times n})^{-1}k_{Vv'}$.

Often in GP regression a zero prior mean is used. However, using an informative prior mean can improve the accuracy of the trained model. By using a prior mean, many of the trends in f_{LES} can be incorporated into our model prior to making expensive

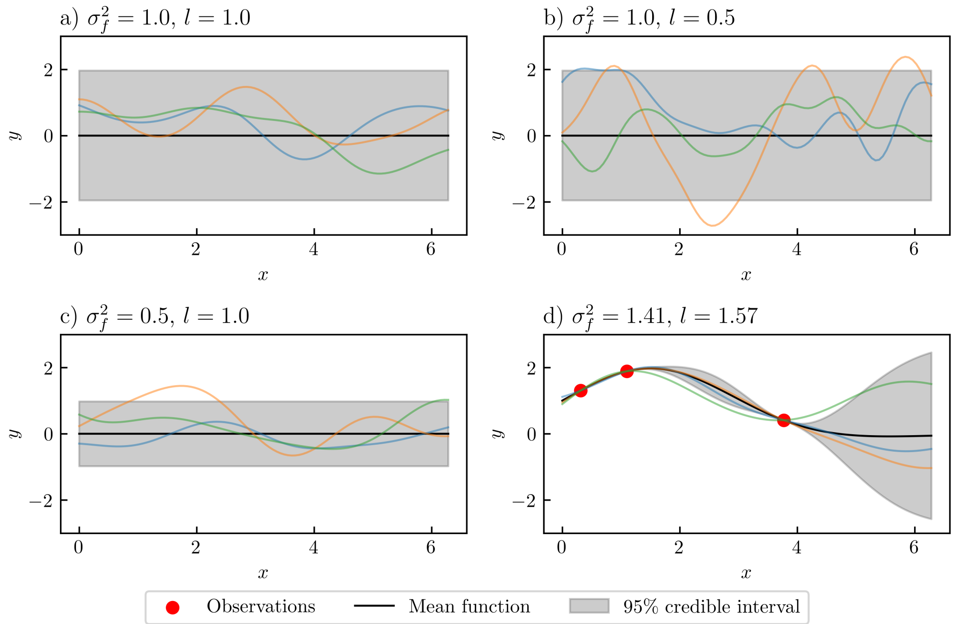

Figure 4 Demonstration of basic GP regression: a) shows the prior mean and covariance function prior to fitting with 3 GPs drawn from the distribution shown in colour; b) shows the effect of decreasing the lengthscale hyperparameter; c) the effect of variance hyperparameter; and d) the posterior mean and covariance functions.

evaluations of $C^*_{T,LES}$. Therefore, after training our model will likely better describe the true relationship between S_x, S_y, θ and f_{LES}. In this study, we will use both $C^*_{T,wake}$ and the analytical model of C^*_T as the prior mean for the standard GP regression. For the wake model prior mean we also vary the specified ambient TI input parameter.

We expect f_{LES} to be a smooth function of input variables S_x, S_y and θ, and to vary more rapidly with θ than S_x or S_y. Therefore we will use an anisotropic squared-exponential covariance function,

$$k(v, v') = \sigma_f^2 \exp\left(-\frac{(S_x - S_x')^2}{2l_1^2}\right) \exp\left(-\frac{(S_y - S_y')^2}{2l_2^2}\right) \exp\left(-\frac{(\theta - \theta')^2}{2l_3^2}\right) \tag{9}$$

where $\sigma_f^2 > 0$ is the signal variance hyperparameter and $l_i > 0$ is the lengthscale hyperparameter for each dimension. This is also called an ARD (automatic relevance detection) kernel. If we consider $v = v'$ then we can see that σ_f^2 determines the variance of $g(v)$. Therefore σ_f^2 determines the prior uncertainty the model has about the value of $g(v)$. As the lengthscale hyperparameter l_i gets smaller then $k(v, v')$ decreases (for $v \neq v'$). Equally if l_i increases then $k(v, v')$ will also increase. A GP with a small l_i will therefore vary more rapidly across the parameter space in the ith dimension.

Due to numerical issues associated with the matrix inversion/linear system solve operations in the formulae for the posterior GP, it is common to add a nugget $\sigma^2 > 0$ to the kernel matrix. The hyperparameters σ_f^2 and l_i are selected automatically during the fitting process by maximising the log marginal likelihood [36]. This approach selects the model which maximises the fit to the data.

Figure 4 shows the impact of the hyperparameters in an example GP regression setting (using the squared exponential covariance function). The mean function and 95% credible interval (+/-1.96 times the standard deviation) prior to fitting are shown in figure 4a with 3 GPs drawn from the distribution (coloured lines). The effect of decreasing the lengthscale hyperparameter l_i is shown in figure 4b. The prior mean and 95% credible interval are unchanged however the example GPs drawn vary more rapidly because of the shorter lengthscale. Figure 4c shows the same setup as figure 4a but with a smaller value of σ_f^2. The example GPs still vary slowly but the magnitude of the variations is now smaller. Figure 4d shows the GPs conditioned on observations with hyperparameters selected by maximising the log marginal likelihood.

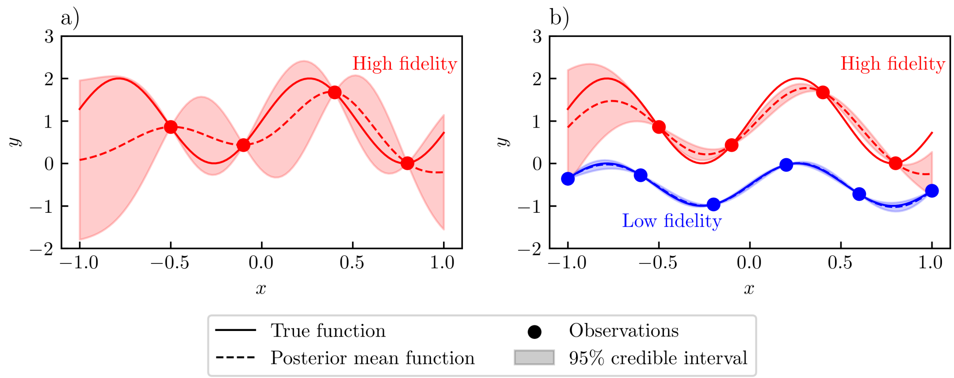

Figure 5 Demonstration of a) basic GP regression and b) multi-fidelity GP regression. In this example $f(x) = 1 + sin(6x)$ for the high-fidelity data and $f(x) = -0.5 + 0.5sin(6x)$ for the low-fidelity data.

4.2 | Non-linear multi-fidelity Gaussian Process regression

In many applications there are several computational models available. These models can have varying accuracies and computational costs. The models which are more computationally expensive typically give more accurate predictions. The GP regression framework can be extended to combine information from low and high-fidelity models [37]. This type of modelling uses the low-fidelity observations to speed up the learning process and the high-fidelity observations to ensure accuracy. In our scenario we will combine evaluations of from a low-fidelity ($C^*_{T,wake}$) and a high-fidelity ($C^*_{T,LES}$) model. Note that for the multi-fidelity models in this study we set the ambient TI to 10% for the wake model and use a zero prior mean. We will keep the number of high-fidelity training points fixed at 50 and we will vary the number of low-fidelity training points used.

We combine information from our high and low-fidelity models using a nonlinear information fusion algorithm [38]. The framework is based on the autoregressive multi-fidelity scheme given by:

$$g_{high}(v) = \rho(g_{low}(v)) + \delta(v) \tag{10}$$

where $g_{low}(v)$ is a model with a GP denoted f_{wake} and $g_{high}(v)$ is a model with a GP denoted f_{LES}. ρ is a model with a GP which maps the low-fidelity output to the high-fidelity output and $\delta(v)$ is a model with a GP which is a bias term. The non-linear multi-fidelity framework can learn non-linear space-dependent correlations between models of different accuracies. To reduce the computational cost and complexity of implementation the autoregressive scheme given by equation 10 is simplified. Firstly, the GP prior $g_{low}(v)$ is replaced by the GP posterior $g_{low,*}(v)$ and secondly the GPs ρ and δ are assumed to be independent. Equation 10 can then be summarised as

$$g_{high}(v) = h_{high}(v, g_{low,*}(v)) \tag{11}$$

where h_{high} is a model with a GP which has both v and $g_{low,*}(v)$ as inputs. More details of h_{high} and the implementation of the multi-fidelity framework are given in Perdikaris *et. al.* [38].

Figure 5 shows an example of how a multi-fidelity GP can outperform a standard GP regression. We implement the non-linear multi-fidelity framework using the 'emukit' package [39]. We first maximise the log marginal likelihood whilst keeping the Gaussian noise variance fixed at a low value of 1×10^{-6}. The fitting process is then repeated whilst allowing the Gaussian noise variance to be optimised too. This is to prevent a high noise local optima from being selected.

5 | RESULTS

In this study, we build various statistical emulators of f_{LES} using different techniques and compare the performance. A summary of the techniques is shown in the list below:

1 Standard Gaussian Process regression (see section 4.1)

   a **GP-analytical-prior**: Gaussian Process using analytical model (equation 4) prior mean

   b **GP-wake-TI10-prior**: Gaussian Process using wake model (section 3.2) with ambient TI=10% prior mean

   c **GP-wake-TI1-prior**: Gaussian Process using wake model with ambient TI=1% prior mean

   d **GP-wake-TI5-prior**: Gaussian Process using wake model with ambient TI=5% prior mean

   e **GP-wake-TI15-prior**: Gaussian Process using wake model with ambient TI=15% prior mean

2 Non-linear multi-fidelity Gaussian Process regression (see section 4.2)

   a **MF-GP-nlow500**: multi-fidelity Gaussian Process using 500 low-fidelity training points

   b **MF-GP-nlow250**: multi-fidelity Gaussian Process using 250 low-fidelity training points

   c **MF-GP-nlow1000**: multi-fidelity Gaussian Process using 1000 low-fidelity training points

The code and data used to produce the results in this section is available open-access at the following GitHub repository: https://github.com/AndrewKirby2/ctstar_statistical_model.

5.1 | Performance of standard GP regression

We first assessed the accuracy of the standard GP models (section 4.1) by performing leave-one-out cross-validation (LOOCV). This is a method of estimating the accuracy of a statistical model when making predictions on data not used to train the model. We trained our model on 49 of the 50 training points and then calculated the prediction accuracy for the single high-fidelity data point which is excluded from the training set. This is then repeated for all data points in turn, and we took the average accuracy as an estimate of the model test accuracy. The standard GP models were implemented using the 'GPy' package[40].

The standard GP gave accurate predictions of f_{LES} with average errors of less than 2%. Table 1 shows the accuracy of the standard GP models compared to the analytical and wake models. We calculated the errors by using the expression $|\overline{m}_{\sigma^2} - C^*_{T,LES}|/0.75$ where $\overline{m}_{\sigma^2}$ is the posterior mean function of the emulator. The reference value for C^*_T of 0.75 was chosen because this is the prediction from the analytical model. Both GP models give similar maximum errors of approximately 6%. Using the wake model as a prior mean gave a lower mean absolute error of 1.26%. The GP models reduced the average prediction error and significantly reduced the maximum error compared to the wake model and analytical model of C^*_T.

Table 1 Accuracy of models for C^*_T prediction.

Model	MAE (%)	Maximum error (%)
GP-analytical-prior	1.87	6.09
GP-wake-TI10-prior	1.26	6.11
Analytical model	5.26	22.0
Wake model (TI=10%)	4.60	9.28

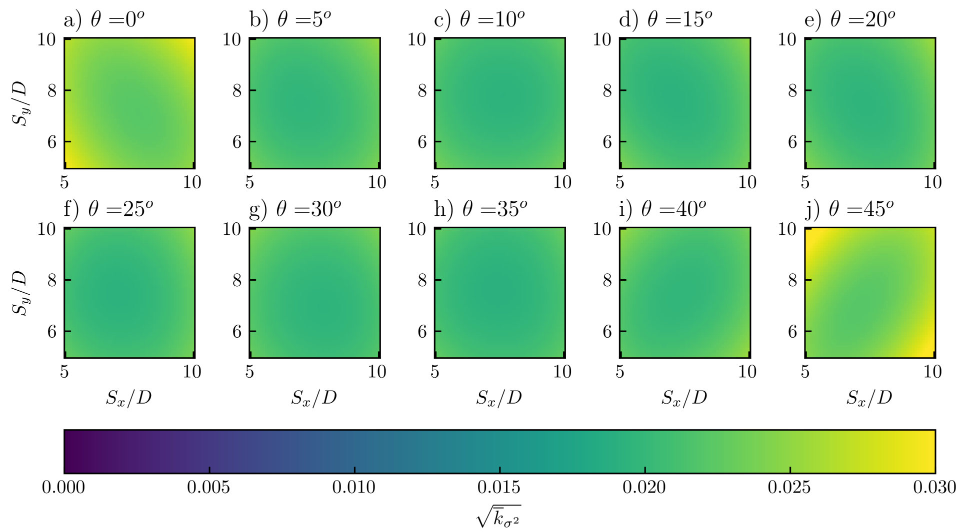

Figure 6 Posterior variance function of **GP-wake-TI10-prior** model.

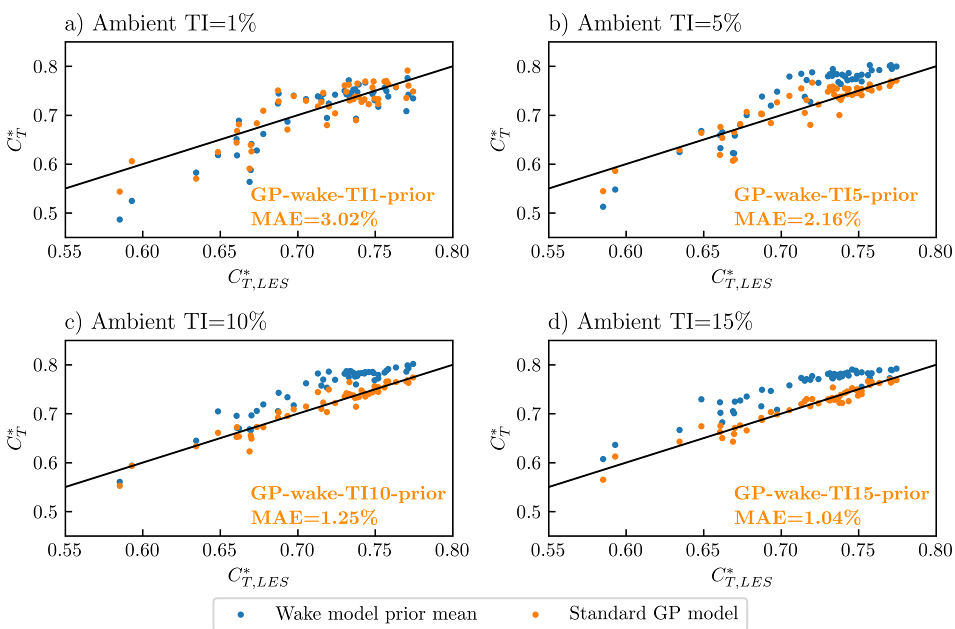

Figure 7 Sensitivity of fitted GP models to the ambient TI chosen for wake model prior means.

The model **GP-wake-TI10-prior** has a high degree of confidence when making predictions in regions of the parameter space. Figure 6 shows the square root of the posterior covariance function $\overline{k}_{\sigma^2}$, which quantities the uncertainty of the emulator. The uncertainty is uniform throughout the parameter space with regions of slightly higher uncertainty at $\theta = 0^o$ and 45^o.

We also assessed the sensitivity of the model accuracy to the ambient TI used in the wake model prior mean. Figure 7 shows the impact of ambient TI on the wake model prior mean and the fitted GP model. Increasing the ambient TI increased the value of $C^*_{T,wake}$. This is because of the enhanced wake recovery behind wind turbines. Increasing the ambient TI in the wake model results in $C^*_{T,wake}$ overpredicting $C^*_{T,LES}$. The MAE from the LOOCV procedure for each fitted GP is shown in the bottom right corner.

The fitted GPs became more accurate when the wake model ambient TI was increased. Increasing the ambient TI for the wake model causes the wakes to recover faster. The wakes become shorter in the streamwise direction and wider in the spanwise direction. As such, $C^*_{T,wake}$ becomes less sensitive to the turbine layout. When an ambient TI of 1% and 5% is used for the wake model, $C^*_{T,wake}$ is more sensitive to turbine layout than $C^*_{T,LES}$ (figures 7a and 7b). When the ambient TI is increased to 10% and above, the relationship between $C^*_{T,wake}$ and $C^*_{T,LES}$ becomes simpler (figures 7c and 7d). This seems to explain why the fitted GPs become more accurate.

5.2 | Performance of non-linear multi-fidelity GP regression

We then assessed the accuracy of the multi-fidelity GP models (section 4.2). All models used the 50 high-fidelity ($C^*_{T,LES}$) training points and a varying number of low-fidelity ($C^*_{T,wake}$) training points (using an ambient TI of 10% for $C^*_{T,wake}$). The results from LOOCV are shown in table 2. For the LOOCV we train our model on 49 out of the 50 high-fidelity data points and all low-fidelity data points. Then we average the error in predicting the high-fidelity data point left of the training set and repeat this in turn for data points. Increasing the number of low-fidelity training points from 250 to 500 reduced the mean and maximum error. However, increasing this to 1000 low-fidelity training points did not increase accuracy and increased the fitting and prediction time. This is because the number of high-fidelity training points is fixed. There is a threshold where the model of the relationship between f_{LES} and f_{wake}, denoted ρ, limits the final accuracy of the emulator of f_{LES}.

The posterior mean $\overline{m}_{\sigma^2}$ of $g_{low}(v)$ is an emulator of f_{wake} and $g_{high}(v)$ is an emulator of f_{LES}. Figure 8 gives the predictions from the posterior mean of $g_{high}(v)$ (for **MF-GP-nlow500**). The lowest $\overline{m}_{\sigma^2}$ values were for a wind direction of $\theta = 0^o$. $\overline{m}_{\sigma^2}$

Table 2 Performance of the multi-fidelity Gaussian Process models.

Model	MAE (%)	Maximum error (%)	Training time (s)	Prediction time (s)
MF-GP-nlow250	1.46	7.12	6.15	0.00157
MF-GP-nlow500	0.828	3.75	9.73	0.00167
MF-GP-nlow1000	0.866	3.55	26.8	0.00236

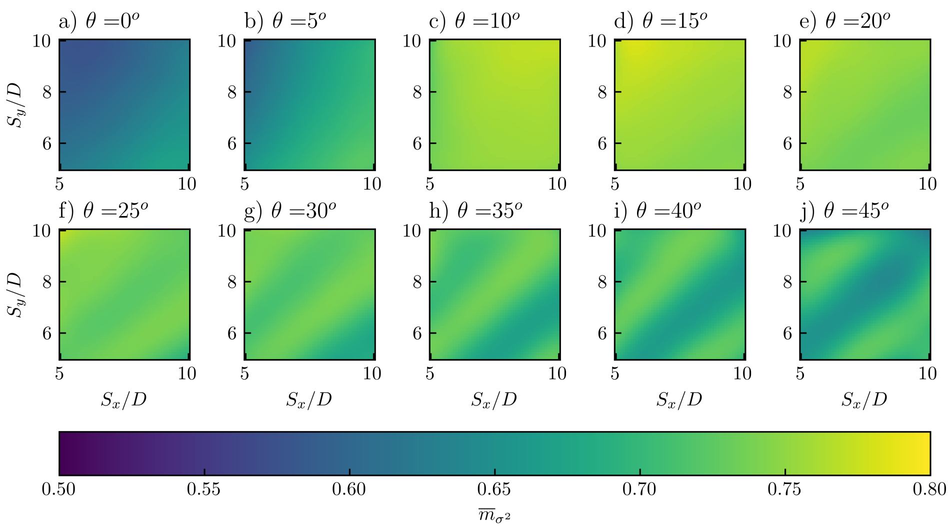

Figure 8 Posterior mean function for $g_{high}(v)$ of **MF-GP-nlow500**.

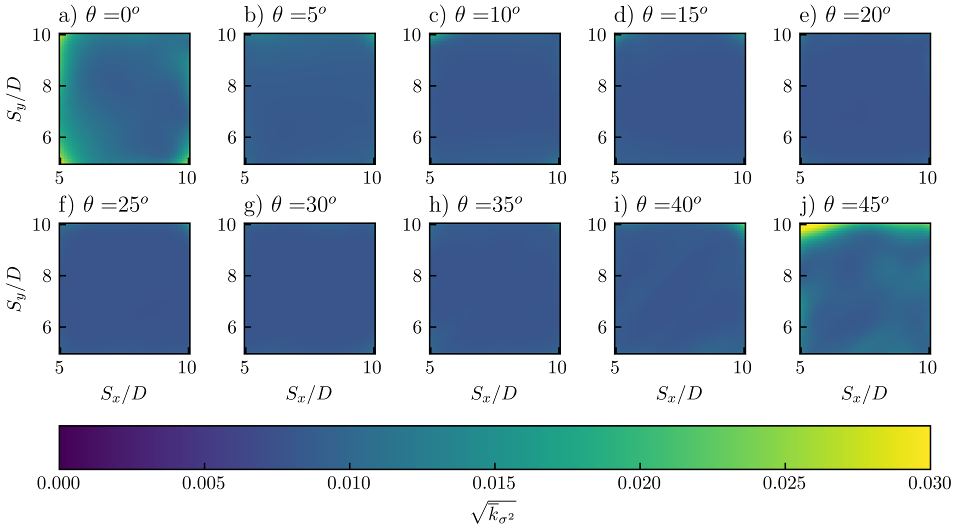

Figure 9 Posterior variance function for $g_{high}(v)$ of **MF-GP-nlow500**.

increased rapidly with θ reaching a maximum of slightly over 0.75 at $\theta = 10^o$. For large values of θ (above $\theta = 25^o$) there were local minima in $\overline{m}_{\sigma^2}$ which appear in figure 8 as diagonal strips of low $\overline{m}_{\sigma^2}$ values. The main diagonal strip occurs along the line of $S_y = S_x \tan(\theta)$. There are two smaller strips either side of with positions given by $S_y = 2\tan(\theta)$ and $S_y = 0.5\tan(\theta)$ (this is discussed further in section 6).

The uncertainty the model **MF-GP-nlow500** has in predicting f_{LES} is shown in figure 9. The model uncertainty is uniform throughout the parameter space with slightly higher values at $\theta = 0^o$ and 45^o. Compared to the posterior variance of **GP-wake-TI10-prior** (shown in figure 6) the uncertainty is lower. By incorporating information from $C^*_{T,wake}$, the multi-fidelity GP model has more confidence about predicting f_{LES}.

The prediction errors from the LOOCV (for **MF-GP-nlow500**) are shown in figure 10. The box plot of prediction errors in figure 10a shows that this model had no significant bias whereas both the wake and analytical models systemically overestimated $C^*_{T,LES}$. Figures 10b-d show that for the statistical model there appears to be no part of the parameter space which had larger errors.

The multi-fidelity approach used in this study builds a statistical model of both the low-fidelity (f_{wake}) and high-fidelity (f_{LES}) model. We can use the posterior means of $g_{low}(v)$ and $g_{high}(v)$ to see the differences between the wake model and LES. The posterior mean for both models are shown in figure 11. For the wake model the change in $\overline{m}_{\sigma^2}$ with θ is greater than for the LES (especially between $\theta = 0^o$ and 10^o). For larger values of θ, there is a larger difference in $\overline{m}_{\sigma^2}$ between waked and unwaked layouts for the low-fidelity model compared to the high-fidelity one. This suggests than the wake model is more sensitive to changes in wind directions than the LES.

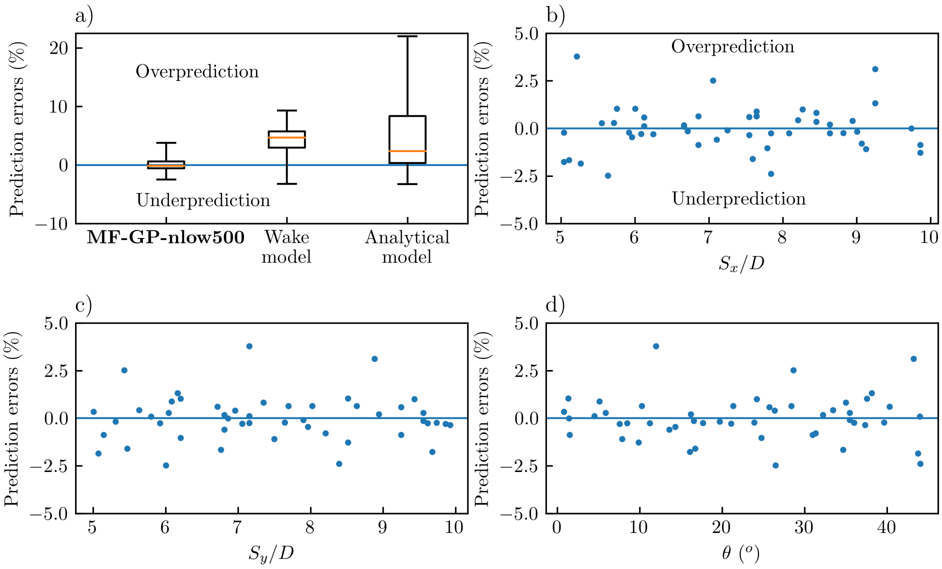

Figure 10 Comparison of LOOCV prediction errors (%) for different models a) and LOOCV prediction error (%) of **MF-GP-nlow500** against input parameters b) S_x/D, c) S_y/D and d) $\theta(^o)$. Note that for the box plot in a) the orange line is the median LOOCV error and the box is the interquartile range of LOOCV error.

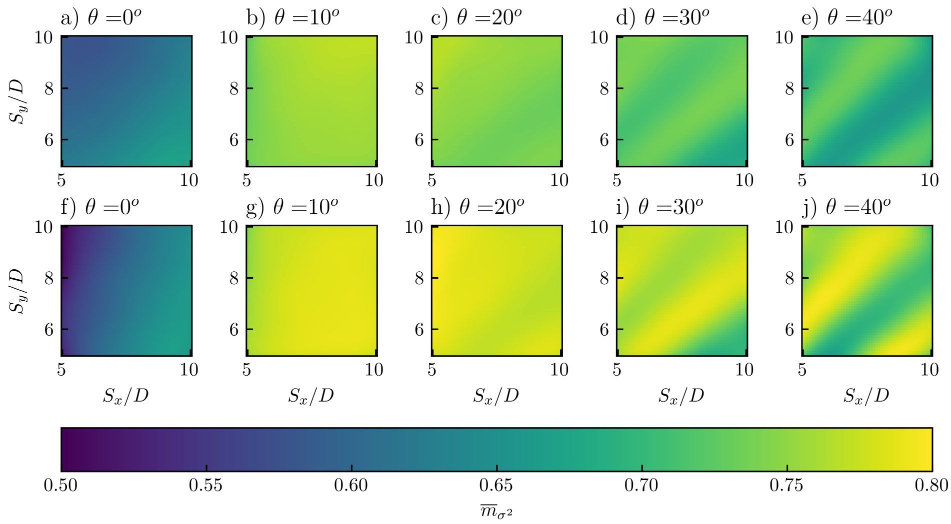

Figure 11 Posterior mean function of **MF-GP-nlow500** for different values of θ for a) to e) $g_{high}(v)$ and f) to j) $g_{low}(v)$.

5.3 | Prediction of wind farm performance

We use the predicted values of $C^*_{T,LES}$ from the emulators to predict the power output of wind farms under various mesoscale atmospheric conditions, following the concept of the two-scale momentum theory. We predict the (farm-averaged) turbine power coefficient C_p using $C^*_{T,LES}$ predictions from **MF-GP-nlow500**. We call this prediction of farm performance $C_{p,model}$. Firstly, we use the $C^*_{T,LES}$ prediction from the LOOCV procedure as C^*_T in equation 1 to calculate β for a given value of wind extractability ζ. We substitute this value of β into the expression $C_p = \beta^3 C^*_T{}^{\frac{3}{2}} C'_T{}^{-\frac{1}{2}}$ (which is only valid for actuator discs) to calculate $C_{p,model}$. We compare the value of $C_{p,model}$ with the turbine power coefficient recorded in the LES, $C_{p,LES}$. The effect of the coarse LES

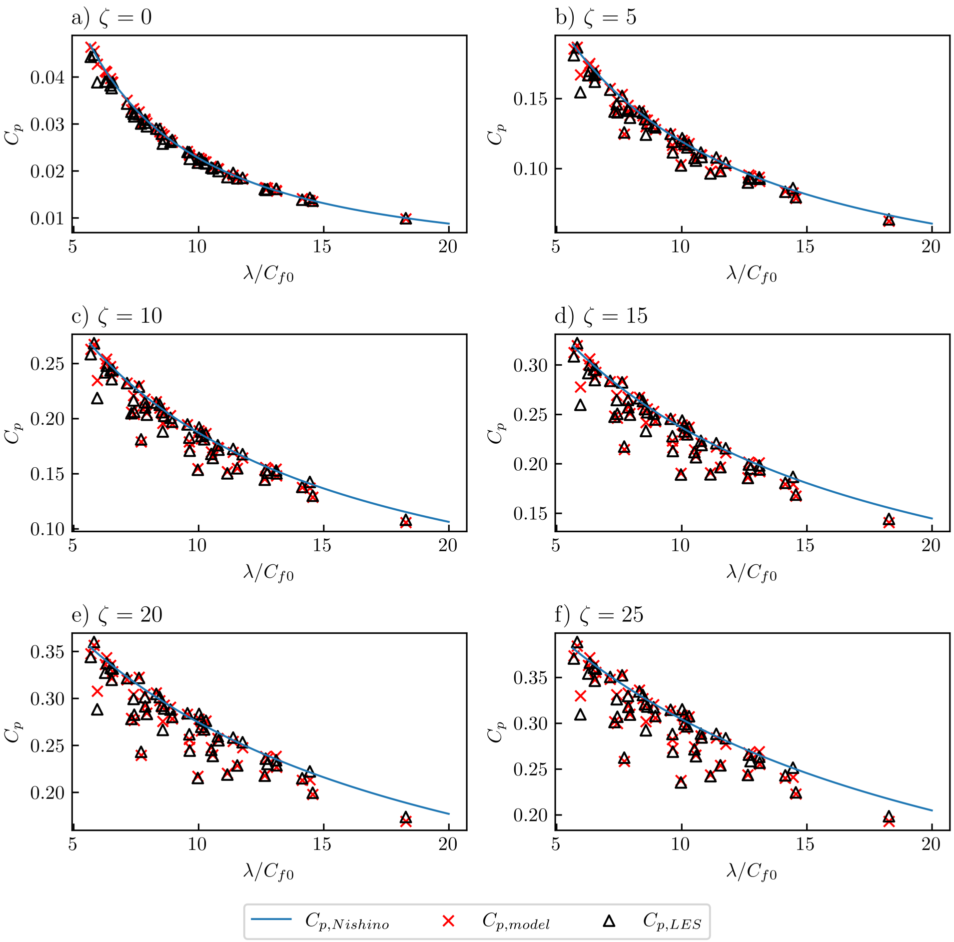

Figure 12 Comparison of C_p predictions with LES results for a realistic range of ζ values.

resolution on turbine thrust (and hence also ABL response and C_p) has already been corrected[8]. The LES was performed with periodic horizontal boundary conditions and a fixed momentum supply, i.e., $\zeta = 0$. However, the $C_{p,LES}$ has also been adjusted for a given ζ by scaling the velocity fields assuming Reynolds number independence[8].

Similarly, the analytical model of C_T^* can be used to give a theoretical prediction of wind farm performance called $C_{p,Nishino}$[8], which is given by

$$C_{p,Nishino} = \frac{64C_T'}{(4+C_T')^3}\left[\frac{-\zeta + \sqrt{\zeta^2 + 4\left(\frac{16C_T'}{(4+C_T')^2}\frac{\lambda}{C_{f0}} + 1\right)(1+\zeta)}}{2\left(\frac{16C_T'}{(4+C_T')^2}\frac{\lambda}{C_{f0}} + 1\right)}\right]^3. \tag{12}$$

We will compare the accuracy of both $C_{p,model}$ and $C_{p,Nishino}$ in predicting $C_{p,LES}$.

Both $C_{p,model}$ and $C_{p,LES}$ are shown in figure 12 for a realistic range of wind extractability factors, along with the results from $C_{p,Nishino}$ (equation 12). $C_{p,Nishino}$ provides an approximate upper limit of farm-averaged C_p as it predicts very well the effects of array density and large-scale atmospheric response. The statistical model accurately predicts the effect of turbine layout on farm performance which becomes more important with larger ζ values. As ζ increases, there is a larger difference between $C_{p,LES}$ and $C_{p,Nishino}$. Also, $C_{p,model}$ becomes slightly less accurate when ζ increases.

Table 3 shows the average prediction errors of $C_{p,model}$ and $C_{p,Nishino}$. We quantified the mean absolute error using two different reference powers. Using $C_{p,LES}$ as the reference power, $C_{p,Nishino}$ had an error of around 5% and the error increases

Table 3 Comparison of models for C_p prediction.

$\frac{1}{50}\sum_{i=1}^{50}\lvert C_{p,i}-C_{p,LES}\rvert/C_{p,LES}$			$\frac{1}{50}\sum_{i=1}^{50}\lvert C_{p,i}-C_{p,LES}\rvert/C_{p,Betz}$		
ζ	$C_{p,Nishino}$	$C_{p,model}$	ζ	$C_{p,Nishino}$	$C_{p,model}$
0	2.82%	2.15%	0	0.142%	0.108%
5	4.38%	1.48%	5	0.954%	0.338%
10	5.16%	1.35%	10	1.67%	0.459%
15	5.66%	1.30%	15	2.24%	0.542%
20	6.02%	1.26%	20	2.72%	0.601%
25	6.30%	1.24%	25	3.11%	0.648%

with ζ. The mean absolute error of $C_{p,model}$ was typically less than 1.5% and this decreased slightly as ζ increases (due to the reference power $C_{p,LES}$ increasing). We also use the power of an isolated ideal turbine, $C_{p,Betz}$, as a reference power. $C_{p,Betz}$ is calculated using the actuator disc theory with the expression $C_{p,Betz} = 64C_T'/(4+C_T')^3$ (note that in this study $C_T' = 1.33$ and hence $C_{p,Betz} = 0.563$). In this case the mean absolute error increased with ζ for both $C_{p,model}$ and $C_{p,Nishino}$. However, the average prediction error of $C_{p,model}$ remained below 0.65%.

6 | DISCUSSION

Data-driven modelling of the internal turbine thrust coefficient C_T^* is a novel approach to modelling turbine-wake interactions. Data-driven models of wind farm performance typically focus on predicting the power output, which, however, depends on flow physics across a wide range of scales. Current data-driven approaches are either not generalisable to different atmospheric responses, or would require a very large set of expensive training data, such as finite-size wind farm LES data. Data-driven models of C_T^* captures the effects of turbine-wake interactions, whilst also being applicable to different atmospheric responses (following the concept of the two-scale momentum theory).

The statistical emulator of C_T^* developed in this study was able to predict the farm power C_p of Kirby et. al.[8] with an average error of less than 0.65%. The high accuracy and very low computational cost of this approach shows the potential of this approach for modelling turbine-wake interactions. It has several advantages over traditional approaches using the superposition of wake models. Information from turbulence-resolving LES is included which ensures a high accuracy. It will also be more advantageous as wind farms become larger because wake models struggle to capture the complex multi-scale flows physics which are important for large farms. The statistical model of C_T^* may therefore allow fast and accurate predictions of wind farm performance.

All emulators developed in this study gave substantially better predictions of $C_{T,LES}^*$ compared to the analytical and wake models. Both the mean and maximum prediction errors were reduced by the emulators. The standard GP regression approach had a mean prediction error of 1.26% and maximum error of approximately 6%. The accuracy depends on the size of the LES data set and could be further decreased with a larger training set. The multi-fidelity GP approach gave more accurate predictions of $C_{T,LES}^*$ compared to the standard GP regression. This is because non-linear information fusion algorithm has incorporated information from many low-fidelity data points to improve the emulator of the high-fidelity (LES) model. This approach has the advantage that, unlike the standard GP regression approach, it is not necessary to evaluate the prior mean before making a prediction. Therefore, to predict C_T^* it is only necessary to evaluate the posterior mean of the high-fidelity emulator for a specific turbine layout.

The shape of the posterior mean in figure 8 gives insights into the physics of turbine-wake interactions. This is because $C_{T,LES}^*$ is low when a layout has a high degree of turbine-wake interactions. For the turbine operating conditions used, $C_{T,LES}^*$ is close to 0.75 when a layout has a small degree of wake interactions. Figure 8a shows $C_{T,LES}^*$ when the wind direction is perfectly aligned

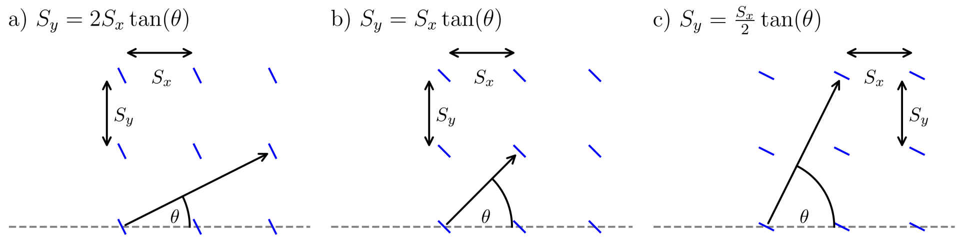

Figure 13 Positions of local minima in the function $g_{high}(S_x, S_y, \theta)$ corresponding to different alignments of turbines.

with the rows of turbines ($\theta = 0$). This gives wind farms with a high degree of wake interactions which results in low $C^*_{T,LES}$ values. For $\theta = 0^o$, increasing S_x/D increases C^*_T because there is a larger streamwise distance between turbines for the wakes to recover. When the cross-streamwise spacing (S_y/D) is increased the degree of wake interactions increases, i.e., $C^*_{T,LES}$ decreases. This is because there is a lower array density which results in a lower turbulence intensity within the farm and hence slower wake recovery. Yang[41] found that increasing the cross-streamwise spacing in infinitely-large wind farms increased the power of individual turbines and concluded that this was due to reduced wake interactions. However, the increase in turbine power found by Yang[41] may be also explained by to a faster farm-averaged wind speed caused by a reduced array density rather than reduced wake interactions.

When the wind direction θ increases, $C^*_{T,LES}$ increases to a maximum of just over 0.75 at $\theta = 10^o$ (figure 8c). This result agrees qualitatively with another study[42] in which it was found that the maximum farm power was produced by an intermediate wind direction. When θ increases above 20^o regions of low $C^*_{T,LES}$ appear diagonally (see figures 8f-j). The regions of low $C^*_{T,LES}$ are centred on the surfaces given by $S_y = 2S_x \tan(\theta)$, $S_y = S_x \tan(\theta)$ and $S_y = 0.5S_x \tan(\theta)$. These regions correspond to turbines being aligned along different axes throughout the farm (see figure 13). There are longer streamwise distance between turbines for these arrangements (compared to $\theta = 0^o$) and so the $C^*_{T,LES}$ values are higher than for $\theta = 0^o$.

The accuracy of the statistical emulators could be further improved in future studies. Both the standard and multi-fidelity GP models can be improved by adding more evaluations of $C^*_{T,LES}$. From table 2, the accuracy of the multi-fidelity GP models did not improve once we used more than 500 $C^*_{T,wake}$ evaluations. This shows that the error in predicting $C^*_{T,LES}$ for **MF-GP-nlow500** is not due to the model of f_{wake}. Instead the error arises from the learnt relationship between f_{wake} and f_{LES}.

The statistical emulators developed are not applicable to all wind farms because of the limited nature of our data set. A limitation of the developed model is that it is only applicable to farms with perfectly aligned layouts. It should also be noted that our model was trained on data from simulations of a neutrally stratified boundary layer. Therefore a larger LES data set with an extended parameter space would be required to account for the effect of atmospheric stability on wake interactions and the resulting C^*_T. Another limitation of our model is that it assumes all turbines have the same resistance coefficient C'_T. It is likely that this condition can be strictly satisfied only in the fully developed region of a large farm where the wind speed does not change in the streamwise or cross-streamwise directions.

Although we considered only actuator discs in this study for demonstration, the proposed approach using a data-driven model of C_T* can be applied to power prediction of real turbines as well in future studies. In this study, we calculate $C_{p,model}$ using the expression $C_{p,model} = \beta^3 {C^*_T}^{\frac{3}{2}} {C'_T}^{-\frac{1}{2}}$. This assumes that the relationship between C^*_p and C'_T is given by $C^*_p = {C^*_T}^{\frac{3}{2}} {C'_T}^{-\frac{1}{2}}$, which is only valid for actuator discs. For real turbines, the relationship between C^*_p and C'_T can be calculated using BEM theory[43] according to the turbine design and operating conditions (noting that the turbine induction factor can still be estimated as $a = C'_T/(4 + C'_T)$). $C_{p,model}$ can then be calculated using equation 5 with β found using equation 1. However, for a data-driven model of C^*_T to be applicable to real turbines, it will be necessary to model the impact of a variable C'_T rather than assuming a fixed C'_T value as in this study.

7 | CONCLUSIONS

In this study we proposed a new data-driven approach to modelling turbine wake interactions and resulting flow resistance in large wind farms. We developed statistical emulators of the farm-internal turbine thrust coefficient $C^*_{T,LES}$ as a function of turbine layout and wind direction. C^*_T represents the flow resistance within a wind farm and reflects the characteristics of the turbine-scale flows including wake and turbine blockage effects. We developed several emulators using both standard GP regression and multi-fidelity GP regression. The standard GP was trained using data from 50 infinitely-large wind farm LES (and using a low-fidelity wake model as a prior mean). The multi-fidelity GP was trained using data from both LES and wake model simulations. We estimated the test accuracy of the model by performing leave-one-out cross-validation and assessed the error in predicting $C^*_{T,LES}$. All emulators had a mean test error of less than 2% for predicting $C^*_{T,LES}$. The multi-fidelity GP gave the best performance with a mean prediction error of 0.849% and maximum prediction error of 3.78% with no bias for under or over-prediction. This is low compared to the mean error of the wake model (4.60%) and analytical C^*_T model (5.26%) which both had a bias for overpredicting $C^*_{T,LES}$.

We used an emulator of $C^*_{T,LES}$ to make predictions of wind farm performance under various mesoscale atmospheric conditions (characterised by the wind extractability factor ζ) using the two-scale momentum theory [24]. Our predictions of farm power production had an average error of less than 1.5% under realistic wind extractability scenarios compared to the LES. When the error in power prediction is expressed relative to the power of an isolated ideal turbine the average prediction error is less than 0.7%. We also used a previously proposed analytical model of C^*_T [25] to predict farm power output with an average error of less than 3.5% (with the power of an isolated turbine as the reference power). The analytical model correctly predicts the trends in farm performance with array density under different scenarios of large-scale atmospheric response, although it tends to overpredict the power where turbine-wake interactions are important. Using statistical emulators of C^*_T is a new approach to modelling turbine-wake interactions and flow resistance within large wind farms. The approach can be extended in future studies by increasing the size of the training data set, for example, to account for the effects of C'_T and atmospheric stability conditions on C^*_T. The very low computational cost and high accuracy of the model could be beneficial for future wind farm optimisation.

ACKNOWLEDGMENTS

The first author (AK) acknowledges the NERC-Oxford Doctoral Training Partnership in Environmental Research (NE/S007474/1) for funding and training.

Author contributions

T.N. derived the theory. A.K. and T.D.D. performed the simulations. F-X.B. provided assistance and guidance for the machine learning methodology. A.K. wrote the paper with corrections from T.N., F-X.B and T.D.D.

Financial disclosure

None reported.

Conflict of interest

The authors report no conflict of interest.

Data availability statement

The data and code that support the findings of this study are openly available at https://github.com/AndrewKirby2/ctstar_statistical_model. This includes the results from the wind farm LES and wake model simulations. The repository also includes the code for the results presented in sections 5.1, 5.2 and 5.3.

Author ORCID

A. Kirby, https://orcid.org/0000-0001-8389-1619; F-X. Briol https://orcid.org/0000-0002-0181-2559; T. Nishino, https://orcid.org/0000-0001-6306-7702.

How to cite this article: Kirby A., Briol F-X., Dunstan T.D., and Nishino T. (2023), Data-driven modelling of wind turbine wake interactions in large wind farms, *Wind Energy*, *xxxx*.

APPENDIX

A ESTIMATED HYPERPARAMETERS

In this section we present the estimated hyperparameters for each model in section 5. The hyperparameters for the standard GP models are shown in table A1. Unlike the LOOCV procedure in section 5, the models are fitted to all 50 LES data points $C^*_{T,LES}$. The hyperparameter values in table A1 will therefore be slightly different but very similar to the models in section 5. Equation 9 shows the meaning of each of the hyperparameters. For **GP-analytical-prior**, l_3 is the smallest lengthscale. This suggests that $C^*_{T,LES}$ is more sensitive to wind direction than turbine spacing.

The kernel for the multi-fidelity GP models is shown in equation A1. The kernel is the product and sum of different anisotropic squared-exponential covariance functions. Table A2 gives the estimated hyperparameters for the multi-fidelity GP models. For table A2 all 50 LES data points have been used for the fitting process.

$$k_{high}(v,v';\theta) = k_{high,\rho}(v,v';\theta_{high,\rho}) \cdot k_{high,f}(g_{low,*}(v), g_{low,*}(v');\theta_{high,f}) + k_{high,\delta}(v,v';\theta_{high,\delta}) \quad \text{(A1)}$$

Table A1 Estimated hyperparameters for standard GP regression models.

Hyperparameter	**GP-analytical-prior**	**GP-wake-TI1-prior**	**GP-wake-TI5-prior**	**GP-wake-TI10-prior**	**GP-wake-TI15-prior**
σ_f^2	5.25×10^{-3}	1.22×10^{-3}	1.27×10^{-3}	9.09×10^{-4}	1.19×10^{-3}
l_1	5.27	2.51	1.74×10^{3}	1.03×10^{4}	5.06
l_2	4.90	1.26×10^{3}	1.94×10^{3}	3.57	5.91
l_3	6.16×10^{-1}	2.02×10^{-1}	4.55×10^{-1}	2.03	6.25×10^{-1}
σ^2	1.47×10^{-4}	4.06×10^{-4}	3.83×10^{-4}	1.28×10^{-4}	4.10×10^{-5}

Table A2 Estimated hyperparameters for multi-fidelity GP regression models.

Hyperparameter		**MF-GP-nlow250**	**MF-GP-nlow500**	**MF-GP-nlow100**
k_{low}	σ_f^2	2.09×10^{-1}	9.51×10^{-2}	9.70×10^{-2}
	l_1	3.31	1.42	1.40
	l_2	2.51	1.18	1.10
	l_3	7.31×10^{-1}	5.12×10^{-1}	5.07×10^{-1}
$k_{high,\rho}$	σ_f^2	2.22×10^{-5}	7.91×10^{-6}	2.34×10^{-5}
	l_1	3.77	3.92×10^{4}	1.23×10^{1}
	l_2	6.29	6.94	9.52
	l_3	9.25	10.0	6.66
$k_{high,f}$	σ_f^2	2.82×10^{2}	2.00×10^{3}	4.89×10^{2}
	l	1.15×10^{-1}	1.96×10^{-1}	1.89×10^{-1}
$k_{high,\delta}$	σ_f^2	5.16×10^{-1}	5.42×10^{-1}	5.00×10^{-1}
	l_1	1.18×10^{4}	8.76×10^{4}	2.33×10^{4}
	l_2	1.45×10^{4}	1.17×10^{5}	2.58×10^{4}
	l_3	1.01×10^{4}	5.11×10^{5}	4.93×10^{3}
σ_{low}^2		1.09×10^{-4}	2.75×10^{-6}	1.84×10^{-6}
σ_{high}^2		5.59×10^{-4}	5.46×10^{-5}	4.42×10^{-5}

References

1. Porté-Agel F, Bastankhah M, Shamsoddin S. Wind-Turbine and Wind-Farm Flows: A Review. *Boundary-Layer Meteorology* 2020; 174: 1-59. doi: 10.1007/s10546-019-00473-0

2. Bleeg J, Purcell M, Ruisi R, Traiger E. Wind farm blockage and the consequences of neglecting its impact on energy production. *Energies* 2018; 11: 1609. doi: 10.3390/en11061609

3. Carbon Trust . Global Blockage Effect in Offshore Wind (GloBE) [accessed 07/11/2022]. https://www.carbontrust.com/our-projects/large-scale-rd-projects-offshore-wind/global-blockage-effect-in-offshore-wind-globe; 2022.

4. Jensen NO. A note on wind generator interaction. *Risø-M-2411 Risø National Laboratory Roskilde* 1983.

5. Bastankhah M, Porté-Agel F. A new analytical model for wind-turbine wakes. *Renewable Energy* 2014; 70: 116-123. doi: 10.1016/j.renene.2014.01.002

6. Katic I, Hojstrup J, Jensen NO. A simple model for cluster efficiency. *Proceedings of the European wind energy association conference and exhibition, Rome, Italy* 1986: 407-409.

7. Zong H, Porté-Agel F. A momentum-conserving wake superposition method for wind farm power prediction. *Journal of Fluid Mechanics* 2020; 889: A8. doi: 10.1017/jfm.2020.77

8. Kirby A, Nishino T, Dunstan TD. Two-scale interaction of wake and blockage effects in large wind farms. *Journal of Fluid Mechanics* 2022; 953: A39. doi: 10.1017/jfm.2022.979

9. Stevens RJAM, Gayme DF, Meneveau C. Effects of turbine spacing on the power output of extended wind-farms. *Wind Energy* 2016; 19: 359-370. doi: 10.1002/we.1835

10. Fitch AC, Olson JB, Lundquist JK, et al. Local and mesoscale impacts of wind farms as parameterized in a mesoscale NWP model. *Monthly Weather Review* 2012; 140. doi: 10.1175/MWR-D-11-00352.1

11. Abkar M, Porté-Agel F. A new wind-farm parameterization for large-scale atmospheric models. *Journal of Renewable and Sustainable Energy* 2015; 7. doi: 10.1063/1.4907600

12. Pan Y, Archer CL. A Hybrid Wind-Farm Parametrization for Mesoscale and Climate Models. *Boundary-Layer Meteorology* 2018; 168: 469-495. doi: 10.1007/s10546-018-0351-9

13. Zehtabiyan-Rezaie N, Iosifidis A, Abkar M. Data-driven fluid mechanics of wind farms: A review. *Journal of Renewable and Sustainable Energy* 2022; 14: 32703. doi: 10.1063/5.0091980

14. Renganathan SA, Maulik R, Letizia S, Iungo GV. Data-driven wind turbine wake modeling via probabilistic machine learning. *Neural Computing and Applications* 2022; 34: 6171-6186. doi: 10.1007/s00521-021-06799-6

15. Optis M, Perr-Sauer J. The importance of atmospheric turbulence and stability in machine-learning models of wind farm power production. *Renewable and Sustainable Energy Reviews* 2019; 112: 27-41. doi: 10.1016/j.rser.2019.05.031

16. Japar F, Mathew S, Narayanaswamy B, Lim CM, Hazra J. Estimating the wake losses in large wind farms: A machine learning approach. *ISGT 2014* 2014: 1-5. doi: 10.1109/ISGT.2014.6816427

17. Yan C, Pan Y, Archer CL. A general method to estimate wind farm power using artificial neural networks. *Wind Energy* 2019; 22: 1421-1432. doi: 10.1002/we.2379

18. Zhang J, Zhao X. Wind farm wake modeling based on deep convolutional conditional generative adversarial network. *Energy* 2022; 238: 121747. doi: https://doi.org/10.1016/j.energy.2021.121747

19. Wilson B, Wakes S, Mayo M. Surrogate modeling a computational fluid dynamics-based wind turbine wake simulation using machine learning. *2017 IEEE Symposium Series on Computational Intelligence (SSCI)* 2017: 1-8. doi: 10.1109/SSCI.2017.8280844

20. Ti Z, Deng XW, Yang H. Wake modeling of wind turbines using machine learning. *Applied Energy* 2020; 257: 114025. doi: https://doi.org/10.1016/j.apenergy.2019.114025

21. Ti Z, Deng XW, Zhang M. Artificial Neural Networks based wake model for power prediction of wind farm. *Renewable energy* 2021; 172: 618-631. doi: https://doi.org/10.1016/j.renene.2021.03.030

22. Park J, Park J. Physics-induced graph neural network: An application to wind-farm power estimation. *Energy* 2019; 187. doi: 10.1016/j.energy.2019.115883

23. Bleeg J. A Graph Neural Network Surrogate Model for the Prediction of Turbine Interaction Loss. *Journal of Physics: Conference Series* 2020; 1618. doi: 10.1088/1742-6596/1618/6/062054

24. Nishino T, Dunstan TD. Two-scale momentum theory for time-dependent modelling of large wind farms. *Journal of Fluid Mechanics* 2020; 894: A2. doi: 10.1017/jfm.2020.252

25. Nishino T. Two-scale momentum theory for very large wind farms. *Journal of Physics: Conference Series* 2016; 753: 032054. doi: 10.1088/1742-6596/753/3/032054

26. Patel K, Dunstan TD, Nishino T. Time-dependent upper limits to the performance of large wind farms due to mesoscale atmospheric response. *Energies* 2021; 14: 6437. doi: 10.3390/en14196437

27. Sacks J, Welch WJ, Mitchell TJ, Wynn HP. Design and analysis of computer experiments. *Statistical Science* 1989; 4: 409-423. doi: 10.1214/ss/1177012413

28. Currin C, Mitchell T, Morris M, Ylvisaker D. Bayesian prediction of deterministic functions, with applications to the design and analysis of computer experiments. *Journal of the American Statistical Association* 1991; 86: 953-963. doi: 10.1080/01621459.1991.10475138

29. Johnson ME, Moore LM, Ylvisaker D. Minimax and maximin distance designs. *Journal of Statistical Planning and Inference* 1990; 26: 131-148. doi: 10.1016/0378-3758(90)90122-B

30. Santner TJ, Williams BJ, Notz W. *The design and analysis of computer experiments*. second ed. 2018.

31. Wynne G, Briol FX, Girolami M. Convergence guarantees for gaussian process means with misspecified likelihoods and smoothness. *Journal of Machine Learning Research* 2021; 22.

32. Shapiro CR, Gayme DF, Meneveau C. Filtered actuator disks: Theory and application to wind turbine models in large eddy simulation. *Wind Energy* 2019; 22: 1414-1420. doi: 10.1002/we.2376

33. Niayifar A, Porté-Agel F. Analytical modeling of wind farms: A new approach for power prediction. *Energies* 2016; 9. doi: 10.3390/en9090741

34. Pedersen MM, Laan v. dP, Friis-Møller M, Rinker J, Réthoré PE. DTUWindEnergy/PyWake: PyWake. 2021. doi: 10.5281/zenodo.2562662

35. Crespo A, Hernández J. Turbulence characteristics in wind-turbine wakes. *Journal of Wind Engineering and Industrial Aerodynamics* 1996; 61: 71-85. doi: 10.1016/0167-6105(95)00033-X

36. Rasmussen CE, Williams CKI. *Gaussian Processes for Machine Learning*. the MIT Press . 2018

37. Peherstorfer B, Willcox K, Gunzburger M. Survey of multifidelity methods in uncertainty propagation, inference, and optimization. *SIAM Review* 2018; 60. doi: 10.1137/16M1082469

38. Perdikaris P, Raissi M, Damianou A, Lawrence ND, Karniadakis GE. Nonlinear information fusion algorithms for data-efficient multi-fidelity modelling. *Proceedings of the Royal Society A: Mathematical, Physical and Engineering Sciences* 2017; 473. doi: 10.1098/rspa.2016.0751

39. Paleyes A, Pullin M, Mahsereci M, Lawrence N, González J. Emulation of physical processes with Emukit. 2019.

40. GPy . GPy: A Gaussian process framework in python. http://github.com/SheffieldML/GPy; since 2012.

41. Yang X, Kang S, Sotiropoulos F. Computational study and modeling of turbine spacing effects infinite aligned wind farms. *Physics of Fluids* 2012; 24: 11510. doi: 10.1063/1.4767727

42. Stevens RJAM, Gayme DF, Meneveau C. Large eddy simulation studies of the effects of alignment and wind farm length. *Journal of Renewable and Sustainable Energy* 2014; 6: 023105. doi: 10.1063/1.4869568

43. Nishino T, Hunter W. Tuning turbine rotor design for very large wind farms. *Proceedings of the Royal Society A: Mathematical, Physical and Engineering Sciences* 2018; 474(2220): 1–20. doi: 10.1098/rspa.2018.0237

3.1 Statement of authorship

Statement of Authorship for joint/multi-authored papers for PGR thesis

To appear at the end of each thesis chapter submitted as an article/paper

The statement shall describe the candidate's and co-authors' independent research contributions in the thesis publications. For each publication there should exist a complete statement that is to be filled out and signed by the candidate and supervisor **(only required where there isn't already a statement of contribution within the paper itself).**

Title of Paper	Data-driven modelling of turbine wake interactions and flow resistance in large wind farms
Publication Status	Published
Publication Details	Kirby A, Briol F-X, Dunstan TD, Nishino T. Data-driven modelling of turbine wake interactions and flow resistance in large wind farms. *Wind Energy*. 2023; 26(9): 968-984. doi:10.1002/we.2851

Student Confirmation

Student Name:	Andrew Kirby		
Contribution to the Paper	Performed the large-eddy simulations and wake model simulations, developed data-driven machine learning models and drafted manuscript.		
Signature Andrew Kirby		Date	05/02/2024

Supervisor Confirmation

By signing the Statement of Authorship, you are certifying that the candidate made a substantial contribution to the publication, and that the description described above is accurate.

Supervisor name and title: Dr Takafumi Nishino		
Supervisor comments I believe that Andrew made a substantial contribution (more than 70%) to this publication, and the description described above is accurate.		
Signature Nishino	Date	25/07/2024

This completed form should be included in the thesis, at the end of the relevant chapter.

Chapter 4

An analytical model of momentum availability for predicting large wind farm power

This chapter presents a journal article titled *'An analytical model of momentum availability for predicting large wind farm power'* published in the *'Journal of Fluid Mechanics'* (`https://doi.org/10.1017/jfm.2023.844`). The article spans the pages 79-99 in the thesis.

Offshore wind farms are becoming larger. Therefore, the aerodynamics which determines the farm efficiency may change. For large offshore farms, farm-scale flow effects are starting to be observed, e.g. farm blockage and gravity wave excitation. Our previous work (chapter 2) showed that power losses due to farm-scale flows could be more than twice as large as the losses due to turbine-scale flows as future wind farms become larger. This motivates the development of new models to predict farm-scale flows with low computational cost.

In this chapter, we present a simple new analytical model to predict farm-atmosphere interactions. The model considers the impact of net momentum advection, pressure gradient forcing and turbulent entrainment on farm performance. We derive the model using a quasi-1D steady control volume analysis. The model is compared against existing finite wind farm LES in the literature. This initial comparison shows a good agreement between the model and simulation results.

The proposed model is a new way of predicting the power output of large wind farms. The chapter also outlines a new general framework for modelling farm-scale flows. This could provide a more physically realistic approach to predicting farm efficiency at low cost.

An analytical model of momentum availability for predicting large wind farm power

Andrew Kirby[1] †, Thomas D. Dunstan[2], and Takafumi Nishino[1]

[1]Department of Engineering Science, University of Oxford, Parks Road, Oxford OX1 3PJ, UK

[2]Met Office, FitzRoy Road, Exeter EX1 3PB, UK

(Received xx; revised xx; accepted xx)

Turbine-wake and farm-atmosphere interactions influence wind farm power production. For large offshore farms, the farm-atmosphere interaction is usually the more significant effect. This study proposes an analytical model of the 'momentum availability factor' to predict the impact of farm-atmosphere interactions. It models the effects of net advection, pressure gradient forcing and turbulent entrainment, using steady quasi-1D flow assumptions. Turbulent entrainment is modelled by assuming self-similar vertical shear stress profiles. We used the model with the 'two-scale momentum theory' to predict the power of large finite-sized farms. The model compared well with existing results of large-eddy simulations (LES) of finite wind farms in conventionally neutral boundary layers. The model captured most of the effects of atmospheric boundary layer (ABL) height on farm performance by considering the undisturbed vertical shear stress profile of the ABL as an input. In particular, the model predicted the power of staggered wind farms with a typical error of 5% or less. The developed model provides a novel way of instantly predicting the power of large wind farms, including the farm blockage effects. A further simplification of the model to analytically predict the 'wind extractability factor' is also presented. This study provides a novel framework for modelling farm-atmosphere interactions. Future studies can use the framework to better model large wind farms.

Key words: Authors should not enter keywords on the manuscript, as these must be chosen by the author during the online submission process and will then be added during the typesetting process (see Keyword PDF for the full list). Other classifications will be added at the same time.

MSC Codes *(Optional)* Please enter your MSC Codes here

1. Introduction

Wind energy is a key technology for the renewable energy transition. To meet future energy demands, wind energy capacity will need to increase rapidly and individual farms will likely

† Email address for correspondence: andrew.kirby@trinity.ox.ac.uk

become larger (Veers *et al.* 2022). A key aspect for designing wind farms is predicting their power output. However, it is difficult to model the aerodynamics of large wind farms because of the multi-scale nature of flows involved (Porté-Agel *et al.* 2020).

Traditionally, there are two main approaches to predicting wind farm performance at a low computational cost. For the first approach, semi-analytical 'wake' models predict the velocity deficit in the wake behind a turbine (e.g. Jensen 1983; Bastankhah & Porté-Agel 2014). To model an entire wind farm, individual wakes are superposed using different techniques (e.g. Katic *et al.* 1986; Zong & Porté-Agel 2020). Wake models are commonly used to optimise the layout of turbines in a farm. However, they do not consider the atmospheric response to wind farms and thus they perform poorly for extended wind farms (e.g. Stevens *et al.* 2016). The second approach uses 'top-down' models (e.g. Frandsen 1992; Frandsen *et al.* 2006; Calaf *et al.* 2010). Top-down models consider the response of an idealised atmospheric boundary layer (ABL) to an infinitely large wind farm. They cannot however, predict the impact of turbine layout (placement of turbines within a farm) on farm performance. Recent studies have coupled the wake and top-down models together (e.g. Stevens *et al.* 2016; Starke *et al.* 2021). This approach however, is still limited by the limitations of the constituent models, e.g., idealised ABL profiles and wake superposition methods.

More recently, models have been developed to predict the interaction between wind farms and the atmosphere. Meneveau (2012) extended top-down models to finite wind farms by considering the development of an internal boundary layer. Luzzatto-Fegiz & Caulfield (2018) modelled the impact of entrainment on farm performance by using a three layer model. This model was extended to finite wind farms by Bempedelis *et al.* (2023). Smith (2010) predicted the impact of gravity waves on wind farm performance by solving a two layer model using fast fourier transforms. This approach was later extended to a three layer model (Allaerts & Meyers 2018, 2019). The model was further extended to include the impact of vertically varying free-atmospheres (Devesse *et al.* 2022). All of these approaches require solving differential equations numerically to predict wind farm performance.

Nishino & Dunstan (2020) developed the 'two-scale momentum theory' to better understand the power generation mechanism of large wind farms. This splits the multi-scale problem of wind farm aerodynamics into 'internal' turbine/array-scale and 'external' farm/atmospheric-scale sub-problems. The sub-problems are coupled together using the conservation of momentum. As farms become larger, one of the grand challenges facing the wind energy community is to understand the impact of farm-atmosphere interaction (Veers *et al.* 2019). Kirby *et al.* (2022) confirmed this by performing large-eddy simulations (LES) of 50 different periodic turbine layouts. They introduced the concepts of 'turbine-scale losses' due to turbine-wake interactions and 'farm-scale losses' caused by the atmospheric response to the whole farm. For large offshore farms, the farm-scale losses were found to be typically more than twice as large as the turbine-scale losses. This highlights the importance of modelling farm-scale flows to predict the performance of future large farms.

Unlike most large wind farm models, the two-scale momentum theory does not assume any specific profiles of the ABL (such as a logarithmic law), allowing for the external sub-problem to be modelled in various manners. For the external modelling, it is crucial to accurately predict how the momentum available to the farm site increases due to the presence of the turbines, i.e., the momentum availability. Recent studies (Patel *et al.* 2021; Legris *et al.* 2023) used 'twin' numerical weather prediction (NWP) simulations to calculate the momentum availability and thus predict how farm-scale losses (including the so-called farm blockage losses) change with atmospheric conditions. However, this approach would be too computationally expensive for wind farm optimisation unless a sufficiently long set of twin NWP (such as those reported by van Stratum *et al.* (2022)) has already been conducted for candidate wind farm sites.

In the present study we propose a simple analytical model to predict the momentum availability for large wind farms. This model, together with the two-scale momentum theory, allows us to predict the power of a large wind farm analytically. The model is derived using quasi-1D control volume analysis and assuming self-similar vertical shear stress profiles. In section 2, we summarise the two-scale momentum theory and the key wind farm parameters. Section 3 presents the derivation of the new momentum availability factor model. In section 4 we compare the predictions of farm power with existing finite wind farm LES. The model is further discussed in section 5 and concluding remarks are given in section 6.

2. Two-scale momentum theory

By considering the conservation of momentum for a control volume with and without a wind farm present, Nishino & Dunstan (2020) derived the non-dimensional farm momentum (NDFM) equation:

$$C_T^* \frac{\lambda}{C_{f0}} \beta^2 + \beta^\gamma = M \tag{2.1}$$

where β is the farm wind-speed reduction factor defined as $\beta \equiv U_F/U_{F0}$ (with U_F defined as the average wind speed in the nominal farm-layer of height H_F, and U_{F0} is the farm-layer-averaged speed without the presence of the turbines); C_T^* is the (farm-averaged) 'internal' turbine thrust coefficient defined as $C_T^* \equiv \sum_{i=1}^n T_i / \frac{1}{2}\rho U_F^2 nA$ (where T_i is the thrust of turbine i, A is the rotor swept area and n is the number of turbines in the farm); λ is the array density defined as $\lambda \equiv nA/S_F$ (where S_F is the wind farm area); C_{f0} is the natural friction coefficient of the surface defined as $C_{f0} \equiv \tau_{w0}/\frac{1}{2}\rho U_{F0}^2$ (where τ_{w0} is the undisturbed bottom shear stress); γ is the bottom friction exponent defined as $\gamma \equiv \log_\beta(\tau_w/\tau_{w0})$ (assumed to be 2 in this study); and M is the momentum availability factor given by:

$$M = \frac{X - C - \left[\frac{\partial p}{\partial x_F}\right] - \frac{\partial[\rho U]}{\partial t}}{X_0 - C_0 - \left[\frac{\partial p_0}{\partial x_{F0}}\right] - \frac{\partial[\rho U_0]}{\partial t}} \tag{2.2}$$

where U is the velocity in the hub-height wind direction (i.e. streamwise direction) x_F, X represents the net streamwise momentum injection through the top and side boundaries of the control volume (due to advection and Reynolds stress), C is the streamwise component of the Coriolis force averaged over the control volume, $\partial p/\partial x_F$ is the pressure gradient in the direction x_F and the subscript 0 refers to values without the turbines present. Any imbalance between the momentum supplied to the control volume and total bottom drag (i.e., turbine thrust and surface drag) will accelerate or decelerate the flow, giving the time derivative terms in equation 2.2 (Nishino & Dunstan 2020). In this study we ignore the Coriolis terms and time derivative terms (i.e., we assume stationary atmospheric conditions) and use a fixed definition for the farm-layer height of $H_F = 2.5H_{hub}$ where H_{hub} is the turbine hub-height, following Kirby *et al.* (2022).

The theoretical framework Nishino & Dunstan (2020) used to derive equation 2.1 is known as the 'two-scale momentum theory'. The left-hand side of equation 2.1 is expected to depend primarily on turbine-scale or 'internal' conditions. This includes turbine layout and operating conditions, and the hub-height wind speed and direction. The right-hand side of equation 2.1 is assumed to depend on 'external' farm-scale conditions.

The farm wind-speed reduction factor β can be calculated using 2.1 for a set of C_T^*, γ and M. Using β, the average turbine power coefficients can be calculated using

$$C_p = \beta^3 C_p^* \tag{2.3}$$

where C_p is the (farm-averaged) turbine power coefficient defined as $C_p \equiv \sum_{i=1}^{n} P_i / \frac{1}{2}\rho U_{F0}^3 nA$ (P_i is power of turbine i in the farm) and C_p^* is the (farm-averaged) 'internal' turbine power coefficient defined as $C_p^* \equiv \sum_{i=1}^{n} P_i / \frac{1}{2}\rho U_F^3 nA$.

3. Momentum availability factor model

The momentum availability factor M describes the increase in momentum supplied to the farm site due to the presence of the turbines (equation 3.1). We introduce new variables M_{F0} defined as the total net momentum flux into the farm control volume without the turbines present, and M_F as the total net momentum flux with the turbines. ΔM_F is the change in momentum flux due to the presence of the turbines, defined as $\Delta M_F \equiv M_F - M_{F0}$.

ΔM_F can be decomposed into the contributions from different physical mechanisms. For this study, we will consider only the contributions from net momentum advection, pressure gradient forcing (PGF) and turbulent entrainment (equation 3.1). Equation 3.1 provides a new framework for modelling the impact of farm-scale flows.

$$\begin{aligned} M = \frac{M_F}{M_{F0}} &= 1 + \frac{\Delta M_F}{M_{F0}} \\ &= 1 + \frac{\Delta M_{F,Advection}}{M_{F0}} + \frac{\Delta M_{F,PGF}}{M_{F0}} + \frac{\Delta M_{F,Entrainment}}{M_{F0}} \end{aligned} \tag{3.1}$$

In this study we propose simple analytical models for the components of equation 3.1. For each component we consider a control volume of height H_F around the farm (note that this control volume can be different from the control volume used to derive equation 2.1). The height of the control volume can be chosen arbitrarily but choosing H_F allows terms to be linked to farm wind-speed reduction factor β. We use a steady quasi-1D analysis for the advection and PGF terms. The entrainment term is modelled by assuming self-similar vertical shear stress profiles (above the top turbine-tip). However, the modelling framework is not specific to the analytical models proposed in the next sections. Equation 3.1 can be a starting point for future studies using more sophisticated approaches for each component.

3.1. *Net momentum advection*

Figure 1 shows a rectangular wind farm control volume. L is the length of the farm in the hub-height wind direction and W is the farm width. Using a quasi-1D approach, we define the spanwise- and vertically-averaged wind speed throughout the control volume as $U_{F0}\beta_{local}(x)$. In our notation $x = 0$ is at the front of the farm and $x = L$ is at the rear. Note that in figure 1a, $\beta_{local}(0)$ is not exactly equal to 1 since the wind speed decelerates upstream of the farm due to the farm blockage effect. Our proposed model of net momentum advection can therefore capture the impact of farm blockage.

By considering the conservation of mass of an elemental control volume (shown by the bold box in figure 1), the mass flux out of the farm control volume at position x can be expressed as

$$\dot{m}_{out}(x) = -\rho H_F W U_{F0} \frac{\mathrm{d}\beta_{local}(x)}{\mathrm{d}x}. \tag{3.2}$$

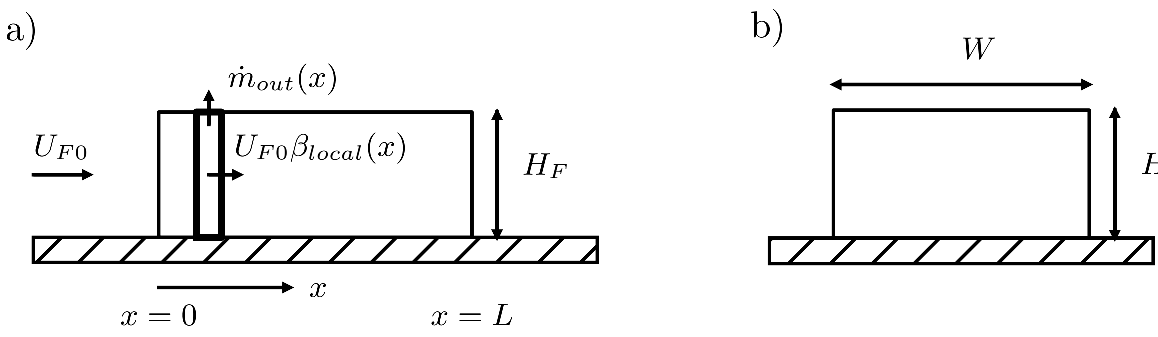

Figure 1: Control volume analysis for net momentum advection calculation a) side view and b) front view.

Note that this could be mass flux out of the top or sides of the farm control volume. The momentum flux into the control volume at the front surface (i.e. $x = 0$) is given by

$$\dot{m}_{in,front}U_{in,front} = \rho U_{F0}^2 \beta_{local}(0)^2 H_F W \tag{3.3}$$

noting that a positive value represents a net inflow of momentum. The net momentum flux through the rear surface (i.e. $x = L$) is given by

$$\dot{m}_{in,rear}U_{in,rear} = -\rho U_{F0}^2 \beta_{local}(L)^2 H_F W. \tag{3.4}$$

The momentum flux through the top surface is the integral of the mass flux and streamwise velocity at each position x, i.e.

$$\dot{m}_{in,top}U_{in,top} = -\int_0^L \dot{m}_{out}(x) U_{F0}\beta_{local}(x)\,\mathrm{d}x. \tag{3.5}$$

We substitute 3.2 into 3.5 and integrate to obtain

$$\dot{m}_{in,top}U_{in,top} = \rho U_{F0}^2 H_F W \left[\frac{1}{2}\beta_{local}(L)^2 - \frac{1}{2}\beta_{local}(0)^2\right]. \tag{3.6}$$

The total net momentum inflow into the control volume is given by the sum of equations 3.3, 3.4 and 3.6, i.e.,

$$\Delta M_{F,Advection} = \frac{1}{2}\rho U_{F0}^2 H_F W \left[\beta_{local}(0)^2 - \beta_{local}(L)^2\right]. \tag{3.7}$$

This expression relates the change in momentum advection to the velocity at the front and rear of the farm.

3.2. *Pressure gradient forcing*

LES results in the literature have shown that large wind farms can induce additional pressure gradients across them (e.g., Allaerts & Meyers 2017; Wu & Porté-Agel 2017; Lanzilao & Meyers 2022). When farms induce additional pressure gradients, a velocity reduction at the front of the farm is commonly observed. This velocity reduction at the front of the farm is commonly known as ‘wind-farm blockage’. Typically, a velocity increase and pressure reduction at the rear of the farm can also occur. Figure 2 shows example streamwise variations of $\beta_{local}(x)$ and pressure.

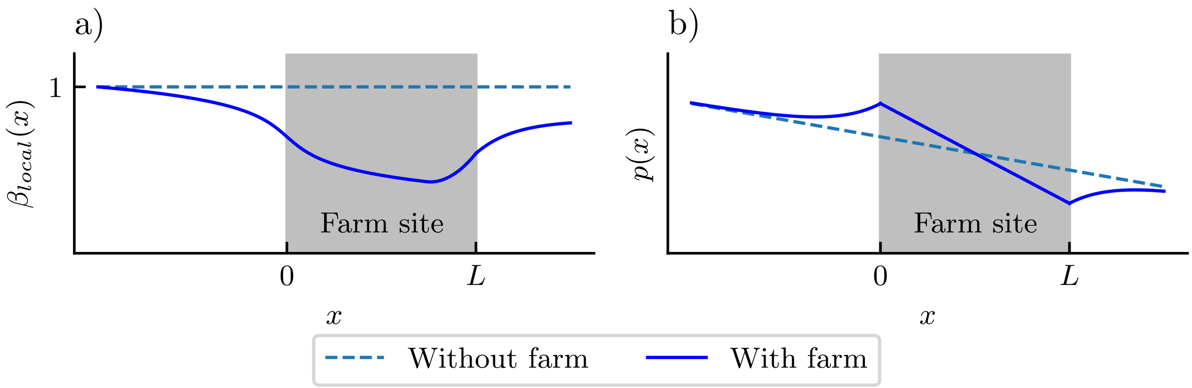

Figure 2: Example variations of a) local farm wind-speed reduction factor $\beta_{local}(x)$ and b) pressure $p(x)$ with streamwise location.

In this section we propose a simple model for $\Delta M_{F,PGF}$. We apply Bernoulli's equation as an approximation to link the pressure increase to the velocity reduction at the front of the farm. We neglect changes in gravitational potential energy. It is assumed that changes in pressure are uniform up to the control volume height H_F.

Our aim here is to model an increased pressure difference across the farm Δp. The physical mechanism increasing the pressure difference is not directly considered (e.g. gravity waves) but is implicitly included in Δp. Δp is composed of a pressure increase at the front surface of the farm control volume Δp_{front} and pressure decrease at the rear surface Δp_{rear}.

The velocity reduction in front of the farm takes place over a distance of $L_{induction}$. Without the farm present, the background pressure force is balanced by the bottom shear stress over this region, i.e.,

$$h_0 \Delta p_0 = \frac{1}{2}\rho C_{f0} U_{F0}^2 L_{induction} \tag{3.8}$$

where h_0 is the ABL height without the farm present. Therefore, the ratio of friction head loss to dynamic pressure is given by $L_{induction} C_{f0}/h_0$. Although $L_{induction}$ can be an order of magnitude larger than h_0, a typical value of C_{f0} is 0.002 to 0.003. The dynamic pressure is therefore typically one to two orders of magnitude larger than the friction head loss and background pressure gradient. As such, as a first order approach we consider only pressure changes due to changes in dynamic pressure, justifying the use of Bernoulli's equation.

Bernoulli's equation is applied on a streamline from far upstream to the front of the farm. The increase in pressure force on the front surface of the control volume is therefore given by:

$$\Delta p_{front} H_F W = \frac{1}{2}\rho U_{F0}^2 H_F W \left[1 - \beta_{local}(0)^2\right]. \tag{3.9}$$

We then assume that $\Delta p_{rear} = \Delta p_{front}$ and therefore $\Delta p = 2\Delta p_{front}$. This is a strong assumption and in reality this would depend on the atmospheric conditions. The LES results of Wu & Porté-Agel (2017) and Lanzilao & Meyers (2022) show approximately equal and opposite pressure changes at the front and rear of the farm, suggesting that this approximation is valid. However, the LES of Allaerts & Meyers (2017) and Lanzilao & Meyers (2023) suggest that this assumption is likely to only be valid for certain atmospheric stratifications. $\Delta M_{F,PGF}$ is then given by:

	$\Gamma = 1K/km$		$\Gamma = 5K/km$	
	Staggered	Aligned	Staggered	Aligned
$\beta_{local}(0)^2 + \beta_{local}(L)^2$	1.519	1.579	1.361	1.473
$1 + \beta^2$	1.639	1.696	1.548	1.611
Percentage error	7.99%	7.40%	13.7%	9.37%

Table 1: Percentage errors of approximation $\beta_{local}(0)^2 + \beta_{local}(L)^2 \approx 1 + \beta^2$ using data from Wu & Porté-Agel (2017)

$$\Delta M_{F,PGF} = \Delta p H_F W = \frac{1}{2}\rho U_{F0}^2 H_F W \left[2 - 2\beta_{local}(0)^2\right]. \tag{3.10}$$

Combining advection and PGF terms gives:

$$\Delta M_{F,Advection} + \Delta M_{F,PGF} = \frac{1}{2}\rho U_{F0}^2 H_F W \left[2 - \beta_{local}(0)^2 - \beta_{local}(L)^2\right]. \tag{3.11}$$

Generally, the velocity at the front of the farm is close to the undisturbed value. The velocity at the rear of the farm tends to be close to the farm-averaged value. As a simple first-order approach, we assume that the small velocity reduction at the front of the farm, $1-\beta_{local}(x)$, is equal to the small increase at the rear (relative to the farm-averaged wind speed), $\beta_{local}(L)-\beta$. As such we can say that $\beta_{local}(0)^2 + \beta_{local}(L)^2 \approx 1 + \beta^2$. Applying this approximation to equation 3.11:

$$\Delta M_{F,Advection} + \Delta M_{F,PGF} = \frac{1}{2}\rho U_{F0}^2 H_F W \left(1 - \beta^2\right). \tag{3.12}$$

To check the validity of this approximation, we used data from finite wind farm LES performed by Wu & Porté-Agel (2017). We take the hub-height wind speed normalised by the inflow value as a proxy for $\beta_{local}(x)$. Note that H_F has been defined so that the hub-height wind speed is approximately equal to the farm-layer-averaged speed (Kirby *et al.* 2022). For the four farms simulated by Wu & Porté-Agel (2017), this assumption gives an overestimation on the order of 10% (table 1).

Dividing by the initial momentum supply M_{F0} gives:

$$\frac{\Delta M_{F,Advection}}{M_{F0}} + \frac{\Delta M_{F,PGF}}{M_{F0}} = \frac{\frac{1}{2}\rho U_{F0}^2 H_F W \left(1-\beta^2\right)}{\tau_{w0} L W} = \frac{1}{C_{f0}} \frac{H_F}{L} \left(1 - \beta^2\right). \tag{3.13}$$

Although this is an approximation, equation 3.13 shows that when advection and PGF terms are combined, the dependence on farm inlet and outlet velocities disappears. Interestingly, this suggests that the impact of farm-scale flows may not directly depend on the wind speed at the front of the farm.

3.3. *Turbulent entrainment*

Wind farms increase the turbulent mixing within the ABL. This increases the momentum entrainment into the farm (Stevens & Meneveau 2017). This mechanism supplies momentum to the control volume through the shear stress at the top surface. $\Delta M_{F,Entrainment}$ can be expressed as

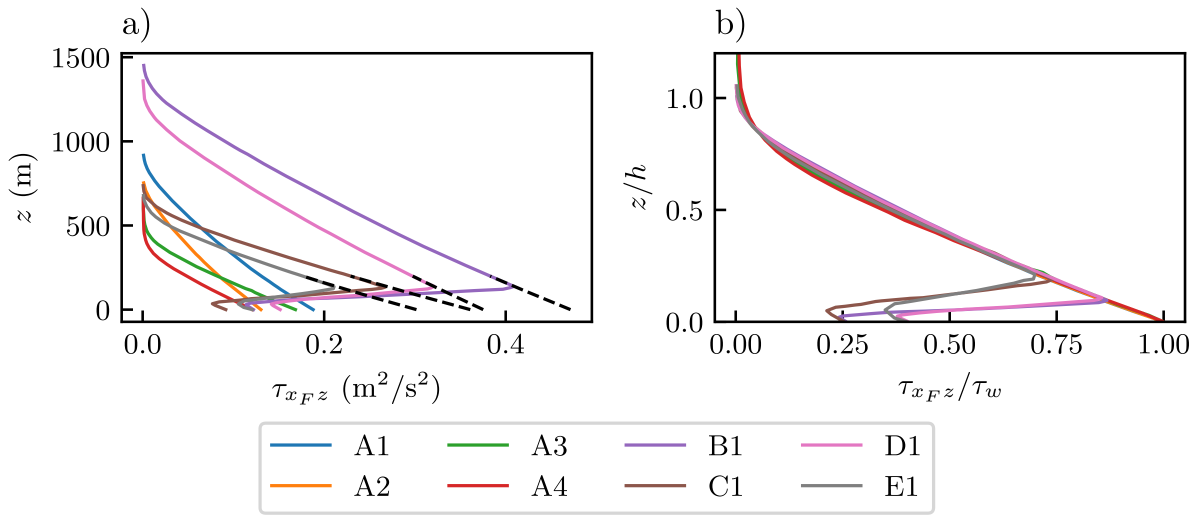

Figure 3: a) Vertical profiles of shear stress from horizontally periodic LES with and without the farm present (Abkar & Porté-Agel 2013) b) normalised vertical profiles.

$$\frac{\Delta M_{F,Entrainment}}{M_{F0}} = \frac{\tau_t LW - \tau_{t0} LW}{\tau_{w0} LW} = \frac{\tau_t - \tau_{t0}}{\tau_{w0}} \tag{3.14}$$

where τ_t is the shear stress at the top of the control volume.

The ABL can be stratified with different profiles of potential temperature which can change farm performance (Porté-Agel *et al.* 2020). In this study we consider conventionally neutral boundary layers (CNBLs) because many wind farm LES studies adopted ABLs with these profiles. CNBLs have self-similar vertical shear stress profiles (Liu *et al.* (2021)). Therefore, if the surface stress and the boundary layer height are known, then the shear stress at any height can be determined. Note that the height is normalised by $h = h_{0.05}/(1 - 0.05^{2/3})$ where $h_{0.05}$ is the height where the shear stress is 5% of the surface value.

The self-similarity of shear stress profiles can also be applied to large wind farms. Abkar & Porté-Agel (2013) performed horizontally periodic LES of CNBLs with and without turbines present. Figure 3a shows the vertical profiles of the shear stress (note this is the stress in the hub-height wind direction, x_F). Above the turbine top tip (126.5m in Abkar & Porté-Agel (2013)) the vertical profiles have a similar shape. This suggests that the stress profiles above the turbines is equivalent to an 'empty' CNBL with a higher surface stress.

The black dotted lines in figure 3a show the stress profiles above the turbines extrapolated to the surface (using a second order polynomial regression). This corresponds to the total bottom stress, i.e., surface shear stress and turbine thrust. When the stress profiles of Abkar & Porté-Agel (2013) are normalised by the total bottom stress and new ABL height, they fall onto the same curve (figure 3b). This shows that the CNBLs containing wind farms also follow approximately the same self-similar shear stress profile. Figure 3b shows that wind farms increase the total bottom stress and boundary layer height of CNBLs.

The self-similarity of stress profiles can be used to predict momentum entrainment into large finite-sized wind farms. As a first order approach, we consider the vertical shear stress profile horizontally-averaged across the farm. Figure 4 shows a schematic of the shear stress profile with and without the farm present. Here, h is the ABL height with the farm present averaged across the farm site. With the farm present, the shear stress is scaled by M and the heights scaled by h/h_0.

To determine τ_t, we need to calculate the undisturbed shear stress at a height of $H_F h_0/h$

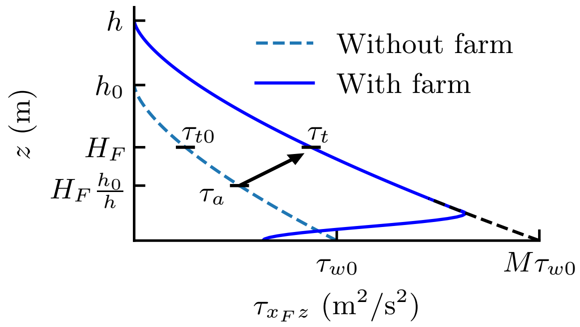

Figure 4: Schematic of vertical shear stress profiles with and without the wind farm.

(denoted as τ_a). This is found by linearly interpolating the stress between the top of the control volume and the surface, i.e.,

$$\tau_a = \tau_{w0} - (\tau_{w0} - \tau_{t0})\frac{h_0}{h}. \tag{3.15}$$

Whilst the shear stress profile is not strictly linear, it is approximately linear away from the top of the ABL. τ_t can then be expressed in terms of M and the undisturbed shear stress profile

$$\tau_t = M\tau_a = M\left(1 - \frac{h_0}{h}\right)\tau_{w0} + M\frac{h_0}{h}\tau_{t0}. \tag{3.16}$$

Equation 3.16 can be substituted into equation 3.14 to calculate $\Delta M_{F,Entrainment}$,

$$\frac{\Delta M_{F,Entrainment}}{M_{F0}} = \frac{(\tau_t - \tau_{t0})LW}{\tau_{w0}LW} = M + M\frac{h_0}{h}\left(\frac{\tau_{t0}}{\tau_{w0}} - 1\right) - \frac{\tau_{t0}}{\tau_{w0}}. \tag{3.17}$$

The different sources of momentum increase can be summed to calculate M. Subsituting equations 3.13 and 3.17 into 3.1 we obtain

$$M = 1 + \frac{1}{C_{f0}}\frac{H_F}{L}\left(1 - \beta^2\right) + M + M\frac{h_0}{h}\left(\frac{\tau_{t0}}{\tau_{w0}} - 1\right) - \frac{\tau_{t0}}{\tau_{w0}} \tag{3.18}$$

which can be rearranged to give

$$M = \frac{1 + \frac{1}{C_{f0}}\frac{H_F}{L}\left(1 - \beta^2\right) - \frac{\tau_{t0}}{\tau_{w0}}}{\frac{h_0}{h}\left(1 - \frac{\tau_{t0}}{\tau_{w0}}\right)}. \tag{3.19}$$

Using equation 3.1 we can simply sum the different sources of momentum increase. The result is a single equation to model the impact of farm-scale flows on farm performance. Equation 3.19 is an approximate expression for M as a function of β and h/h_0. Different models could be used to predict h/h_0 in this formula for M. In the next section we present a simple first order model for h/h_0 as a function of β.

3.4. *Boundary layer height increase*

In this section we present a simple model for increase in ABL height h/h_0 in response to a wind farm. We use a quasi-1D analysis of a boundary layer flow over a farm (see figure

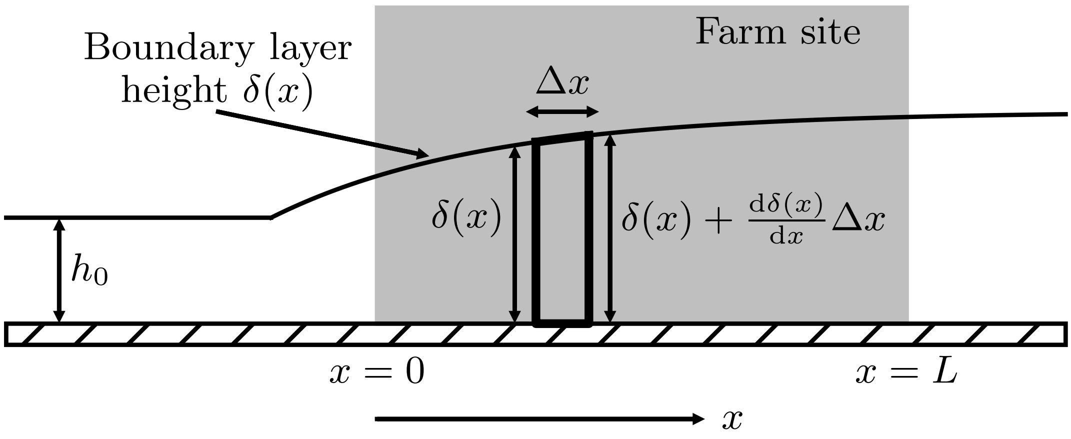

Figure 5: Quasi-1D control volume analysis for ABL flow over a wind farm.

5). Here $\delta(x)$ is the ABL height at steamwise position x. We assume there is no mass flux between the boundary layer and free atmosphere above. The quasi-1D approach neglects the effect of flow bypassing around the sides of the farm.

We consider the conservation of mass across a control volume encompassing a section of the ABL (in bold in figure 5). The velocity averaged over the height of the ABL at position x is denoted $U_A(x)$. We assume that the streamwise variation of $U_A(x)$ is the same as the streamwise variation of $\beta_{local}(x)$. This is strictly not true, but could give a reasonable first-order approximation of $U_A(x)$. Therefore $U_A(x) = U_{A0}\beta_{local}(x)$ where U_{A0} is the velocity averaged throughout the undisturbed ABL. The mass flux in through the left hand side of the control volume is given by:

$$\dot{m}_{in} = \rho U_{A0}\beta_{local}(x)\delta(x)W. \tag{3.20}$$

Taking the limit as Δx approaches 0, the mass flux out of the right hand side is given by:

$$\begin{aligned}
\dot{m}_{out} &= \rho\left[U_{A0}\beta_{local}(x) + U_{A0}\frac{d\beta_{local}(x)}{dx}dx\right]\left[\delta(x) + \frac{d\delta(x)}{dx}dx\right]W \\
\dot{m}_{out} &= \rho U_{A0}\beta_{local}(x)\delta(x)W + \rho U_{A0}\beta_{local}(x)\frac{d\delta(x)}{dx}dxW + \\
&\quad \rho U_{A0}\frac{d\beta_{local}(x)}{dx}dx\delta(x)W
\end{aligned} \tag{3.21}$$

whilst neglecting second order terms. From the mass conservation, $\dot{m}_{in} = \dot{m}_{out}$,

$$\begin{aligned}
\rho U_{A0}\beta_{local}(x)\frac{d\delta(x)}{dx}W &= -\rho U_{A0}\delta(x)\frac{d\beta_{local}(x)}{dx}W \\
\frac{\frac{d\delta(x)}{dx}}{\delta(x)} &= -\frac{\frac{d\beta_{local}(x)}{dx}}{\beta_{local}(x)}.
\end{aligned} \tag{3.22}$$

Both sides of equation 3.22 can be integrated from far upstream to a given position, resulting in

$$\delta(x) = \frac{h_0}{\beta_{local}(x)} \tag{3.23}$$

	$\Gamma = 1K/km$		$\Gamma = 5K/km$	
	Staggered	Aligned	Staggered	Aligned
$1/\beta$	1.250	1.200	1.349	1.281
$\frac{1}{L}\int_0^L \frac{\mathrm{d}x}{\beta_{local}(x)}$	1.253	1.202	1.354	1.285
Percentage error	0.244%	0.160%	0.414%	0.248%

Table 2: Percentage errors of approximation in equation 3.24 using data from Wu & Porté-Agel (2017)

using the condition that at far upstream $\delta(x) = h_0$ and $\beta_{local}(x) = 1$. To find h, $\delta(x)$ is averaged between $x = 0$ and $x = L$ (as h is the ABL height averaged across the wind farm site):

$$\frac{h}{h_0} = \frac{1}{L}\int_0^L \frac{\mathrm{d}x}{\beta_{local}(x)} \approx \frac{1}{\beta} \tag{3.24}$$

where the relationship between β and $\beta_{local}(x)$ is given by $\beta = \int_0^L \beta_{local}(x)\mathrm{d}x$. If $\beta_{local}(x)$ is constant, the left hand side of equation 3.24 is equal to $1/\beta$, which we assume to be generally true. In reality, the more $\beta_{local}(x)$ varies the less accurate this assumption becomes. If $\beta_{local}(x)$ is close to zero at any point the approximation in equation 3.24 becomes less accurate. To check the validity of this assumption, we again use the LES data from Wu & Porté-Agel (2017). For the four farms simulated by Wu & Porté-Agel (2017), the maximum error of this assumption was about 0.4% (table 2). Therefore the approximation is reasonable for realistic profiles of $\beta_{local}(x)$.

The derivation of equation 3.24 neglects horizontal flow deflections around the farm. This assumption is reasonable so long as the mass flux through the top surface of the farm control volume is much greater than through the sides. The mass flux through the top surface is given by ρwLW (where w is the average vertical velocity through the top surface). The mass flux through the side surfaces is given by $2\rho vLH_F$ (where v is the average lateral velocity at the side surfaces). If we suppose that v and w are of similar magnitudes, then neglecting horizontal deflections is reasonable so long as $W >> H_F$ (i.e. $2.5H_{hub}$).

Substituting equation 3.24 into equation 3.19, we get the following expression for M

$$M = \frac{1 + \frac{1}{C_{f0}}\frac{H_F}{L}\left(1-\beta^2\right) - \frac{\tau_{t0}}{\tau_{w0}}}{\beta\left(1 - \frac{\tau_{t0}}{\tau_{w0}}\right)}. \tag{3.25}$$

Equation 3.25 is a single algebraic equation to predict the impact of farm-scale flows on farm performance. It includes the effects of net advection, PGF and turbulent entrainment. The only environmental parameter needed is the undisturbed shear stress profile. Equation 3.25 can be used with the two-scale momentum theory to predict farm power. In section 4 we compare the predictions of farm power output with the results from finite wind farm LES reported in the literature.

4. Comparison with finite wind farm LES

The two-scale momentum theory presented in section 2 can be used to predict wind farm power. For arrays of actuator-discs (or aerodynamically ideal turbines operating below the rated wind speed), $C_p^* = \alpha C_T^*$ where $\alpha \equiv U_T/U_F$ (U_T is the streamwise velocity averaged over the rotor swept area). We can estimate α using the expresion $\alpha = \sqrt{C_T^*/C_T'}$ where $C_T' \equiv T_i/\frac{1}{2}\rho U_{T,i}^2 A$ is a turbine resistance coefficient describing the turbine operating conditions (note that this is strictly valid only for infinitely large regular arrays of turbines where the thrust of each individual turbine is identical to farm-averaged turbine thrust). The C_p of an actuator disc is therefore given by

$$C_p = \beta^3 C_p^* = \beta^3 C_T^{*\,\frac{3}{2}} C_T'^{\,-\frac{1}{2}}. \tag{4.1}$$

Note that, when considering an isolated turbine, C_T' is related to the classic turbine thrust coefficient by the relation $C_T' = C_T/(1-a)^2$ (where a is the turbine induction factor). C_T^* generally depends on the turbine layout, but its upper limit may be predicted by using an analogy to the classical actuator-disc theory (Nishino 2016), as

$$C_T^* = \frac{16C_T'}{(4+C_T')^2}. \tag{4.2}$$

Note that equation 4.2, like the classical actuator disc theory, is only valid for induction factors of up to 0.5. Since this model predicts an upper limit of C_T^* for a given C_T', it can be used to predict an upper limit to farm performance (Kirby *et al.* 2022). Using this model with $\beta = 1$, the power coefficient of an isolated turbine $C_{p,Betz}$ can also be retrieved as

$$C_{p,Betz} = \frac{64C_T'}{(4+C_T')^3}. \tag{4.3}$$

It is important to note that equations 4.1 and 4.2 are only strictly valid when $U_{T,i}$ is the same for all turbines. However, in this study we only consider wind farms in which C_T' is the same for all turbines, and in this case, equations 4.1 and 4.2 can be applied in an approximate manner even when $U_{T,i}$ varies throughout the farm.

We used the new model of M (equation 3.25) with the two-scale momentum theory (equation 2.1) with $\gamma = 2$ to predict wind farm power, i.e., solving

$$\left(C_T^* \frac{\lambda}{C_{f0}} + 1\right)\beta^2 = \frac{1 + \frac{1}{C_{f0}}\frac{H_F}{L}\left(1-\beta^2\right) - \frac{\tau_{t0}}{\tau_{w0}}}{\beta\left(1 - \frac{\tau_{t0}}{\tau_{w0}}\right)} \tag{4.4}$$

for β, which is then substituted into equation 4.1 to calculate C_p. The definitions of C_p, C_T^* and C_T' are summarised in table 3.

We compared the predictions against finite wind farm LES results from Wu & Porté-Agel (2017), Allaerts & Meyers (2017) and Lanzilao & Meyers (2022). We selected these studies because they simulated large wind farms (longer than 15km in the streamwise direction). They published the undisturbed vertical shear stress profile which is a required input to the model of M. These studies were also selected because the results are normalised by the power of an isolated turbine rather than the front row turbine power. The 3 studies performed LES of 4 farms with staggered turbine layouts and 6 farms with aligned layouts.

Kirby *et al.* (2022) reported that C_T^* varied with turbine layout due to turbine-wake interactions. The upper limit of C_T^* was predicted well by equation 4.2. Staggered layouts will tend to have C_T^* values close to this upper limit; hence, equations 4.2 and 4.4 can be used to predict their C_p and give a direct comparison with staggered wind farm LES. Kirby *et al.* (2022) also showed that turbine wake interactions could reduce C_T^* by up to about 20% depending on turbine spacings and wind direction. However, the effect of turbine spacing

Symbol	Name	Formula	Note
C_p	Average turbine power coefficient	$\frac{\sum_{i=1}^{n} P_i}{\frac{1}{2}\rho U_{F0}^3 nA}$	U_{F0} is the undisturbed farm-layer-averaged wind speed.
C_p^*	Average 'internal' turbine power coefficient	$\frac{\sum_{i=1}^{n} P_i}{\frac{1}{2}\rho U_F^3 nA}$	U_F is the farm-layer-averaged wind speed with the turbines present.
C_T'	Turbine resistance coefficient	$\frac{T_i}{\frac{1}{2}\rho U_{T,i}^2 A}$	U_T is the wind speed averaged over the rotor swept area.
C_T^*	Average 'internal' turbine thrust coefficient	$\frac{\sum_{i=1}^{n} T_i}{\frac{1}{2}\rho U_F^2 nA}$	Determined by turbine operating conditions and layout.

Table 3: Summary of turbine power and thrust coefficients.

on C_T^* was not studied explicitly for any specific wind direction; therefore, we cannot make a direct comparison with LES of aligned layouts. Nonetheless, we used a 20% reduced C_T^* value to predict a lower limit to C_p (with the largest turbine-scale loss expected for aligned layouts with a small turbine spacing). This allows a qualitative comparison with LES of aligned wind farms, showing whether our model can correctly capture the observed trends of farm performance under different ABL conditions.

We used the analytical model to predict the farm-averaged power normalised by the isolated turbine power, i.e., $C_p/C_{p,Betz}$. Allaerts & Meyers (2017) and Lanzilao & Meyers (2022) used an actuator-disc no rotation model for the turbines with $C_T' = 1.33$. For these studies we used C_T^* from the actuator-disc theory (equation 4.2) as an upper limit for C_T^* in 4.4 and then used the expression $C_p/C_{p,Betz} = \beta^3$. For this C_T' value, the actuator-disc theory gives $C_T^* = 0.75$. Wu & Porté-Agel (2017) used an actuator-disc with rotation implementation for the turbines. As the value of C_T' was unknown, we used the published thrust coefficient curves (Wu & Porté-Agel 2015) to find an upper limit to C_T^*. For the lower limit, we used a 20% reduced C_T^* value in equation 4.4 and then the expression $C_p/C_{p,Betz} = \beta^3 0.8^{1.5}$ (assuming that C_T' is unaffected by the turbine layout). Note that this expression comes from equation 4.1 using a C_T^* value which is 80% of the upper limit.

Lanzilao & Meyers (2022) normalised the turbine power by the power of an imaginary turbine row 10km upstream of the farm. However, small reductions in wind speed were observed 10km upstream for the stratified boundary layer. We instead normalised farm powers from this study by the imaginary upstream power for the neutrally stratified case. This is because the neutrally stratified case had a much smaller reduction in wind speed upstream of the farm. The imaginary upstream turbine power of the staggered and aligned farms in the stratified boundary layer were 6.24MW and 6.17MW respectively (Lanzilao 2023). For the staggered farm in the neutrally stratified case it was 6.61MW (Lanzilao 2023).

A summary of comparisons between the model predictions and LES is shown in figure 6. Generally, the staggered LES results are close to the upper limits predicted by the two-scale model. The aligned layouts are close to the lower limit of the predictions, except for the results from Γ1 in Wu & Porté-Agel (2017) where the LES power is higher than the model predictions. The analytical model predicts well the decrease in farm performance with decreasing capping inversion layer height (1000m, 500m and 250m for cases S1, S2 and S4,

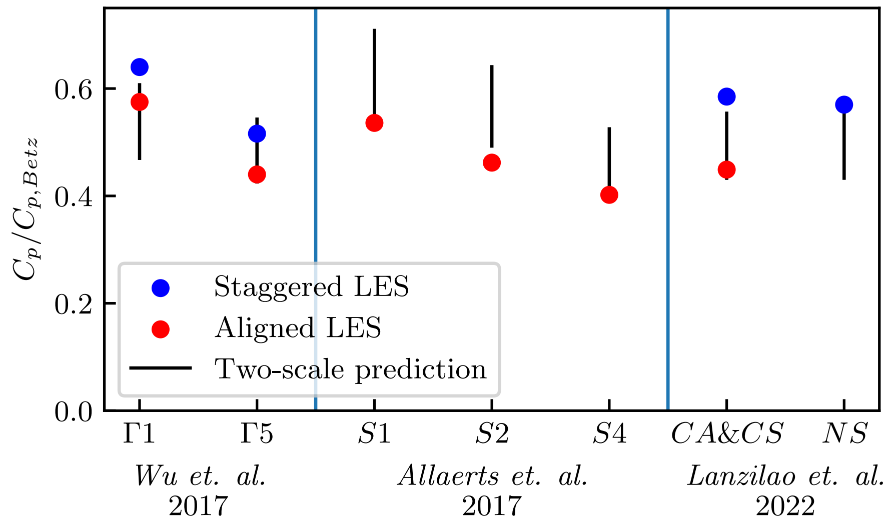

Figure 6: Comparison of farm-average performance predicted by the two-scale model and results from LES. The upper end of each black line corresponds to the upper limit of farm performance predicted by the two-scale model (i.e., without 'turbine-scale loss') whereas the lower end corresponds to the lower limit predicted assuming that the turbine-wake interaction causes a 20% reduction of C_T^*.

	Wu et. al. 2017		*Lanzilao et. al.* 2022	
	$\Gamma = 1K/km$	$\Gamma = 5K/km$	CS	NS
λ	0.0160	0.0160	0.0314	0.0314
C_{f0}	0.00557	0.00501	0.00314	0.00314
H_F/L	0.00875	0.00875	0.0188	0.0188
τ_{t0}/τ_{w0}	0.571	0.391	0.475	0.475
β_{model}	0.847	0.816	0.821	0.821
M_{model}	2.41	2.40	5.74	5.74
$C_{p,model}/C_{p,Betz}$	0.607	0.543	0.554	0.544
$C_{p,LES}/C_{p,Betz}$	0.639	0.521	0.585	0.570
$(C_{p,model} - C_{p,LES})/C_{p,LES}$	-5.00%	4.33%	-5.39%	-2.87%
$(C_{p,model} - C_{p,LES})/C_{p,Betz}$	-3.20%	2.25%	-3.15%	-1.63%

Table 4: Model parameters and percentage errors in predicting the average power of staggered wind farm LES.

respectively) observed by Allaerts & Meyers (2017). For the results of Lanzilao & Meyers (2022), the staggered wind farms had very similar performances in the neutral (NS) and conventionally neutral (CS) boundary layers. The two-scale predictions are exactly the same for these two cases because the shear stress profiles were identical.

Note that we made direct comparisons between the two-scale model predictions (without turbine-scale losses) and LES for staggered layouts because these layouts are close to 'optimal' and give a C_T^* value close to the theoretical value given by equation 4.2 (irrespective of turbine spacing). For the aligned layouts, the exact value of C_T^* depends on turbine spacing and therefore a direct comparison is not currently possible. Table 4 shows the percentage error in farm power predicted for the four staggered farms. When normalised by the farm power predicted by LES, the error was typically around 5% or less. Normalising by the isolated turbine power predicted theoretically gave errors of around 3% or less.

5. Discussion

This study proposes a novel framework for modelling farm-atmosphere interactions. Equation 3.1 is a general expression for the farm momentum increase as the sum of contributions from different mechanisms. This allows each mechanism to be modelled separately. In this study we considered contributions from net momentum advection (including farm blockage), PGF and entrainment. Equation 3.1 could provide a framework for combining different or improved models of each mechanism in the future.

We have proposed simple analytical models for each mechanism increasing farm momentum supply. The models make quasi-1D and steady flow assumptions. The simple momentum availability factor model can be coupled with the two-scale momentum theory to predict farm power. The predictions for staggered farms had a typical error of around 5% or less. The model predictions are for the average power of a finite-sized farm rather than just the power in the fully developed region, i.e., the model captures the effect of the development region and the farm size.

The only environmental parameter required as an input to the model is the undisturbed vertical shear stress profile of the ABL. The model seems to capture most of the impact of ABL height. The proposed model also considers the effect of farm blockage (or the reduction of wind speed upstream of the farm) as part of the advection modelling. This is a physics-based approach to instantly predicting the power of a finite-sized farm without tuning or empirical coefficients.

Our model derivation suggests the effects of farm blockage and increased PGF could (at least partly) counteract. Note that this is a direct result of our assumption that the pressure changes at the front and rear of the farm are of equal magnitude. A strong free-atmosphere stratification reduces the wind speed in front of the farm (Wu & Porté-Agel 2017; Lanzilao & Meyers 2022). This reduces the net advection of momentum into the farm. When this occurs, an additional pressure gradient tends to be induced across the farm, which increases the momentum supply to the farm. This suggests the negative effect of farm blockage on the farm power could be somewhat counteracted by the increased PGF. The extent to which these effects counteract will likely depend on atmospheric conditions. For cases NS and CS in Lanzilao & Meyers (2022), the atmospheric conditions are kept constant except for the free-atmosphere stratification. The CNBL case (CS) showed a much greater farm blockage yet both cases had a similar farm-averaged power, supporting the above argument. The very recent LES study of Lanzilao & Meyers (2023) also suggests farm blockage often occurs with an increased PGF. However, the degree to which these effects counteract remains unclear. Hence, the relationship between farm blockage and PGF seems important and requires further investigation in the future.

Our model can provide physical insight into how farm efficiency changes with atmospheric conditions. Figure 7 shows the predicted values of M and β for the LES studies considered. The model predicts an approximately linear relationship between M and β for a given atmospheric condition, as observed previously by Patel *et al.* (2021). The linear relationship is further explained in appendix A. For the results of Allaerts & Meyers (2017), S1 had the highest initial inversion layer and S4 the lowest. Figure 7 shows that the momentum increase (or the value of M) is relatively insensitive to the initial inversion layer height. However, to achieve a certain momentum increase, a lower inversion layer has a greater wind speed reduction (i.e. a larger value of $(1-\beta)$ in figure 7). The lower wind speed results in S4 having a lower farm efficiency than S1 (see figure 6).

A thicker ABL can increase the farm momentum supply with a smaller wind speed reduction. To illustrate this, we consider the momentum response of two ABLs; a thin ABL (with $H_F/h_0 = 0.75$) and a thick ABL (with $H_F/h_0 = 0.25$). For both ABLs we use a typical

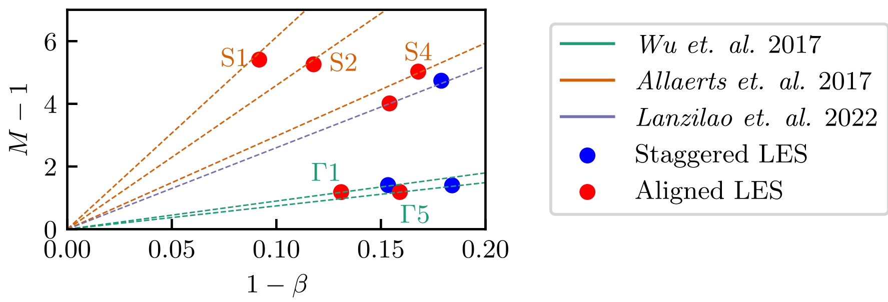

Figure 7: Predicted values of momentum availability factor (M) and farm wind-speed reduction factor (β). β is calculated using equation 4.4 and M using equation 3.25 for the flow conditions and farm configuration used in the LES. Note that the lines are calculated using equation A 5.

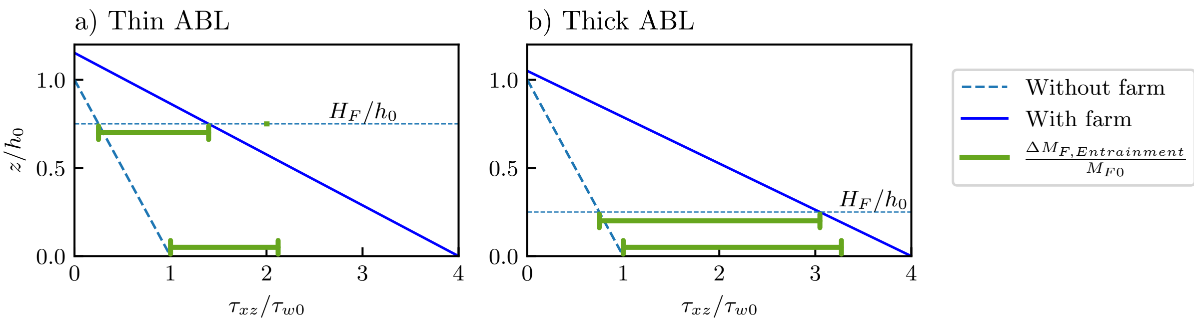

Figure 8: Contribution of entrainment to farm momentum availability factor M for a) thin initial ABL and b) thick initial ABL.

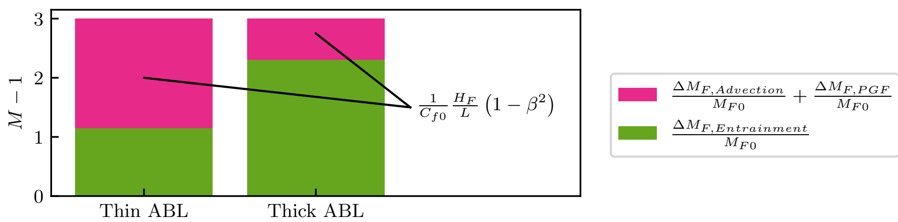

Figure 9: Decomposition of farm momentum availability factor M into entrainment, and advection and PGF terms for a) a thin initial ABL and b) a thick initial ABL. Note that the heights of green bars in this figure correspond to the width of green bars in figure 8.

value for large offshore farms of $\frac{1}{C_{f0}}\frac{H_F}{L} = 7.5$ and set $M = 4$ (which physically means that the 'internal' conditions of the farm are adjusted to achieve $M = 4$). The value of β can be calculated using equation 3.25 for both scenarios. The new and undisturbed shear stress profiles are shown in figure 8. The thin ABL has a smaller entrainment of momentum at the top of the control volume. The top of the control volume is closer to the top of the boundary layer where the velocity shear is lower. Therefore the thin ABL is less efficient at entraining momentum into the farm. With less momentum entrainment, more momentum has to be supplied through advection and PGF in order to achieve the set level of M (see figure 9). These mechanisms increase the momentum supply by reducing the farm-averaged wind speed (equation 3.13). In thicker ABLs, more momentum is supplied to the farm through entrainment, and the advection and PGF supply less momentum. Thicker ABLs can therefore sustain higher wind speeds in the farm and thus have a higher farm efficiency.

This study only presents a preliminary comparison with wind farm LES. To fully validate the proposed model, a comparison with a larger set of LES would be required which will be the focus of future work. A comparison of model predictions with field observations (such as SCADA data) could also be investigated in future studies. A limitation of the proposed model is that the quasi-1D analysis captures only the first-order effects. However, the model still gave a close agreement with LES results. More detailed flow physics were not considered explicitly (e.g. gravity wave excitation) but could be included in future studies. Future work will also aim to predict C_T^* for different turbine layouts and operating conditions. As an example, Legris *et al.* (2023) and Kirby *et al.* (2023) used a wake model to predict C_T^* for different farm designs. Future studies will also focus on the farm-atmosphere interaction under more realistic atmospheric conditions.

It should also be noted that, in reality, the assumption of scale separation is not expected to be strictly valid. The entrainment of momentum into the wind farm could depend on the exact turbine layout and not just the farm-average wind speed reduction. Therefore, to capture higher-order effects, the entrainment component of the model may need some parameters that depend on the internal (turbine-scale) conditions.

6. Conclusions

In this study, we proposed an analytical model of the momentum availability factor for large wind farms. This is a simple model to instantly predict the impact of farm-scale flows on farm performance. This study considered changes in net advection, PGF and turbulent entrainment as the factors contributing to the momentum availability. We derived the model using a steady quasi-1D control volume analysis and assuming self-similar vertical shear stress profiles. The only environmental parameters required as input to the model are the undisturbed vertical shear stress profiles. We used the new model with the two-scale momentum theory (Nishino & Dunstan 2020) to predict large farm power production. The model compared well with existing LES of finite wind farms in CNBLs. The model captured the impact of ABL height and farm size on farm performance. A direct comparison with LES of staggered farms showed a typical error of 5% or less.

This study also provides a new framework for modelling farm-atmosphere interactions. The momentum availability factor is expressed as the sum of contributions from different physical mechanisms. As such, the different mechanisms can be modelled separately. We used first-order analytical models for the different components. Despite the simplicity, the model predicts farm power with close agreement to finite wind farm LES. Only one algebraic equation needs to be solved analytically to calculate the farm wind-speed reduction factor β and thus predict farm performance. It also provides a physics-based method to predict farm blockage effects and the impact of ABL height. Future studies could use more advanced models for the different components of the momentum availability factor. This could provide more accurate predictions of wind farm power production.

Acknowledgements. The first author (AK) acknowledges the NERC-Oxford Doctoral Training Partnership in Environmental Research (NE/S007474/1) for funding and training. We also thank Mr. Luca Lanzilao, Prof. Johan Meyers and Prof. Richard Stevens for providing additional data from their studies.

Funding. This work was supported by the Natural Environmental Research Council (NERC) award NE/S007474/1.

Declaration of Interests. The authors report no conflict of interest.

Author ORCID. A. Kirby, https://orcid.org/0000-0001-8389-1619; T. Nishino, https://orcid.org/0000-0001-6306-7702.

Author contributions. A.K. and T.N. derived the analytical model. A.K. made a comparison of the model and existing LES results in the literature, and A.K. wrote the paper with corrections from T.N. and T.D.D.

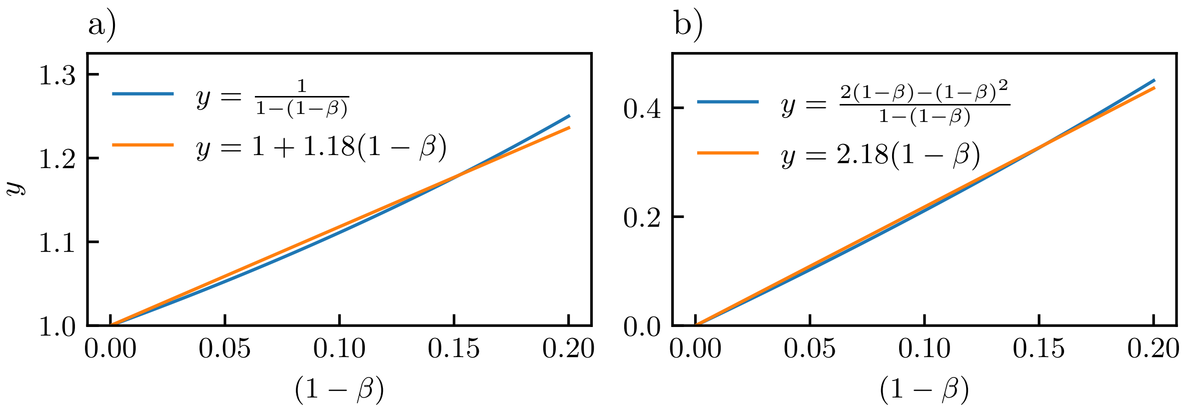

Figure 10: Linear approximations for terms a) $\frac{1}{1-(1-\beta)}$ and b) $\frac{2(1-\beta)-(1-\beta)^2}{1-(1-\beta)}$ in M expression (equation A 3).

Appendix A. Approximate expression for wind extractability factor ζ

Patel *et al.* (2021) used twin NWP simulations to calculate M for a realistic wind farm site. They found, for most cases, that M varied almost linearly with the farm induction factor $(1-\beta)$. As such, M can be modelled as

$$M = 1 + \zeta(1-\beta) \tag{A 1}$$

where ζ is the 'wind extractability factor' (which is identical to what Nishino & Dunstan (2020) originally proposed as 'momentum response factor'). Kirby *et al.* (2022) reported that ζ varied with atmospheric conditions and decreased exponentially with wind farm size. The analytical model of M developed in this study can be used to derive an approximate expression for ζ, as the equation 3.25 can be expressed as

$$M = \frac{1}{\beta} + \frac{\frac{1}{C_{f0}}\frac{H_F}{L}}{1-\frac{\tau_{t0}}{\tau_{w0}}}\frac{(1-\beta)(1+\beta)}{\beta}. \tag{A 2}$$

This can than be expressed in terms of farm induction factor $(1-\beta)$, e.g.,

$$M = \frac{1}{1-(1-\beta)} + \frac{\frac{1}{C_{f0}}\frac{H_F}{L}}{1-\frac{\tau_{t0}}{\tau_{w0}}}\frac{2(1-\beta)-(1-\beta)^2}{1-(1-\beta)}. \tag{A 3}$$

The functions of $(1-\beta)$ in equation A 3 are approximately linear for a realistic range of $(1-\beta)$ (see figure 10). The analytical model of M (equation 3.25) developed in this study therefore predicts the quasi-linear momentum response observed in NWP simulations. We use linear interpolation for $(1-\beta)$ between 0 and 0.2 (a realistic range) to find linear approximations to the functions of $(1-\beta)$. As such M can be approximated by:

$$M_{approx} = 1 + 1.18(1-\beta) + \frac{\frac{2.18}{C_{f0}}\frac{H_F}{L}}{1-\frac{\tau_{t0}}{\tau_{w0}}}(1-\beta). \tag{A 4}$$

Equation A 4 can be used to derive an approximate expression for ζ, i.e.,

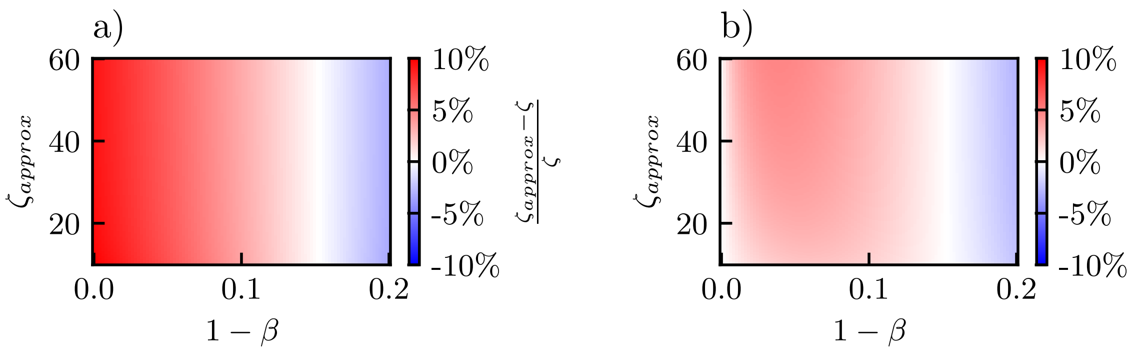

Figure 11: Percentage error of a) ζ_{approx} and b) M_{approx}.

$$\zeta_{approx} = 1.18 + \frac{\frac{2.18}{C_{f0}}\frac{H_F}{L}}{1-\frac{\tau_{t0}}{\tau_{w0}}} \tag{A 5}$$

using the expression $\zeta = (M-1)/(1-\beta)$. Equation A 5 predicts the inverse relationship of ζ with farm size reported by Kirby *et al.* (2022). This expression can be further simplified by assuming that the vertical shear stress profile is linear up to the boundary layer height (as assumed in the discussion of figure 8 earlier). The expression for ζ_{approx} then becomes

$$\zeta_{approx} = 1.18 + \frac{2.18h_0}{C_{f0}L} \tag{A 6}$$

where we refer to L/h_0 as the farm size ratio.

The minimum value of ζ depends on the response of the ABL. If the ABL height is constant (i.e. with a rigid lid), then ζ tends to zero for an infinitely large farm. The minimum value of ζ is non-zero even for an infinitely large farm if the ABL height increases in response to the farm. Differentiating equation 3.25 (with $L=\infty$) gives

$$\zeta = \frac{\mathrm{d}(M-1)}{\mathrm{d}(1-\beta)} = \frac{1}{\beta^2} \tag{A 7}$$

which gives $\zeta = 1$ for $(1-\beta) = 0$ and $\zeta = 1.56$ for $(1-\beta) = 0.2$. Note that to derive equation A 6, we performed a linear regression for $0 < (1-\beta) < 0.2$, giving a minimum value of ζ_{approx} of 1.18. Therefore, the minimum value of ζ for realistic ABLs is expected to be 1.

The discrepancy between ζ_{approx} and the 'true' ζ (obtained without the linear approximations) is a function only of ζ_{approx} and $(1-\beta)$. Figure 11a shows the percentage error of ζ_{approx} for a realistic range of ζ_{approx} and $(1-\beta)$. The maximum error is approximately 10% and this occurs for low values of $(1-\beta)$. However, for low values of $(1-\beta)$, the value of M_{approx} is relatively insensitive to the value of ζ_{approx}. Figure 11b shows the percentage error of M_{approx} which is typically less than 5% for realistic farms.

Appendix B. Sensitivity of farm performance to farm length L

Depending on the farm layout, the streamwise farm length L could vary with wind direction. Hence, it is useful to know how the farm power changes with increasing the farm size ratio L/h_0. Equations 2.1, A 1 and A 6 are solved for β, which is then substituted into equation 4.1. The results are shown for a low surface roughness in figure 12a and a high roughness

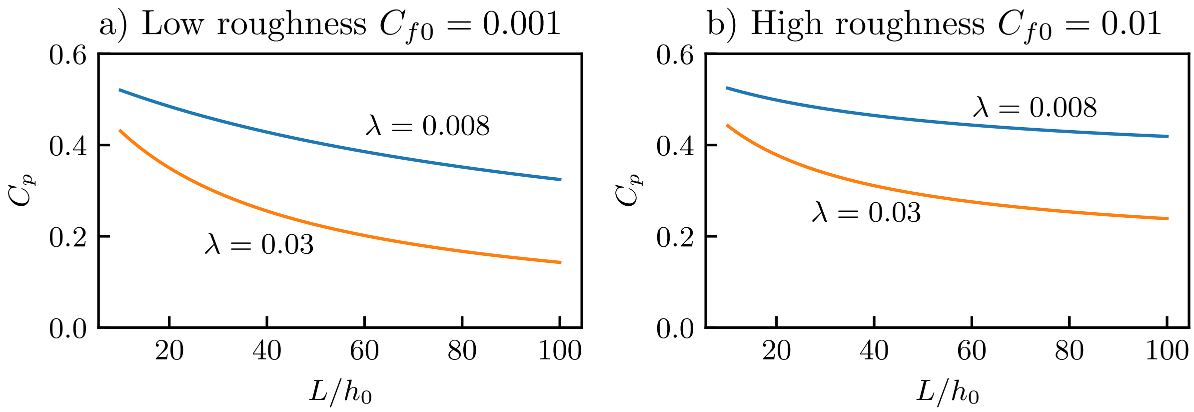

Figure 12: Sensitivity of farm-averaged power coefficient C_p to farm size ratio L/h_0 for low ($\lambda = 0.008$) and high ($\lambda = 0.03$) array densities for a) low and b) high surface roughness values, for a fixed turbine resistance coefficient of $C_T' = 1.33$.

in figure 12b. Note that the results in figure 12 are for a C_T' value of 1.33 and C_T^* calculated using 4.2. L/h_0 varies from 10 to 100, corresponding to a 10km long farm in a 1km ABL height, up to 30km long farm in a 300m ABL height, for example. Figure 12 shows results for farms with both a high array density ($\lambda = 0.03$) and a low density ($\lambda = 0.008$). This corresponds to farms with average turbine spacings of $5D$ and $10D$ respectively.

Figure 12 shows that, for all scenarios, the farm power decreases with increasing the farm length. The farm power is most sensitive to the farm length for small farm size ratios (i.e. shorter wind farms or thicker ABLs). This suggests that as wind farms become larger, the performance could become less sensitive to wind direction. It should also be noted that the farm power is generally higher when the surface roughness is higher, even though the wind extractability factor decreases as the surface roughness increases (equation A 6). This is because the effective array density λ/C_{f0} decreases as the surface roughness increases (Nishino & Dunstan 2020).

REFERENCES

Abkar, M. & Porté-Agel, F. 2013 The effect of free-atmosphere stratification on boundary-layer flow and power output from very large wind farms. *Energies* **6**, 2338–2361.

Allaerts, D. & Meyers, J. 2017 Boundary-layer development and gravity waves in conventionally neutral wind farms. *Journal of Fluid Mechanics* **814**, 95–130.

Allaerts, D. & Meyers, J. 2018 Gravity waves and wind-farm efficiency in neutral and stable conditions. *Boundary-Layer Meteorology* **166**, 269–299.

Allaerts, D. & Meyers, J. 2019 Sensitivity and feedback of wind-farm-induced gravity waves. *Journal of Fluid Mechanics* **862**, 990–1028.

Bastankhah, M. & Porté-Agel, F. 2014 A new analytical model for wind-turbine wakes. *Renewable Energy* **70**, 116–123.

Bempedelis, N., Laizet, S. & Deskos, G. 2023 Turbulent entrainment in finite-length wind farms. *Journal of Fluid Mechanics* **955**, A12.

Calaf, M., Meneveau, C. & Meyers, J. 2010 Large eddy simulation study of fully developed wind-turbine array boundary layers. *Physics of Fluids* **22**, 1–16.

Devesse, K., Lanzilao, L., Jamaer, S., van Lipzig, N. & Meyers, J. 2022 Including realistic upper atmospheres in a wind-farm gravity-wave model. *Wind Energy Science* **7**, 1367–1382.

Frandsen, S. 1992 On the wind speed reduction in the center of large clusters of wind turbines. *Journal of Wind Engineering and Industrial Aerodynamics* **39**, 251–265.

Frandsen, S., Barthelmie, R., Pryor, S., Rathmann, O., Larsen, S., Højstrup, J. & Thøgersen, M. 2006 Analytical modelling of wind speed deficit in large offshore wind farms. *Wind Energy* **9**, 39–53.

Jensen, N. O. 1983 A note on wind generator interaction. *Risø-M-2411 Risø National Laboratory Roskilde* .

Katic, I., Hojstrup, J. & Jensen, N. O. 1986 A simple model for cluster efficiency. *Proceedings of the European wind energy association conference and exhibition, Rome, Italy* pp. 407–409.

Kirby, Andrew, Briol, François-Xavier, Dunstan, Thomas D & Nishino, Takafumi 2023 Data-driven modelling of turbine wake interactions and flow resistance in large wind farms. *Wind Energy* **26**, 968–984.

Kirby, A., Nishino, T. & Dunstan, T. D. 2022 Two-scale interaction of wake and blockage effects in large wind farms. *Journal of Fluid Mechanics* **953**, A39.

Lanzilao, L. 2023 personal communication.

Lanzilao, L. & Meyers, J. 2022 Effects of self-induced gravity waves on finite wind-farm operations using a large-eddy simulation framework. *Journal of Physics: Conference Series* **2265**, 22043.

Lanzilao, L. & Meyers, J. 2023 A parametric large-eddy simulation study of wind-farm blockage and gravity waves in conventionally neutral boundary layers. *arXiv* **2306.08633**.

Legris, L., Pahus, M. L., Nishino, T. & Perez-Campos, E. 2023 Prediction and mitigation of wind farm blockage losses considering mesoscale atmospheric response. *Energies* **16**.

Liu, L., Gadde, S. N. & Stevens, R. J. A. M. 2021 Universal wind profile for conventionally neutral atmospheric boundary layers. *Phys. Rev. Lett.* **126**, 104502.

Luzzatto-Fegiz, P. & Caulfield, C. P. 2018 Entrainment model for fully-developed wind farms: Effects of atmospheric stability and an ideal limit for wind farm performance. *Phys. Rev. Fluids* **3**, 93802.

Meneveau, C. 2012 The top-down model of wind farm boundary layers and its applications. *Journal of turbulence* **13**, N7.

Nishino, T. 2016 Two-scale momentum theory for very large wind farms. *Journal of Physics: Conference Series* **753**, 032054.

Nishino, T. & Dunstan, T. D. 2020 Two-scale momentum theory for time-dependent modelling of large wind farms. *Journal of Fluid Mechanics* **894**, A2.

Patel, K., Dunstan, T. D. & Nishino, T. 2021 Time-dependent upper limits to the performance of large wind farms due to mesoscale atmospheric response. *Energies* **14**, 6437.

Porté-Agel, F., Bastankhah, M. & Shamsoddin, S. 2020 Wind-turbine and wind-farm flows: A review. *Boundary-Layer Meteorology* **174**, 1–59.

Smith, R. B. 2010 Gravity wave effects on wind farm efficiency. *Wind Energy* **13**, 449–458.

Starke, G. M., Meneveau, C., King, J. R. & Gayme, D. F. 2021 The area localized coupled model for analytical mean flow prediction in arbitrary wind farm geometries. *Journal of Renewable and Sustainable Energy* **13**.

Stevens, R. J. A. M., Gayme, D. F. & Meneveau, C. 2016 Generalized coupled wake boundary layer model: applications and comparisons with field and les data for two wind farms. *Wind Energy* **19**, 2023–2040.

Stevens, R. J. A. M. & Meneveau, C. 2017 Flow structure and turbulence in wind farms. *Annual Review of Fluid Mechanics* **49**.

van Stratum, B., Theeuwes, N., Barkmeijer, J., van Ulft, B. & Wijnant, I. 2022 A one-year-long evaluation of a wind-farm parameterization in harmonie-arome. *Journal of Advances in Modeling Earth Systems* **14**, e2021MS002947, e2021MS002947 2021MS002947.

Veers, P., Dykes, K., Basu, S., Bianchini, A., Clifton, A., Green, P., Holttinen, H., Kitzing, L., Kosovic, B., Lundquist, J. K., Meyers, J., O'Malley, M., Shaw, W. J. & Straw, B. 2022 Grand challenges: wind energy research needs for a global energy transition. *Wind Energy Science* **7**, 2491–2496.

Veers, P., Dykes, K., Lantz, E., Barth, S., Bottasso, C. L., Carlson, O., Clifton, A., Green, J., Green, P., Holttinen, H., Laird, D., Lehtomäki, V., Lundquist, J. K., Manwell, J., Marquis, M., Meneveau, C., Moriarty, P., Munduate, X., Muskulus, M., Naughton, J., Pao, L., Paquette, J., Peinke, J., Robertson, A., Rodrigo, J. S., Sempreviva, A. M., Smith, J. C., Tuohy, A. & Wiser, R. 2019 Grand challenges in the science of wind energy. *Science* **366**, eaau2027.

Wu, K. L. & Porté-Agel, F. 2017 Flow adjustment inside and around large finite-size wind farms. *Energies* **10**, 2164.

Wu, Y. T. & Porté-Agel, F. 2015 Modeling turbine wakes and power losses within a wind farm using les: An application to the horns rev offshore wind farm. *Renewable Energy* **75**, 945–955.

Zong, H. & Porté-Agel, F. 2020 A momentum-conserving wake superposition method for wind farm power prediction. *Journal of Fluid Mechanics* **889**, A8.

4.1 Statement of authorship

Statement of Authorship for joint/multi-authored papers for PGR thesis

To appear at the end of each thesis chapter submitted as an article/paper

The statement shall describe the candidate's and co-authors' independent research contributions in the thesis publications. For each publication there should exist a complete statement that is to be filled out and signed by the candidate and supervisor **(only required where there isn't already a statement of contribution within the paper itself).**

Title of Paper	An analytical model of momentum availability for predicting large wind farm power
Publication Status	Published
Publication Details	Kirby A, Dunstan TD, Nishino T. An analytical model of momentum availability for predicting large wind farm power. *Journal of Fluid Mechanics*. 2023;976:A24. doi:10.1017/jfm.2023.844

Student Confirmation

Student Name:	Andrew Kirby		
Contribution to the Paper	Developed the analytical model, compared results with existing simulation results in the literature and drafted manuscript.		
Signature Andrew Kirby		Date	05/02/2024

Supervisor Confirmation

By signing the Statement of Authorship, you are certifying that the candidate made a substantial contribution to the publication, and that the description described above is accurate.

Supervisor name and title: Dr Takafumi Nishino		
Supervisor comments I believe that Andrew made a substantial contribution (more than 80%) to this publication, and the description described above is accurate.		
Signature T. Nishino	Date	25/07/2024

This completed form should be included in the thesis, at the end of the relevant chapter.

Chapter 5

Turbine- and farm-scale power losses in wind farms: an alternative to wake and farm blockage losses

This chapter presents a journal article titled *'Turbine- and farm-scale power losses in wind farms: an alternative to wake and farm blockage losses'* submitted to the journal *'Wind Energy Science'* and published in *'Wind Energy Science Discussions'* (`https://doi.org/10.5194/wes-2024-79`). The article spans the pages 104-132 in the thesis. Note that there are some minor differences in the text from the published version.

Traditionally, the aerodynamic loss of wind farm power is classified into a downstream 'wake loss' and an upstream 'farm blockage loss'. Additionally, there is a wind speed reduction within the wind farm due to the farm-atmosphere interaction. In order to accurately predict farm performance, it is important that our models capture the relevant fluid mechanical processes.

In this chapter we analyse an existing dataset of 43 finite-size wind farm LES. We find that neither the 'wake loss' nor 'farm blockage loss' is well correlated with the overall farm efficiency. This suggests that these metrics may not be appropriate for future large wind farms. We also find that the recorded 'wake losses' does not correspond to the degree of turbine-wake interactions within the farm. This suggests that downstream power losses may be due to the farm-atmosphere interactions rather than turbine wakes.

We also apply our new concepts of turbine- and farm-scale efficiencies to the LES dataset. The farm-scale efficiency was strongly correlated with the overall farm efficiency. The turbine-scale efficiency varied with the turbine layout but not with the atmospheric conditions. Conversely, the farm-scale efficiency varied predominantly with the atmospheric conditions. These new metrics could provide a better way of understanding wind farm performance.

Turbine- and farm-scale power losses in wind farms: an alternative to wake and farm blockage losses

Andrew Kirby[1], Takafumi Nishino[1], Luca Lanzilao[2], Thomas D. Dunstan[3], and Johan Meyers[2]

[1]Department of Engineering Science, University of Oxford, Parks Road, Oxford OX1 3PJ, UK
[2]Department of Mechanical Engineering, KU Leuven, Celestijnenlaan 300 – box 2421, B-3001 Leuven, Belgium
[3]Met Office, FitzRoy Road, Exeter EX1 3PB, UK

Correspondence: Andrew Kirby (andrew.kirby@trinity.ox.ac.uk)

Abstract. Turbine-wake and farm-atmosphere interactions can reduce wind farm power production. To model farm performance, it is important to understand the impact of different flow effects on the farm efficiency (i.e., farm power normalised by the power of the same number of isolated turbines). In this study we analyse the results of 43 large-eddy simulations (LES) of wind farms in a range of conventionally neutral boundary layers (CNBLs). First, we show that the farm efficiency η_f is not well correlated with the wake efficiency η_w (i.e., farm power normalised by the power of front row turbines). This suggests that existing metrics, classifying the loss of farm power into wake loss and farm blockage loss, are not best suited for understanding large wind farm performance. We then validate the assumption of scale separation in the two-scale momentum theory (Nishino & Dunstan, *J. Fluid Mech.*, vol. 894, 2020, p. A2) using the LES results. Building upon this theory, we propose two new metrics for wind farm performance, a turbine-scale efficiency η_{TS}, reflecting the losses due to turbine-wake interactions, and a farm-scale efficiency η_{FS}, indicating the losses due to farm-atmosphere interactions. The LES results show that η_{TS} is insensitive to the atmospheric condition, whereas η_{FS} is insensitive to the turbine layout. Finally, we show that a recently developed analytical wind farm model predicts η_{FS} with an average error of 5.7% from the LES results.

1 Introduction

To meet future energy demands wind energy capacity will need to increase rapidly. It is likely that individual wind farms will become larger (Veers et al., 2022). When wind turbines are placed together in a farm they produce less power than in isolation. Predicting this power loss is key for designing wind farms. However, this remains difficult due to the multi-scale nature of wind farm aerodynamics (Porté-Agel et al., 2020).

Behind every turbine is a turbulent wake. When the wakes impact downstream turbines they can cause significant power losses. Turbine wakes have been investigated extensively using large-eddy simulations (LES) (e.g., Porté-Agel et al., 2013; Wu and Porté-Agel, 2015; Stevens et al., 2016) and wind tunnel experiments (e.g., Vermeer et al., 2003; Bastankhah and Porté-Agel, 2017; Hyvärinen et al., 2018). Measurements from wind farms show that downstream turbines produce less power than the first upstream row (Barthelmie et al., 2010; Nygaard, 2014). Historically, this power degradation has been attributed to turbine-wake interactions.

Large wind farms can act as additional resistance to the atmospheric boundary layer (ABL) (Stevens and Meneveau, 2017). This can act to reduce the wind speed within and upstream of the farm (Porté-Agel et al., 2020). The upstream wind speed reduction is often referred to as the 'farm blockage' or 'global blockage' effect (Bleeg et al., 2018). LES of large wind farms (Wu and Porté-Agel, 2017; Allaerts and Meyers, 2017; Lanzilao and Meyers, 2024) show that an internal boundary layer forms in response to the increased flow resistance from the farm. The atmospheric response causes a velocity reduction within the farm, in addition to the turbine wakes. How much of the downstream power degradation is caused by turbine wakes compared to the larger scale atmospheric response? It is important to make sure that we predict farm power losses by modelling the correct physical processes. Recently, Lanzilao and Meyers (2024) performed LES of large wind farms operating in conventionally neutral boundary layers (CNBLs), where the turbine layout and operating conditions were fixed but different ABL heights and thermal stratifications above the ABL were tested. Depending on these conditions of the atmosphere, the 'wake efficiency' η_w (farm-averaged power normalised by the average power of the first row turbines) was found to vary significantly from 0.48 to 1.23. This raises the question: What physical processes are responsible for the different downstream power losses?

An alternative approach to understanding wind farm aerodynamics is the 'two-scale momentum theory' developed by Nishino and Dunstan (2020), who proposed to split the multi-scale problem into 'internal' turbine-scale and 'external' farm-scale sub-problems. The two sub-problems are coupled together by considering the conservation of momentum and matching the farm-average wind speed. Using the two-scale momentum theory, Kirby et al. (2022) proposed the new concepts of turbine-scale and farm-scale power losses to understand farm performance, where the farm-average wind speed (rather than the wind speed upstream of the farm) plays a key role. The turbine-scale losses are due to farm-internal flow interactions (i.e., turbine-wake interactions), whereas the farm-scale losses are due to the atmospheric response to the whole farm (i.e., reduction of farm-average wind speed).

In this study we compare the two different classifications of wind farm power losses using LES of large finite-size wind farms. We use the LES results reported by Lanzilao and Meyers (2024) and also perform new simulations with different turbine layouts, which allow us to fully validate the 'two-scale separation' assumption and thus the concepts of turbine- and farm-scale losses. The LES data are available in a public database (Lanzilao and Meyers, 2023b). We first summarise the two-scale momentum theory in Sect. 2. The LES methodology is then briefly described in Sect. 3. A validation of the two-scale separation assumption along with the turbine- and farm-scale losses are presented in Sect. 4. We also compare the farm-scale losses from the wind farm LES with predictions from an analytical wind farm model in Sect. 4. The results are discussed in Sect. 5 and concluding remarks given in Sect. 6.

2 Theory

2.1 Two-scale momentum theory

By considering the momentum balance for a control volume with and without a wind farm present, Nishino and Dunstan (2020) derived the non-dimensional farm momentum (NDFM) equation:

$$C_T^* \frac{\lambda}{C_{f0}} \beta^2 + \beta^\gamma = M \tag{1}$$

where β is the farm wind-speed reduction factor which is defined as $\beta \equiv U_F/U_{F0}$ (where U_F is the average wind speed in the nominal farm-layer of height H_F, and U_{F0} is the farm-layer-averaged speed without turbines present); the (farm-averaged) 'internal' turbine thrust coefficient C_T^* is defined as $C_T^* \equiv \sum_{i=1}^n T_i / \frac{1}{2}\rho U_F^2 nA$ (where T_i is the thrust of turbine i, n is the number of turbines in the farm and A is the rotor swept area); the array density λ is defined as $\lambda \equiv nA/S_F$ (where S_F is the farm area); the natural surface friction coefficient C_{f0} is defined as $C_{f0} \equiv \tau_{w0}/\frac{1}{2}\rho U_{F0}^2$ (where τ_{w0} is the bottom shear stress without turbines present); γ is the bottom friction exponent defined as $\gamma \equiv \log_\beta(\tau_w/\tau_{w0})$ (assumed to be 2.0 in this study, following Nishino and Dunstan (2020) and also as justified later in Sect. 4.2); and M is the momentum availability factor defined by $M \equiv M_F/M_{F0}$, where M_F is the net momentum flux into the farm control volume with the turbines present and M_{F0} the case without the turbines present. In this study we use a fixed definition of the farm-layer height $H_F = 2.5H_{hub}$ (where H_{hub} is the turbine hub-height) following Kirby et al. (2022).

Patel et al. (2021) used numerical weather prediction (NWP) simulations to calculate M for a realistic offshore wind farm site in the North Sea. They found, for most cases, an approximately linear relationship between M and β. Therefore M can be modelled as

$$M = 1 + \zeta(1 - \beta) \tag{2}$$

where ζ is called the wind extractability factor. Kirby et al. (2022) showed that ζ was a time-dependent parameter which varied with atmospheric conditions and inversely with farm size. More recently, Kirby et al. (2023b) proposed an analytical model of ζ, as discussed later in Sect. 4.4.

Equations (1) and (2) can be solved to calculate the farm wind-speed reduction factor β for a given farm design and atmospheric condition (i.e. λ, C_T^*, C_{f0}, γ and ζ). Using β, the farm power can be calculated using

$$C_p = \beta^3 C_p^* \tag{3}$$

where the (farm-averaged) turbine power coefficient is defined as $C_p \equiv \sum_{i=1}^n P_i / \frac{1}{2}\rho U_{F0}^3 nA$ (P_i is power of turbine i in the farm) and the (farm-averaged) 'internal' turbine power coefficient defined as $C_p^* \equiv \sum_{i=1}^n P_i / \frac{1}{2}\rho U_F^3 nA$.

2.2 Analytical model of near-ideal wind farm performance

Generally, the 'internal' turbine thrust coefficient C_T^* depends on the turbine layout (Kirby et al., 2022). However, as suggested by Nishino (2016) and later confirmed by Kirby et al. (2022), an approximate upper limit of C_T^* can be predicted by using an analogy to the classical actuator disc theory

$$C_T^* = 4\alpha(1-\alpha) = \frac{16C_T'}{(4+C_T')^2} \tag{4}$$

where $C_T' \equiv T_i/\frac{1}{2}\rho U_{T,i}^2 A$ is a turbine resistance coefficient which represents the turbine operating conditions, and $U_{T,i}$ is the streamwise velocity averaged across the rotor swept area of turbine i. Kirby et al. (2022) showed that some specific turbine layouts could exceed this C_T^* value slightly, presumably due to local blockage effects (Nishino and Draper, 2015).

The two-scale momentum theory described in Sect. 2.1 can predict the performance of arrays of actuator discs (or aerodynamically ideal turbines operating below rated conditions). For actuator discs $C_p^* = \alpha C_T^*$ where $\alpha \equiv U_T/U_F$ is the local wind-speed reduction factor, and α can be estimated using $\alpha = \sqrt{C_T^*/C_T'}$. It is useful to note that this is strictly valid only for infinite regular arrays of actuator discs where the thrust of each turbine is identical to the farm-averaged turbine thrust. The (farm-averaged) power coefficient of an actuator disc is given by

$$C_p = \beta^3 \alpha C_T^* = \beta^3 {C_T^*}^{\frac{3}{2}} {C_T'}^{-\frac{1}{2}}. \tag{5}$$

Using the analytical model of C_T^* (Eq. (4)), Eq. (1), (2) and (5) can be solved to give a theoretical prediction of near-ideal wind farm performance, denoted $C_{p,Nishino}$. If we assume $\gamma = 2.0$, we can derive a single analytical expression for $C_{p,Nishino}$, i.e.,

$$\begin{aligned} C_{p,Nishino} =& \frac{64C_T'}{(4+C_T')^3} \times \\ & \left[\frac{-\zeta + \sqrt{\zeta^2 + 4\left(\frac{16C_T'}{(4+C_T')^2}\frac{\lambda}{C_{f0}}+1\right)(1+\zeta)}}{2\left(\frac{16C_T'}{(4+C_T')^2}\frac{\lambda}{C_{f0}}+1\right)} \right]^3. \end{aligned} \tag{6}$$

Meanwhile, the power coefficient of an isolated turbine $C_{p,Betz}$ is given by

$$C_{p,Betz} = \frac{64C_T'}{(4+C_T')^3} \tag{7}$$

which gives a maximum turbine performance of $C_{p,Betz} = 16/27$ when $C_T' = 2.0$. These two theoretical predictions of performance ($C_{p,Nishino}$ and $C_{p,Betz}$) will be used to define the turbine-scale and farm-scale efficiencies later in Sect. 4.3.

3 Large-eddy simulation methodology

In this paper we analyse the LES of wind farms in CNBLs performed by Lanzilao and Meyers (2024) with 5 new simulation cases. Here we briefly summarise the main details of LES methodology, for more details see Lanzilao and Meyers (2024).

The turbines are modelled using an actuator disc model with no rotation (Calaf et al., 2010; Meyers and Meneveau, 2010). The turbine forces are projected onto the numerical grid using a Gaussian convolution filter (Calaf et al., 2010). Recently, Shapiro et al. (2019) proposed an additional correction factor for actuator disk models to avoid over-prediction of power and thrust. Unfortunately, this correction factor was not yet included in the LES database of Lanzilao and Meyers (2024), and therefore it was also not used for the additional cases performed here. Instead, as a next best approximation, we use the correction factor of Shapiro et al. (2019) in a postprocessing step (see Sect. 4.3 for more details). Here this correction is applied to the theoretical predictions outlined in Sect. 2. This is to ensure that the comparison with the theory is using the overpredicted turbine power and thrust which is actually implemented in the simulations (rather than the intended values). The turbines have a diameter D of 198 m and a hub height H_{hub} of 119 m. The thrust is calculated using a disk-based thrust coefficient of $C_T' = 1.94$ giving a traditional thrust coefficient of $C_T = 0.88$. A yaw controller is used to keep all turbine discs perpendicular to the incident flow to each turbine.

Table 1 summarises the wind farm designs considered in this study. In addition to the 'standard' design used by Lanzilao and Meyers (2024), we also consider 3 additional designs, namely 'aligned', 'half length' and 'double spacing'. The 'standard' farm consists of 16 rows and 10 columns of turbines in a staggered layout. The streamwise and spanwise spacing between turbines is $5D$ giving a capacity density of approximately $10\ \mathrm{MW\ km^{-2}}$. This is a dense wind farm but this density is being considered in some development areas. The farm has a length of 14.85 km and a width of 9.4 km. For the 3 additional farm designs (aligned, half length and double spacing) the turbine layout, farm length and turbine spacing were changed, respectively, from the standard design (table 1). Note that the farm length is the distance between the first and last turbine rows, and the 'half length' case has 8 rows rather than 16 rows. For all simulations the computational domain size is $L_x \times L_y \times L_z = 50\ \mathrm{km} \times 30\ \mathrm{km} \times 25\ \mathrm{km}$. The grid resolution is $\Delta x = 31.25\ \mathrm{m}$, $\Delta y = 21.74\ \mathrm{m}$ and $\Delta z = 5\ \mathrm{m}$ in the lowest $1.5\ \mathrm{km}$ of the domain, following the set-up used by Lanzilao and Meyers (2024).

Table 1. A summary of wind farm designs considered in this study.

Design	Turbine layout	Farm length	Farm width	Turbine spacing	Number of turbines
Standard	Staggered	14.85 km	9.4 km	$5D \times 5D$	160
Aligned	Aligned	14.85 km	9.4 km	$5D \times 5D$	160
Half length	Staggered	6.93 km	9.4 km	$5D \times 5D$	80
Double spacing	Staggered	14.85 km	9.4 km	$10D \times 10D$	40

The bottom boundary conditions are given by the classical Monin-Obukhov similarity theory (Moeng, 1984). Periodic boundary conditions are applied at the streamwise and spanwise edges of the domain. The inflow condition is given by a concurrent precursor simulation (Stevens et al., 2014) which is applied using a wave-free fringe technique that avoids spurious excitation of gravity waves (Lanzilao and Meyers, 2023a). Moreover, to prevent the reflection of gravity waves, a Rayleigh damping layer is applied in the upper part of the domain (Lanzilao and Meyers, 2023a).

The atmospheric stratification is varied by changing the capping inversion height, capping inversion strength and free-atmosphere lapse rate. Table 2 shows a summary of the different atmospheric stratifications. All combinations of these parameters were considered for the 'standard' farm design by Lanzilao and Meyers (2024). We use the notation introduced by Lanzilao and Meyers (2024), e.g., H500-C5-G4 refers to a capping inversion height of 500 m, capping inversion strength of 5 K and free-atmosphere lapse rate of 4 $\mathrm{K\ km^{-1}}$.

Table 2. A summary of atmospheric stratifications.

Capping inversion height [m]	1000, 500, 300, 150
Capping inversion strength [K]	2, 5, 8
Free-atmosphere lapse rate [$\mathrm{K\ km^{-1}}$]	1, 4, 8

4 Results

In the following we first investigate the wake and farm-blockage losses observed in the LES performed by Lanzilao and Meyers (2024) in Sect. 4.1. We then present in Sect. 4.2 a validation of the 'two-scale separation' assumption in the two-scale momentum theory proposed by Nishino and Dunstan (2020). We apply the concepts of 'turbine-scale' and 'farm-scale' losses (Kirby et al., 2022) to the LES results in Sect. 4.3. Finally, we the assess the accuracy of an analytical model (Kirby et al., 2023b) in predicting the 'farm-scale' losses.

4.1 Wake and farm blockage losses

Here we reanalyse the results of wind farm LES performed by Lanzilao and Meyers (2024), who reported that the farm normalised power relative to the first-row power (i.e., wake efficiency) varied from 0.48 to 1.23 for the same turbine layout and wind direction. The aim of this section is therefore to investigate the physical mechanisms changing the farm normalised power.

There are 3 commonly used efficiencies for wind farm performance. Firstly, the 'wake efficiency' η_w (sometimes called 'normalised power') is defined as

$$\eta_w \equiv \frac{P_{farm}}{P_1} \tag{8}$$

where P_{farm} is the farm-averaged turbine power and P_1 is the first-row-averaged turbine power. Secondly, the 'non-local' efficiency η_{nl} is defined by (Allaerts and Meyers, 2018)

$$\eta_{nl} \equiv \frac{P_1}{P_\infty} \tag{9}$$

where P_∞ is the power output of an isolated turbine under the same atmospheric conditions. This represents the power loss due to the velocity reduction in front of the farm, i.e., due to farm blockage. Finally the 'farm efficiency' η_f is defined as

$$\eta_f \equiv \frac{P_{farm}}{P_\infty} \equiv \eta_w \eta_{nl}. \tag{10}$$

The farm efficiency η_f quantifies the overall power losses caused by placing turbines together in a farm.

As noted by Lanzilao and Meyers (2024), the farm LES results show a relatively strong negative correlation between η_w and η_{nl} (figure 1). When the farm blockage increases (i.e. η_{nl} decreases), the downstream power losses decrease (i.e. η_w increases). These two effects counteract each other to a certain extent. This means that η_w is affected not only by turbine-wake interactions but also by larger farm-scale flow effects causing farm blockage.

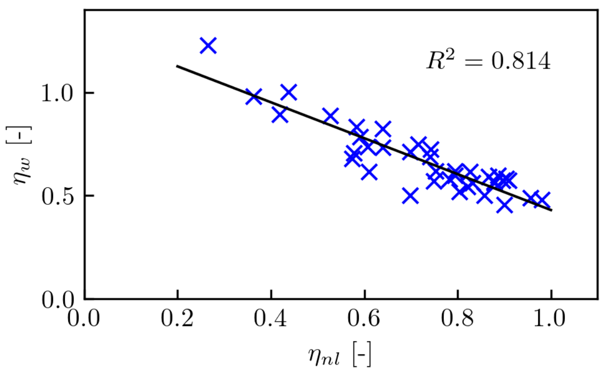

Figure 1. Relationship between wake efficiency η_w and non-local efficiency η_{nl} for all 38 LES cases from Lanzilao and Meyers (2024). The R^2 value shows the coefficient of determination.

The correlation between η_w and η_{nl} is caused by the induced pressure gradients across the farm. To illustrate this, the pressure perturbation for cases H300-C2-G1 and H300-C8-G1 is shown in Fig. 2. Case H300-C2-G1 has a low degree of farm blockage ($\eta_{nl} = 0.857$) and a relatively small induced pressure gradient. Conversely, H300-C8-G1 has a high degree of farm blockage ($\eta_{nl} = 0.437$) and a large induced pressure gradient. Essentially, H300-C8-G1 has a larger driving force across the farm, meaning that the velocity tends to stay high across the farm despite the lower velocity at the front. This causes η_w to be higher ($\eta_w = 1.00$ compared to $\eta_w = 0.501$ for H300-C2-G1).

The LES results also show that the overall farm efficiency η_f is not well correlated with either the wake efficiency η_w or the non-local efficiency η_{nl}. Figure 3(a) shows the weak correlation between η_f and η_w. This shows that the 'wake efficiency' or

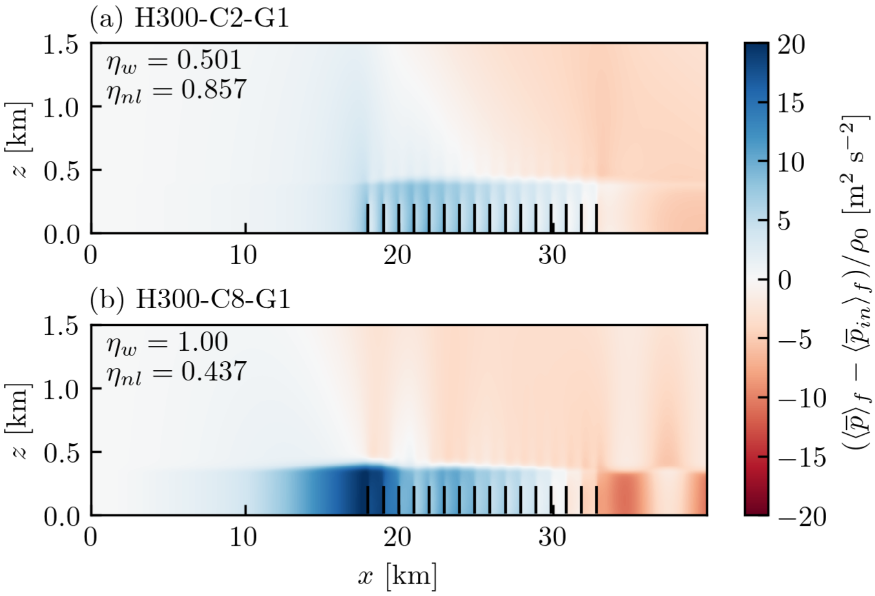

Figure 2. Time-averaged pressure perturbation averaged across the farm width for cases **(a)** H300-C2-G1 and **(b)** H300-C8-G1.

'normalised power' is not a good indicator of wind farm efficiency. The correlation between η_f and η_{nl} is also relatively weak as shown in Fig. 3(b). The negative farm blockage effect is mostly counteracted by the increased pressure gradient across the farm which increases η_w.

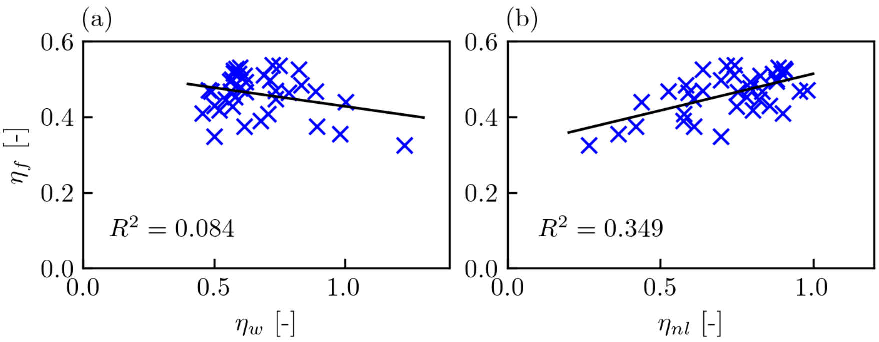

Figure 3. (a) Relationship between farm efficiency η_f and wake efficiency η_w and **(b)** relationship between farm efficiency η_f and non-local efficiency η_{nl}, for all 38 LES cases from Lanzilao and Meyers (2024). The R^2 values shows the coefficient of determination.

To better understand why the same turbine layout results in a very wide range of η_w from 0.48 to 1.23, now we will investigate whether this could be explained by either 1) different 'effective' turbine layouts caused by changes in local wind directions within the farm, or 2) different wake recovery rates. In the following, we will again focus on the two illustrative cases, H300-C2-G1 and H300-C8-G1. The capping inversion height is the same for both but H300-C2-G1 gives $\eta_w = 0.501$ whereas H300-C8-G1 gives $\eta_w = 1.00$.

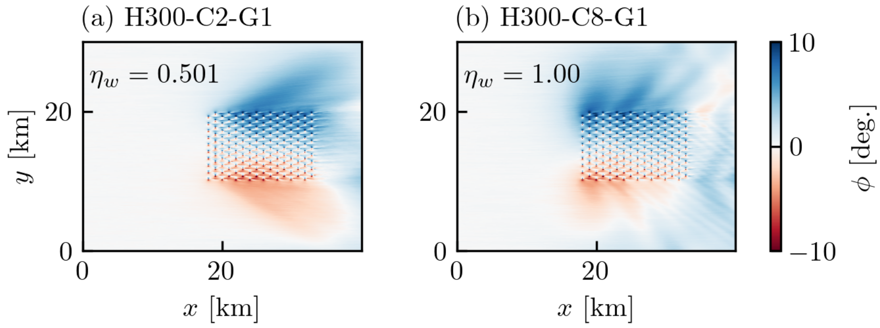

Figure 4. Time-averaged flow angle at the turbine hub height for cases **(a)** H300-C2-G1 and **(b)** H300-C8-G1.

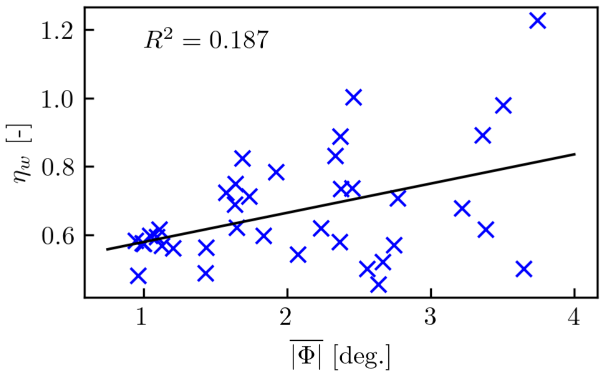

Figure 5. Relationship between wake efficiency η_w and the farm-averaged absolute turbine yaw angle $\overline{|\Phi|}$ for all 38 LES cases from Lanzilao and Meyers (2024). The R^2 value shows the coefficient of determination.

First, we show that the large difference in η_w cannot be explained by different ‘effective’ turbine layouts. The local flow direction for cases H300-C2-G1 and H300-C8-G1 is shown in Fig. 4. Both cases have an outward flow direction of approximately 5^o at the sides. However, both cases have similar variations of the local flow directions across the farm. Figure 5 shows there is not a strong relationship between η_w and the farm-averaged absolute turbine yaw angle $\overline{|\Phi|}$ for all 38 cases, indicating that the large variation of η_w cannot be explained by the change of effective turbine layout.

Next, we show that the wake recovery behind each turbine is also uncorrelated with the wake efficiency η_w. The farm flow profiles are shown in Fig. 6(a) for H300-C2-G1 and in Fig. 6(c) for H300-C8-G1. The individual wake deficits look similar but rather it is the farm-scale flows which are different. A closer view of individual wakes towards the center of the farm is shown

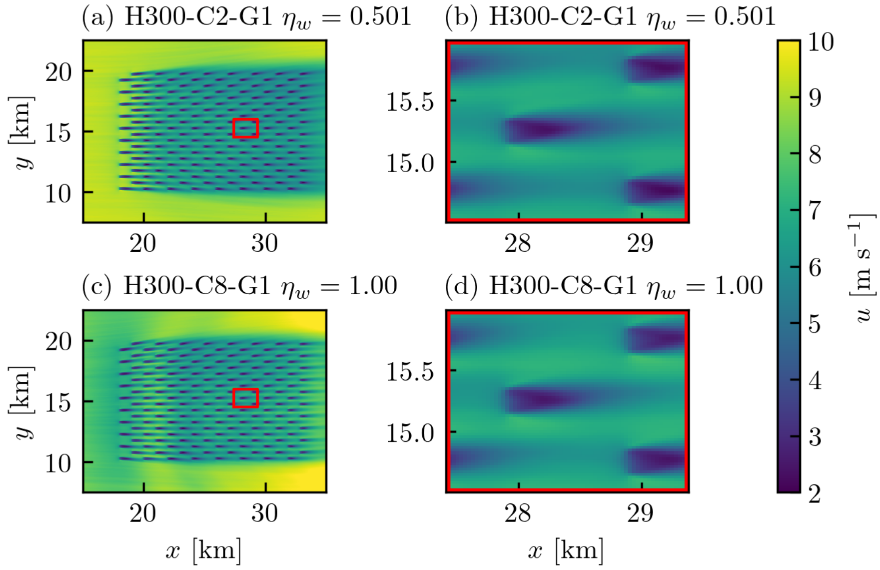

Figure 6. Time-averaged u velocity contours at the turbine hub height for case H300-C2-G1 **(a)** across the whole farm and **(b)** inside the farm; and for case H300-C8-G1 **(c)** across the whole farm and **(d)** inside the farm.

in Fig. 6(b) and 6(d). Despite one case having $\eta_w = 0.501$ and the other having $\eta_w = 1.00$, the wakes look almost identical. This suggests that the characteristics of individual turbine wake recovery are not contributing to the difference in η_w.

A more quantitative comparison in Fig. 7 shows that both cases have similar wake velocity deficits. Here we calculated the wake velocity deficit by defining new coordinates x_i and y_i local to each turbine (see Fig. 7(b)). x_i is perpendicular to each rotor and y_i parallel. We averaged the wake velocity deficits (relative to the undisturbed velocity $u_\infty(z)$ recorded in the precursor simulation) for each turbine in the 11th row. This row was chosen because the flow profiles are characteristic of the average flow profile across the entire farm. Figures 7(c)-(f) show that both horizontal and vertical wake deficit profiles are approximately Gaussian, and the wake deficit profiles and wake recovery rate are both similar. H300-C8-G1 has a slightly smaller normalised wake velocity deficit compared to H300-C2-G1, but this is not sufficient to explain the large difference in η_w values.

The wake recovery across the entire farm is also similar for the two cases. We calculated the wake width by fitting a Gaussian function to the wake deficit profiles shown in Fig. 7. Note that the centre of Gaussian function was not fixed to the rotor centre. The wake width σ was calculated as the geometric mean of the wake width in the horizontal σ_y and vertical σ_z directions, i.e., $\sigma = \sqrt{\sigma_y \sigma_z}$. The wake width as a function of downstream distance for turbine rows 3 to 16 is shown in Fig. 8. The first two rows were excluded as the wake recovery was much slower. An approximately linear growth in wake width can be seen for both cases. We calculated the wake expansion coefficient k^* using the equation $\sigma/D = k^* x_i/D + \epsilon$ where ϵ is the initial wake width. We then averaged the value of k^* across the 3rd to 16th rows to obtain a farm-averaged k^*, which is shown in Fig. 8. The value of k^* was found to be higher than the values reported by Bastankhah and Porté-Agel (2014). This is presumably

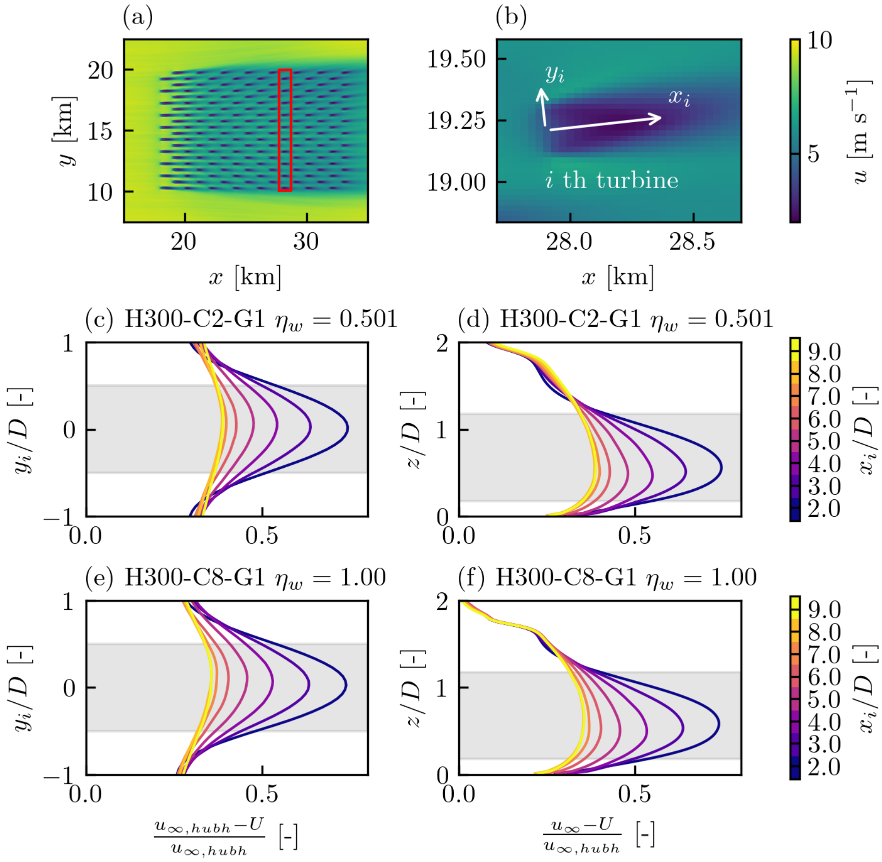

Figure 7. (a) Time-averaged u velocity contours at the turbine hub height for case H300-C2-G1 with the 11th row highlighted in red, and **(b)** new 'local' coordinates x_i and y_i. Normalised wake velocity deficit profiles averaged for all 10 turbines in the 11th row, plotted in the horizontal (y_i) direction at the hub height and in the vertical (z) directions through the rotor center, respectively, for **(c)**, **(d)** case H300-C2-G1 and **(e)**, **(f)** case H300-C8-G1.

because the turbulence levels are higher within a large wind farm. Most importantly, the average wake growth rate is higher for the case with the lower value of η_w. This again demonstrates that η_w is not strongly related to local wake recovery behind each turbine.

To confirm this trend further, we calculated the farm-averaged wake expansion coefficient k^* for 29 of the farm LES cases from Lanzilao and Meyers (2024). The cases with the lowest capping inversion (150 m) were excluded as they did not have Gaussian wake deficit profiles in the vertical direction, due to the vicinity of the capping-inversion base to the turbine-tip height. Figure 9(a) shows that there is no correlation between the farm efficiency η_f and the wake expansion coefficient k^*. Figure 9(b) shows that low η_w values cannot be explained by a slower wake recovery. On the contrary, these LES results show that cases with a low η_w value tend to have a faster wake recovery.

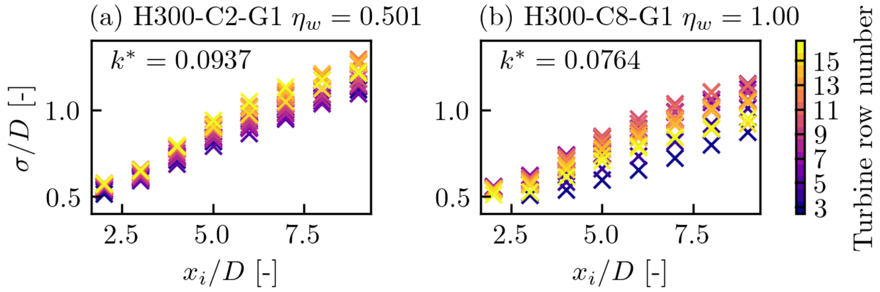

Figure 8. Normalised wake width with streamwise distance for different turbine rows for cases **(a)** H300-C2-G1 and **(b)** H300-C8-G1.

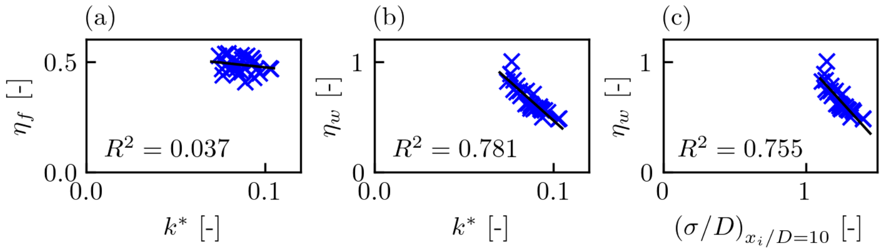

Figure 9. (a) Relationship between farm efficiency η_f and wake expansion coefficient k^* and **(b)** relationship between wake efficiency η_w and wake expansion coefficient k^*. R^2 shows the coefficient of determination.

The wake efficiency η_w has been extensively used to analyse farm performance as it is a relatively easy parameter to calculate, e.g. using SCADA data. However, these LES results (for a fixed staggered turbine layout with different ABL conditions) suggest that this wake efficiency parameter η_w is not a good indicator of the turbine-wake interactions within the farm.

4.2 Validation of two-scale separation assumption

The two-scale momentum theory provides an alternative way of understanding wind farm performance. This theory is particularly useful when the 'two-scale separation' assumption is valid, meaning that the farm 'internal' parameters (C_T^* and γ) depend only on 'internal' or turbine-scale conditions, whereas the 'external' parameter (ζ) depends only on 'external' or farm-scale conditions. This assumption allows the turbine-scale and farm-scale flows to be modelled separately; however, this assumption has not been fully validated in previous studies. In the following we present a first validation of the two-scale separation assumption using 4 new LES results as well as the previous LES results from Lanzilao and Meyers (2024).

Here we calculate ζ_{LES} directly from the momentum availability factor M_{LES} and the farm wind-speed reduction factor β_{LES} obtained from LES (Eq. (11)). M_{LES} is given by Eq. (12a) which can be simplified into Eq. (12b) and (12c). The bottom friction exponent γ was not recorded in the present LES results, but we can expect that this varies between 1.5 and 2.0 (Kirby et al., 2022). Considering Eq. (12c), a typical value of $\lambda C_T^*/C_{f0}$ is 17.5 for the farms in this study meaning that the total force due to turbine thrust is much larger than the force due to the bottom friction (and hence, the impact of γ is very small). For example, if we suppose that $\beta = 0.75$, using $\gamma = 1.5$ gives $M_{LES} = 10.5$ whereas $\gamma = 2.0$ gives $M_{LES} = 10.4$. Since the value of M_{LES} is largely insensitive to the value of γ, we will use $\gamma = 2.0$ in the following analysis.

$$\zeta_{LES} = \frac{M_{LES} - 1}{1 - \beta_{LES}} \tag{11}$$

$$\begin{aligned} M_{LES} &= \frac{\sum_{i=1}^{n} T_i + \tau_w S}{\tau_{w0} S} && \text{(12a)} \\ &= \frac{\sum_{i=1}^{n} T_i}{\tau_{w0} S} + {\beta_{LES}}^{\gamma} && \text{(12b)} \\ &= \frac{\lambda C^*_{T,LES}}{C_{f0}} {\beta_{LES}}^{2} + {\beta_{LES}}^{\gamma} && \text{(12c)} \end{aligned}$$

Figure 10 shows the relationship between M_{LES} and β_{LES} obtained for 3 different atmospheric conditions. As can be seen from the figure, the wind extractability factor ζ_{LES} changes with the atmospheric conditions but it is not sensitive to the turbine layout. The aligned turbine layouts result in a lower wind speed reduction (i.e., lower value of $1 - \beta_{LES}$) because they present a lower flow resistance. However, the value of ζ_{LES} is almost identical for aligned and staggered layouts under a given atmospheric condition. A farm with a staggered layout but doubled turbine spacing ($10D \times 10D$) also follows approximately the same relationship (see Fig. 10(b)). This demonstrates that the linear relationship is valid for a wide range of β. It can also be seen that ζ_{LES} decreases with decreasing capping inversion height. This trend was predicted by the theoretical model of ζ proposed by Kirby et al. (2023b). The values of ζ_{LES} for all atmospheric conditions tested in this study are shown in Fig. 11(a). As shown theoretically by Nishino and Dunstan (2020), for a given wind farm, there is a positive monotonic relationship between ζ and wind farm efficiency. Therefore effects of different atmospheric conditions on the wind farm efficiency reported by Lanzilao and Meyers (2024) can be explained by different wind extractability factors ζ.

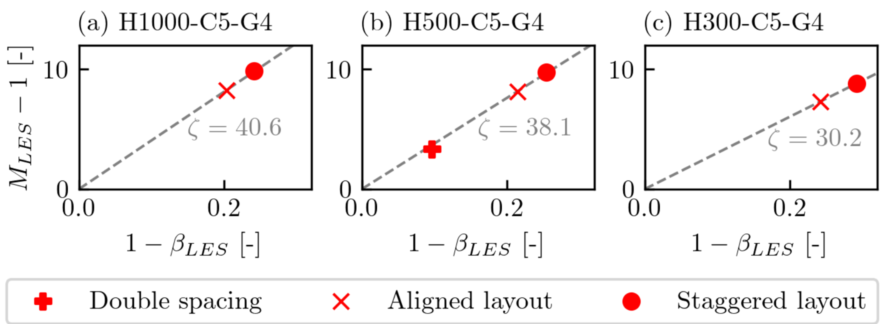

Figure 10. Relationship between momentum availability factor M_{LES} and farm wind-speed reduction factor β_{LES} for **(a)** H1000-C5-G4, **(b)** H500-C5-G4 and **(c)** H300-C5-G4 atmospheric conditions.

The LES results also show that the internal turbine thrust coefficient $C^*_{T,LES}$ is insensitive to atmospheric conditions (Fig. 11(b)). Apart from the lowest capping inversion cases (H150), the staggered turbine layout consistently gives a high $C^*_{T,LES}$ value of about 1.0 irrespective of atmospheric stratification (Fig. 11(b)), whereas the aligned turbine layout consistently gives a lower $C^*_{T,LES}$ value than the staggered one. This trend is expected as Kirby et al. (2022) showed that increased turbine-wake interactions reduce the value of C^*_T. Turbine-wake interactions reduce C^*_T because the waked turbines experience a lower incident wind speed and so produce less thrust.

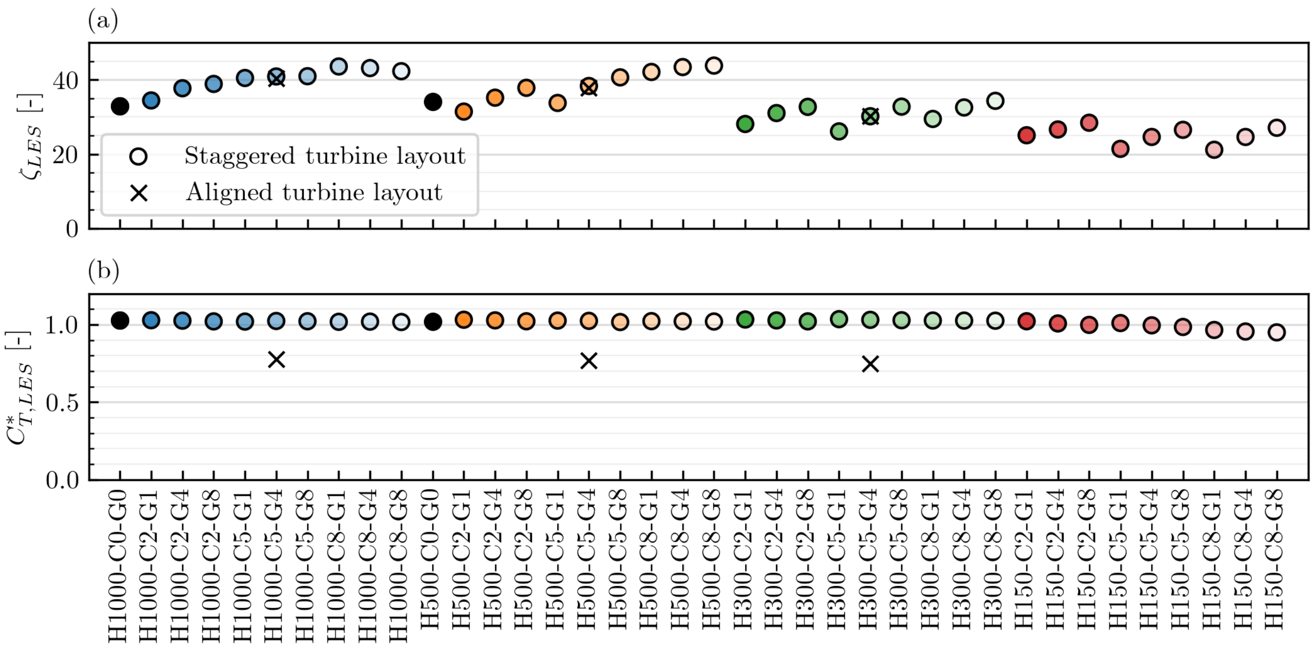

Figure 11. Values of **(a)** wind extractability factor ζ and **(b)** 'internal' turbine thrust coefficient C^*_T for all atmospheric conditions tested.

These LES results in Fig. 10 and 11 strongly indicate that the assumption of 'two-scale separation' is valid for large finite wind farms, at least in a practical range of CNBLs tested in this study. This means that the impact of turbine-scale flows (i.e., turbine-wake interactions) and farm-scale flows (i.e., farm-atmosphere interaction) could be modelled separately through the modelling of C^*_T and ζ, as suggested originally by Nishino and Dunstan (2020), to predict wind farm power in a less complicated and more physically meaningful manner.

4.3 Turbine-scale and farm-scale power losses

Turbine-scale and farm-scale power losses (Kirby et al. (2022); see also Stevens (2023)) are alternative metrics for wind farm performance, as illustrated in Fig. 12. The turbine-scale power losses are due to the internal flow interactions within the farm (i.e., turbine-wake interactions). Farm-scale power losses are due to the interaction between the ABL and the farm as a whole.

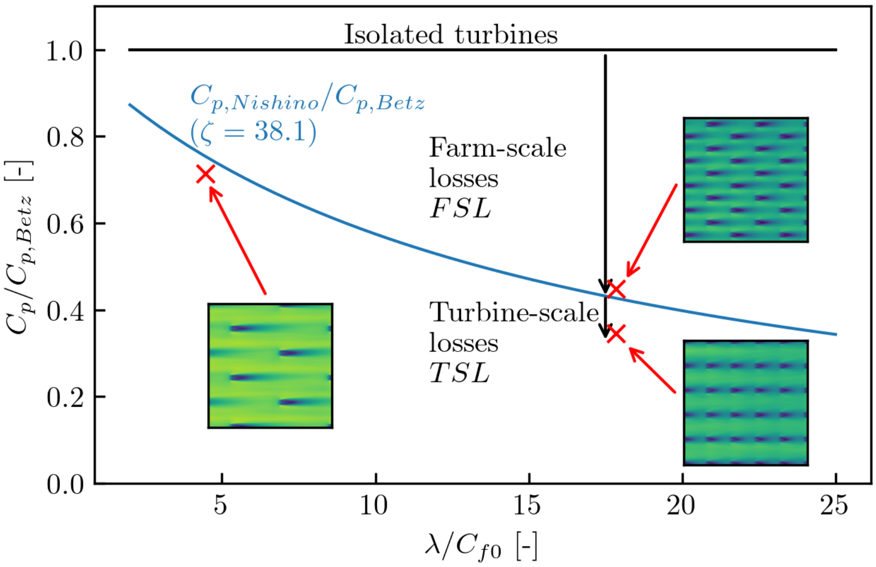

Figure 12. Schematic of the overall farm efficiency $C_p/C_{p,Betz}$ against the effective array density λ/C_{f0}, illustrating farm-scale and turbine-scale power losses. The blue line shows the near-ideal farm performance predicted by the two-scale momentum theory for a given set of conditions (corresponding to Fig. 10(b) with $\zeta = 38.1$), whereas the red crosses show the results of 3 farm LES cases discussed in Fig. 10(b).

Here we propose a slight modification to these new metrics for wind farm performance, namely the 'turbine-scale efficiency' η_{TS} and 'farm-scale efficiency' η_{FS}[1] defined as:

$$\eta_{TS} \equiv \frac{C_p}{C_{p,Nishino}} \tag{13}$$

$$\eta_{FS} \equiv \frac{C_{p,Nishino}}{C_{p,Betz}}. \tag{14}$$

η_{TS} and η_{FS} are related to the overall wind farm efficiency $C_p/C_{p,Betz}$ by

$$\frac{C_p}{C_{p,Betz}} \equiv \eta_{TS}\eta_{FS}. \tag{15}$$

Note that $C_p/C_{p,Betz}$ is slightly different from the overall farm efficiency η_f used by Lanzilao and Meyers (2024). Here we normalise by the turbine performance predicted using the actuator disc theory, $C_{p,Betz}$, for a given turbine resistance coefficient

[1] Note that the turbine-scale efficiency η_{TS} and farm-scale efficiency η_{FS} are related to the 'turbine-scale loss factor' Π_T and 'farm-scale loss factor' Π_F introduced by Kirby et al. (2022) by the following expressions $\eta_{TS} \equiv 1 - \Pi_T$ and $\eta_{FS} \equiv 1 - \Pi_F$.

($C_T' = 1.94$ in this study). This is instead of the isolated turbine power found using LES, P_∞, which is slightly different from the power predicted by the actuator disc theory. We normalised all values by $C_{p,Betz}$ to ensure the predicted power coefficients from the LES, C_p, and the theory, $C_{p,Nishino}$, are normalised by the same value. A summary of the efficiency metrics used in this study is given in table 3.

As can be seen from Eq. (15), the overall farm efficiency is the product of turbine-scale efficiency η_{TS} and farm-scale efficiency η_{FS}. For convenience, we can also introduce an alternative set of metrics, namely the 'turbine-scale loss' TSL defined in Eq. (16) and 'farm-scale loss' FSL defined in Eq. (17). The only difference from η_{TS} and η_{FS} is that TSL and FSL both have the same denominator $C_{p,Betz}$. This allows the two losses to be simply added up (instead of multiplied) to obtain the total loss as in Eq. (18).

$$TSL \equiv \frac{C_{p,Nishino} - C_p}{C_{p,Betz}} \equiv \eta_{FS}\left(1 - \eta_{TS}\right) \tag{16}$$

$$FSL \equiv \frac{C_{p,Betz} - C_{p,Nishino}}{C_{p,Betz}} \equiv 1 - \eta_{FS} \tag{17}$$

$$\frac{C_p}{C_{p,Betz}} \equiv 1 - (TSL + FSL) \tag{18}$$

Table 3. A summary of wind farm efficiency metrics.

Efficiency metric	Notes
$\eta_f = P_{farm}/P_\infty$	P_{farm} - farm-averaged turbine power
	P_∞ - isolated turbine power
$\eta_w = P_{farm}/P_1$	P_1 - front-row-averaged turbine power
$\eta_{nl} = P_1/P_\infty$	
$C_p/C_{p,Betz}$	C_p - farm-averaged power coefficient
	$C_{p,Betz}$ - ideal power coefficient for isolated turbines
$\eta_{TS} = C_p/C_{p,Nishino}$	$C_{p,Nishino}$ - near-ideal power coefficient for turbines in a farm
$\eta_{FS} = C_{p,Nishino}/C_{p,Betz}$	

In this study we calculate η_{TS} and η_{FS} using ζ_{LES} obtained from each LES case. Shapiro et al. (2019) proposed a correction factor N for the overpredicted velocity through an actuator disc as

$$N = \left(1 + \frac{C_T'}{2}\frac{1}{\sqrt{3\pi}}\frac{\Delta}{D}\right)^{-1}. \tag{19}$$

where Δ is the Gaussian kernel width used for projecting turbine forces onto the numerical grid. In this study $\Delta = 32.61$ m in the y and z directions, which gives $N = 0.950$, meaning that the turbine thrust and power are corrected by N^2 and N^3, respectively. Since the correction factor of Shapiro et al. (2019) was not implemented in the LES, we apply it here as a postprocessing step, to correct for possible overpredictions of power and thrust.

To calculate η_{TS} and η_{FS} we used the procedure summarised in Fig. 13. Essentially, we solved Eq. (1) and (2) for β using $\zeta = \zeta_{LES}$ and the parameter values in table 4. Note that we used 0.974 as the value of C_T^* which has been corrected (i.e., adjusted upwards) to account for LES resolution effects. The $5D \times 5D$ turbine spacing gives an array density λ of 0.0314. The value of the farm-layer-height is given by $H_F = 2.5H_{hub}$ and for the turbines simulated H_{hub} is 119 m. $C_{p,Nishino}/C_{p,Betz}$ is given by the value of β^3.

Step 1. Obtain M_{LES} from $M_{LES} = \frac{\sum_{i=1}^{n} T_{i,LES}}{\tau_{w0} S} + {\beta_{LES}}^2$

Step 2. Obtain ζ_{LES} from $\zeta_{LES} = \frac{M_{LES}-1}{1-\beta_{LES}}$

Step 3. Obtain β from $C_T^* \frac{\lambda}{C_{f0}} \beta^2 + \beta^2 = 1 + \zeta_{LES}(1-\beta)$

n.b. C_T^* in Eq. (4) is multiplied by $1/N^2$ to account for LES resolution effects

Step 4. Obtain η_{FS} from $\eta_{FS} = \beta^3$

Step 5. Obtain η_{TS} from $\eta_{TS} = \frac{1}{\beta^3} \times \frac{C_{p,LES}}{C_{p,Betz}}$

n.b. $C_{p,Betz}$ in Eq. (7) is multiplied by $1/N^3$ to account for LES resolution effects

Figure 13. Procedure used to calculate turbine-scale efficiency η_{TS} and farm-scale efficiency η_{FS}.

Figure 14 compares the farm performance for 3 different atmospheric conditions (including the 2 cases discussed earlier in Sect. 4.1) for demonstration. As can be seen from figure 14(a), the wake and non-local efficiencies are both sensitive to capping inversion strength. These two effects mostly canceled each other out, giving similar farm efficiencies for these 3 cases. Conversely, Fig. 14(b) shows that the turbine-scale efficiency η_{TS} is almost unchanged for the 3 cases. This reflects the fact that the turbine layout was unchanged, so the turbine-scale flows were very similar (as shown earlier in Fig. 6). η_{TS} is slightly greater than 1, which means that, on the turbine-scale (i.e., for a given farm-averaged wind speed) these 'clustered' turbines

Table 4. Parameter values used to calculate turbine-scale efficiency η_{TS} and farm-scale efficiency η_{FS}.

Quantity	Value
C_T^*	0.974
λ	0.0314
H_F	297.5 m
γ	2.0

perform slightly better than isolated turbines (this will be further discussed later in this section). The close agreement between $C_p/C_{p,Betz}$ and η_{FS} means that all the power losses in these 3 cases are on the farm-scale, i.e., due to the farm-atmosphere interaction.

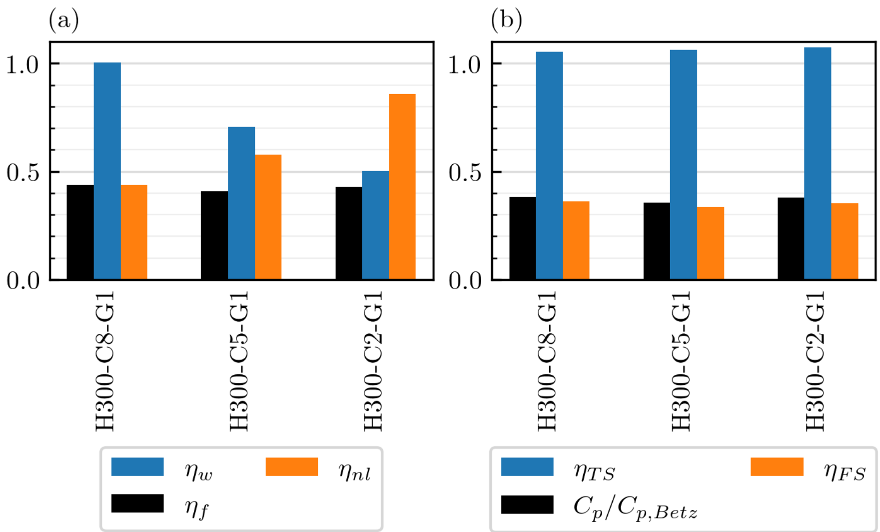

Figure 14. Comparison of wind farm performance for cases H300-C8-G1, H300-C5-G1 and H300-C2-G1 using **(a)** wake efficiency η_w and non-local efficiency η_{nl} and **(b)** turbine-scale efficiency η_{TS} and farm-scale efficiency η_{FS}.

Figure 15 shows the values of η_{TS} and η_{FS} for the same staggered farm under 38 different atmospheric conditions. Almost all the variation in $C_p/C_{p,Betz}$ is explained by η_{FS}. This reflects the physical observation that different stratifications affect the large-scale farm-atmosphere interaction, changing the power generation efficiency on the farm-scale. The value of η_{TS} is nearly the same for most cases with a value of approximately 1.05 (discussed later in this section). The 6 cases with a lower η_{TS} are all with the lowest capping inversion height of 150 m. These cases show a larger change in wind direction within the farm, changing the turbine-scale flow characteristics and thus η_{TS}.

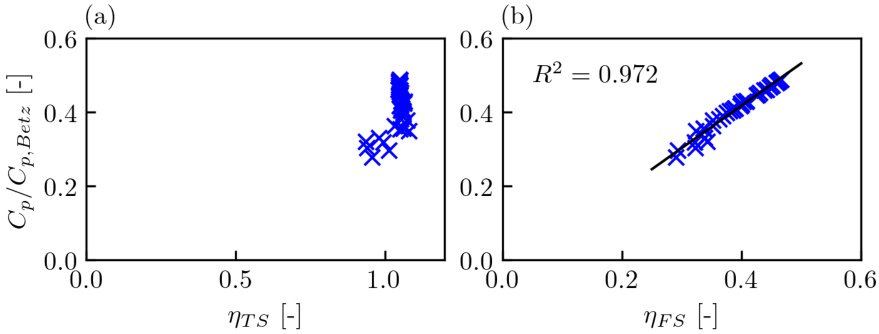

Figure 15. (a) Relationship between the overall farm efficiency $C_p/C_{p,Betz}$ and turbine-scale efficiency η_{TS} and **(b)** farm-scale efficiency η_{FS}, for all 38 LES cases with the dense staggered turbine layout. The R^2 value shows the coefficient of determination.

Next, we examine how the impact of changing the turbine layout is captured by the new efficiency metrics, for the 3 atmospheric conditions discussed earlier in Fig. 10. As can be seen from Fig. 16, changing the layout from 'staggered' to 'aligned' changes the value of η_{TS} from approximately 1.05 to just above 0.8 for all 3 cases. Given that in 'aligned' cases the second row of turbines produces much less power than the first, it might appear that $\eta_{TS} \approx 0.8$ is fairly high. However, this is reasonable since the overall farm efficiency η_f decreases by about 23% when the layout is changed from staggered to aligned for all 3 atmospheric conditions considered. The farm-scale efficiency η_{FS} is practically unchanged with turbine layout. Conversely, the the existing metrics η_w and η_{nl} are both affected by the turbine layout, implying that the effect of turbine layout needs to be considered explicitly in the modelling of both wake and farm blockage losses. Using η_{TS} and η_{FS} instead allows us to separate the effect of turbine layout from the effect of atmospheric conditions.

It is also worth noting that, for all these cases, the power losses are larger on the farm-scale than on the turbine-scale. Figure 16 shows that η_{FS} is smaller than η_{TS} for both staggered and aligned layouts, despite the small turbine spacing ($5D$) considered in these cases. This agrees qualitatively with the predictions made by Kirby et al. (2022).

The new efficiency metrics η_{TS} and η_{FS} are also applicable to smaller farms and larger turbine spacings. Here we simulated two additional layouts under the H500-C5-G4 atmospheric condition. In one case, 'half length', the streamwise length of the farm was halved to 6.93 km (shown in Fig. 17(b)). In the other case, 'double spacing', the turbine spacing was doubled in the x and y directions to $10D \times 10D$ (shown in Fig. 17(c)) whilst the farm size was kept constant. The results are compared with the 'standard' case in Fig. 18, showing that the changes in overall farm efficiency are mostly due to changes in η_{FS}. The 'half length' case gives a higher η_{FS} because the farm-scale wind speed reduction (due to farm-atmosphere interaction) is less severe for smaller wind farms. The 'double spacing' case gives an even higher η_{FS} because of the low array density, which reduces the total farm thrust and thus the farm-atmosphere interaction compared to the 'standard' case. The turbine-scale efficiency η_{TS} is similar and close to 1 for all 3 cases, reflecting the fact that turbine-wake interactions have limited impact for these staggered turbine arrays.

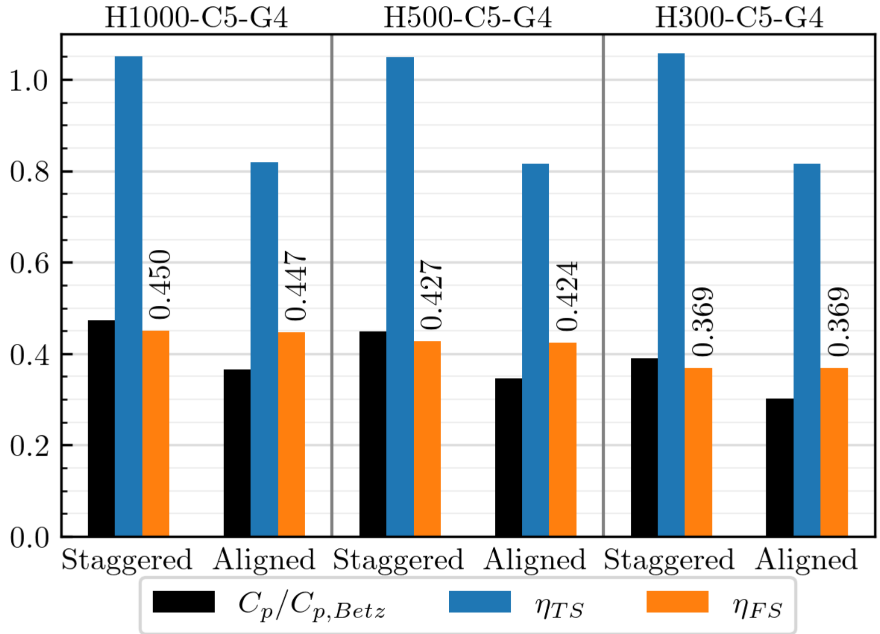

Figure 16. Comparison of farm performance for staggered and aligned turbine layouts in H1000-C5-G4, H500-C5-G4 and H300-C5-G4 atmospheric conditions using **(a)** wake efficiency η_w and non-local efficiency η_{nl} and **(b)** turbine-scale efficiency η_{TS} and farm-scale efficiency η_{FS}.

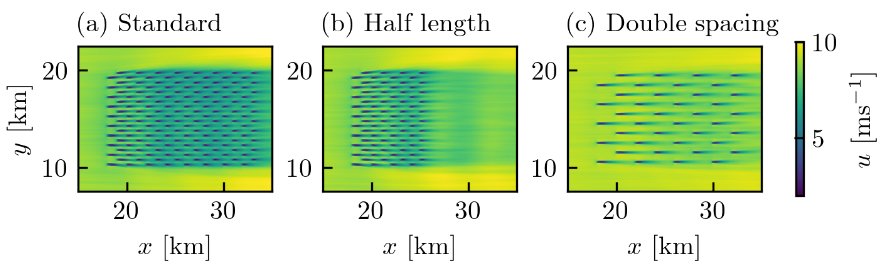

Figure 17. Time-averaged u velocity contours at the turbine hub height for **(a)** 'standard' turbine layout, **(b)** 'half length' layout and **(c)** 'double spacing' layout.

It is worth noting that the staggered turbine layout with a $5D \times 5D$ spacing consistently gives η_{TS} of approximately 1.05 (see Fig. 15 and 18), meaning that, on the turbine-scale, the turbines are more efficient at extracting power than isolated turbines.
330 When η_{TS} is greater than 1, this means that the velocity upstream of each turbine (and upstream of the local induction region) is higher than the farm-averaged velocity U_F. Therefore this may depend on how U_F (i.e., the height of the farm-layer H_F) is defined. This could also be due to the 'local blockage' effect caused by neighbouring turbines (Ouro and Nishino, 2021;

Nishino and Draper, 2015). It is important to note that $\eta_{TS} = 1$ does not mean the maximum possible performance at the turbine-scale. It means the performance, at the turbine-scale, is equivalent to an isolated turbine that experiences the farm-average wind speed. The performance of an isolated turbine can be exceeded slightly due to local flow confinement effects. When the turbine spacing was doubled η_{TS} was reduced to 0.975 (Fig. 18(b)). This shows that the close turbine spacing caused η_{TS} to be greater than 1. Note that while a close lateral turbine spacing can increase η_{TS} slightly above 1, it also reduces η_{FS} thereby reducing the overall farm efficiency $C_p/C_{p,Betz}$.

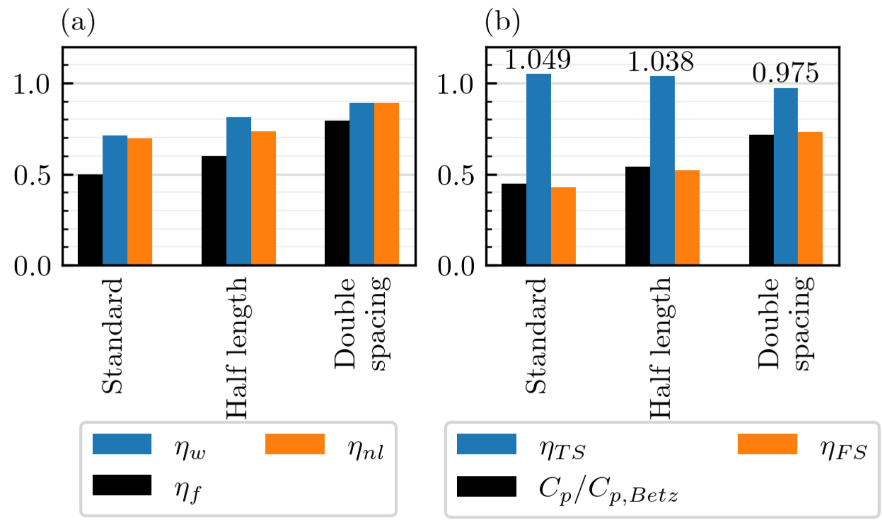

Figure 18. Comparison of farm performance for ‘standard’, ‘half-length’ and ‘double spacing’ turbine layouts under H500-C5-G4 atmospheric conditions using **(a)** wake efficiency η_w and non-local efficiency η_{nl} and **(b)** turbine-scale efficiency η_{TS} and farm-scale efficiency η_{FS}.

4.4 Analytical wind farm model

In this section we assess the accuracy of an analytical wind farm model (Kirby et al., 2023b) to predict η_{FS}. This analytical model predicts the farm-scale flows only and not the turbine-wake interactions. Hence, here we only compare the predictions of the farm-scale efficiency η_{FS} and not the turbine-scale efficiency η_{TS}. A summary of this farm model is shown in Fig. (19). Essentially, rather than using ζ_{LES} to calculate η_{FS}, here we predict η_{FS} using the expression

$$\zeta = 1.18 + \frac{\frac{2.18}{C_{f0}}\frac{H_F}{L}}{1 - \frac{\tau_{t0}}{\tau_{w0}}} \tag{20}$$

where L is the streamwise farm length and τ_{t0} is the undisturbed shear stress at a height H_F in the hub-height wind direction. Using this approach, we can predict η_{FS} instantly using only the undisturbed atmospheric conditions. Figure 20(a) shows the

Input parameters

Turbine/farm design $C_T',\ \lambda,\ L,\ H_F$

Environmental $C_{f0},\ \frac{\tau_{t0}}{\tau_{w0}}$

Step 1. Obtain β from $C_T^* \frac{\lambda}{C_{f0}} \beta^2 + \beta^2 = 1 + \left[1.18 + \frac{\frac{2.18}{C_{f0}} \frac{H_F}{L}}{1 - \frac{\tau_{t0}}{\tau_{w0}}} \right] (1 - \beta)$

n.b. C_T^* is calculated using Eq. (4) and is then multiplied by $1/N^2$ to account for LES resolution effects

Step 2. Obtain η_{FS} from $\eta_{FS} = \beta^3$

Figure 19. Input parameters and procedure used to calculate η_{FS} from the analytical model (Kirby et al., 2023b).

predictions of η_{FS} for three different atmospheric conditions. The model correctly predicts the effect of capping inversion layer height on η_{FS}. It is important to note that this model (Eq. (20)) currently only considers the impact of capping inversion height, and not capping inversion strength or free-atmosphere stratification. Figure 20(b) shows the distribution of percentage errors when predicting η_{FS} for 29 atmospheric states (we excluded the lowest capping inversion cases 'H150' where the capping inversion was below H_F). The model gives good predictions of η_{FS} with a mean absolute percentage error of 5.68%. It is likely that the impact of free atmospheric stratification, not considered in the current model, causes some spread and contributes to this error. There is a slight bias for underpredicting η_{FS} but the median percentage error is below 5%. The prediction accuracy for the smaller farm and greater turbine spacing cases are also summarised in table 5, showing that this first-order model gives satisfactory predictions for these cases as well.

Table 5. LES and analytical model predictions of η_{FS} for 'standard', 'half length' and 'double spacing' layouts under H500-C5-G4 atmospheric conditions.

Case	η_{FS} (LES)	η_{FS} (Analytical model)	Percentage error (%)
Standard	0.427	0.413	-3.59%
Half length	0.523	0.579	+10.7%
Double spacing	0.733	0.744	+1.47%

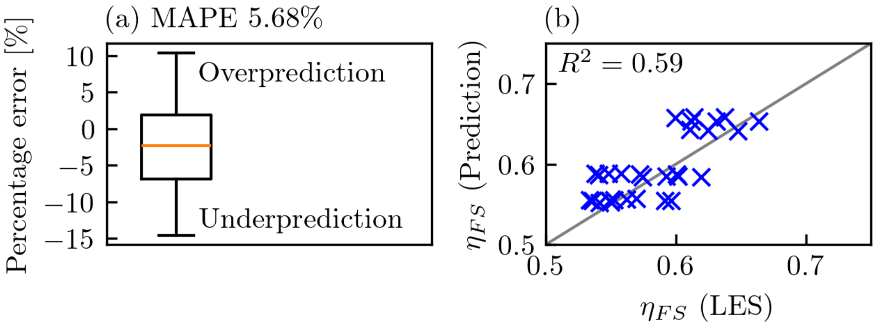

Figure 20. (a) Comparison of farm-scale efficiency η_{FS} obtained from LES and analytical predictions (Kirby et al., 2023b) for 3 cases and **(b)** box plot showing the distribution of prediction percentage errors for 29 cases.

5 Discussion

Power losses for downstream rows of turbines in a wind farm (relative to the first row) are commonly attributed to wake effects. For large farms, the downstream power losses are also affected by the atmospheric response, but it has been a challenge to model this effect accurately. In this study our LES results showed that, for a large staggered array of 160 turbines, the downstream power degradation was not due to turbine-wake interactions, i.e., individual turbine wakes (or more specifically, local flow regions having a lower flow speed than the "average" flow speed) were not directly causing the reduction of downstream turbine power (in the sense that how the power of downstream turbines would have been reduced if they had been located in such a locally slower flow region). It is worth noting that Porté-Agel et al. (2013) used LES to show that turbine wake effects could reduce farm power by up to 35% by simulating different wind directions. However, this power loss was calculated relative to the optimal wind direction and not the power of the front row turbines. Furthermore, the wind farm simulated by Porté-Agel et al. (2013) was less than 20% the size of the 'standard' farm considered in this study. A recent study by Kirby et al. (2022) suggests that the relative importance of power losses due to turbine-wake interactions decreases with increasing farm size. The present study suggests that the farm-atmosphere interaction could play a leading role in power losses for offshore wind farms as they become larger in the future.

Our LES results also showed that there was only a weak relationship between the farm blockage loss and the overall farm efficiency. This was due to the strong negative correlation between the blockage loss (represented by η_{nl}) and the wake loss (represented by η_w). This suggests that farm blockage, to a first order, acts to redistribute power across the farm rather than reduce the farm power. This has also been observed in the LES performed by Lanzilao and Meyers (2022) and Stipa et al. (2023). The different stratifications changed the farm blockage but the overall farm efficiency changed only slightly.

The turbine-scale efficiency η_{TS} and farm-scale efficiency η_{FS} are useful new metrics for understanding wind farm performance. They allow the impacts of turbine layout and farm-atmosphere interaction to be assessed separately. The farm-scale efficiency η_{FS} is insensitive to the turbine layout and so the losses due to the atmospheric interaction can be assessed even before the turbine layout is decided. It is worth noting that, although actuator discs (or ideal turbines) were considered in this study, the new metrics η_{FS} and η_{TS} can be applied to wind farms with real (non-ideal) turbines as well. When the turbines are non-ideal, the power loss due to turbine design (relative to the power of ideal actuator discs) will reduce η_{TS} (as C_p in Eq. (13) decreases) but not η_{FS}.

For all turbine layouts and atmospheric conditions considered in this study, η_{FS} was lower than η_{TS}. This means that more power is lost due to the farm-atmosphere interaction than due to turbine-scale flow effects. This was true even for the large farms with an aligned layout and close turbine spacing, where η_{TS} was about 0.8 whilst η_{FS} was less than 0.5. All staggered cases gave η_{TS} close to 1, suggesting that the different farm efficiencies could be explained by different levels of farm-atmosphere interaction rather than changing losses due turbine-wake interactions. These results suggest the importance of focusing more on the modelling of η_{FS} (or the modelling of wind extractability factor ζ) in future studies of large wind farms.

The modelling approach used in Nishino and Dunstan (2020) is to view the farm as a single unit experiencing the farm-averaged wind speed U_F. This approach helps to simplify the stresses that are expected to occur throughout the farm. Different farm layouts have different levels of flow heterogeneity and stresses. Therefore this can lead to complexity when comparing different farm layouts and hence the turbine-scale losses presented here. This effect should be investigated in future research.

In this study the assumption of 'two-scale separation' was shown to be valid for large finite wind farms. This means that the modelling of large wind farms could be split into the modelling of turbine-wake interactions and the modelling of farm-atmosphere interactions, as suggested originally by Nishino and Dunstan (2020). It should be noted, however, that the present LES results are still for an idealised wind farm situation, i.e., quasi-steady situation with a horizontally homogeneous atmosphere. We found that the wind extractability factor ζ was insensitive to the internal/turbine-scale flow conditions (i.e., turbine layout and spacing). However, there may still be ways to manipulate the turbine-scale flows to increase ζ, and hence the overall farm efficiency. One way could be to introduce some medium-scale unsteadiness by varying turbine operating conditions in time and thereby increasing momentum entrainment into the farm (e.g., Goit and Meyers, 2015).

Another limitation of the present study is that we relied on a single LES dataset. In this study we focused mostly on a large and relatively dense wind farm. To test the applicability to a wider range of wind farm situations, future work can apply the new concepts of η_{TS} and η_{FS} to various wind farm LES with different flow conditions (e.g., Baas et al., 2023). Future work could also work on validating the proposed models against wind farm SCADA data. The environmental input parameters (C_{f0} and τ_{t0}/τ_{w0}) could be calculated using ERA5 data. Data on the surface shear stress and boundary layer height from ERA5 could be used to estimate the shear stress ratio τ_{t0}/τ_{w0}.

Future work should also focus on improving the analytical model of the momentum availability factor M and the wind extractability factor ζ (Kirby et al., 2023b). One improvement could be to explicitly model the impact of gravity waves on the farm pressure field (e.g., Smith, 2024). It will also be useful to improve the modelling of turbine-scale flows. Kirby et al. (2023a) developed a statistical model to predict C_T^* as a function of turbine layout for a fixed C_T' value of 1.33. Future work can extend this model to other turbine operating conditions.

6 Conclusions

In this study we analysed a large LES suite of wind farms in CNBLs. For all 38 simulation cases with the same staggered turbine layout, the overall farm efficiency η_f was not well correlated with the wake efficiency η_w (often referred to as normalised power) or the non-local efficiency η_{nl} (i.e., farm blockage effects). Identical turbine layouts with different atmospheric stratifications (above the turbines) were found to give significantly different η_w values, which could not be explained by changes in 'effective' turbine layout (due to changes in local wind direction) or changes in the rate of wake recovery. These results suggest that turbine-wake interactions do not play a leading role in downstream power losses in large wind farms.

The assumption of two-scale separation (Nishino and Dunstan, 2020) was validated in this study, using finite-size wind farm LES for the first time. The 'internal' parameter C_T^* was found to be insensitive to 'external' atmospheric conditions, whereas the 'external' parameter ζ was shown to be insensitive to the turbine layout. This means that the assumption of two-scale separation is valid for large offshore wind farms, at least under the ideal 'quasi-steady' situation considered in this study.

Building upon the two-scale momentum theory, we have proposed new metrics of wind farm efficiency. The turbine-scale efficiency η_{TS} represents power losses due to internal turbine-wake interactions. The farm-scale efficiency η_{FS} reflects the losses due to the farm-atmosphere interaction. As can be expected from the validity of the two-scale separation, η_{TS} and η_{FS} are useful concepts for understanding the aerodynamic performance of wind farms. For all turbine layouts simulated, η_{FS} was found to be much lower than η_{TS}. This suggests that farm-scale flows have a greater impact on the overall farm efficiency than turbine-scale flows. The analytical model developed recently by Kirby et al. (2023b) was shown to predict η_{FS} with an average error of 5.68% from the LES results. Further developments in the modelling of farm-scale efficiency η_{FS} will be crucial in future studies of large wind farms.

Code and data availability. The code to reproduce the results and figures is available in the github repository https://github.com/AndrewKirby2/LES_CNBL_analysis. The LES data is available at the KU Leuven RDR dataset https://doi.org/10.48804/L45LTT.

Author contributions. T.N. derived the theory. L.L. performed the simulations. A.K. analysed the data from the simulations. A.K. and T.N. drafted the manuscript with guidance from L.L., T.D.D, and J.M. Funding was acquired by T.N., T.D.D. and J.M.

Competing interests. At least one of the (co-)authors is a member of the editorial board of *Wind Energy Science*.

Acknowledgements. A.K. acknowledges the NERC-Oxford Doctoral Training Partnership in Environmental Research (NE/S007474/1) for funding and training. L.L. and J.M. acknowledge support from the Research Foundation Flanders (FWO, Grant No. G0B1518N), from the project FREEWIND, funded by the Energy Transition Fund of the Belgian Federal Public Service for Economy, SMEs, and Energy (FOD

Economie, K.M.O., Middenstand en Energie) and from the European Union Horizon Europe Framework programme (HORIZON-CL5-2021-D3-03-04) under grant agreement no. 101084205. The computational resources and services in this work were provided by the VSC (Flemish Supercomputer Center), funded by the Research Foundation Flanders (FWO) and the Flemish Government department EWI.

References

Allaerts, D. and Meyers, J.: Boundary-layer development and gravity waves in conventionally neutral wind farms, Journal of Fluid Mechanics, 814, 95–130, https://doi.org/10.1017/jfm.2017.11, 2017.

Allaerts, D. and Meyers, J.: Gravity Waves and Wind-Farm Efficiency in Neutral and Stable Conditions, Boundary-Layer Meteorology, 166, 269–299, https://doi.org/10.1007/s10546-017-0307-5, 2018.

Baas, P., Verzijlbergh, R., van Dorp, P., and Jonker, H.: Investigating energy production and wake losses of multi-gigawatt offshore wind farms with atmospheric large-eddy simulation, Wind Energy Science, 8, 787–805, https://doi.org/10.5194/wes-8-787-2023, 2023.

Barthelmie, R. J., Pryor, S. C., Frandsen, S. T., Hansen, K. S., Schepers, J. G., Rados, K., Schlez, W., Neubert, A., Jensen, L. E., and Neckelmann, S.: Quantifying the impact of wind turbine wakes on power output at offshore wind farms, Journal of Atmospheric and Oceanic Technology, 27, 1302–1317, https://doi.org/10.1175/2010JTECHA1398.1, 2010.

Bastankhah, M. and Porté-Agel, F.: A new analytical model for wind-turbine wakes, Renewable Energy, 70, 116–123, https://doi.org/10.1016/j.renene.2014.01.002, 2014.

Bastankhah, M. and Porté-Agel, F.: A New Miniature Wind Turbine for Wind Tunnel Experiments. Part II: Wake Structure and Flow Dynamics, Energies, 10, https://doi.org/10.3390/en10070923, 2017.

Bleeg, J., Purcell, M., Ruisi, R., and Traiger, E.: Wind farm blockage and the consequences of neglecting its impact on energy production, Energies, 11, 1609, https://doi.org/10.3390/en11061609, 2018.

Calaf, M., Meneveau, C., and Meyers, J.: Large eddy simulation study of fully developed wind-turbine array boundary layers, Physics of Fluids, 22, 1–16, https://doi.org/10.1063/1.862466, 2010.

Goit, J. and Meyers, J.: Optimal control of energy extraction in wind-farm boundary layers, Journal of Fluid Mechanics, 768, 5–50, https://doi.org/10.1017/jfm.2015.70, 2015.

Hyvärinen, A., Lacagnina, G., and Segalini, A.: A wind-tunnel study of the wake development behind wind turbines over sinusoidal hills, Wind Energy, 21, 605–617, https://doi.org/https://doi.org/10.1002/we.2181, 2018.

Kirby, A., Nishino, T., and Dunstan, T. D.: Two-scale interaction of wake and blockage effects in large wind farms, Journal of Fluid Mechanics, 953, A39, https://doi.org/10.1017/jfm.2022.979, 2022.

Kirby, A., Briol, F.-X., Dunstan, T. D., and Nishino, T.: Data-driven modelling of turbine wake interactions and flow resistance in large wind farms, Wind Energy, 26, 968–984, https://doi.org/https://doi.org/10.1002/we.2851, 2023a.

Kirby, A., Dunstan, T. D., and Nishino, T.: An analytical model of momentum availability for predicting large wind farm power, Journal of Fluid Mechanics, 976, A24, https://doi.org/10.1017/jfm.2023.844, 2023b.

Lanzilao, L. and Meyers, J.: Effects of self-induced gravity waves on finite wind-farm operations using a large-eddy simulation framework, Journal of Physics: Conference Series, 2265, 22 043, https://doi.org/10.1088/1742-6596/2265/2/022043, 2022.

Lanzilao, L. and Meyers, J.: An Improved Fringe-Region Technique for the Representation of Gravity Waves in Large Eddy Simulation with Application to Wind Farms, Boundary-Layer Meteorology, 186, 567–593, https://doi.org/10.1007/s10546-022-00772-z, 2023a.

Lanzilao, L. and Meyers, J.: A reference database of wind-farm large-eddy simulations for parametrizing effects of blockage and gravity waves, https://doi.org/10.48804/L45LTT, 2023b.

Lanzilao, L. and Meyers, J.: A parametric large-eddy simulation study of wind-farm blockage and gravity waves in conventionally neutral boundary layers, Journal of Fluid Mechanics, 979, A54, https://doi.org/10.1017/jfm.2023.1088, 2024.

Meyers, J. and Meneveau, C.: Large Eddy Simulations of large wind-turbine arrays in the atmospheric boundary layer, https://doi.org/10.2514/6.2010-827, 2010.

Moeng, C.-H.: A Large-Eddy-Simulation Model for the Study of Planetary Boundary-Layer Turbulence, Journal of Atmospheric Sciences, 41, 2052 – 2062, https://doi.org/10.1175/1520-0469(1984)041<2052:ALESMF>2.0.CO;2, 1984.

Nishino, T.: Two-scale momentum theory for very large wind farms, Journal of Physics: Conference Series, 753, 032 054, https://doi.org/10.1088/1742-6596/753/3/032054, 2016.

Nishino, T. and Draper, S.: Local blockage effect for wind turbines, Journal of Physics: Conference Series, 625, 012 010, https://doi.org/10.1088/1742-6596/625/1/012010, 2015.

Nishino, T. and Dunstan, T. D.: Two-scale momentum theory for time-dependent modelling of large wind farms, Journal of Fluid Mechanics, 894, A2, https://doi.org/10.1017/jfm.2020.252, 2020.

Nygaard, N. G.: Wakes in very large wind farms and the effect of neighbouring wind farms, Journal of Physics: Conference Series, 524, 12 162, https://doi.org/10.1088/1742-6596/524/1/012162, 2014.

Ouro, P. and Nishino, T.: Performance and wake characteristics of tidal turbines in an infinitely large array, Journal of Fluid Mechanics, 925, https://doi.org/10.1017/jfm.2021.692, 2021.

Patel, K., Dunstan, T. D., and Nishino, T.: Time-dependent upper limits to the performance of large wind farms due to mesoscale atmospheric response, Energies, 14, 6437, https://doi.org/10.3390/en14196437, 2021.

Porté-Agel, F., Wu, Y. T., and Chen, C. H.: A numerical study of the effects of wind direction on turbine wakes and power losses in a large wind farm, Energies, 6, 5297–5313, https://doi.org/10.3390/en6105297, 2013.

Porté-Agel, F., Bastankhah, M., and Shamsoddin, S.: Wind-Turbine and Wind-Farm Flows: A Review, Boundary-Layer Meteorology, 174, 1–59, https://doi.org/10.1007/s10546-019-00473-0, 2020.

Shapiro, C. R., Gayme, D. F., and Meneveau, C.: Filtered actuator disks: Theory and application to wind turbine models in large eddy simulation, Wind Energy, 22, 1414–1420, https://doi.org/10.1002/we.2376, 2019.

Smith, R. B.: The wind farm pressure field, Wind Energy Science, 9, 253–261, https://doi.org/10.5194/wes-9-253-2024, 2024.

Stevens, R.: Understanding wind farm power densities, Journal of Fluid Mechanics, 958, F1, https://doi.org/10.1017/jfm.2023.113, 2023.

Stevens, R. J., Graham, J., and Meneveau, C.: A concurrent precursor inflow method for Large Eddy Simulations and applications to finite length wind farms, Renewable Energy, 68, https://doi.org/10.1016/j.renene.2014.01.024, 2014.

Stevens, R. J. A. M. and Meneveau, C.: Flow Structure and Turbulence in Wind Farms, Annual Review of Fluid Mechanics, 49, https://doi.org/10.1146/annurev-fluid-010816-060206, 2017.

Stevens, R. J. A. M., Gayme, D. F., and Meneveau, C.: Effects of turbine spacing on the power output of extended wind-farms, Wind Energy, 19, 359–370, https://doi.org/10.1002/we.1835, 2016.

Stipa, S., Ajay, A., Allaerts, D., and Brinkerhoff, J.: The Multi-Scale Coupled Model: a New Framework Capturing Wind Farm-Atmosphere Interaction and Global Blockage Effects, Wind Energy Science Discussions, 2023, 1–44, https://doi.org/10.5194/wes-2023-75, 2023.

Veers, P., Dykes, K., Basu, S., Bianchini, A., Clifton, A., Green, P., Holttinen, H., Kitzing, L., Kosovic, B., Lundquist, J. K., Meyers, J., O'Malley, M., Shaw, W. J., and Straw, B.: Grand Challenges: wind energy research needs for a global energy transition, Wind Energy Science, 7, 2491–2496, https://doi.org/10.5194/wes-7-2491-2022, 2022.

Vermeer, L. J., Sørensen, J. N., and Crespo, A.: Wind turbine wake aerodynamics, Progress in Aerospace Sciences, 39, 467–510, https://doi.org/https://doi.org/10.1016/S0376-0421(03)00078-2, 2003.

Wu, K. L. and Porté-Agel, F.: Flow adjustment inside and around large finite-size wind farms, Energies, 10, 2164, https://doi.org/10.3390/en10122164, 2017.

Wu, Y. T. and Porté-Agel, F.: Modeling turbine wakes and power losses within a wind farm using LES: An application to the Horns Rev offshore wind farm, Renewable Energy, 75, 945–955, https://doi.org/10.1016/j.renene.2014.06.019, 2015.

5.1 Statement of authorship

Statement of Authorship for joint/multi-authored papers for PGR thesis

To appear at the end of each thesis chapter submitted as an article/paper

The statement shall describe the candidate's and co-authors' independent research contributions in the thesis publications. For each publication there should exist a complete statement that is to be filled out and signed by the candidate and supervisor **(only required where there isn't already a statement of contribution within the paper itself).**

Title of Paper	Turbine- and farm-scale power losses in wind farms: an alternative to wake and farm blockage losses
Publication Status	Submitted to *Wind Energy Science* and published in *Wind Energy Science Discussions*
Publication Details	Kirby, A., Nishino, T., Lanzilao, L., Dunstan, T. D., and Meyers, J.: Turbine- and farm-scale power losses in wind farms: an alternative to wake and farm blockage losses, Wind Energ. Sci. Discuss. [preprint], https://doi.org/10.5194/wes-2024-79, in review, 2024.

Student Confirmation

Student Name:	Andrew Kirby		
Contribution to the Paper	Analysed the simulation data and drafted the manuscript.		
Signature Andrew Kirby		Date	22/05/2024

Supervisor Confirmation

By signing the Statement of Authorship, you are certifying that the candidate made a substantial contribution to the publication, and that the description described above is accurate.

Supervisor name and title: Dr Takafumi Nishino			
Supervisor comments I believe that Andrew made a substantial contribution (more than 60%) to this publication, and the description described above is accurate.			
Signature Nishino		Date	25/07/2024

This completed form should be included in the thesis, at the end of the relevant chapter.

Chapter 6

Conclusions

The aim of this thesis was to improve the understanding and modelling of wind farm efficiency. This was done by considering the flow physics on both the turbine-scale and the farm-scale. Section 6.1 summarises the main results presented in the thesis. An outlook for future research is described in section 6.2.

6.1 Main conclusions

6.1.1 Statistical modelling of turbine-scale flow effects

Both turbine-scale and farm-scale flows affect wind farm efficiency. We firstly focused on turbine-scale flows which include the commonly studied turbine-wake interactions. We modelled turbine-wake interactions using a parameter called the 'internal' turbine thrust coefficient C_T^*. This is different from traditional thrust coefficients because the reference wind speed is the farm-averaged wind speed. Using C_T^* in the analysis of wind farm efficiency is analogous to using the 'local' thrust coefficient C_T' in the analysis of wind turbine efficiency.

To predict turbine-wake interactions, we developed a statistical model of C_T^* as a function of turbine layout (Chapter 3). Data for the model came from a combination of high- and low-fidelity wind farm simulations. The high-fidelity data source was a suite of 50 wind farm LES. The low-fidelity data came from wake model wind farm simulations. For both data sources, different combinations of turbine layout and wind directions were included.

We developed several statistical emulators of C_T^* using both standard Gaussian Process (GP) regression and multi-fidelity GP regression. The standard GP was trained only on the LES data. The multi-fidelity GP was trained on both the LES and wake model data using an information fusion algorithm. We estimated the test error of the emulators for predicting C_T^* by performing leave-one-out cross-validation. The best multi-fidelity GP had a mean absolute test error of 0.849% and the best standard GP 1.04%. The test error was substantially lower for the emulators than the wake model (4.60%).

The C_T^* emulators can be used to predict wind farm power under different mesoscale atmospheric conditions using the existing two-scale momentum theory. This is a new approach for predicting wake losses in large wind farms. The low computational cost and high accuracy of the emulators could be beneficial for wind farm optimisation.

However, the statistical emulators of C_T^* have a number of limitations. They are not currently applicable to all wind farms. The data used to train the models considered only regular turbine layouts. As such, the emulators cannot predict C_T^* for irregular turbine layouts. Another limitation is that the training data only includes turbines at one fixed operating condition. Therefore, this approach is not yet applicable to the full range of operating conditions that wind turbines in a farm may experience.

6.1.2 Turbine- and farm-scale power losses

To better understand the impact of turbine-scale and farm-scale flows on farm performance we developed the new concepts of turbine-scale loss and farm-scale loss. The farm-scale loss quantifies the power loss due to the farm-atmosphere interaction (including wind farm blockage). The turbine-scale loss gives the losses due to internal flow interactions only (including turbine-wake interactions). These two new concepts offer a novel approach to understand and analyse wind farm efficiency.

Combining wind farm LES with the two-scale momentum theory, we calculated the turbine-scale and farm-scale losses for hypothetical large wind farms (Chapter 2). We found that, for a realistic range of farm designs and atmospheric conditions, the farm-scale losses are typically more than twice as large as the turbine-scale losses. This shows that the efficiency of large farms is determined mostly by the farm-atmosphere interaction, rather than the turbine-wake interactions. This suggests that the potential of layout optimisation for large farms may be limited. These results also suggest that traditional engineering wake models may not be the most appropriate modelling technique for large offshore wind farms.

We used the same combined computational-theoretical approach to show that larger wind farms had greater farm-scale losses and smaller turbine-scale losses (and a lower overall efficiency) for a given array density. This suggests that wind farm models calibrated on small farms may not be accurate for future larger wind farms where the impact of turbine wakes is reduced.

We also analysed an existing LES dataset of a finite-size wind farm under 38 different atmospheric conditions (Chapter 5). We first analysed the data using the existing commonly used concepts of 'wake losses' and 'farm blockage losses'. There was a strong negative correlation between the wake losses and farm blockage losses. There was no strong relationship between either the wake or farm blockage losses and the overall farm efficiency (the farm-averaged power normalised by the power of an isolated turbine power). For large farms, changes in the recorded wake loss or farm blockage loss may not correspond to changes in overall farm efficiency. Therefore, these existing concepts may not be applicable to future large farms.

In contrast to the existing concepts of wake losses and farm blockage losses, the turbine- and farm-scale losses gave a simple, consistent understanding of farm performance. The turbine-scale loss varied predominantly with the turbine layout and the farm-scale loss varied mostly with atmospheric conditions. This analysis also confirmed that farm-scale losses are much greater than turbine-scale losses for large wind farms.

6.1.3 Analytical modelling of farm-scale flow effects

Since, for large farms, farm-scale flows are more important than turbine wakes, this motivated the development of a model to predict farm-scale flow effects (Chapter 5). We developed a simple analytical model to predict farm-scale flows by modelling the farm 'momentum availability factor' (i.e., how much the presence of the turbines increase the momentum supply to the farm site). The new model captures the impact of pressure gradient forcing, turbulent entrainment and net advection using steady quasi-one-dimensional flow assumptions. This model provides a new way of modelling farm-scale flow effects (e.g. farm blockage and the farm-atmosphere interaction) at a very low computational cost.

The new model of the momentum availability factor can be combined with the existing two-scale momentum theory to predict wind farm power. A comparison with existing wind farm LES studies gave a typical prediction error of 5% or less for staggered turbine layouts. A more thorough validation with a suite of 38 wind farm LES gave a mean absolute prediction error of 5.68%. Despite the simplicity of the model, the complex multi-scale flow effects can be predicted with a satisfactory degree of accuracy.

A limitation of the newly developed model is that it does not consider the impact of free-atmosphere stratification on farm-scale flows. It also does not explicitly consider the role of gravity waves on the induced pressure gradients across the farm. Another limitation is that the current modelling framework does not yet include the effect of wakes from neighbouring wind farms. Additionally, the modelling framework has not yet been validated using measurements from existing wind farms.

6.1.4 Summary

Overall, the work in this thesis has developed a new understanding of power losses in large wind farms. The new concepts of turbine-scale and farm-scale losses provide a novel approach to analysing wind farm efficiency. We used these new concepts to show that, for large offshore wind farms, power losses due to farm-scale flows are typically more than twice as large as for turbine-scale flows. We also showed that turbine- and farm-scale losses give a simpler and more consistent understanding of the overall farm efficiency than the existing concepts of 'wake losses' and 'farm blockage losses'.

In addition to a new understanding of farm efficiency, this thesis presents two new models to predict both the turbine-scale and farm-scale flow effects. Firstly we developed a statistical emulator to predict turbine-scale wake effects at a low computational cost. Secondly, we proposed a new analytical model to predict farm-scale flow effects (e.g. farm-atmosphere interactions). These new models could be promising new approaches to predicting the efficiency of large farms and optimising wind farm design.

6.2 Outlook

The results in this thesis provide several new avenues for future research. A natural progression would be to improve the models of both the turbine-scale and farm-scale flow physics.

Currently the statistical emulators of C_T^* are only applicable to perfectly regular turbine layouts. However, in reality wind farms may have complex irregular layouts. Therefore, future work could focus on extending this approach to arbitrary layouts. This could involve the creation of a large dataset of wind farm simulations with irregular layouts. This would also require the development of new parameters to describe the geometric characteristics of the turbine layouts.

Another limitation of the C_T^* emulators developed in this study is that they are only valid for the turbine operating condition given by $C_T' = 1.33$. In reality the operating conditions of a turbine will vary with the wind speed. Future work could extend the statistical emulators to different turbine operating conditions by including C_T' as an input parameter. This would require more wind farm simulations with different turbine thrust coefficients.

For the new analytical model of farm-scale flows there are a number of possible improvements. Currently the mechanisms inducing the pressure gradient across the farm are not considered explicitly, such as the creation of gravity waves and changes to the capping inversion height. This has been shown to depend on the free-atmosphere stratification which is not considered in the current model. Future work could extend the model to directly consider the effects of gravity waves and free-atmosphere stratification.

The model has been derived assuming that the boundary layer height is greater than the wind-farm-layer height. However, this assumption may not be satisfied when the boundary layer height is very low, for example stable boundary layers. As wind turbines become larger, this situation will occur more frequently. Therefore future work could focus on re-deriving the model to correctly capture the effects of turbulent entrainment in this scenario.

The model of the momentum availability factor was derived using quasi-steady flow assumptions. However, the flow in the atmospheric boundary layer is rarely stationary with changes in wind direction and complex weather patterns. The data used to validate this model (wind farm LES) is also highly idealised with stationary conditions. It is therefore an interesting avenue of future work to test how well the model applies to realistic non-stationary atmospheric conditions.

Future work could also investigate the applicability of other concepts in this thesis to realistic non-stationary atmospheric conditions. When applied to wind farm LES of a stationary CNBL, the concepts of turbine-scale and farm-scale loss appear to work well. However, would these concepts be sufficient for analysing the performance of real wind farms operating in varying atmospheric conditions? This could be investigated using existing datasets of NWP simulations or LES with more realistic atmospheric conditions.

Offshore wind farms are very expensive projects requiring large capital investments. Any models used to make decisions about wind farms must be carefully validated using data from existing wind farms. A limitation of the research presented in this thesis is that any models and concepts are only tested against LES. Future work could compare the recorded farm performance data against *a priori* predictions from the models developed in this thesis.

Bibliography

[1] Paris agreement to the united nations framework convention on climate change. `https://unfccc.int/process-and-meetings/the-paris-agreement/the-paris-agreement`, 2015. Accessed on: 25/10/2023.

[2] M. Abkar and F. Porté-Agel. The effect of free-atmosphere stratification on boundary-layer flow and power output from very large wind farms. *Energies*, 6:2338–2361, 2013.

[3] M. Abkar and F. Porté-Agel. Influence of atmospheric stability on wind-turbine wakes: A large-eddy simulation study. *Physics of Fluids*, 27:035104, 2015.

[4] M. Abkar and F. Porté-Agel. A new wind-farm parameterization for large-scale atmospheric models. *Journal of Renewable and Sustainable Energy*, 7:013121, 2015.

[5] M. Abkar, A. Sharifi, and F. Porté-Agel. Large-eddy simulation of the diurnal variation of wake flows in a finite-size wind farm. *Journal of Physics: Conference Series*, 625:012031, 2015.

[6] M. Abkar, A. Sharifi, and F. Porté-Agel. Wake flow in a wind farm during a diurnal cycle. *Journal of Turbulence*, 17:420–441, 2016.

[7] D. Allaerts and J. Meyers. Boundary-layer development and gravity waves in conventionally neutral wind farms. *Journal of Fluid Mechanics*, 814:95–130, 2017.

[8] D. Allaerts and J. Meyers. Gravity waves and wind-farm efficiency in neutral and stable conditions. *Boundary-Layer Meteorology*, 166:269–299, 2018.

[9] D. Allaerts and J. Meyers. Sensitivity and feedback of wind-farm-induced gravity waves. *Journal of Fluid Mechanics*, 862:990–1028, 2019.

[10] R. J. Barthelmie and L. E. Jensen. Evaluation of wind farm efficiency and wind turbine wakes at the nysted offshore wind farm. *Wind Energy*, 13:573–586, 2010.

[11] R. J. Barthelmie, G. C. Larsen, S. T. Frandsen, L. Folkerts, K. Rados, S. C. Pryor, B. Lange, and G. Schepers. Comparison of wake model simulations with offshore wind turbine wake profiles measured by sodar. *Journal of Atmospheric and Oceanic Technology*, 23:888 – 901, 2006.

[12] R. J. Barthelmie, S. C. Pryor, S. T. Frandsen, K. S. Hansen, J. G. Schepers, K. Rados, W. Schlez, A. Neubert, L. E. Jensen, and S. Neckelmann. Quantifying the impact of wind turbine wakes on power output at offshore wind farms. *Journal of Atmospheric and Oceanic Technology*, 27:1302–1317, 2010.

[13] M. Bastankhah and F. Porté-Agel. A new analytical model for wind-turbine wakes. *Renewable Energy*, 70:116–123, 2014.

[14] M. Bastankhah and F. Porté-Agel. A new miniature wind turbine for wind tunnel experiments. part ii: Wake structure and flow dynamics. *Energies*, 10:923, 2017.

[15] M. Bastankhah, C. R. Shapiro, S. Shamsoddin, D. F. Gayme, and C. Meneveau. A vortex sheet based analytical model of the curled wake behind yawed wind turbines. *Journal of Fluid Mechanics*, 933:A2, 2022.

[16] M. Bastankhah, B. L. Welch, L. A. Martínez-Tossas, J. King, and P. Fleming. Analytical solution for the cumulative wake of wind turbines in wind farms. *Journal of Fluid Mechanics*, 911, 2021.

[17] N. Bempedelis, S. Laizet, and G. Deskos. Turbulent entrainment in finite-length wind farms. *Journal of Fluid Mechanics*, 955:A12, 2023.

[18] J. Bleeg. A graph neural network surrogate model for the prediction of turbine interaction loss. *Journal of Physics: Conference Series*, 1618:062054, 2020.

[19] J. Bleeg and C. Montavon. Blockage effects in a single row of wind turbines. *Journal of Physics: Conference Series*, 2265:22001, 5 2022.

[20] J. Bleeg, M. Purcell, R. Ruisi, and E. Traiger. Wind farm blockage and the consequences of neglecting its impact on energy production. *Energies*, 11:1609, 2018.

[21] F. Blondel and M. Cathelain. An alternative form of the super-gaussian wind turbine wake model. *Wind Energy Science*, 5:1225–1236, 2020.

[22] D. Cabezón, E. Migoya, and A. Crespo. Comparison of turbulence models for the computational fluid dynamics simulation of wind turbine wakes in the atmospheric boundary layer. *Wind Energy*, 14:909–921, 2011.

[23] M. Calaf, C. Meneveau, and J. Meyers. Large eddy simulation study of fully developed wind-turbine array boundary layers. *Physics of Fluids*, 22:1–16, 2010.

[24] M. Calaf, M. B. Parlange, and C. Meneveau. Large eddy simulation study of scalar transport in fully developed wind-turbine array boundary layers. *Physics of Fluids*, 23:126603, 2011.

[25] Carbon Trust. Global blockage effect in offshore wind (globe) [accessed 07/11/2022]. `https://www.carbontrust.com/our-projects/large-scale-rd-projects-offshore-wind/global-blockage-effect-in-offshore-wind-globe`, 2022.

[26] B. Cañadillas, R. Foreman, G. Steinfeld, and N. Robinson. Cumulative interactions between the global blockage and wake effects as observed by an engineering model and large-eddy simulations. *Energies*, 16:2949, 2023.

[27] L. P. Chamorro and F. Porté-Agel. Effects of thermal stability and incoming boundary-layer flow characteristics on wind-turbine wakes: A wind-tunnel study. *Boundary-Layer Meteorology*, 136:515–533, 2010.

[28] NOAA Climate.gov. Climate change: Atmospheric carbon dioxide [accessed 13/10/2023]. https://www.climate.gov/news-features/understanding-climate/climate-change-atmospheric-carbon-dioxide, 2023.

[29] A. S. Dar and F. Porté-Agel. An analytical model for wind turbine wakes under pressure gradient. *Energies*, 15:5345, 2022.

[30] K. Devesse, L. Lanzilao, S. Jamaer, N. van Lipzig, and J. Meyers. Including realistic upper atmospheres in a wind-farm gravity-wave model. *Wind Energy Science*, 7:1367–1382, 2022.

[31] K. Devesse, L. Lanzilao, and J. Meyers. A meso-micro atmospheric perturbation model for wind farm blockage. *arXiv.org*, 2023.

[32] T. D. Dunstan, T. Murai, and T. Nishino. Validation of a theoretical model for large turbine array performance under realistic atmospheric conditions. *AMS 23rd Symposium on Boundary Layers and Turbulence*, 2018.

[33] M. Dörenkämper, B. Witha, G. Steinfeld, D. Heinemann, and M. Kühn. The impact of stable atmospheric boundary layers on wind-turbine wakes within offshore wind farms. *Journal of Wind Engineering and Industrial Aerodynamics*, 144:146–153, 2015.

[34] T H Ellison and J S Turner. Turbulent entrainment in stratified flows. *Journal of Fluid Mechanics*, 6:423–448, 1959.

[35] The Crown Estate. Offshore wind report 2022. Technical report, The Crown Estate, 2023.

[36] Wind Europe. Wind energy in europe: 2022 statistics and the outlook for 2023-2027. Technical report, Wind Europe, 2023.

[37] J. Fischereit, R. Brown, X. G. Larsén, J. Badger, and G. Hawkes. Review of mesoscale wind-farm parametrizations and their applications. *Boundary-Layer Meteorology*, 182:175–224, 2022.

[38] A. C. Fitch. Climate impacts of large-scale wind farms as parameterized in a global climate model. *Journal of Climate*, 28:6160 – 6180, 2015.

[39] A. C. Fitch, J. B. Olson, and J. K. Lundquist. Parameterization of wind farms in climate models. *Journal of Climate*, 26:6439 – 6458, 2013.

[40] A. C. Fitch, J. B. Olson, J. K. Lundquist, J. Dudhia, A. K. Gupta, J. Michalakes, and I. Barstad. Local and mesoscale impacts of wind farms as parameterized in a mesoscale nwp model. *Monthly Weather Review*, 140:3017–3038, 2012.

[41] P. Flaszyński, F. Wasilczuk, M. Piotrowicz, J. Telega, K. Mitraszewski, and K. S. Hansen. Numerical simulations for a parametric study of blockage effect on offshore wind farms. *Wind energy*, 27:53–74, 2023.

[42] S. Frandsen. On the wind speed reduction in the center of large clusters of wind turbines. *Journal of Wind Engineering and Industrial Aerodynamics*, 39:251–265, 1992.

[43] S. Frandsen, R. Barthelmie, S. Pryor, O. Rathmann, S. Larsen, J. Højstrup, and M. Thøgersen. Analytical modelling of wind speed deficit in large offshore wind farms. *Wind Energy*, 9:39–53, 2006.

[44] S. T. Frandsen, H. E. Jørgensen, R. Barthelmie, O. Rathmann, J. Badger, K. Hansen, S. Ott, P.-E. Rethore, S. E. Larsen, and L. E. Jensen. The making of a second-generation wind farm efficiency model complex. *Wind Energy*, 12:445–458, 2009.

[45] J. R. Garratt. *The atmospheric boundary layer*. Cambridge University Press, 1992.

[46] N. S. Ghaisas and C. L. Archer. Geometry-based models for studying the effects of wind farm layout. *Journal of Atmospheric and Oceanic Technology*, 33:481–501, 2016.

[47] N. S. Ghaisas, C. L. Archer, S. Xie, S. Wu, and E. Maguire. Evaluation of layout and atmospheric stability effects in wind farms using large-eddy simulation. *Wind Energy*, 20:1227–1240, 2017.

[48] International Energy Agency (IEA). World energy outlook 2023. Technical report, IEA, 2023.

[49] IPCC. *Summary for Policymakers*, pages 3–32. Cambridge University Press, Cambridge, United Kingdom and New York, NY, USA, 2021.

[50] S. Jamaer, D. Allaerts, J. Meyers, and N. P. M. van Lipzig. A novel framework for spatio-temporal analysis of temperature profiles applied to europe. *Journal of Applied Meteorology and Climatology*, 62:1855–1873, 2023.

[51] F. Japar, S. Mathew, B. Narayanaswamy, C. M. Lim, and J. Hazra. Estimating the wake losses in large wind farms: A machine learning approach. *ISGT 2014, Washington, DC, USA*, pages 1–5, 2014.

[52] N. O. Jensen. A note on wind generator interaction. *Risø-M-2411 Risø National Laboratory Roskilde*, 1983.

[53] I. Katic, J. Hojstrup, and N. O. Jensen. A simple model for cluster efficiency. *Proceedings of the European wind energy association conference and exhibition, Rome, Italy*, pages 407–409, 1986.

[54] A. Keane, P. E. O. Aguirre, H. Ferchland, P. Clive, and D. Gallacher. An analytical model for a full wind turbine wake. *Journal of Physics: Conference Series*, 753:32039, 9 2016.

[55] A. Keane, I. Nisbet, G. Calvo, G. Pickering, J. Tulloch, G. More, and N. Koronka. Wind farm cumulative induction zone effect and the impact on energy yield estimation. *Renewable Energy*, 181:1209–1222, 2022.

[56] L. Lanzilao and J. Meyers. Set-point optimization in wind farms to mitigate effects of flow blockage induced by atmospheric gravity waves. *Wind Energy Science*, 6:247–271, 2021.

[57] L. Lanzilao and J. Meyers. Effects of self-induced gravity waves on finite wind-farm operations using a large-eddy simulation framework. *Journal of Physics: Conference Series*, 2265:22043, 5 2022.

[58] L. Lanzilao and J. Meyers. A new wake-merging method for wind-farm power prediction in the presence of heterogeneous background velocity fields. *Wind Energy*, 25:237–259, 2022.

[59] L. Lanzilao and J. Meyers. A parametric large-eddy simulation study of wind-farm blockage and gravity waves in conventionally neutral boundary layers. *Journal of Fluid Mechanics*, 979:A54, 2024.

[60] L. Legris, M. L. Pahus, T. Nishino, and E. Perez-Campos. Prediction and mitigation of wind farm blockage losses considering mesoscale atmospheric response. *Energies*, 16:386, 2023.

[61] T. Levick, A. Neubert, D. Friggo, P. Downes, R. Ruisi, and J. Bleeg. Validating the next generation of turbine interaction models. *Journal of Physics: Conference Series*, 2257:12010, 4 2022.

[62] C. Li, L. Liu, X. Lu, and R. J. A. M. Stevens. Analytical model of fully developed wind farms in conventionally neutral atmospheric boundary layers. *Journal of Fluid Mechanics*, 948:A43, 2022.

[63] P. B. S. Lissaman. Energy effectiveness of arbitrary arrays of wind turbines. *Journal of Energy*, 3:323–328, 1979.

[64] L. Liu, S. N. Gadde, and R. J. A. M. Stevens. Geostrophic drag law for conventionally neutral atmospheric boundary layers revisited. *Quarterly Journal of the Royal Meteorological Society*, 147:847–857, 2021.

[65] L. Liu, S. N. Gadde, and R. J. A. M. Stevens. Universal wind profile for conventionally neutral atmospheric boundary layers. *Phys. Rev. Lett.*, 126:104502, 3 2021.

[66] L. Liu and R. J. A. M. Stevens. Vertical structure of conventionally neutral atmospheric boundary layers. *Proceedings of the National Academy of Sciences*, 119:e2119369119, 2022.

[67] H. Lu and F. Porté-Agel. Large-eddy simulation of a very large wind farm in a stable atmospheric boundary layer. *Physics of Fluids*, 23:065101, 2011.

[68] H. Lu and F. Porté-Agel. On the impact of wind farms on a convective atmospheric boundary layer. *Boundary-Layer Meteorology*, 157:81–96, 2015.

[69] P. Luzzatto-Fegiz and C. P. Caulfield. Entrainment model for fully-developed wind farms: Effects of atmospheric stability and an ideal limit for wind farm performance. *Phys. Rev. Fluids*, 3:93802, 9 2018.

[70] L. Ma, T. Nishino, and A. F. Antoniadis. Prediction of the impact of support structures on the aerodynamic performance of large wind farms. *Journal of Renewable and Sustainable Energy*, 11:063306, 2019.

[71] O. Maas. Large-eddy simulation of a 15 gw wind farm: Flow effects, energy budgets and comparison with wake models. *Frontiers in Mechanical Engineering*, 9, 2023.

[72] O. Maas and S. Raasch. Wake properties and power output of very large wind farms for different meteorological conditions and turbine spacings: A large-eddy simulation case study for the german bight. *Wind Energy Science*, 7:715–739, 2022.

[73] L. A. Martínez-Tossas, M. J. Churchfield, and S. Leonardi. Large eddy simulations of the flow past wind turbines: Actuator line and disk modeling. *Wind Energy*, 18:1047–1060, 2015.

[74] L. A. Martínez-Tossas, M. J. Churchfield, and C. Meneveau. Optimal smoothing length scale for actuator line models of wind turbine blades based on gaussian body force distribution. *Wind Energy*, 20:1083–1096, 2017.

[75] J. Meyers and C. Meneveau. Large eddy simulations of large wind-turbine arrays in the atmospheric boundary layer. *48th AIAA Aerospace Sciences Meeting Including the New Horizons Forum and Aerospace Exposition*, 2010.

[76] J. Meyers and C. Meneveau. Optimal turbine spacing in fully developed wind farm boundary layers. *Wind Energy*, 15:305–317, 2012.

[77] B R Morton, Geoffrey Ingram Taylor, and John Stewart Turner. Turbulent gravitational convection from maintained and instantaneous sources. *Proceedings of the Royal Society of London. Series A. Mathematical and Physical Sciences*, 234:1–23, 1956.

[78] A. Niayifar and F. Porté-Agel. Analytical modeling of wind farms: A new approach for power prediction. *Energies*, 9:741, 2016.

[79] K. Nilsson, S. Ivanell, K. S. Hansen, R. Mikkelsen, J. N. Sørensen, S. P. Breton, and D. Henningson. Large-eddy simulations of the lillgrund wind farm. *Wind Energy*, 18:449–467, 2015.

[80] T. Nishino. Two-scale momentum theory for very large wind farms. *Journal of Physics: Conference Series*, 753:032054, 2016.

[81] T. Nishino and S. Draper. Local blockage effect for wind turbines. *Journal of Physics: Conference Series*, 625:012010, 2015.

[82] T. Nishino and T. D. Dunstan. Two-scale momentum theory for time-dependent modelling of large wind farms. *Journal of Fluid Mechanics*, 894:A2, 2020.

[83] T. Nishino and W. Hunter. Tuning turbine rotor design for very large wind farms. *Proceedings of the Royal Society A: Mathematical, Physical and Engineering Sciences*, 474:1–20, 2018.

[84] T. Nishino and R. H. J. Willden. Effects of 3-d channel blockage and turbulent wake mixing on the limit of power extraction by tidal turbines. *International Journal of Heat and Fluid Flow*, 37:123–135, 2012.

[85] N. G. Nygaard. Wakes in very large wind farms and the effect of neighbouring wind farms. *Journal of Physics: Conference Series*, 524:12162, 6 2014.

[86] N. G. Nygaard, L. Poulsen, E. Svensson, and J. G. Pedersen. Large-scale benchmarking of wake models for offshore wind farms. *Journal of Physics: Conference Series*, 2265:22008, 5 2022.

[87] N. G. Nygaard, S. T. Steen, L. Poulsen, and J. G. Pedersen. Modelling cluster wakes and wind farm blockage. *Journal of Physics: Conference Series*, 1618:062072, 2020.

[88] M. Optis and J. Perr-Sauer. The importance of atmospheric turbulence and stability in machine-learning models of wind farm power production. *Renewable and Sustainable Energy Reviews*, 112:27–41, 2019.

[89] M. L. Pahus, T. Nishino, A. Kirby, and C. R. Vogel. Control co-design of a large offshore wind farm considering the effect of wind extractability. *Journal of Physics: Conference Series*, 2767:92026, 6 2024.

[90] J. Park and J. Park. Physics-induced graph neural network: An application to wind-farm power estimation. *Energy*, 187:115883, 2019.

[91] K. Patel, T. D. Dunstan, and T. Nishino. Time-dependent upper limits to the performance of large wind farms due to mesoscale atmospheric response. *Energies*, 14:6437, 2021.

[92] J. G. Pedersen, E. Svensson, L. Poulsen, and N. G. Nygaard. Turbulence optimized park model with gaussian wake profile. *Journal of Physics: Conference Series*, 2265:22063, 5 2022.

[93] A. Peña, P.-E. Réthoré, C. B. Hasager, and K. S. Hansen. *Results of wake simulations at the Horns Rev I and Lillgrund wind farms using the modified Park model.* DTU Wind Energy, 2013.

[94] S. B. Pope. *Large-Eddy Simulation*, pages 558–640. Cambridge University Press, 2000.

[95] F. Porté-Agel, M. Bastankhah, and S. Shamsoddin. Wind-turbine and wind-farm flows: A review. *Boundary-Layer Meteorology*, 174:1–59, 2020.

[96] F. Porté-Agel, H. Lu, and Y.T. Wu. A large-eddy simulation framework for wind energy applications. *Fifth International Symposium on Computational Wind Engineering*, 2010.

[97] F. Porté-Agel, Y. T. Wu, and C. H. Chen. A numerical study of the effects of wind direction on turbine wakes and power losses in a large wind farm. *Energies*, 6:5297–5313, 2013.

[98] S. A. Renganathan, R. Maulik, S. Letizia, and G. V. Iungo. Data-driven wind turbine wake modeling via probabilistic machine learning. *Neural Computing and Applications*, 34:6171–6186, 4 2022.

[99] T. Revaz and F. Porté-Agel. Large-eddy simulation of wind turbine flows: A new evaluation of actuator disk models. *Energies*, 14:3745, 2021.

[100] B. Sanderse, S. P. van der Pijl, and B. Koren. Review of computational fluid dynamics for wind turbine wake aerodynamics. *Wind Energy*, 14:799–819, 2011.

[101] H. Sarlak, T. Nishino, L. A. Martínez-Tossas, C. Meneveau, and J. N. Sørensen. Assessment of blockage effects on the wake characteristics and power of wind turbines. *Renewable Energy*, 93:340–352, 2016.

[102] J. Schneemann, F. Theuer, A. Rott, M. Dörenkämper, and M. Kühn. Offshore wind farm global blockage measured with scanning lidar. *Wind Energy Science*, 6:521–538, 2021.

[103] J Schreiber, A Balbaa, and C L Bottasso. Brief communication: A double-gaussian wake model. *Wind Energy Science*, 5:237–244, 2020.

[104] A. Segalini and J.-Å. Dahlberg. Blockage effects in wind farms. *Wind Energy*, 23:120–128, 2020.

[105] C. R. Shapiro, D. F. Gayme, and C. Meneveau. Filtered actuator disks: Theory and application to wind turbine models in large eddy simulation. *Wind Energy*, 22:1414–1420, 2019.

[106] C. R. Shapiro, G. M. Starke, C. Meneveau, and D. F. Gayme. A wake modeling paradigm for wind farm design and control. *Energies*, 12:2956, 2019.

[107] W. Z. Shen, J. H. Zhang, and J. N. Sørensen. The actuator surface model: A new navier-stokes based model for rotor computations. *Journal of Solar Energy Engineering, Transactions of the ASME*, 131:011002, 2009.

[108] J. Smagorinsky. General circulation experiments with the primitive equations. *Monthly Weather Review*, 91:99–164, 1963.

[109] R. B. Smith. Gravity wave effects on wind farm efficiency. *Wind Energy*, 13:449–458, 2010.

[110] I Sood, E Simon, A Vitsas, B Blockmans, G C Larsen, and J Meyers. Comparison of large eddy simulations against measurements from the lillgrund offshore wind farm. *Wind Energy Science*, 7:2469–2489, 2022.

[111] R. J. A. M. Stevens. Dependence of optimal wind turbine spacing on wind farm length. *Wind Energy*, 19:651–663, 2016.

[112] R. J. A. M. Stevens, D. F. Gayme, and C. Meneveau. Large eddy simulation studies of the effects of alignment and wind farm length. *Journal of Renewable and Sustainable Energy*, 6:023105, 2014.

[113] R. J. A. M. Stevens, D. F. Gayme, and C. Meneveau. Coupled wake boundary layer model of wind-farms. *Journal of Renewable and Sustainable Energy*, 7:023115, 2015.

[114] R. J. A. M. Stevens, D. F. Gayme, and C. Meneveau. Effects of turbine spacing on the power output of extended wind-farms. *Wind Energy*, 19:359–370, 2016.

[115] R. J. A. M. Stevens, D. F. Gayme, and C. Meneveau. Generalized coupled wake boundary layer model: applications and comparisons with field and les data for two wind farms. *Wind Energy*, 19:2023–2040, 2016.

[116] R. J. A. M. Stevens, L. A. Martínez-Tossas, and C. Meneveau. Comparison of wind farm large eddy simulations using actuator disk and actuator line models with wind tunnel experiments. *Renewable Energy*, 116:470–478, 2018.

[117] R. J. A. M. Stevens and C. Meneveau. Flow structure and turbulence in wind farms. *Annual Review of Fluid Mechanics*, 49:311–339, 2017.

[118] R. J. A. M. Stevens and C. Meneveau. Large eddy simulation study of extended wind farms with large inter turbine spacing. *Journal of Physics: Conference Series*, 1618:062011, 2020.

[119] A. Stieren and R. J. A. M. Stevens. Impact of wind farm wakes on flow structures in and around downstream wind farms. *Flow*, 2:E21, 8 2022.

[120] S. Stipa, A. Ajay, D. Allaerts, and J. Brinkerhoff. The multi-scale coupled model: a new framework capturing wind farm-atmosphere interaction and global blockage effects. *Wind Energy Science Discussions*, 2023:1–44, 2023.

[121] J. M. I. Strickland, S. N. Gadde, and R. J. A. M. Stevens. Wind farm blockage in a stable atmospheric boundary layer. *Renewable energy*, 197:50–58, 2022.

[122] J. M. I. Strickland and R. J. A. M. Stevens. Effect of thrust coefficient on the flow blockage effects in closely-spaced spanwise-infinite turbine arrays. *Journal of Physics: Conference Series*, 1618:062069, 2020.

[123] J. M. I. Strickland and R. J. A. M. Stevens. Investigating wind farm blockage in a neutral boundary layer using large-eddy simulations. *European Journal of Mechanics - B/Fluids*, 95:303–314, 2022.

[124] R. B. Stull. *An introduction to boundary layer meteorology.* Kluwer Academic, 1988.

[125] F. Tartari and T. Nishino. Numerical study on the limit of power extraction by a dense cross-stream array of wind turbines. *European Journal of Mechanics, B/Fluids*, 65:350–358, 2017.

[126] Z. Ti, X. W. Deng, and H. Yang. Wake modeling of wind turbines using machine learning. *Applied Energy*, 257:114025, 2020.

[127] Z. Ti, X. W. Deng, and M. Zhang. Artificial neural networks based wake model for power prediction of wind farm. *Renewable energy*, 172:618–631, 2021.

[128] M. P. van der Laan, N. N. Sørensen, P.-E. Réthoré, J. Mann, M. C. Kelly, N. Troldborg, J. G. Schepers, and E. Machefaux. An improved k- model applied to a wind turbine wake in atmospheric turbulence. *Wind Energy*, 18:889–907, 2015.

[129] P. Veers, K. Dykes, S. Basu, A. Bianchini, A. Clifton, P. Green, H. Holttinen, L. Kitzing, B. Kosovic, J. K. Lundquist, J. Meyers, M. O'Malley, W. J. Shaw, and B. Straw. Grand challenges: wind energy research needs for a global energy transition. *Wind Energy Science*, 7:2491–2496, 2022.

[130] P. J. H. Volker, J. Badger, A. N. Hahmann, and S. Ott. The explicit wake parametrisation v1.0: a wind farm parametrisation in the mesoscale model wrf. *Geoscientific Model Development*, 8:3715–3731, 2015.

[131] S. Voutsinas. On the analysis of wake effects in wind parks. *Wind Engineering*, 14:204–219, 1990.

[132] J. R. West and S. K. Lele. Wind turbine performance in very large wind farms: Betz analysis revisited. *Energies*, 13:1–25, 2020.

[133] B. Wilson, S. Wakes, and M. Mayo. Surrogate modeling a computational fluid dynamics-based wind turbine wake simulation using machine learning. *2017 IEEE Symposium Series on Computational Intelligence (SSCI)*, pages 1–8, 2017.

[134] World Meteorological Organization (WMO). State of the global climate 2022. Technical report, WMO, 2023.

[135] K. L. Wu and F. Porté-Agel. Flow adjustment inside and around large finite-size wind farms. *Energies*, 10:2164, 2017.

[136] Y. T. Wu, T. L. Liao, C. K. Chen, C. Y. Lin, and P. W. Chen. Power output efficiency in large wind farms with different hub heights and configurations. *Renewable Energy*, 132:941–949, 2019.

[137] Y. T. Wu and F. Porté-Agel. Large-eddy simulation of wind-turbine wakes: Evaluation of turbine parametrisations. *Boundary-Layer Meteorology*, 138:345–366, 2011.

[138] Y. T. Wu and F. Porté-Agel. Atmospheric turbulence effects on wind-turbine wakes: An les study. *Energies*, 5:5340–5362, 2012.

[139] Y. T. Wu and F. Porté-Agel. Simulation of turbulent flow inside and above wind farms: Model validation and layout effects. *Boundary-Layer Meteorology*, 146:181–205, 2013.

[140] Y. T. Wu and F. Porté-Agel. Modeling turbine wakes and power losses within a wind farm using les: An application to the horns rev offshore wind farm. *Renewable Energy*, 75:945–955, 2015.

[141] S. Xie and C. L. Archer. A numerical study of wind-turbine wakes for three atmospheric stability conditions. *Boundary-Layer Meteorology*, 165:87–112, 2017.

[142] C. Yan, Y. Pan, and C. L. Archer. A general method to estimate wind farm power using artificial neural networks. *Wind Energy*, 22:1421–1432, 2019.

[143] X. Yang, S. Kang, and F. Sotiropoulos. Computational study and modeling of turbine spacing effects infinite aligned wind farms. *Physics of Fluids*, 24:11510, 2012.

[144] X. Yang and F. Sotiropoulos. On the predictive capabilities of les-actuator disk model in simulating turbulence past wind turbines and farms. *Proceedings of the American Control Conference*, pages 2878–2883, 2013.

[145] X. Yang and F. Sotiropoulos. Les investigation of infinite staggered wind-turbine arrays. *Journal of Physics: Conference Series*, 555:012109, 2014.

[146] A. Zapata, T. Nishino, and P. L. Delafin. Theoretically optimal turbine resistance in very large wind farms. *Journal of Physics: Conference Series*, 854:01205, 2017.

[147] N. Zehtabiyan-Rezaie and M. Abkar. An extended k-ϵ model for wake-flow simulation of wind farms. *Renewable Energy*, 222:119904, 2024.

[148] N. Zehtabiyan-Rezaie, A. Iosifidis, and M. Abkar. Data-driven fluid mechanics of wind farms: A review. *Journal of Renewable and Sustainable Energy*, 14:32703, 2022.

[149] J. Zhang and X. Zhao. Wind farm wake modeling based on deep convolutional conditional generative adversarial network. *Energy*, 238:121747, 2022.

[150] H. Zong and F. Porté-Agel. A momentum-conserving wake superposition method for wind farm power prediction. *Journal of Fluid Mechanics*, 889:A8, 2020.

[151] Ørsted. Ørsted presents update on its long-term financial targets [accessed 27/04/2022]. https://orsted.com/en/company-announcement-list/2019/10/1937002, 2019.